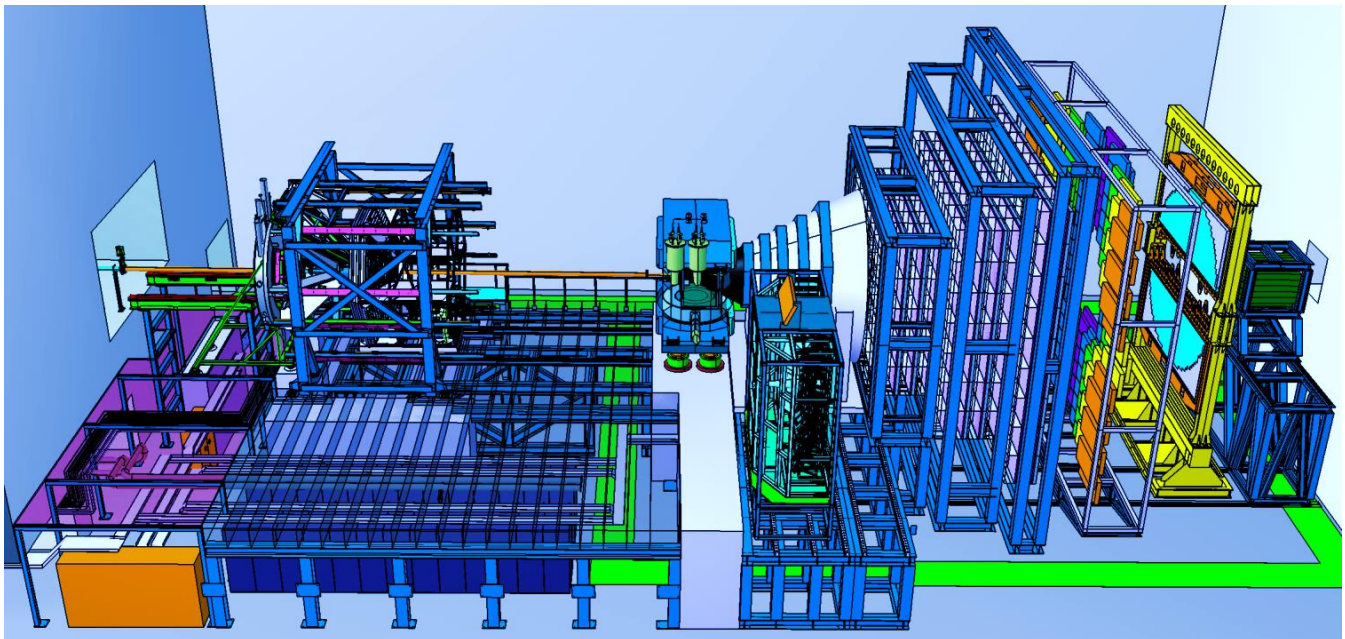

CBM

Compressed Baryonic Matter experiment at FAIR

PROGRESS REPORT

2013

CBM Progress Report 2013

ISBN 978-3-9815227-1-6

Editors: Volker Friese and Christian Sturm
v.friese@gsi.de c.sturm@gsi.de

Reviewers: C. Blume, M. Deveaux, V. Friese, N. Herrmann, J. Heuser, C. Höhne, W. Müller, P. Senger, C. Sturm

Printed in Darmstadt by GSI

This work was supported by
the Seventh Framework Programme (FP7) of the European Commission through projects AIDA, CRISP and HadronPhysics3;
the Bundesministerium für Bildung und Forschung, Germany, through grants 05P09PXFC5, 05P12PXFCE, 05P12RFFC7, 05P12RFFCM, 05P12RFFCP, 05P12RGFCG, 05P12RGGHM, 05P12VHFCE, 05P12VHFCF, 05PRVHFC7, and 06HD9123I;
the Deutsche Forschungsgemeinschaft, Germany, through grant GRK 1039;
the Hessian Loewe Initiative through the Helmholtz International Center for FAIR (HIC4FAIR);
the Helmholtz Graduate School HIRe;
the Helmholtz Research School H-QM;
the GSI Helmholzzentrum für Schwerionenforschung mbH, Germany, through F&E cooperations with Goethe-Universität Frankfurt, Justus-Liebig-Universität Gießen and Bergische Universität Wuppertal (WKAMPE1012);
the Department of Science and Technology, Government of India;
the Department of Atomic Energy, Government of India;
the Council of Scientific and Industrial Research, Government of India;
the University Grants Commission, Government of India;
the Indo-FAIR Co-ordination Centre, Bose Institute, Kolkata, India;
the Strategic Grants POSDRU/89/1.5/S/58852 and PN-II-ID-PCE-IDEI 34/05.10.2011, Romania;
the NASR/CAPACITATI-Modul III, Romania, contract nr. 179EU;
the NASR/NUCLEU Project PN09370103, Romania;
the FAIR Russia Research Center (FRRC), Russia;
and the Federal Agency for Atomic Research (Rosatom), Russia.

Preface

Dear Colleagues,

The year 2013 was very successful for FAIR and CBM.

Using the biggest drilling machines available in Europe, the 1400 x 60 m deep reinforced concrete pillar foundations have almost been completed - a half year earlier as planned.

With special focus on the Technical Design Reports, in the meantime TDRs on the Silicon Tracking System, the Superconducting Magnet and on the RICH have been approved. The TDRs on the PSD, the TOP-RPC and the MuCh have been submitted and are presently under evaluation by the FAIR-ECE. Hence, the CBM Collaboration has submitted six out of nine TDRs totally foreseen. Congratulations and many thanks!

With the year progressing, we should concentrate on submission of the remaining TDRs as well as on the engineering design of the experiment components. On this note, I wish everyone continued success in your activities.

Peter Senger

Contents

Status of the Compressed Baryonic Matter (CBM) experiment at FAIR

P. Senger and the CBM collaboration
GSI, Darmstadt, Germany

The Compressed Baryonic Matter (CBM) experiment will be one of the major scientific pillars of the future Facility for Antiproton and Ion Research (FAIR) in Darmstadt. The goal of the CBM research program is to explore the QCD phase diagram in the region of high net-baryon densities using high-energy nucleus-nucleus collisions. A sketch of the QCD phase diagram is shown in figure 1, highlighting the expected structures at large baryon chemical potentials: a first order-phase transition separating the hadronic phase from quarkyonic matter [2], followed towards larger baryon-chemical potentials by the quark-gluon plasma at high temperatures, and by exotic phases at low temperatures. At small baryon-chemical potentials, theory predicts a smooth crossover between hadronic and partonic matter. According to transport calculations, baryonic densities of about 6 times saturation density can be reached in central collisions between gold nuclei at 10 A GeV, an energy which will be provided by the future SIS100 machine. At these densities, quarkyonic matter is expected to be created. A similar state of matter, a mixture of strange baryons and free quarks, is predicted to exist in the core of neutron stars at densities beyond 4 times saturation density [3].

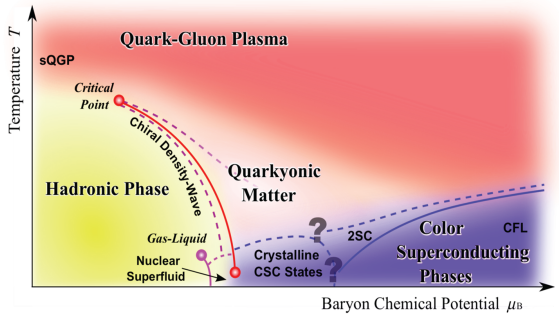

Figure 1: Sketch of the QCD phase diagram [1]

The CBM research program includes the study of the equation-of-state of nuclear matter at neutron star core densities, the search for the chiral phase transition, and for new forms of strongly interacting matter. The CBM detector is designed to measure rare diagnostic probes such as multi-strange hyperons, charmed particles and vector mesons decaying into lepton pairs with unprecedented precision and statistics. In the following, the results of the technical developments in 2013 will be briefly reviewed.

The superconducting dipole magnet

The design of the CBM SC dipole magnet has been optimized. It has a large aperture (gap height 140 cm, gap width 260 cm) in order to host the Silicon Tracking System. The field integral is 1 Tm. Detailed quench calculations have been performed, and the quench protection system has been designed. The Technical Design Report has been approved in January 2014.

The Micro-Vertex Detector

A refined geometry of the CBM-MVD based on 4 detector stations has been developed. Together with IPHC Strasbourg the 0.18 μm CMOS process has been investigated with respect to radiation hardness and noise. The 2^{nd} generation of MAPS read-out and TRBv3-based data acquisition has been developed. The Analysis of the CERN-SPS test beam data has been concluded, reproducing the intrinsic features of the MAPS chips mounted in the prototype and validating the general concept of the MVD integration.

The Silicon Tracking System

For the CBM Silicon Tracking System (STS) double-sided micro-strip sensors in all required dimensions (6.2×6.2 cm^2, 6.2×4.2 cm^2, 6.2×2.2 cm^2) have been produced in cooperation with CiS, Erfurt, Germany and Hamamatsu, Japan. The front side strips are inclined by 7.5°. In order to interconnect short strips in the sensor corners to a strip in the opposite corner the sensors are equipped either with a second metallization layer, or with pads for an additional micro-cable. The performance of both options will be investigated. Each sensor (2048 strips) will read out via 16 low-mass micro cables (128 wires each) by 16 free-streaming ASICs 125 channels each). A mockup of such a module has been produced, and the tab-bonding of the cables has been successfully tested. Several of these modules consisting of a sensor, the cables and the front-end board carrying 8 ASICs will be mounted on a light-weight carbon ladder. Up to 16 of these ladders will be integrated into a detector station. A mechanical mockup of a half station has been built. A prototype CO_2 cooling system has been designed. Several prototype modules comprising single and daisy-chained sensors, read-out cables and a free-streaming read-out-system has been successfully tested in December 2013 with a proton beam at COSY/Research Center Jülich. The STS Technical Design Report submitted to FAIR in December 2012 has been approved in August 2013.

The Ring Imaging Cherenkov (RICH) detector

The analysis of beam time data from the test campaign in 2012 has been finalized. Important results have been ob-

tained on the performance of the different photon sensors, on the optimal wavelength-shifter coverage, and on the requirements for mirror alignment and gas purity. In the lab new testing devices for single photon scans of photon sensors and the mirror surface have been set up. A larger prototype of the mirror wall is being constructed to perform tests of its stability while minimizing the material budget. The RICH Technical Design Report has been submitted in June 2013, and was approved in January 2014.

The Transition Radiation Detector

The analysis of the test beam established that all full size prototypes (by the groups from Bukarest, Frankfurt and Münster) perform according to the specification in terms of electron-pion separation. Several promising foam-type radiator materials have been identified. The SPADIC 1.0 readout chip has been finalized and tested and can now be commissioned for the upcoming test beams. Also, feature extraction algorithms have been implemented and are ready for tests with real data. The writing of the Technical Design Report is in progress.

The Muon Detection System

The layout of the Muon Chamber system (MuCh) and its performance have been optimized by replacing the first 20 cm thick iron absorber by a 60 cm thick carbon absorber. The mechanical structures supporting the detectors and the absorbers have been designed. A large area (31×31 cm^2) triple-GEM chamber made from single-mask foils has been built by the group in VECC Kolkata and successfully tested in December 2013 with a proton beam at COSY/FZ Jülich. Various prototype hybrid detector systems based on GEM and micromegas technologies have been built and tested at PNPI Gatchina. A full-size prototype Straw-chamber has been built at JINR Dubna. The development of a read-out ASIC has been started at MEPhI in Moscow. The MuCh Technical Design Report has been submitted in December 2013.

The time-of-flight system

The CBM - TOF - wall will mostly be composed of differential impedance matched strip MRPCs that are adjusted to the strongly polar angle dependent particle fluxes by implementing different strip lengths and employing low resistance electrodes where necessary. The low resistance electrodes can be constructed by ceramic, low resistivity glass or for more moderate rate requirements by thin standard glasses. Supermodule designs based on pad - MRPCs for the small polar angles are made available and might offer some advantage in terms of cost and rate capability.The exact layout of the wall is being optimized with the help of a newly created generic geometry description in the CBM simulation framework that also includes a proper description of the passive materials. For the first time a free streaming data processing chain based an the PADI and GET4 ASICs was realized with prototype detectors signals demonstrating the feasibility to achieve system timing resolutions in the order of 80 ps without any noticable dead time. First step are undertaken towards a common software framework capable of handling test beam data and simulations in a consistent way. The TOF Technical Design Report has been submitted in December 2013.

The Projectile Spectator Detector

The layout of the Projectile-Spectator detector (PSD), its distance from the target, and the settings of the magnetic field have been optimized in order to improve the performance in determining the reaction plane and the collision centrality over the full SIS100/300 beam energy range. The PSD Technical Design Report has been submitted in April 2013.

DAQ and First Online Event Selection (FLES)

In order to achieve the required precision, the measurements will be performed at very high reaction rates of 1 to 10 MHz. This requires a novel data read-out and analysis concept based on free streaming front-end electronics and a high-performance computing cluster for online event reconstruction and selection. The development of the full read-out and analysis chain based on detector hits with time stamps is in progress. The FLES system consists of a scalable supercomputer with custom FPGA-based input interface cards and a fast event-building network. It will be largely constructed from standard components, and will be located in the new FAIR data center. The submission of the DAQ/FLES Technical Design Report is planned for 2014.

Status of the Technical Design Reports

Subsystem	Status TDR
Superconducting Dipole Magnet	approved
Micro-Vertex Detector	submission 2014
Silicon Tracking System	approved
Ring Imaging Cherenkov Detector	approved
Time-of-Flight wall	in evaluation
Transition Radiation Detector	submission 2014
Muon Tracking Chambers	in evaluation
Projectile Spectator Detector	in evaluation
Electromagnetic Calorimeter	submission 2014
DAQ/First Level Event Selection	submission 2014

References

[1] K. Fukushima and T. Hatsuda, Rept. Prog. Phys. **74** (2011) 014001

[2] L. McLerran and R. D. Pisarski, Nucl. Phys. **A 796** (2007) 83

[3] M. Orsaria *et al.*, arXiv:1308.1657

The CBM building

W. Niebur, C. Ehmer, T. Heinz, E. Schwab, and A. Wolf
GSI, Darmstadt, Germany

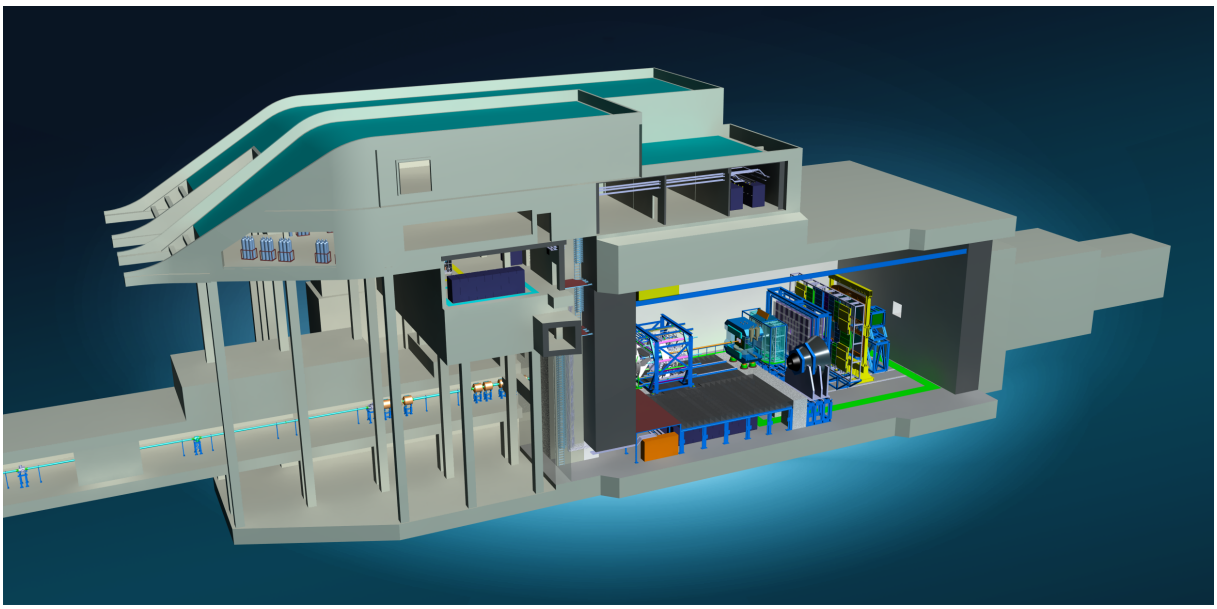

Figure 1: The CBM building housing CBM as well as the HADES experimental setup

After four years of work, the planning of the building housing the CBM as well as HADES experiment is now completed. The building (see Fig. 1) has a length of 114.5 m, a width of 31.75 m and a total height of 34.5 m. It comprises five levels with a total area of 2275 m^2, housing the technical infrastructure, meeting rooms, staff rooms, assembly rooms and control rooms and, last but not least, the experimental setup itself on 799 m^2. The cave for the experiment is 36.75 m long, 21.75 m wide and has a height of 17.4 m. For the movement of heavy loads, the building is equipped with two cranes of 30 t each.

The beam dump with a total length of 16.5 m will be made of 548 steel slabs with a thickness of 1.2 to 3.6 cm and a feed size of 2 m × 1.6 m (see Fig. 2), in total 407 m^3 of iron with a weight of about 3200 t. The steel slabs will be recycled from the cosmic ray shower experiment KASCADE which was operated at the Karlsruhe Institute of Technology KIT until the year 2011.

The construction of the building will consume 43455 m^3 of armoured concrete. The total weight of the building, excluding the experimental set, amounts to 112061 t. Because of its weight and of the rather soft subsoil on the FAIR building site, the building will be grounded on 117 concrete poles, with a diameter of 1.2 m and a length of 32 m - 40 m each (see Fig. 3). In total, 4683 m of boreholes will be drilled into the ground for this purpose. The drilling of the boreholes and the pouring of the concrete have already started and will be finished in summer 2014. The construction time of the CBM building will be about 2 - 2.5 years.

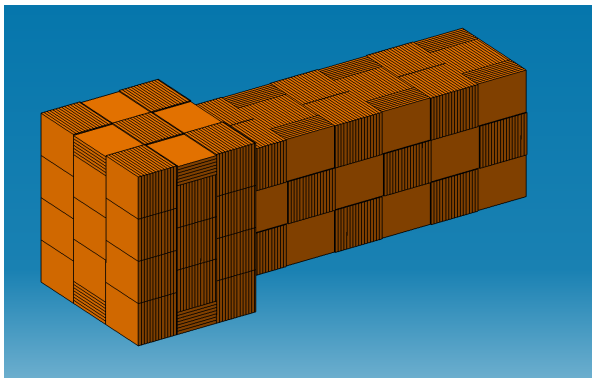

Figure 2: Design of the CBM beam dump which will be made of 548 recycled steel slabs

Fig. 4 shows the engineering design of the CBM experimental setup, the muon chamber system (MUCH) in measuring position and the ring imaging cherenkov detector (RICH) in stand-by position.

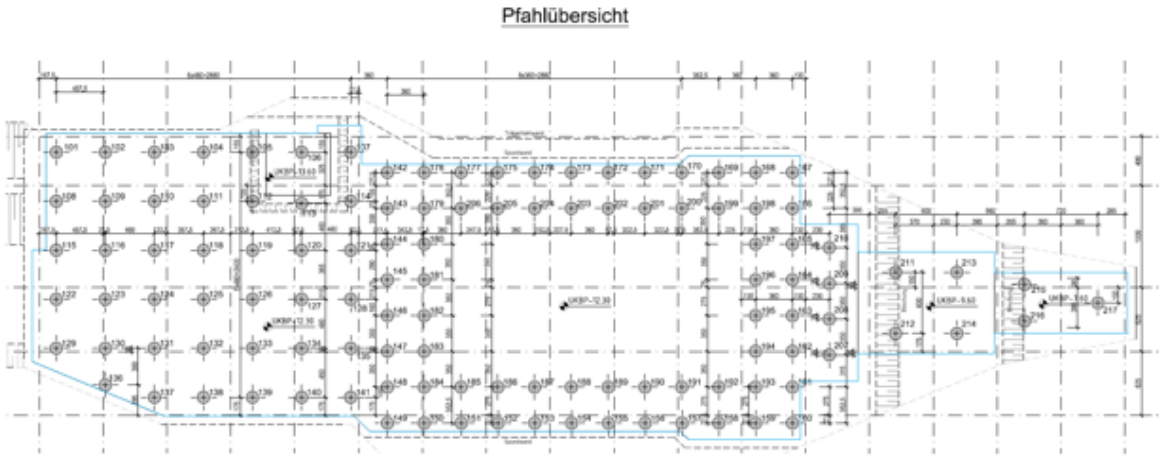

Figure 3: Grounding of the CBM building on 117 poles (taken from FAIR CC)

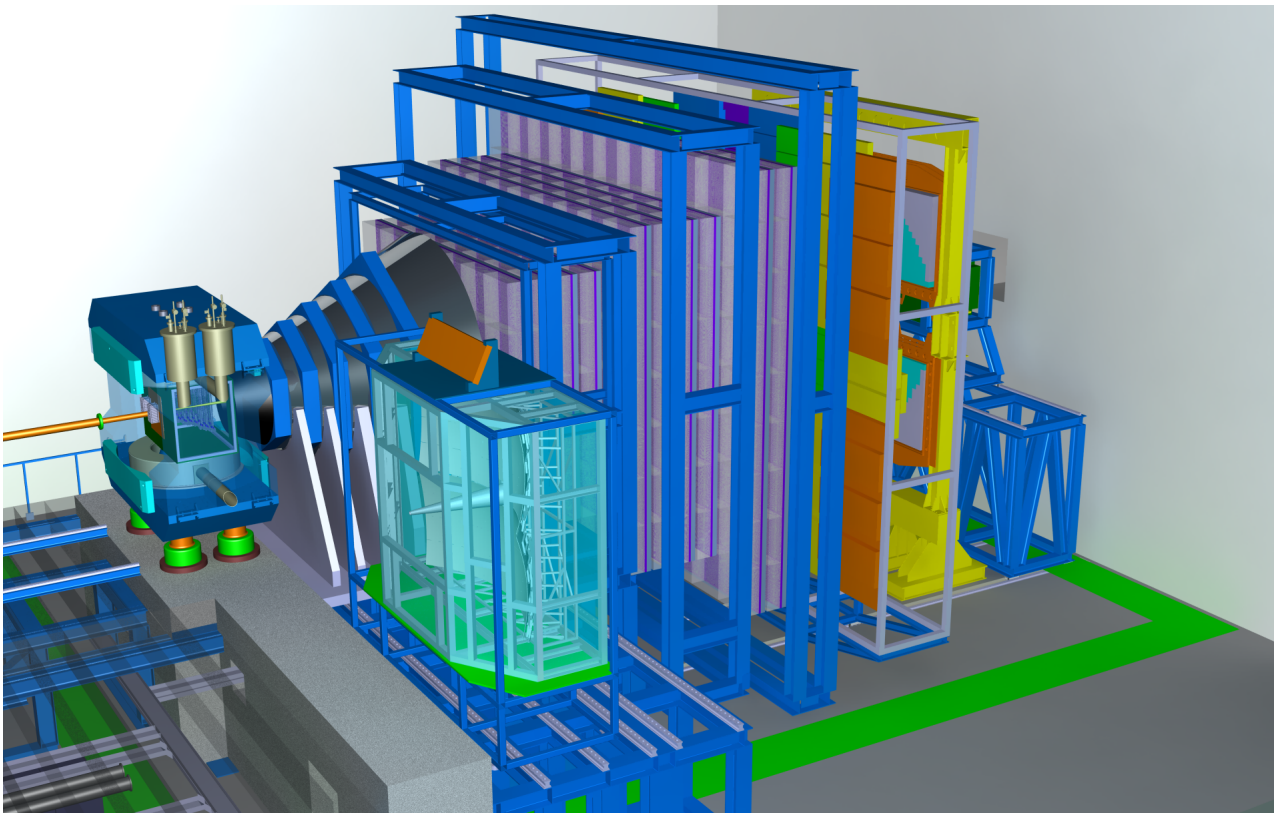

Figure 4: Engineering design of the CBM experimental setup - the ring imaging cherenkov detector (RICH) in stand-by position and the muon chamber system (MUCH) in measuring position

Superconducting Dipole Magnet

Superconducting dipole magnet for the Compressed Baryonic Matter (CBM) experiment at FAIR

P. Akishin[1], *A. Bychkov*[1], *E. Floch*[2], *Yu. Gusakov*[1], *V. Ivanov*[1], *P. Kurilkin*[1], *V. Ladygin*[1], *H. Leibrock*[2], *A. Malakhov*[1], *G. Moritz*[2], *C. Mühle*[2], *W. F. J. Müller*[2], *W. Niebur*[2], *H. Ramakers*[2], *P. Senger*[2], *A. Shabunov*[1], *P. Szwangruber*[2], *F. Toral*[3], *Y. Xiang*[2], *and C. Will*[2]

[1]JINR, Dubna, Russia; [2]GSI, Darmstadt, Germany; [3]CIEMAT, Madrid, Spain

The CBM superconducting dipole magnet is a central part of the detector system. The target station and the Silicon Tracking System are placed in the magnet gap. The magnet has to provide a vertical magnetic field with a bending power of 1 Tm over a length of 1 m from the target. A perspective view of the magnet is shown in Fig. 1.

The magnet gap has a height of 140 cm and a width of 250 cm in order to accommodate the STS with a polar angle acceptance of $\pm 25°$ and a horizontal acceptance of $\pm 30°$. The magnet is of H-type with a warm iron yoke/pole and cylindrical superconducting coils in two separate cryostats like the SAMURAI magnet at RIKEN [1, 2]. The potted coil has 1749 turns. The wire, similar to the CMS wire, has Nb-Ti filaments embedded in a copper matrix and is soldered in a copper stabilizer with a total Cu/SC ratio of about 13 in the conductor. The operating current and the maximal magnetic field in the coils are 686 A and 3.25 T, respectively. The coil case made of stainless steel contains 20 liters of liquid helium for one coil. The vertical force in the coils is about 250 t. The cold mass is suspended from the room-temperature vacuum vessel by six suspension links. Six cylindrical support struts compensate the vertical forces.

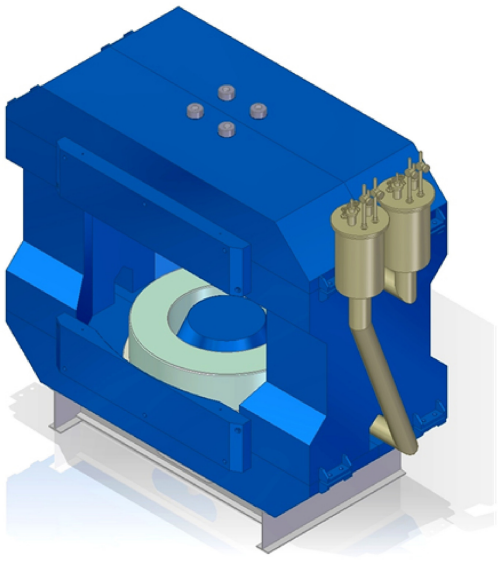

Figure 1: View of the CBM superconducting magnet

Table 1: Parameters of the CBM dipole magnet

Type	H-type, SC magnet
number of turns	1749 per coil
windings of coil	impregnated close coiling
maximum current	686 A
magnetomotive force	1.2 MA turns/coil
current density	48 A/mm2
central field	1.08 T
field integral	1 Tm
maximum field at coil	3.25 T
inductance	396 – 150 H
stored energy	5.15 MJ
Coil	
inner diameter	1.37 m (at 4 K)
outer diameter	1.82 m (at 4 K)
cross section	149.2 x 168 mm^2 (at 4 K)
weight	1644 kg/coil
Pole	
shape	circular type
gap	1.4 m
diameter	0.8/1.16 m
height	0.5 m
Yoke	
width	4.4 m
depth	2.0 m
height	3.7 m
weight	170 t

The energy stored in the magnet is about 5 MJ. The magnet will be self-protecting. However, in order to limit the temperature rise to 100 K in case of a quench, the energy will be dumped in an external resistor. The parameters of the magnet are listed in Table 1.

References

[1] H. Sato *et al.*, *Design of a large-gap superconducting dipole magnet for the SAMURAI spectrometer*, RIKEN Accel. Prog. Rep.**43** (2010) 180

[2] H. Sato *et al.*, *Superconducting Dipole Magnet for SAMURAI Spectrometer*, IEEE Trans. ASC **23** (2013) 4500308

[3] The CBM collaboration, *Technical Design Report for the CBM Superconducting Dipole Magnet*, Darmstadt 2014

Design calculations for the superconducting dipole magnet for the Compressed Baryonic Matter (CBM) experiment at FAIR

P. Akishin[1], *A. Bychkov*[1], *E. Floch*[2], *Yu. Gusakov*[1], *V. Ivanov*[1], *P. Kurilkin*[1], *V. Ladygin*[1], *H. Leibrock*[2], *A. Malakhov*[1], *G. Moritz*[2], *C. Mühle*[2], *W. F. J. Müller*[2], *W.'Niebur*[2], *H. Ramakers*[2], *P. Senger*[2], *A. Shabunov*[1], *P. Szwangruber*[2], *F. Toral*[3], *Y. Xiang*[2], *and C. Will*[2]

[1]JINR, Dubna, Russia; [2]GSI, Darmstadt, Germany; [3]CIEMAT, Madrid, Spain

Calculations have been performed to design the coil case, the coil vessel, the support links and the quench protection scheme for the CBM superconducting dipole magnet. The general parameters of the magnet are discussed in a separate contribution to this Progress Report. The code TOSCA was used for calculating electromagnetic forces exerted on the coil, while the structural analysis was made using the code ANSYS. The radial and vertical forces were calculated at 1.08 T with TOSCA as a function of the azimuthal angle of the coil. The radial force points towards the outer direction, while the vertical force attracts the coil toward the iron yoke. The integrated forces along the coil circumference are radially 60 t and vertically 254 t. The ANSYS calculation was based on the results of TOSCA. A detailed description of the engineering design of the superconducting coils can be found in Ref. [1]

Coil case and winding

The coil case is designed considering two main functions: one is to protect the windings against magnetic forces during operation, and the other is to use the case as a container for liquid helium (LHe) to cool the winding. The total volume of LHe in the coil case and the current leads box is about 20 liters. The case is welded of stainless steel 316LN [2] with a minimal thickness of 20 mm. The cross section is 230 mm by 230 mm. The coil is wound on the coil case and separated from it by four sets of the spacers made of NEMA G10 and two aluminum circular shims.

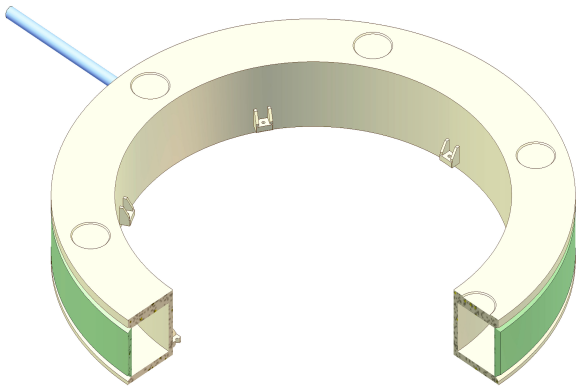

Figure 1: Top view and the cross section of the coil

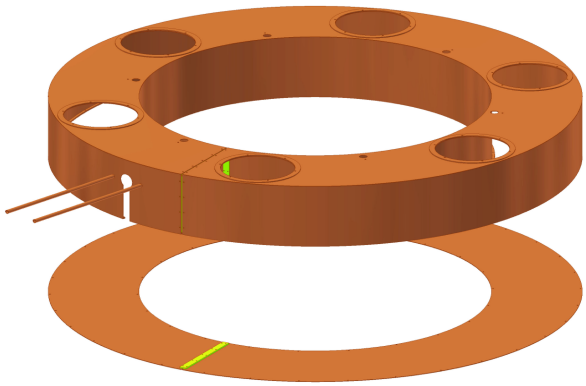

Figure 2: Top view of the thermal shield

The space between the spacers is used for the liquid helium circulation. Two sets of the spacers are glued on the aluminum shims, one directly on the bobbin, the other one directly on the coil. The cable has two layers of insulation with total thickness of 0.26 mm and 0.31 mm. Because of the same winding pattern, only one turn out of 1749 shall be lost. The winding is done with pretension of 20 kg and brush impregnation. Each layer is insulated with three layers of 0.1 mm fiber glass fabric with epoxy resin. To reduce the heat flux to the helium system, the outer surface of the casing will be wrapped with 20 layers of a multi-layer insulation.

Termal shield

The thermal shield (Fig. 2) consists of two main pieces: the top shield and the cover. The shield has a radial cut for an electrical break. All pieces are made of copper sheets each 2 mm thick. The top shield has oval copper cooling pipes with an outer dimension of 20 mm $\times$ 8 mm for cold helium gas to intercept thermal radiation from the cryostat. To reduce the heat flux to the helium system, the outer surface of the thermal shield will be wrapped with 20 layers of insulation. The thermal shield is suspended by the support struts.

Suspension

The coil case (4,5 K) and the thermal shield (80 K) are suspended from the room-temperature (RT) vacuum vessel

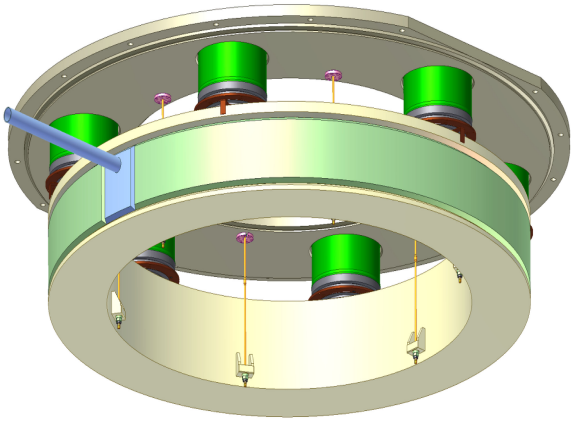

Figure 3: Top view of the coil suspension

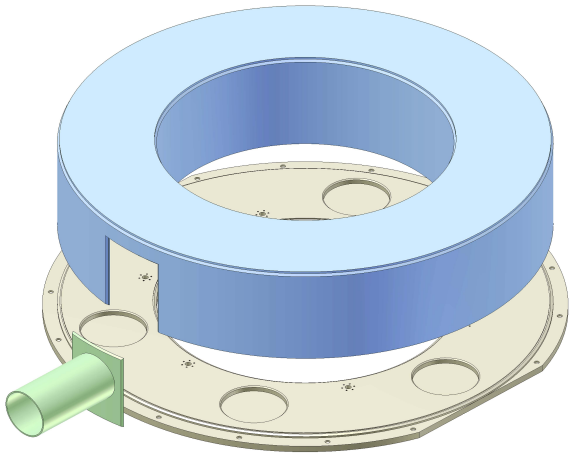

Figure 5: Top view of the vacuum vessel

using six support struts and six tie rods (Fig. 3). The support struts (Fig. 4a) are placed between the iron yoke and the coil case and act against the vertical component of the Lorentz forces. The nominal compression force per strut is 42 tons [3]. The support strut consists of four composite tubes nested coaxially in each other and connected in series by three stainless steel tubes with Z-shaped cross section. The composite tubes are polar wound tubes with glass fibers and epoxy resin. The glass fiber composite has small thermal conductivity at low temperature. The Z-shape tubes are made of the SAE 304 stainless steel. Five layers of MLI are inserted in each gap between the tubes. The middle tube is connected with the thermo shield at a temperature of 80 K. The tie rods (Fig. 4b) made of titanium alloy Ti 5Al 2.5Sn provide the 500 kg pre-compression for each support strut when the magnet is switched off.

Vacuum vessel

The vacuum vessel seals the vacuum around the cold mass to allow the cooling system to reach the desired cryogenic temperature. The vacuum vessel consists of a support ring and a shell. All parts are made of stainless steel SAE 304 [2]. The thickness of the shell is 15–20 mm. The support ring is 48 mm thick. The vacuum vessel will be assembled by welding. Figure 5 shows the top view of the vacuum vessel.

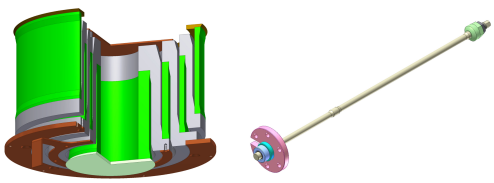

a) b)

Figure 4: Top view of (a) support strut and (b) tie rod

Quench protection

A detailed description of the quench calculations and the quench detection and protection scheme for the CBM dipole magnet can be found in separate contributions to this Progress Report. Quench calculations showed that the magnet is self-protecting against both temperature and voltages: coil-to-ground and coil-to-coil.

Two 3-D simulation codes (GSI and CIEMAT) of the quench process were used in the calculation, detailed descriptions of which are given in Refs. [4] and [5], respectively. The 3-D calculations performed for a magnet without a dump resistor give an average pole temperature of 90 K, a hotspot temperature of 160 K, and a maximum quench voltage of 1240 V. In this case, the entire magnet energy (5.15 MJ) is dissipated in the magnet.

When using an external dump resistor of 2.1 Ω, about 85 % of the 5.15 MJ can be dissipated in the resistor. In this case, the maximum voltage across the magnet of 1441 V occurs when the dump resistor turns on. The average pole temperature and the hotspot temperature are 48 K and 68 K, respectively.

References

[1] The CBM collaboration, *Technical Design Report for the CBM Superconducting Dipole Magnet*, Darmstadt 2014

[2] R. Walsh *et al.*, *Cold work study on a 316LN modified alloy for the ITER TF coil conduit*, AIP Conf. Proc. **1435** (2012) 63

[3] T. Kabo (RIKEN), private communication

[4] P. Szwangruber *et al.*, *Three-Dimensional Quench Calculations for the FAIR Super-FRS Main Dipole'*, IEEE Trans. ASC **23** (2013) 4701704

[5] F. Toral, *Design and Calculation Procedure for Particle Accelerator Superconducting Magnets: Application to an LHC Superconducting Quadrupole*, Ph. D. Thesis, Madrid 2001

Quench calculation for the CBM dipole magnet

P. Kurilkin[1], P. Szwangruber[2], E. Floch[2], F. Toral[3], A. Malakhow[1], and V. Ladygin[1]
[1]LHEP-JINR, Dubna, Russian Federation; [2]GSI, Darmstadt, Germany; [3]CIEMAT, Madrid, Spain

The CBM dipole magnet will store about 5.15 MJ at its nominal current of 686 A. When designing the quench protection scheme for the magnet, it is important to estimate the overall characteristics of the quench process in the coil.

Three types of quench calculations were performed for the CBM dipole magnet: "first approximation", instantaneous quench and 3-D calculation using the GSI [1] and CIEMAT [2] quench programs.

The "first approximation" is a simplified calculation which can be used to obtain a good approximation of the average coil temperature $T_{\rm av}$ and the maximum quench voltage $V_{\rm qm}$ for self-protecting magnets. $T_{\rm av}$ can be derived from the equation

$$\frac{E}{V_{\rm c}} = \int_{4.5K}^{T_{\rm av}} C_{\rm v}(T)dT\,, \qquad (1)$$

where E is the magnet energy, $V_{\rm c}$ is the coil volume and $C_{\rm v}$ is the volumetric specific heat. In our case, $T_{\rm av}$ is 90 K.

Having $T_{\rm av}$, one can estimate $V_{\rm qm}$ using the empiric formula [3]

$$V_{\rm qm} = 0.403 \cdot R_{\rm pole}(T_{\rm av}) \cdot I_{\rm n}\,, \qquad (2)$$

where $I_{\rm n}$ is the nominal current and $R_{\rm pole}(T_{\rm av}) = \rho_{\rm Cu}(T_{\rm av}) \cdot 1749 \cdot 5/A_{\rm Cu}$. In this case, $R_{\rm pole}(T_{\rm av}) = 4.7\,\Omega$ and $V_{\rm qm} = 1307$ V.

Instantaneous quench means that the whole coil is heated up instantaneously above the critical temperature. It is assumed that one coil has uniform temperature ($T_{\rm av}$) and field ($B_{\rm av}$) distributions. At the start of the quench, $T_{\rm av}$ is 10 K and $B_{\rm av} = B_{\rm max}(I_{\rm n})/2$, where $I_{\rm n}$ is the nominal current.

For a short-circuited magnet, the electrical equation [3] gives the current decrease as

$$dI = -\frac{R_{\rm q}(T_{\rm av}) \cdot I}{L_{\rm d}(I)} \cdot dt\,, \qquad (3)$$

where $L_{\rm d}$, $R_{\rm q}$ are the differential inductance and the resistance of the coil, respectively. dt is the time which corresponds to the current increase dI [3]. From the heat equation written for one pole one gets the temperature increase as

$$dT_{\rm av} = \frac{R_{\rm q}(T_{\rm av}) \cdot I^2}{V_{\rm c} \cdot C_{\rm p,av}(T_{\rm av})} \cdot dt\,, \qquad (4)$$

where $V_{\rm c}$ is the coil volume and $C_{\rm p,av}$ the average specific heat. The instantaneous quench calculation takes into account the inductance function $L_{\rm d}(I)$ and $B_{\rm max}(I)$. It gives an average temperature of about 90 K. The resistance of the quenched pole is 4.7 Ω and the maximum quench voltage is 1230 V.

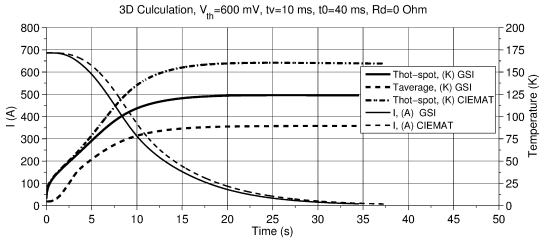

Figure 1: 3-D quench calculation of the CBM dipole: magnet current, hot-spot temperature and average coil temperature

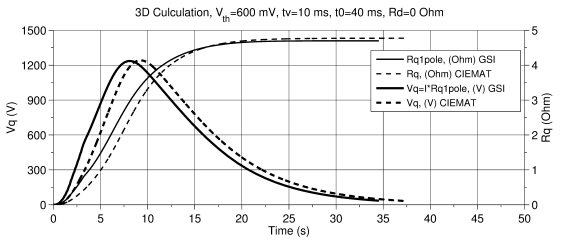

Figure 2: 3-D quench calculation of the CBM dipole: quench voltage and quench resistance

The 3-D quench analysis was performed using the GSI [1] and CIEMAT [2] programs. The results of the calculations when no dump resistor was used are presented in Figs. 1 and 2. The difference between the results calculated with the GSI and CIEMAT models is related to the different field map distribution in the coil and also to different material data bases used in those programs. The maximum hot-spot temperature and quench voltage are 160 K and 1240 V, respectively.

The results presented above show that the CBM dipole magnet is self-protecting.

References

[1] P. Szwangruber *et al.*, *Three-Dimensional Quench Calculations for the FAIR Super-FRS Main Dipole*, IEEE Trans. ASC **23** (2013) 4701704

[2] F. Toral, *Design and Calculation Procedure for Particle Accelerator Superconducting Magnets: Application to an LHC Superconducting Quadrupole*, Ph. D. Thesis, Madrid 2001

[3] E. Floch, *Magnet inductances and quench computations*, MT-INT-ErF-2009-010

Quench detection and protection system for the CBM dipole magnet

P. Kurilkin[1], *P. Szwangruber*[2], *H. Ramakers*[2], *E. Floch*[2], *and F. Toral*[3]
[1]LHEP-JINR, Dubna, Russian Federation; [2]GSI, Darmstadt, Germany; [3]CIEMAT, Madrid, Spain

The CBM dipole magnet has very large dimensions and stores about 5.15 MJ. An adequate protection of the superconducting CBM dipole magnet means minimizing the coil peak temperature and the resistive-inductive voltage imbalances, which can generate large voltages to the ground.

The quench protection of the CBM dipole magnet will be based on the extraction of the stored magnetic energy in an external dump resistor to avoid vaporization of helium. Figs. 1 and 2 present the results of 3-D quench calculations using the GSI [1] and the CIEMAT [2] codes. Detailed information on the data used in the calculations can be found in Ref. [3]. Both models predict a maximum hot-spot temperature on the level of 70 K. The maximum quench voltage is 249 V (190 V) for the GSI and CIEMAT computations, respectively. The maximum voltage across the magnet (1441 V) occurs when the dump resistor turns on. The difference between the calculated results is related to the different field map distribution in the coil and to the different material data bases used in the programs.

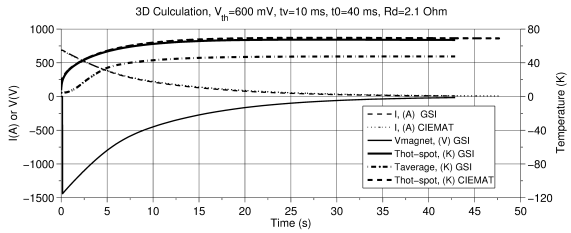

Figure 1: 3-D quench calculation of the CBM dipole: magnet current, magnet voltage and the maximum (hot spot) coil temperature

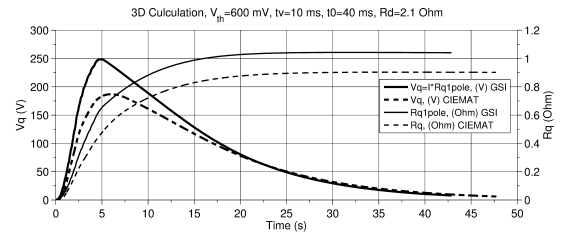

Figure 2: 3-D quench calculation of the CBM dipole: quench voltage and quench resistance

Fig. 3 shows the power supply (PS) scheme, the simplified PS control unit scheme of the magnet, the dump

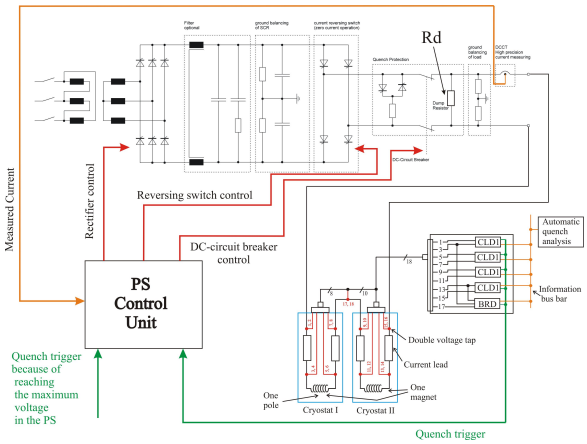

Figure 3: Quench detection and protection scheme (including power supply and voltage taps)

resistor (for quench protection) and the quench detection system. Each magnet pole has a separate cryostat. The current is brought from the room temperature to the cryostat (4.5 K) by current leads (CL). There are four current leads (two per pole). The quench detection system consists of

- four voltage detectors (CLD1) used for current leads,
- a classical bridge detector (BRD) used for the magnet,
- voltage threshold in the power supply unit (safety trigger).

During normal operation the DC-circuit breaker is closed. When a quench occurs, a quench trigger is given by the detection system. Then, the DC-circuit breaker disconnects the PS, and the magnet current is dumped via the dump resistor. The use of a dump resistor of 2.1 Ω provides evacuation of about 85 % of the energy stored in the magnet.

References

[1] P. Szwangruber *et al.*, *Three-Dimensional Quench Calculations for the FAIR Super-FRS Main Dipole*, IEEE Trans. ASC **23** (2013) 4701704

[2] F. Toral, *Design and Calculation Procedure for Particle Accelerator Superconducting Magnets: Application to an LHC Superconducting Quadrupole*, Ph. D. Thesis, Madrid 2001

[3] The CBM collaboration, *Technical Design Report for the CBM Superconducting Dipole Magnet*, Darmstadt 2014

Micro-Vertex Detector

Noise performance and radiation tolerance of CMOS Monolithic Active Pixel Sensors manufactured in a 0.18 μm CMOS process

D. Doering[1], M. Deveaux[1], B. Linnik[1], S. Strohauer[1], J. Stroth[1,2], and the CBM-MVD collaboration
[1]Goethe-Universität, Frankfurt, Germany; [2]GSI Darmstadt, Germany

Modern $0.18\,\mu$m CMOS processes provide numerous features, which may allow for decisive progresses in the read-out speed and the radiation tolerance of the CMOS Monolithic Active Pixel Sensors (MAPS) to be used in the Micro-Vertex-Detector of CBM. Together with the PICSEL group of IPHC Strasbourg, we aim to exploit those features by migrating the successful architecture of our sensors toward this novel technology. This work reports about our findings on the first prototypes manufactured with the new technology.

So far, MAPS match the requirements of CBM in terms of spatial resolution, light material budget and tolerance to non-ionizing radiation. Migrating them from the previously used 0.35 µm CMOS process to a novel 0.18 µm process was done to exploit the known higher tolerance of deep sub-micron processes to ionizing radiation. Moreover, the novel process allows for a first time to use also PMOS transistors in the pixel. This provides the opportunity to discriminate the signal inside the pixels instead of transporting it to the end of the columns, which results into a substantial acceleration of the read-out.

Three prototypes named MIMOSA-32, -32ter and -34 were designed and tested to investigate the novel technology. We observed a correlation between the noise and the surface of the gate of the so-called SF-transistor, which serves as input stage of the on-pixel pre-amplifier. This is shown in Table 1, which displays the noise as a function of the width of the gate of this transistor. The length of the gate of the pixels manufactured in 0.18 µm CMOS (pixel A-C) was 0.2 µm. A reference pixel (pixel R), which was manufactured in 0.35 µm CMOS, an enclosed transistor layout turning into an effective width of several µm was used and the gate length was 0.35 µm.

According to elder results, we expected the (dominantly capacitive) noise of the pixel to decrease once the surface of this gate is reduced. However, we found the opposite trend. Moreover, we observed a strong increase in the number of hot pixels. This is shown in the most right column (Noise 99%) of Table 1. Here, we assumed that 1% of all pixels can be masked and that the common threshold of the pixels of the chip should be set to discriminate the noise of the most noisy non-masked pixel. The noise of this pixel is shown. We find that decreasing the width of the SF-transistor from 1.5 µm to 0.5 µm (pixel A-C) improves the gain of the pixel by 10% but increases the noise slightly by 8% (median noise) and by 54% ("99%-noise"). Moreover, the novel pixels exhibit twice the median noise and up to three times the "99%-noise" of the reference pixel R.

Table 1: Noise and gain in dependence of the source follower gate width (see text)

Pixel	Width $[\mu m]$	Gain $[e/ADU]$	Noise $[e]$	Noise 99% $[e]$
A	1.5	11.1	19.8	41
B	0.9	10.5	20.5	55
C	0.5	10.1	21.3	63
R	-	6.0	10.7	18

Analyzing the effect, we found the signatures of Random Telegraph Noise and 1/f-noise, which affects the SF-transistor and which is amplified within the amplification chain. This effect was observed earlier on MAPS for optical imaging [1, 2], but it was so far unknown in the community developing MAPS for charged particle detection. As suggested by our observations and literature, we increased the gate size in a follow-up prototype and first measurements suggest that this mostly eliminated the additional noise [3].

We studied the tolerance of the above mentioned sensors to ionizing radiation by irradiating them with soft X-rays and testing them hereafter with X-rays from a ^{55}Fe-source and β-rays from a ^{90}Sr-source. The preliminary results of this study suggest that the novel sensors tolerate ionizing doses of up to 3 Mrad without significant losses in performance. On a sensor irradiated with 10 Mrad, the gain of the detector was reduced for so-far unknown reasons. However, the S/N of the device remained sufficient for a reliable charged particle detection.

From this, we conclude the MAPS based on a 0.18 µm CMOS process have the potential to match the requirements of CBM in terms of tolerance to ionizing radiation.

References

[1] P. Martin-Gonthier and P. Magnan, *RTS noise impact in CMOS image sensors readout circuit*, in: Proc. of 16th IEEE Conf. on Electronics, Circuits, and Systems (2009) 928

[2] X. Wang *et al.*, *Random Telegraph Signal in CMOS Image Sensor Pixels*, in: Proc. of International Electronic Devices Meeting (2006) 1

[3] M. Winter, PoS(Vertex2013) 020

A semi-automatic test system for CMOS Monolithic Active Pixel Sensors

B. Linnik[1], *D. Doering*[1], *M. Deveaux*[1], *S. Strohauer*[1], *J. Stroth* [1,2], *and the CBM-MVD collaboration*
[1]Goethe-Universität, Frankfurt, Germany; [2]GSI Darmstadt, Germany

The Micro-Vertex-Detector (MVD) of the future CBM-experiment will rely on CMOS Monolithic Active Pixel Sensors (MAPS). Those sensors match so far the requirements of CBM in terms of excellent spatial resolution, ultra-light material budget and non-ionizing radiation tolerance. Intense R&D is being carried out within a joint research program of the PICSEL group of the IPHC/Strasbourg and the IKF of the Goethe University of Frankfurt/Main in order to improve their tolerance to ionizing radiation and their read-out speed.

A standard problem during this research is to optimize numerous parameters like diode sizes and the size of transistor gates [1] in order to obtain the best possible detection performance for charged particles, the fastest possible read-out speed and the best possible radiation tolerance.

Producing MAPS for charged particle tracking is beyond the intended scope of the CMOS-processes used. Therefore only few simulation tools, which are suited to assist this optimization, are available. Moreover, decisive process parameters were found to be unknown even to the technology providers in the past. To overcome this obstacle and to collect the necessary knowledge, series of process exploration chips are built and tested. Those chips host numerous pixel designs, which vary the (believed to be) relevant sensor parameters in a systematic way. Typical prototypes following this strategy were the MIMOSA-32 and MIMOSA-34 sensors [1], which each provided 32 different kinds of pixels. Moreover, the sensors were manufactured on multiple different wafers to check the dependence of their performances on the wafer properties.

Our measurement protocols foresee to study the temperature dependence of different effects. In addition, we aim to evaluate the radiation tolerance of the sensors with multiple data points. Over all, in the order of thousand individual measurements are needed to perform a full test of a generation of MAPS. This high number of tests call for a semi-automatic test system, which may run 24/7 with limited human intervention.

To build such a system, we complemented the test system received from the PICSEL group of IPHC Strasbourg by an AUTOIT [2] based program named MABS (**M**imosa **A**utomated **B**ot **S**ystem). We avoided modifying the firmware of the test system. Instead, MABS interfaces the GUI of this firmware and executes pre-programmed test protocols by emulating the input of a human user. Moreover, it controls and monitors external devices like the cooling system and the temperature sensors of the test system. In case of errors or unexpected events, MABS pushes error messages to the mobile phone of the system operator.

The data and the run information are stored to a database, which can be accessed by our ROOT-based data analysis software. The human intervention needed for the measurement process is reduced to the necessary exchange of sensors and the installation or removal of the radiation sources needed for testing them.

MABS was successfully tested and validated during a 24/7 measurement campaign, which lasted for several weeks, It successfully demonstrated its capability to execute detailed sensor test protocols with only little human intervention.

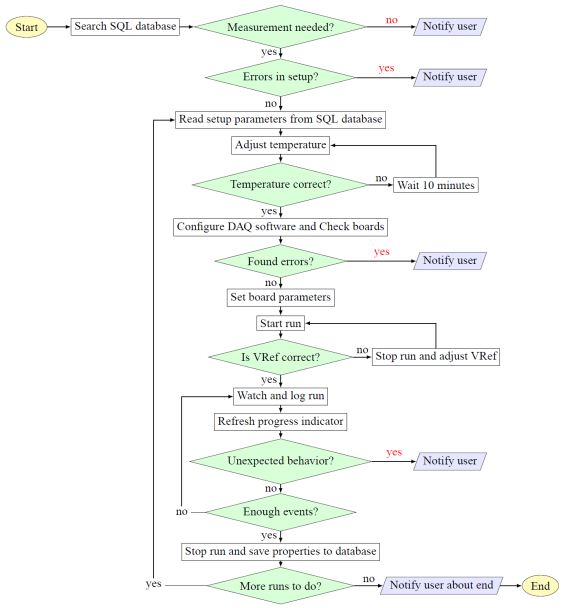

Figure 1: The flow chart of MABS

References

[1] D. Doering *et al.*, *Noise performance and radiation tolerance of CMOS Monolithic Active Pixel Sensors manufactured in a 0.18µm CMOS process*, this report

[2] `http://www.autoitscript.com/site/autoit/`

Quality assessment of ultra-thin CMOS sensors for the Micro Vertex Detector of the CBM experiment at FAIR

M. Koziel[1], *N. Bialas*[1], *M. Deveaux*[1], *B. Milanovic*[1], *J. Stroth*[1,2], *and the CBM-MVD collaboration*
[1]Goethe-Universität, Frankfurt, Germany; [2]GSI, Darmstadt, Germany

The future Compressed Baryonic Matter experiment (CBM) will be equipped with a high-precision micro-vertex detector (MVD) aiming at an outstanding primary and secondary vertex resolution. Highly granular and ultra-light, so-called Monolithic Active Pixel Sensors (MAPS), which are manufactured with standard CMOS processes, will be employed. Imperfections in the CMOS production as well as the subsequent dicing and thinning procedures may limit the production yield of the sensors to about 60-70%. Probe testing the sensors prior to integrating them to the MVD is a mandatory step of the quality assurance related to the mass production of this detector. This is as it allows to recognize and reject sensors with insufficient performance.

The feasibility of probe testing the only 50 μm thick sensors was studied with the MIMOSA-26 prototype, which is considered as a realistic precursor of the final sensor of the MVD. Moreover, the existing readout system of the MVD-prototype [1] could be used for the test.

The probe-tests were carried in the IKF technology lab. As shown in Figure 1, the probe tester was equipped with a probe-card hosting 65 tungsten needles with a minimum pitch of 120 μm. The MIMOSA-26 sensors were held by a chuck adapter with micro-vacuum channels, contacted with the needles and their signals were routed through the probe-card to a so-called adapter-card. The latter was introduced as building it came out to be easier and cheaper than adapting the probe-card itself to our readout system. In addition, a test board hosting a wire-bonded working MIMOSA-26 sensor was manufactured. It is to test the readout chain including the probe-card independently of the delicate issue of contacting of sensors with needles.

After commissioning the system, first tests with 300 μm thick MIMOSA-26 sensors were carried out. The response of the sensors to JTAG programming and to various threshold settings matched our expectations. Next, the 50 μm sensors were probe-tested. The distance between the probe-card and the sensor, which is needed to establish a save contact between sensors and needles, was found smaller than expected from the tests with thicker sensors. This is attributed to the fact that the 50 μm sensors become soft enough to follow the imperfections of the surface of their support. Nevertheless, we succeeded to probe-test the thinned sensors.

In a next step, we are working on implementing a full test protocol, which is suited for testing the sizable number of sensors foreseen in the future mass production. To do so, we intend to update the software of our readout system and to migrate this system from the current TRBv2 to a TRBv3 platform [2].

Concluding, a 50 μm-thin precursor of a final CBM-MVD sensors was successfully tested with a probe-card. This activity and the related know-how found meanwhile some interest of a larger community, which is employing thinned MIMOSA-26 sensors into various experimental setups. This includes the PLUME project [3] and the vertex detector project of the NA-61 experiment at CERN [4].

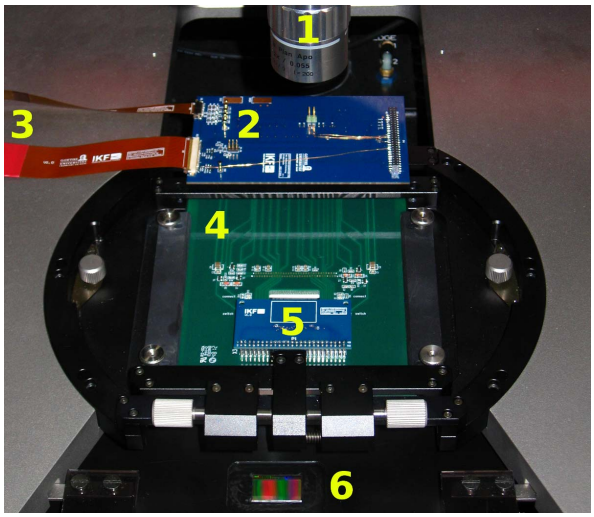

Figure 1: Probe-station setup: (1) microscope lens, (2) adapter-card, (3) connectivity to DAQ, (4) probe-card, (5) test-board hosting the reference sensor and (6) chuck-adapter with one Mimosa-26 sensor

References

[1] M. Koziel *et al.*, Nucl. Instrum. Methods **A 732** (2013) 515C

[2] J. Michel *et al.*, *The next generation of CBM MVD read-out electronics*, this report.

[3] A. Nomerotski *et al.*, Nucl. Instrum. Methods **A 650** (2011) 208

[4] N. Abgrall *et al.* (NA61/SHINE Collaboration), *Report from the NA61/SHINE experiment at the CERN SPS*, CERN-SPSC-2013-028 ; SPSC-SR-124, October 2013, p. 57

Lithographic integration of aluminum read-out traces on CVD diamond for the CBM Micro Vertex Detector

C. Müntz[1], N. Bialas[1], M. Koziel[1], J. Stroth[1,2], R. Weirich[1], R. Visinka[2], A. Meier[3], F. Völklein[3], and the CBM MVD collaboration

[1]Goethe-Universität, Frankfurt, Germany; [2]GSI, Darmstadt, Germany; [3]IMtech, Hochschule RheinMain, Rüsselsheim, Germany

The Micro Vertex Detector (MVD) [1] of the Compressed Baryonic Matter (CBM) experiment at FAIR aims at a challenging material budget of only a few per mille radiation length for each of the detector stations. This allows for the high-precision secondary vertex reconstruction needed to identify e.g. rare open charm particles emitted in violent heavy ion collisions. The detector will be operated in vacuum and relies on dedicated CMOS monolithic active pixel sensors (MAPS) [2] thinned to 50 μm, mounted on sheets of 200 μm thick poly-crystalline CVD diamond [3], which features a thermal conductivity of about 2000 W/mK, i.e. about four times the one of copper, and a high mechanical stability (Young's modulus of 1050 GPa). A conventional sensor module comprises the carrier for mechanical support and cooling, the sensors, dedicated glue and thin flex cables used to control and read-out the sensor. A standard method to connect the sensor is wedge bonding of 25 μm aluminum wires. This concept was realized for the MVD prototype [1]. A feasibility study started in 2013 is focusing on the option to merge the functionalities of the carrier and the read out, aiming at further improving the material budget and at the same time reducing the steps of integration by sparing the dedicated flex cable.

The technology of choice is photolithography of microscopic traces directly on the CVD diamond carrier for reading out and biasing the sensor. Employing aluminum for the traces with a thickness of up to 3 μm is mandatory for reducing the material thickness and the probability of γ-conversion. However, it triggers questions related to mechanical and electrical properties, such as adhesion and conformity of the traces as well as impedances, respectively. These questions were addressed in a study accomplished by GSI Darmstadt (detector laboratory) and Hochschule RheinMain (IMtech) Rüsselsheim, w.r.t. the lithographic part, and the IKF (characterization). Here, we report on the first step of the project, which focuses on placing dedicated aluminum traces on CVD diamond.

Figure 1 depicts the final demonstrator module. Part of this module, as indicated in the plot, is subject of this report.

Different lithographic techniques have been explored, focusing on adhesion reliability, realizing rather thick traces of 3 μm, and getting the known effect of under-etching under control. For example, chemical (wet) etching has been contrasted to the lift-off technique. Figure 2 depicts typical pictures of the samples under evaluation at the IKF.

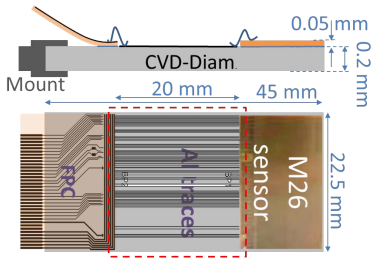

Figure 1: The demonstrator, comprising the sensor ("M26"), the CVD diamond carrier with Al traces and the flex cable to connect to the read out. The broken red line depicts the part of the project reported here.

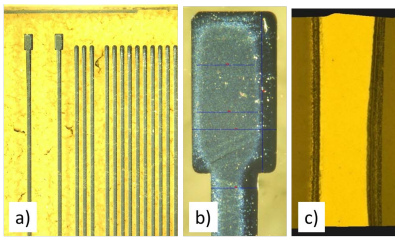

Figure 2: Pictures of Al traces with typical widths of 50 - 100 μm attached to the CVD diamond carrier: a) different geometries, b) zoom of a pad, c) typical under-etching

The electrical characterization is in progress, focusing on high-precision measurements of resistances and line-to-line capacities in view of operating a dedicated pixel sensor. To do so, the Al traces have been connected by means of wire wedge bonding, so far revealing no problem with the adhesion of the 50-100 μm wide Al traces to CVD diamond surface. This has been confirmed with pull tests. The electrical characterization will also allow for assessing the conformity of the traces, e.g. with respect to the trace thickness. In a next step, the employed processes will be further optimized, based on the results, also exploring the option of providing up to 5 μm thick Al traces, before preparing the final demonstrator hosting a sensor chip.

References

[1] M. Koziel *et al.*, Nucl. Instrum. Methods **A 732** (2013) 515C

[2] `http://www.iphc.cnrs.fr/-PICSEL-.html`

[3] `http://www.diamond-materials.com`

Results from the MVD prototype test CERN at the CERN-SPS

S. Amar-Youcef[1], *M. Deveaux*[1], *M. Koziel*[1], *Q. Li*[1], *J. Michel*[1], *B. Milanovic*[1], *C. Müntz*[1], *B. Neumann*[1], *J. Stroth*[1,2], *T. Tischler*[1], *M. Wiebusch*[1], *and the CBM-MVD Collaboration*

[1]Goethe-Universität, Frankfurt, Germany; [2]GSI, Darmstadt, Germany

The prototype of the CBM Micro Vertex Detector (MVD) was commissioned and extensively tested at a beam time at CERN SPS. The performance of the sensors along with the customized frond-end and TRB based DAQ system was investigated regarding the synchronization and long-term stability of the continuous multi-channel readout, the positional stability and the sensor performance (efficiency, resolution, dark occupancy). MIMOSA-26 [1], which represents a sizable precursor to the final sensor of the MVD, was used. It comprises the prototype readout concept including on-chip hit discrimination and data sparsification. Moreover, the sensor is based on a high-resistivity epitaxy layer and was thinned down to a thickness of 50 μm.

12 identical sensors were arranged in four single-sided reference and one double-sided DUT station, whereas "one side" comprises two sensors side by side. The DUT was sandwiched between two reference stations, respectively. According to this, the beam particles were tracked by up to 6 hit points. The setup allowed to vary the relative distance of the stations and the inclination of the DUT relative to the reference system. The temperature of the DUT could be varied independent of the temperature of the reference system. The material budget amounted 0.05% X_0 for each of the reference stations and 0.3% X_0 for the DUT, which corresponds to one fourth of a first MVD station [2].

Thanks to the reliable DAQ system [3], 1.2 TB of data were collected. The most important results extracted from this data will be presented hereafter.

A diversity of measurements at different discriminating thresholds, inclination angles and temperatures were carried out. The data was analyzed by means of a dedicated software. The latter performs data consistency checks, unpacking and high level analysis including QA functionalities and includes an alignment package, which was designed to align the 6 sensors in the telescope setup.

Figures 1 and 2 demonstrate the excellent performance of the MVD prototype. Fig. 1 shows the position of the DUT relative to the reference system based on alignment results as a function of time. A movement of $0.003\ \mu m/min$ was observed. The single point resolution of the DUT including the resolution of the sensor and the positional stability of the mechanics was found to be about $3.5\ \mu m$. This is equivalent to the resolution of the sensor only, suggested by the pixel pitch of $20\ \mu m$, no charge decoding and an average cluster size between 1 and 2. Fig. 2 shows the relation between the efficiency for MIPs of the two DUT-sensors and their dark occupancy. The data was taken varying the on-chip discriminator thresholds of the sensors. We find that the ambitioned performance of 99% efficiency and 10^{-5} dark occupancy are reached for both sensors. Moreover, the dark occupancy can be reduced further by masking $<< 1\%$ of noisy pixels. This suggests that a large part of the dark occupancy is caused by a subset of hot pixels only.

Over all we conclude that the prototype of the MVD reached the requirements of CBM in terms of mechanical stability and sensitivity for minimum ionizing particles.

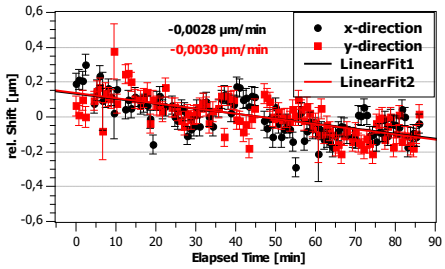

Figure 1: Relative position of the DUT with respect to the reference telescope. Every point corresponds to one spill of the CERN-SPS.

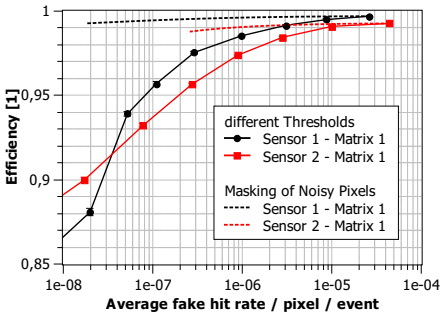

Figure 2: Efficiency as a function of the fake hit rate for two different DUT sensors w/o (solid lines) and w/ (broken lines) masking hot pixels

References

[1] J. Baudot, *First test results of MIMOSA-26, a fast CMOS sensor with integrated zero suppression and digitized output*, IEEE Nucl. Sci. Symp. Conf. Rec. (2009) 1169

[2] T. Tischler, *Layout of the Micro Vertex Detector for the CBM experiment*, this report

[3] B. Milanovic, *Beamtime Results of the MVD Prototype DAQ Network*, CBM Progress Report 2012, p. 5

The next generation of CBM MVD read-out electronics

J. Michel[1], *M. Wiebusch*[1], *J. Stroth*[1,2], *and the CBM-MVD collaboration*
[1]Goethe-Universität, Frankfurt, Germany; [2]GSI, Darmstadt, Germany

The on-going development of the support electronics of the CBM Micro-Vertex-Detector (MVD) focuses on two major aspects: First, the integration in a new DAQ system (based on the TRB3 system developed by HADES) and, second, the design of an integrated control and monitoring interface for systems consisting of several sensors.

The major goal of front-end electronics development was to migrate the read-out to a new, more powerful read-out platform, TRB3. Even though the central parts of software and FPGA designs need not to be changed, the read-out chain between digital electronics and sensors was redesigned to gain better performance and additional monitoring features. Here, also the principal structure of the chain was simplified by dropping the separated connection for control signals and merging all supply and data lines for a sensor on one common cable.

Special care was taken for the most sensitive supply voltage, a biasing voltage for the pixel matrices of the sensors. Several generation and distribution schemes were implemented to investigate which setup results in the best noise performance. Furthermore, all relevant voltages and currents can be monitored remotely to further study the behavior of sensors and, subsequently, to design a matching powering scheme for the final detector setup.

In the current connection scheme, the new FPGA platform can support up to 16 sensors in parallel. Note that this value is mostly limited by the number of I/O connections for the huge number of control and monitoring signals in the current design version and is likely to increase in future iterations. The resources of the FPGA also allow for further data sparsification algorithms like cluster detection as described in [1].

The MVD user software serves three main purposes: Editing the sensor and electronics settings, coordination of data taking, and continuous monitoring of sensor parameters (power consumption, temperature, etc). In order to make the functionality accessible to non-hardware-experts, the development of an elaborate graphical user interface has been initiated.

The user software consists of two parts: a back end software suite implemented in Perl and a web interface front end written in HTML/CSS/Javascript. Though this approach appears intricate, the strict separation of front end and back end has substantial advantages: The DAQ is inherently remotely accessible to multiple users on different machines, while the design flexibility of HTML and CSS helps providing a clear structure and a good overview of the functionality. Furthermore the back end scripts can be also used from the command line or shell scripts to automate complex configure and/or measurement tasks.

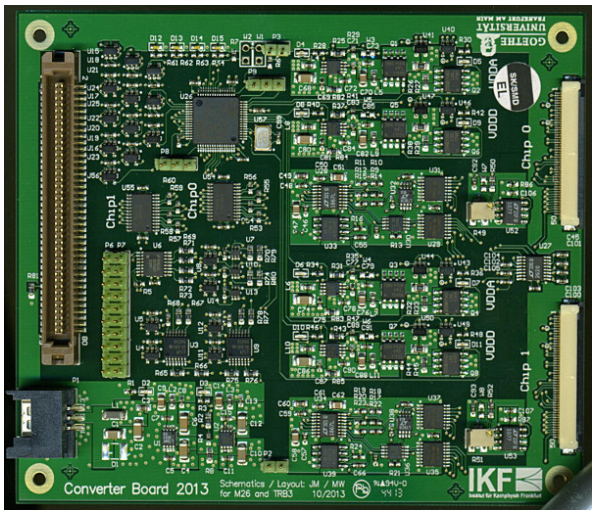

Figure 1: The new Converter Board with power supply, control and monitoring for two sensors

All configuration files are stored in the strictly hierarchical but human readable XML format in order to keep the system transparent to the developer. The user interface does not only include access to all vital configuration options of each individual sensor, but also allows to monitor all information gathered on the converter board, i.e. voltages and currents as mentioned above.

These developments are a further steps towards the final read-out electronics, although it is evident that further steps will be taken this year. The plans foresee to adapt the read-out to a new sensor generation (Mistral) with higher data band-width and to develop cabling schemes for the geometry of the complete MVD detector setup.

References

[1] Q. Li *et al.*, *Implementation of the FPGA-based cluster finder for the CBM-MVD*, this report

Implementation of the FPGA-based cluster finder for the CBM-MVD

Q. Li[1], S. Amar-Youcef[1], M. Deveaux[1], I. Fröhlich[1], B. Milanovic[1], J. Michel[1], C. Müntz[1], J. Stroth[1,2], and the CBM-MVD Collaboration

[1]Goethe-Universität, Frankfurt, Germany; [2]GSI, Darmstadt, Germany

Searching for open charm particles with CBM demands high collision rates of up to 100 kHz Au+Au collisions and performing tracking and secondary decay vertex finding in real time. This generates a significant load to the First Level Event Selector (FLES) of the experiment. To reduce this load, we aim at pre-processing the data provided by the Micro-Vertex-Detector (MVD) of CBM before sending it to the FLES.

Our strategy was studied with the CMOS Monolithic Active Pixel Sensor MIMOSA-26, which features already an on-chip zero suppression and an 1-dimensional cluster finding. To further reduce the data, we implemented and tested algorithms performing a 2-dimensional cluster finding and an efficient cluster encoding [1]. Based on data obtained from the beam test of the MVD-prototype, we concluded that 99.99% of all found cluster types can be encoded, if the most abundant cluster shapes are associated to a 10-bit code. This so-called shape code is packed together whith the x- and y-coordinate of the cluster into 32-bit word. As shown in figure 1, which displays the data volume needed to encode a sensor frame in multiples of 16 bit, the novel encoding scheme reduces the data by a factor of two as compared to the native encoding of MIMOSA-26. Moreover, the fluctuations are reduced, which helps to balance the load of the readout network.

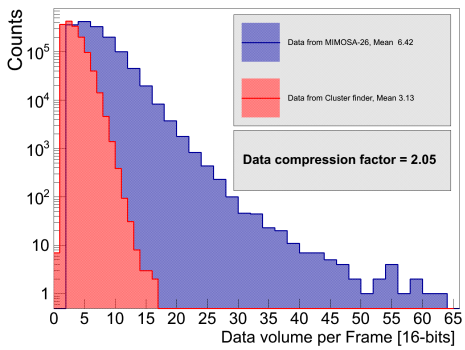

Figure 1: Comparison of the data volume generated by SPS beam test data encoded in proposed format and the native data format of MIMOSA-26. The average cluster size is between 1.6 and 2.6 pixels per cluster depending on the discrimination threshold.

The algorithms are being implemented into the FPGA of the readout controller board (ROC) of the MVD. Figure 2 (left) shows the modules of the current ROC logic. After the sensors' data are cross-checked for possible errors and synchronization problems, they are stored in a frame buffer, which serves as the input for the cluster finder. The output of this cluster finder is transferred to a readout buffer and shipped forward via TRB-net. Figure 2 (right) displays the main logic structure of the cluster finder. The data of each new row arriving at the *Read Row* - module are compared with the potentially incomplete clusters known from previous rows. In case a new state matches geometrically a known cluster, it is added to this cluster. Otherwise, a new cluster is created. Once a cluster does not find new neighbors, it is considered as completed and sent to the *Shape* and *Cluster Coder*-module. Here, the cluster is encoded into the final 32-bit word by means of a look-up table.

To accelerate the encoding, a *fast coder* encodes the 8 most abundant shapes and all fully symmetrical shapes without accessing the table. Moreover, the *look-up table* was subdivided into groups of shapes with identical numbers of fired pixels and each group was ordered such that the most abundant cluster shape is encoded with shortest access times. According to our FPGA-simulations, this optimization accelerated the access by a factor of two.

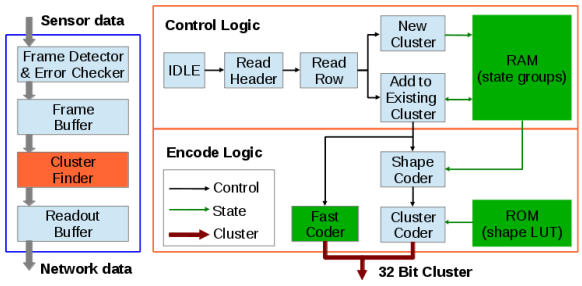

Figure 2: Main modules of ROC logic (left), logic structure of the cluster finder (right).

A first version of the VHDL code was implemented in the FPGA on the TRBv2-board and tested with test patterns. The algorithm recognized the patterns within the anticipated processing time. In a next step, the code will be exposed to real data and finally integrated into the real time data processing chain of the TRBv3-board [2,3].

References

[1] Q. Li *et al.*, CBM Progress Report 2012, p. 6

[2] M. Traxler *et al.*, JINST **6** (2011) C12004

[3] J. Michel *et al.*, *The next generation of CBM MVD read-out electronics*, this report

Layout of the Micro Vertex Detector for the CBM experiment

T. Tischler[1], S. Amar-Youcef[1], M. Deveaux[1], M. Koziel[1], C. Müntz[1], J. Stroth[1,2], and the CBM MVD collaboration

[1]Goethe-Universität, Frankfurt, Germany; [2]GSI, Darmstadt, Germany

The Micro Vertex Detector (MVD) of the CBM experiment will be equipped with CMOS Monolithic Active Pixel Sensors developed at IPHC, Strasbourg. This sensor technology will meet the constraints formulated by the physics cases. The latest sensor prototypes [1] provide the sensor architecture to be used for the sensors being integrated into the MVD and allow for defining the sensor arrangement within the acceptance of the MVD.

The MVD will consist of up to four planar detector stations positioned between 50 and 200 mm downstream the target. The assumed sensor dimensions of $30 \cdot 13$ mm^2 feature an in-active area of $3 \cdot 10$ mm^2 for the on-chip read-out electronics and bonding pads along one side of the chip. This in-active area requires a double-sided positioning of the sensors on the MVD stations to achieve the optimum acceptance coverage. A 500 μm overlap of the active sensor areas optimizes this coverage for inclined tracks. The thickness of the sensors will be 50 μm which requires dedicated sensor positioning tools.

Table 1: The number of sensors required per MVD station

Station Number	Position [mm]	Number of sensors	Carrier material
0	50	8	CVD diamond
1	100	40	CVD diamond
2	150	84	CF-TPG-CF
3	200	160	CF-TPG-CF
Total		296	

Vacuum operation of the MVD requires efficient sensor cooling. At the same time, the material budget of the MVD stations has to be limited due to its significant impact on the tracking and vertexing precision. High performance carbon-based materials - offering the best combination of an excellent heat conductivity and a low contribution to the material budget of the MVD station - will be used as cooling support in the detector acceptance. For the stations positioned at 50 mm and 100 mm, 150 μm thin poly-crystalline CVD diamond carriers [2] are employed serving as mechanical cooling support, while for the third and fourth MVD station 500 μm thick sheets of carbon fibre-encapsulated Thermal Pyrolytic Graphite (TPG) [3] are proposed. Outside of the active area actively cooled aluminum heat sinks are positioned, suspended by dedicated half station support structures leveling the different heat sink dimension of the stations, as shown in figure 1. The MVD half stations are positioned on common base plates to allow the movement of the MVD away from the beam line while beam optimization.

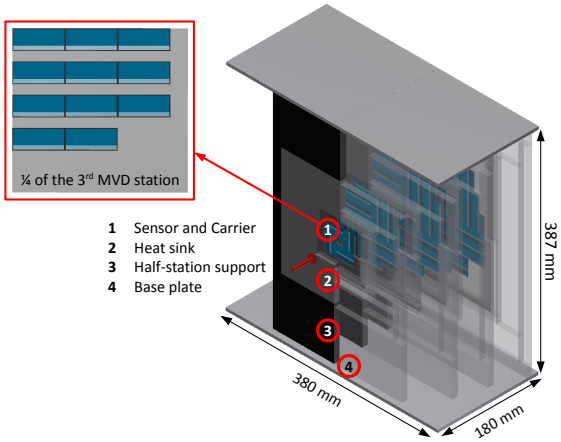

Figure 1: The CAD drawing of the MVD is depicted. For one of the two MVD half station groups is set to transparent for visualization. The beam is coming from lower left. The inlay shows the sensor arrangement on the front side of the third station module. Empty and in-active areas are covered by sensors on the back side.

The material budget benchmark of the first MVD station of $x/X_0 \approx 0.3\%$, crucial for the precision of secondary vertexing, will be met with the current station design and a conservative flex print layout. To meet the benchmark of $x/X_0 \approx 0.5\%$ also for larger polar angles of the other MVD stations, an advanced read-out flex cable design, based on aluminum traces, is mandatory.

References

[1] F. Morel *et al.*, JINST **9** (2014) C01026

[2] `http://www.diamond-materials.com`

[3] K. Arndt, Forum on Tracking Detector Mechanics, June 2013, Oxford, UK

Silicon Tracking System

Full-size prototype microstrip sensors for the CBM Silicon Tracking System

J. Heuser[1], *D. Soyk*[1], *C.J. Schmidt*[1], *Y. Murin*[2], *V. M. Borshchov*[3], *I. Tymchuk*[3], *and M. Protsenko*[3]
[1]GSI, Darmstadt, Germany; [2]JINR, Dubna, Russia; [3]LTU, Kharkov, Ukraine

The CBM Silicon Tracking System will comprise double-sided microstrip sensors of three basic geometries. Those differ in the lengths of their strip-shaped sensing elements, chosen to match the hit densities in their location of deployment in the tracking stations. Strip lengths of about 2 cm, 4 cm and 6 cm have been found adequate to achieve a sufficiently limited hit occupancy even under the harshest running conditions of the CBM experiment [1].

The sensors have in common the number of 1024 strips per side at a read-out pitch of 58 μm, arranged parallel to the sensor edge (n-side) and under a tilt angle of 7.5° on the p-side. This will allow reconstructing space points within a sensor, with the required spatial resolution and at limited combinatorics resulting from the projective geometry. The strips are read out from one edge only, as to integrate the sensors into detector modules with the read-out electronics located at one end. On the stereo side, the strips in one corner of the sensor are not reached directly. They require further electrical connections to their partner strips in the other corner which are attached to the read-out electronics. Two technical solutions are being evaluated, one with metal lines integrated on a second aluminum layer on the sensor, another utilizing an extra thin cable layer bonded onto the sensor. The overall dimensions of the sensors are 6.2 cm width and 2.2 cm, 4.2 cm and 6.2 cm height. A depiction of their layouts can be seen in [2]. This allows producing them with 4" wafer technology, a pre-requisite for a sufficiently large circle of vendors. Also the on-sensor cable as an alternative to the routing lines on a second metal layer are shown there.

In 2013 the production of prototype sensors in all three sizes has been achieved. All sensors of this CBM05 series have a compatible layout of their bonding pads which was worked out within the CBM collaboration and its technology partners. The prototypes were produced in cooperation with the CiS Research Institute for Micro Sensorics and Photovoltaics, Germany, and Hamamatsu Photonics, Japan. The large prototype sensor with double-metal interconnections came from CiS on a GSI bill. The mid-sized sensor has been realized with Hamamatsu with support to GSI from BMBF. The small sensor was ordered at Hamamatsu through JINR. All sensors but the small one are double-sided. The small sensor was made as simple as possible, therefore single-sided, with the specific aim to verify the viability of the on-sensor cable concept. Some of the large sensors were employed in new prototype modules and tested extensively in lab and beam. Such sensor with its integrated double-metal lines is shown in Fig. 1.

A further series of prototype sensors, CBM06, has been designed and launched for production with CiS and Hamamatsu to be available in 2014. They will serve extended effort with the development of prototype detector modules. In view of the preparation of tooling for the technical integration of their components, larger amounts of dummy sensors and dummy ASICs have been produced in 2013, providing no active functionality but the the same contact patters on the same metallic surfaces as the full sensors.

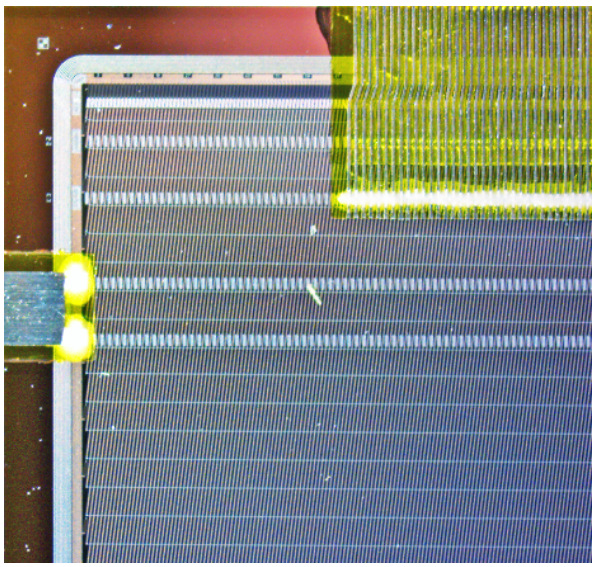

Figure 1: Corner region of a CBM05 sensor produced at CiS. The sensor has been fitted with a bias cable (left) and has a micro read-out cable tab bonded to it (top).

References

[1] J. Heuser *et al.*, *Technical Design Report for the CBM Silicon Tracking System*, GSI Report 2013-4, `http://repository.gsi.de/record/54798`

[2] J. Heuser *et al.*, CBM Progress Report 2012, p. 8, `http://repository.gsi.de/record/51950`

A assembly device for a “sandwich” double-sided silicon microstrip sensor

I. Martinovsky[1], *I. Rudenia*[1], *M. Trushkevich*[1], *A. Djakonova*[1], *Yu. Chikun*[1], *M. Milanovich*[1], *V. Lysakov*[1], *E. Zhuravel*[1], *N. Savich*[1], *Yu. A. Murin*[2], *V. Borshchov*[3], *M. A. Protsenko*[3], *and I. T. Tymchuk*[3]

[1]PLANAR, Minsk, Belarus; [2]JINR, Dubna, Russia; [3]LED Technologies of Ukraine (LTU) Ltd, Kharkov, Ukraine

Some of the current prototype sensors for the CBM Silicon Tracking System were laid out single-sided, to create least complexity for the study of the feasibility of the on-sensor cable. The device for assembly of composite sensors out two single-sided ones, the so called SSSD “sandwich”, is intended for gluing of two single-sided microstrip silicon sensors (SSSD) of sizes 22×62, 42×62 and 62×62 mm^2 back-to-back with high accuracy. A assembled “sandwich” consists of the parts schematically shown in Figure 1 [1]:

1. single-sided sensor with $0°$ angle of strips;
2. single-sided sensor with $7,50°$ angle of strips;
3. back contact for sensor # 1;
4. back contact for sensor # 2;
5. interstripcable for sensor # 2.

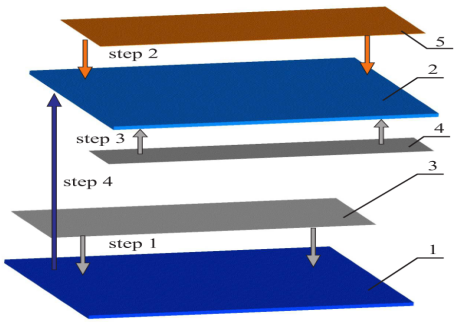

Figure 1: SSSD “sandwich” composition and assembly steps [1]

Precise positioning of the sensors relative to each other is achieved with the help of the special assembly device (Figure 2) allowing accurate orientation of the sensors relative to the reference markers inspected by two optical systems observing the front sides of the sensors to be joined. The device capabilities are as follows:

- fixation of sensors on the vacuum tables;
- the movement of the sensors on coordinates X-Y-Z and F (turning angle);
- orientation of sensors with the help of optical systems and systems of coordinates;
- inspection of sensors position.

The fixture consits of the following parts:

- base;
- movement mechanism of the bottom table according to the coordinates X-Y-Z-F – 1 pcs.;
- movement mechanism of the top table according to the coordinates X-Y-Z-F – 1 pcs.;
- movement mechanism of the both tables along the coordinate Y – 1 pcs.;
- optical system - 2 pcs.;
- mechanism orientation of the optical system – 2 pcs.;
- mounting bracket for optical systems – 1 pc.

Table 1: Assembly device specifications

Alignment accuracy, μm	± 5
Dimensions of sensors, mm	$22(42)(62) \times 62$
Thickness of sensors, μm	280 ± 20
Number of tables (two per sensors, pcs.)	6
Vacuum, MPa)	0,04 – 0,03
Power dissipation, V/Hz/kW	230 / 50 / 0.5
Max. overall dimensions, mm	$510 \times 400 \times 550$
Max. weight, kg	50

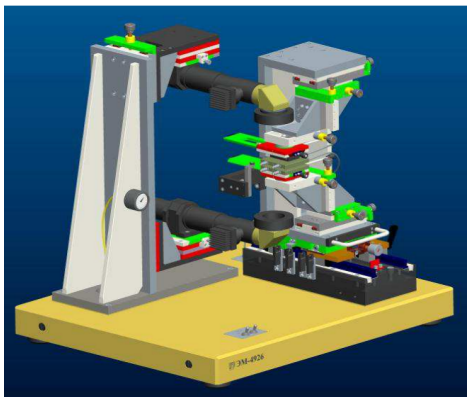

Figure 2: SSSD “sandwich” assembly device

References

[1] V. M. Borshchov *et al.*, CBM Progress Report 2012, p. 9

Silicon strip sensor layout for the CBM Silicon Tracking System

D. Soyk[1], *I. Tymchuk*[2], *J. Heuser*[1], *and C.J. Schmidt*[1]
[1]GSI, Darmstadt, Germany; [2]LTU, Kharkov, Ukraine

The CBM Silicon Tracking System will be equipped with double-sided Silicon micros-strip sensors, where the strips on the p-side are inclined by 7.5° with respect to the n-side strips as well as the sensor edge. The final and homogeneous layouts for the 3 different sensor lengths, namely 22mm, 42mm and 62mm, has been elaborated. Longer sensors may be realized as a daisy-chain of two 62mm sensors. The sensors will be produced by two vendors to avoid the stop of module production in case of problems with any one single vendor.

The stereo angle of 7,5° effects a correlation between the x and y coordinate of a bond pad on a strip. The x distance between to strips on the sensor is 58 μm, equivalent to the pitch of the straight n-side strips. Therefore the second row of bond pads must have a y distance of at least once the multiple of 58 μm/tan(7,5°). On the sensor a pad pattern with x distance of 58 μm and y distance of $\sim$ 440,554 μm is possible, but the minimum producible pitch for the long analog microcables is in x direction 116 μm. In order to contact all strips, a double layered cable needs to be employed und thus a doubly staggered bond pattern is needed.

This leads to a checker-board-pattern where every second pattern-point is alternatingly reserved for a bond pad. The pitch of the bond pads is in x 116 μm and in y $\sim$ 881.108 μm (the center of the pads in the second row is shifted in x direction by 58 μm relative to the center of the first row of pads). Figure 1 shows an exemple of the such pattern.

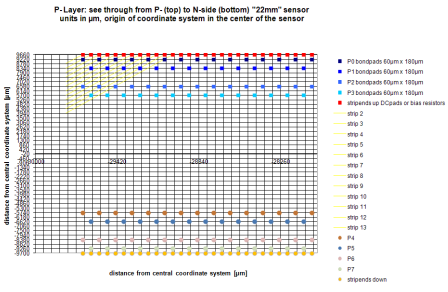

Figure 1: Schematic view on the bond pad and DC pad pattern

As there are different lengths of sensors and as the pad rows should be located on the same x-position on the top edge as on the bottom edge it proved most adequate to allocate the origin of the coordinate system in the center of the sensor. Further, the distance from the coordinate center to the innermost pad row was fixed to be a multiple of the y-pitch of two staggered pad rows, namely 881.108 μm. Consequently the distance from the outermost pad row to the edge of the sensor is a variable of the sensor length, as the pre-chosen lengths are none multiples of this pitch.

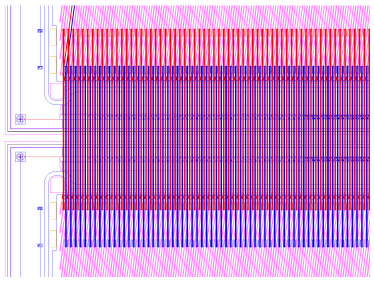

Figure 2: Schematic view of a sensor to sensor daisy chain. The red and blue lines are the leads of the short 58 μm-pitch cable that serves to daisy chain two sensors.

These definitions together with the respective symmetry allow daisy-chaining of sensors of the same as well as different lengths to each other. Figure 2 shows two daisy-chained sensors with a microcable of a constant lead length.

Consequently, also one FEB-design may serve all sensor configurations as well as either sensor side. In Fig. 3 a scheme of a microcable connection between the foreseen CBM STSxyter chip and the STS sensor is shown.

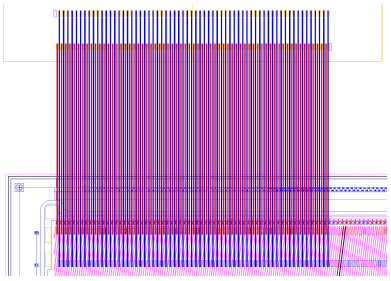

Figure 3: Schematic view of a sensor to chip connection. The red and blue lines are the leads of the microcable on two different layers with a pitch of 116 μm.

All participating vendors will employ this layout of the bond pads even though they may vary the sensor design according to their proprietory design and production preferences.

Performance of neutron irradiated prototype sensors for the CBM Silicon Tracking System

J. Heuser[1], *U. Frankenfeld*[1], *S. Chatterji*[1], *O. Bertini*[1], *P. Larionov*[2,1], *M. Singla*[2,1], *and I. Sorokin*[2,1,3]
[1]GSI, Darmstadt, Germany; [2]Goethe-Universität, Frankfurt, Germany; [3]KINR, Kiev, Ukraine

We report on the performance of prototype microstrip sensors for the CBM Silicon Tracking System (STS) after their exposure to neutron equivalent fluences as they are expected for the running scenario in the CBM experiment.

The neutron fluence at the STS detector is expected to reach about 2×10^{13} $n_{eq}cm^{-2}$ per year, depending on the detailed physics programme performed and accumulating over several years of running. The maximum integrated fluence in some areas of the tracker will amount to 10^{14} $n_{eq}cm^{-2}$ beyond wich the affected detector modules will be replaced [1]. During the CBM experimental runs, periods of two or three months per year, the sensors will be operated at -5°C to limit radiation-induced leakage currents and to prevent from thermal runaway. During the periods of shutdown, the STS detector system may have to be warmed up to allow for maintenance of its components. The radiation damaged sensors will undergo annealing processes, with properties like leakage current, full depletion voltage (V_{fd}) and breakdown voltages changing with temperature and time.

We have irradiated small test sensors from the most recent production of CBM05 prototypes, produced by CiS, Erfurt, Germany. The exposure to neutrons was performed at Institute Jozef Stefan, Ljubljana, Slovenia, within the EU-FP7 project AIDA. The sensors were irradiated in sets of four to the fluences 1×10^{13}, 5×10^{13} and 1×10^{14} $n_{eq}cm^{-2}$. During transport and storage after irradiation, a log of temperature and humidity was kept.

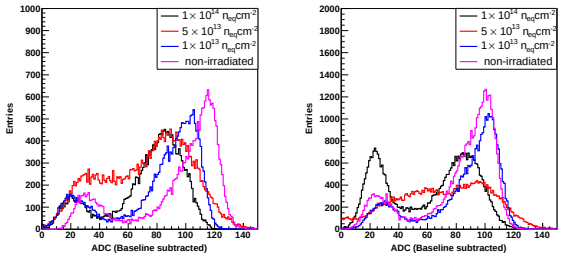

Figure 1: Charge distributions from the sensors' p (left) and n (right) sides as a function of neutron equivalent fluence

The sensors were installed in printed circuit boards allowing to apply bias voltage and to read out a number of strips with fast self-triggering front-end electronics. The sensors were operated in a nitrogen conditioned freezer at -5°C. Through the bias cable, scans of the bulk current and capacitance were made as a function of the applied reverse voltage. The determined depletion voltages as a function of the neutron equivalent fluence are summarized in Table 1. Applying significantly higher bias, the sensors' charge collection performance was determined with reading out signals induced with a ^{241}Am source and its 59 keV and lower energy gamma lines. Spectra of collected charge are shown in Fig. 1, applying a simple clustering algorithm to combine charge simultaneously seen on neighbouring strips. The results are reported in the table, assuming gain calibration factors of 117±3 (p) and 113±3 (n) ADC units for the full signal to yield the charge collection efficiencies. The results are to be verified with further sensor specimen.

Table 1: Charge collection performance of the sensors

fluence	V_{fd}	V_{bias}	peak ADC		eff. (%)	
($n_{eq}cm^{-2}$)	(V)	(V)	p ±5	n	p ±4	n
0	80±2	160±1	116	101	100	90
1×10^{13}	35±5	150±1	104	103	90	91
5×10^{13}	45±5	250±1	93	94	80	84
1×10^{14}	110±2	400±1	93	87	80	77

The leakage currents increase linearly with neutron fluence. The value of the damage constant, α, is initially at around 4.0×10^{-17} Acm^{-1}. After annealing at different temperatures, α can be used to yield the evolution of dark currents and V_{fd}. According to [2], radiation damage in silicon has several contibutions: a constant, a "beneficial annealing" and a "reverse annealing" component. Their determination is in progress.

References

[1] J. Heuser *et al.*, *Technical Design Report for the CBM Silicon Tracking System*, GSI Report 2013-4, `http://repository.gsi.de/record/54798`

[2] M. Moll *et al.*, Nucl. Instrum. Methods **A 439** (2000) 282

Measurement of coupling and interstrip capacitances in silicon microstrip sensors for the CBM experiment at FAIR

I. Sorokin[1,2], *P. Larionov*[1], *and J. Heuser*[1]

[1]Goethe-Universität, Frankfurt, Germany; [2]Kiev Institute for Nuclear Research, Kiev, Ukraine

The main component of the future CBM experiment [1] at FAIR (Darmstadt, Germany) [2] is the Silicon Tracking System [3]. It is going to be based on double-sided silicon strip sensors. Among the important characteristics of silicon strip sensors are the coupling (C_c) and the interstrip capacitances (C_{iImp}, C_{iStrip}), because they affect the signal amplitude [4, 5]. Measurement of these capacitances is therefore important both in the stage of detector prototyping and in the stage of series production for their quality assurance.

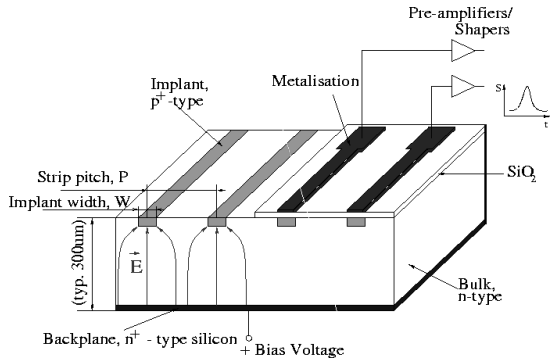

Figure 1: Schematic view of one side of a silicon microstrip sensor

The coupling capacitance (C_c), is the capacitance between a metal strip ("Metalisation" in Fig. 1) and the implant underneath. C_{iImp} — is the total capacitance of an implant to the neighboring metal strips, and C_{iStrip} — is the total capacitance of a metal strip to the neighboring metal strips. The capacitances were measured with a QuadTech 7600 precision LCR meter. To determine the coupling capacitance the test voltage (0.5 V) was applied to the selected implant, and the current, induced on the metal strip above, was measured. To measure C_{iImp}, the test voltage was applied to an implant, the metal strip above the implant was grounded, and the current was picked from the neigboring metal strips (three on each side). For C_{iStrip} measurement the test voltage was applied to a metal strip, and the current was picked up from the neighboring metal strips (three on each side).

In the measurements of C_c and C_{iImp} the observed values decrease at high frequencies (example in Fig. 2) because the resistance of the implant (which is on the order of 100 kΩ/cm) becomes comparable to, or larger than the impedance of the measured capacitance, thus the test signal does not propagate along the whole implant length [5, 6]. Correct values for C_c and C_{iImp} are obtained only at low frequencies.

The obtained values (shown in the table below) were applied to estimate the expected signal amplitude [5]. The developed measurement techniques will be used for further characterization and quality assurance of the sensors.

Sensor, side	C_c, pF/cm	C_{iImp}, pF/cm	C_{iStrip}, pF/cm
CBM02, n	37.8 ± 0.5	1.0 ± 0.5	1.4 ± 0.5
CBM02, p	34.7 ± 0.5	1.4 ± 0.5	2.2 ± 0.5
CBM03′, p	17.2 ± 0.5	1.0 ± 0.5	1.5 ± 0.5

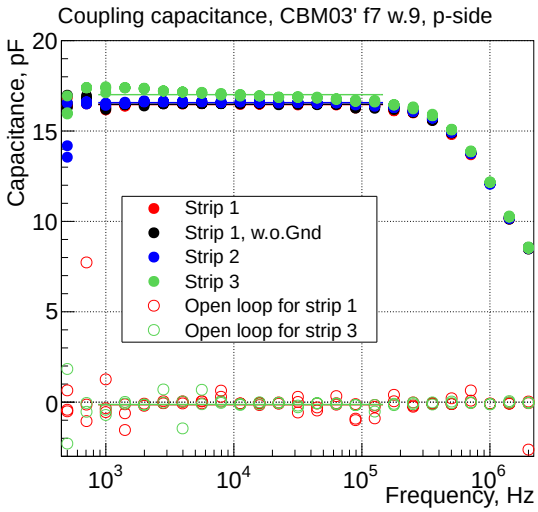

Figure 2: Coupling capacitance as a function of frequency in the CBM03' sensor

References

[1] http://www.fair-center.eu/for-users/experiments/cbm.html

[2] `http://www.fair-center.eu`

[3] J. Heuser *et al.*, *Technical Design Report for the CBM Silicon Tracking System*, GSI Report 2013-4, `http://repository.gsi.de/record/54798`

[4] C. Bozzi, *Signal-to-Noise Evaluations for the CMS Silicon Microstrip Detectors*, CMS Note 1997/ 026, 1997

[5] I. Sorokin, *Characterization of silicon micro-strip sensors, front-end electronics, and prototype tracking detectors for the CBM experiment at FAIR*, submitted as dissertation thesis, Frankfurt am Main

[6] E. Barberis, Nucl. Instrum. Methods **A 342** (1994) 90

Automatized quality assurance of sensors for the CBM Silicon Tracking System

P. Larionov[1] *and U. Frankenfeld*[2]
[1]Goethe-Universität, Frankfurt am Main, Germany; [2]GSI, Darmstadt, Germany

The Silicon Tracking System is the main tracking detector of the Compressed Baryonic Matter (CBM) experiment. It will comprise 8 stations that will be built out of around 1200 double-sided silicon microstrip sensors. The sensors will be AC-coupled and have 7.5 degree stereo angle between p- and n-side strips. The latest sensor prototypes, CBM05, manufactured by CiS, are currently being evaluated for their parameters before the series production will take place [1].

To achieve the required tracking efficiency of the whole tracking system, each sensor has to be evaluated in a number of quality assurance procedures. Some of those allow checking the overall sensor health, as it has already been done with earlier sensor prototypes [2]. This report emphasizes on the procedure that has been developed for advanced quality assurance tests applying to the sensors that have been accepted after the basic check.

The procedure itself comprises automation with LabView software and involves the use of the following equipment: a wafer prober Süss PA300PS with a mechanical accuracy of 2 μm, picoampere meters Keithley 6487 and 2410, and a LCR meter Quad Tech 7600. The following advanced quality tests of silicon sensors can be realized: (a) number of pinholes, (b) leakage current of each strip, (c) number of shorted strips, (d) number of ragged strips. The measurements are being performed in a clean room with temperature and humidity control.

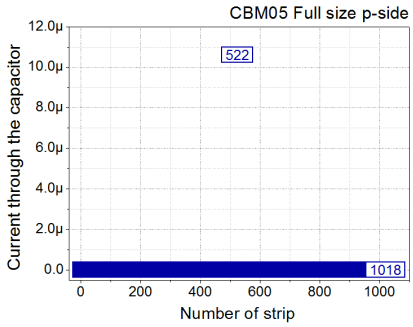

Figure 1: Result of strip current test for a CBM05 sensor

The software includes two communicating programs developed on a master and slave principle, installed on two personal computers. This is needed to decouple the PC with commercial software from the dedicated PC used for the measurements. The master program communicates with the measuring devices and generates the commands for the slave program which in turn manages the wafer prober performance.

The pinhole measurement provides information about defected strips with disrupted capacitive coupling, which cannot be used for charge collection. Figure 1 indicates the result of the pinhole test of a CBM05 sensor prototype detecting one broken capacitor on the p-side of the sensor. Table 1 summarizes results of pinhole measurements for different prototype sensors.

Table 1: Results of the pinhole tests for CBM03' and CBM05 sensor prototypes

Sensor Prototype	Sensor Size	Wafer Number	Number of pinholes *p-side*	*n-side*
CBM03'	Full size	7	0	-
CBM03'	Full size	10	5	-
CBM03'	Full size	13	0	-
CBM05	Full size	4	0	4
CBM05	Full size	6	0	0

Measurement of the leakage current of individual strip helps us to identify the number of strips having relatively high leakage current which have to be masked in the read-out electronics. Figure 2 shows the distribution of strip leakage currents of one prototype sensor. If the number of defective strips is below a certain quality acceptance threshold, the sensor can be used for module assembly and only the bad strips should not be connected to the read-out electronics. Otherwise, the sensor should be discarded.

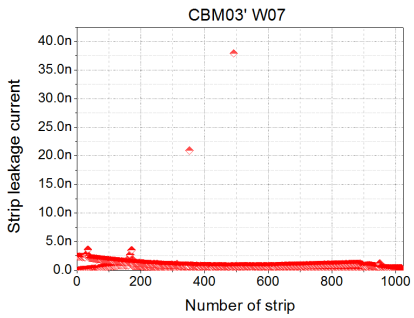

Figure 2: Result of strip current test for a CBM03' sensor prototype

References

[1] J. M. Heuser *et al.*, CBM Progress Report 2012, p. 8

[2] P. Larionov and P. Ghosh, CBM Progress Report 2012, p 11

Quality assurance procedures for STS silicon sensors

E. Lavrik[1], *A. Lymanets*[1,2], *and H.-R. Schmidt*[1]
[1]Universität Tübingen, Tübingen, Germany; [2]Kiev Institute for Nuclear Research, Kiev, Ukraine

The CBM Silicon Tracking System (STS) is a compact array of silicon microstrip sensors [1]. The total number of sensors is about 1300 and they will be delivered from different manufacturers [2]. Thus the operation of the detector requires all sensors to be quality assured in order to meet the requirements with respect to signal-to-noise ratio, radiation hardness and long term operation stability.

Silicon sensors manufactured for the STS detector need to be examined in different ways before being assembled into modules and ladders. Sensors are examined: a) electrically by measuring IV/CV properties of a sensor and its individual strips; b) optically to detect scratches, top metallisation layer lithography defects, dust grains or other foreign objects and others (Fig. 1).

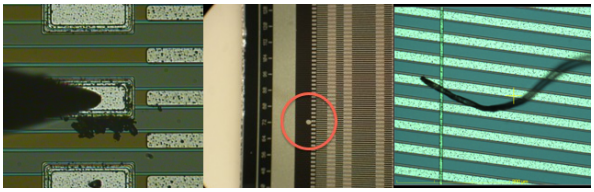

Figure 1: Various defect types found in CBM STS silicon microstrip sensors. From left to right: photo-resist residues, top metallisation layer lithography defect, dust grain.

For optical inspection a clean area has been established in a laboratory at the University of Tübingen. We have built an XY-inspection table based on closed-loop Movtec SMC-300 linear servomotors. Motors X-Y-Z range is 200/75/75 mm, position accuracy is 2 μm, repetition accuracy is 2 μm. This allows to inspect area of two daisy-chained sensors with 6×6 cm^2 size each.

The Moticam 5 MP inspection camera with sensor size of 5.76×4.29 mm^2 and resolution of 2592×1944 pixels combined with $12\times$ magnification lens from Navitar is able to move in Z-direction. This allows to inspect the mechanical properties and dimensions of sensors (e.g., warp, etc.). To scan the object under study a LabVIEW program is being developed which allows to move over the sensor in X and Y directions, take camera images and process them with pattern recognition algorithms from NI Vision package to detect the defects (edge and straight edge detection algorithms, pattern matching, etc.).

In order to make inspection procedure precise and reproducible, the inspection table must be calibrated. A 30×40 cm^2 glass calibration plate from *IMT Masken und Teilungen AG* with effective calibration area grid of

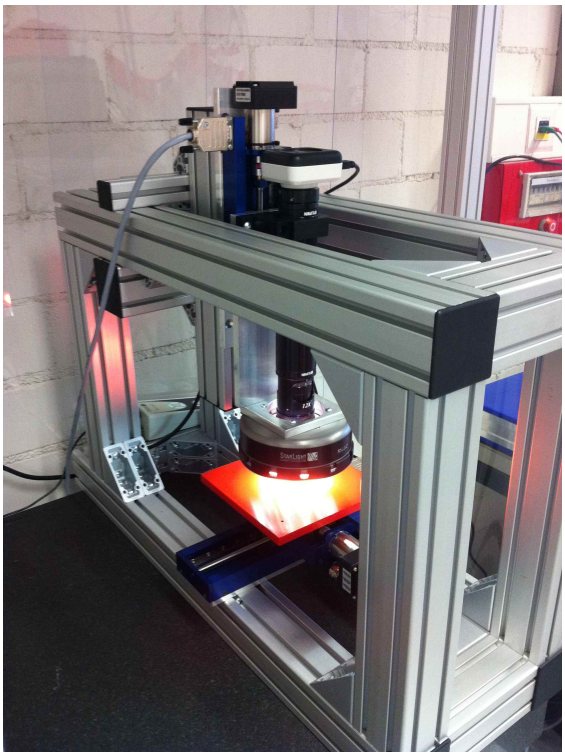

Figure 2: Photo of the optical inspection setup

26×36 cm^2 is used for calibration. The grid is made of calibration crosses distantiated by 1cm from each other. The cross line is 2 mm long and 0.1 mm thick.

To convert points from the real world coordinate space to the servomotor coordinate space the equation (1) is used

$$\vec{x}_m = \mathbf{S}\,\mathbf{R}\,\vec{x}_r, \qquad (1)$$

where S is a stretching matrix, R is a rotation matrix containing the angle between two coordinate systems. To extract the stretching matrix coefficient and the rotation angle a simple Minuit-based fitting program is used. Extracted parameters provide the information required to calibrate the motors and estimate the accuracy. The accuracy for the current version of setup is estimated to be 8 μm.

References

[1] J. M. Heuser *et al.*, Nucl. Instrum. Methods **A 568** (2006) 258

[2] J. Heuser *et al.*, CBM Progress Report 2012, p. 8, `http://repository.gsi.de/record/51950`

Calibration of a laser scanning system for quality assurance of CBM prototype silicon microstrip sensors

P. Ghosh[1,2], *J. Eschke*[2,3], *W. Niebur*[2,3], *H. Malygina*[1,2], *P. Zumbruch*[2], *and B. Kolb*[2]
[1]Goethe-Universität, Frankfurt am Main, Germany; [2]GSI, Darmstadt, Germany; [3]FAIR, Darmstadt, Germany

For the characterization and Quality Assurance (QA) of prototype sensors produced for the Silicon Tracking System (STS) at the Compressed Baryonic Matter Experiment (CBM), a infrared pulsed Laser Testing System (LTS) has been developed. The main aim for the LTS is to scan and characterize the prototype sensors. These QA scans are intended to understand charge sharing in the interstrip region and investigate uniformity of sensor performance in the active area of prototype sensors. The prototype sensor CBM02 which has 256 strips with a pitch of 50 μm on each side has been investigated in the LTS [1]. The strips on the sensors are wire bonded to connectors on a board and readout via self-triggering n-XYTER prototype electronics.

The goal for the LTS is to have automatized quality assurance tests in a controlled manner at several thousands positions across the sensor with focused infra-red laser light ($\sigma_{spotsize} \approx 15$ μm). The duration ($\sim$10 ns) and power (few mW) of the laser pulses are selected such that the absorption of the laser light in the 300 μm thick silicon sensors produces about 24 000 electrons,which is similar to the charge created by minimum ionizing particles (MIP) there.The wavelength of the laser was chosen to be 1060 nm because the absorption depth of infra-red light with this wavelength is of the order of the thickness of the silicon sensors [2].

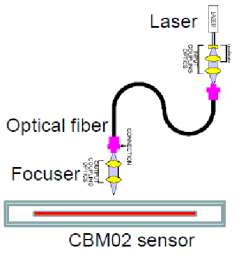

Figure 1: Schematic representation of the laser setup

A schematic view of the measurement setup is shown in Figure 1. The laser light is transmitted through a 6 μm thick optical fiber to a two-lens focusing system, which focuses the light to a spot of about 15 μm diameter and the working distance is about 10 mm. Figure 2 shows a dependence of the distance to the sensor surface as a function of the number of strips fired with a signal just above threshold. With this measurement the proper focus distance has been achieved. Figure 3 shows the charge sharing function between neighboring strips represented in the form of fraction of amplitudes collected by the individual strip.

The LTS has recently been upgraded with motor controls

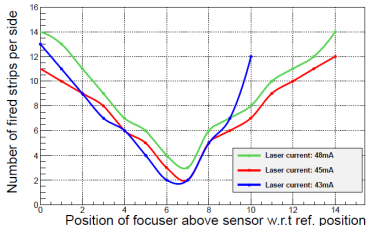

Figure 2: Dependence of distance to focuser from the sensor surface as a function of strips fired

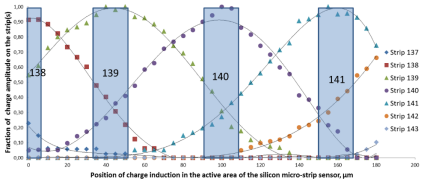

Figure 3: Charge division (fraction of amplitude) in the interstrip region as a function of position of laser spot

using EPICS [3] and programs have been written to step over the active area make several measurements automatically. Figure 4 shows an operator interface of the running system using EPICS tools. The next step is to integrate the data acquisition software DABC [4] plug-in for the EPICS position information for data taking, logging and further analysis using the Go4 analysis software.

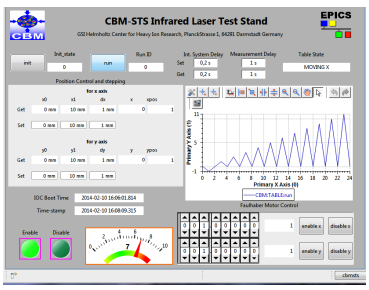

Figure 4: Run time operator interface for the LTS

References

[1] J. M. Heuser *et al.*, CBM Progress Report 2011, p. 17
[2] P. O'Connor *et al.*, Proc. SPIE Vol. 6276 62761W-1, p. 2
[3] `http://www.aps.anl.gov/epics`
[4] `http://dabc.gsi.de`

Development of prototype modules for the CBM Silicon Tracking System

V. M. Borshchov[1], J. M. Heuser[2], I. T. Tymchuk[1], M. A. Protsenko[1], R. A. Kushniruk[1], L. V. Klimova[1], N. F. Chernikova[1], I. Sorokin[2], and T. Balog[2]

[1]LED Technologies of Ukraine (LTU) Ltd, Kharkov, Ukraine; [2]GSI, Darmstadt, Germany

We report on the production of demonstrators modules for the CBM Silicon Tracking System for studying the read-out of differently long strips in sensor or in daisy-chained sensor pair, through long microcables. The design was provided by the GSI team, the technical development and production was performed by the Kharkov team (presently LTU Ltd) within the framework of the STCU partner project with GSI.

Composition of the demonstrators

The demonstrators were developed with regard to the previous experience in developing and investigating the STS detector module prototypes and components [1]-[4]. Except for some improvements and modifications, the demonstrators developed are similar to the previously made demonstrators of the 1-b' type [2]. They comprise:

- one or two daisy-chained new CBM 05 sensors;
- multilayered read-out cables 25cm long;
- flexible boards for bias lines connection;
- rigid holding structure;
- ERNI and LEMO connectors.

The CBM05 sensors (CiS) used in these demonstrators are double-sided 6.2 cm by 6.2 cm silicon microstrip sensors with 1024 strips on each side at a 58 μm pitch. The strips on the P side are tilted at an angle of 7.5 degrees w.r.t. the strips on the N side. The interconnection between the P and N sides of the sensors and the read-out ASICs on FEBs (128 strips/channels from each side of sensor) is accomplished by the use of ultra-light multilayered microcables with the structure identical to that foreseen for the full-scale STS modules. Each multilayered cable consists of:

- two signal layers (adhesiveless dielectric FDI-A-24, 64 40 μm wide traces at a 113 μm pitch),
- three meshed spacers (Kapton 50 μm thick, fill factor about 40%),
- shielding layer (dielectric FDI-A-24).

The daisy-chain connection of the strips on two sensors is realized via daisy-chain cables (dielectric FDI-A-24, 64 or 128 30 μm wide traces at a 58 μm pitch). Bias line connections are via LEMO connectors, and strips read-out connections of the sensor to FEB with the n-XYTER or STS-XYTER ASIC are realized via ERNI connectors.

Table 1: Number of connected strips in the demonstrators

Module	M1	M2	M3	M4
P-side	514-641	0-127	70-197	582-709
N-side	448-575	896-1023	896-1023	448-575
DCC-P	–	–	0-63 960-1023	448-575
DCC-N	–	–	896-1023	448-575

Readout schemes of demonstrators

In the CBM05 microstrip sensors, two types of strips ("long" and "short" ones) and three strip regions can be distinguished, depending on whether their strips have connection pads at both ends ("long" strips region), or at one end only (two "short" strip regions). To study the behavior of "long" and "short" strips on one microstrip sensor and of the connected strips on two daisy-chained sensors four demonstrators were developed and built with strips read-out connections from P and N sides of the sensors and from daisy-chain connection (DCC) of the strips on two sensors. The numbers of the connected strips are given in Table 1, where M1and M2 are single-sensor demonstrators, M3 and M4 are double-sensor ones.

Manufacturing of demonstrators

The manufacturing of the demonstrators required developing and fabricating about 20 types of components over 30 photomasks, as well as the assembly procedures. The work resulted in the four demonstrators shown in Fig. 1. All demonstrators were using production procedures and techniques (SpTAB technology) foreseen to be used with the production of full-scale modules.

Conclusions

The assembled demonstrators were tested in laboratory at GSI and in-beam at COSY. First results of the in-beam test are presented in [5]. They will be applied in future development and manufacturing of detector modules for the CBM STS.

References

[1] V. M. Borshchov *et al.*, CBM Progress Report 2008, p. 12

[2] V. M. Borshchov *et al.*, CBM Progress Report 2009, p. 15

[3] D. Severin *et al.*, CBM Progress Report 2010, p. 15

[4] J. M. Heuser *et al.*, CBM Progress Report 2010, p. 19

[5] J. M. Heuser *et al.*, *In-beam test of prototype modules for the CBM Silicon Tracking System*, this report

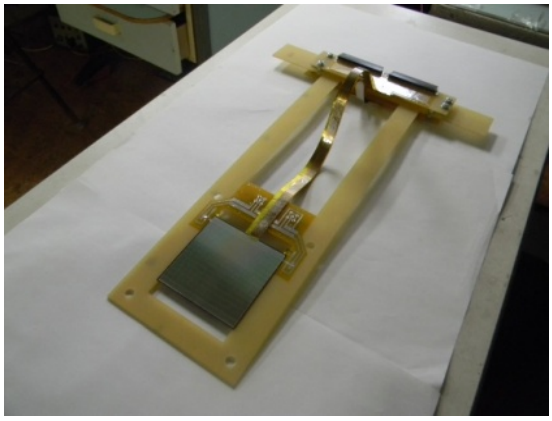

M1

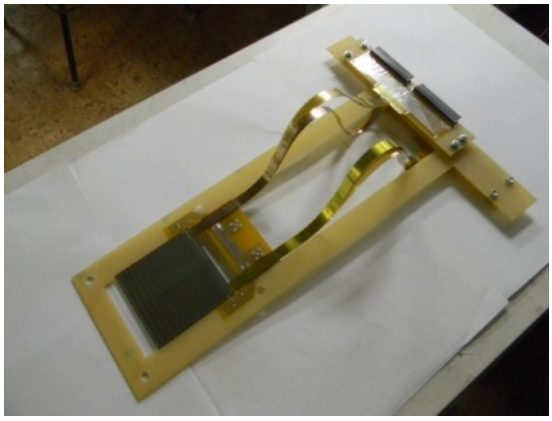

M2

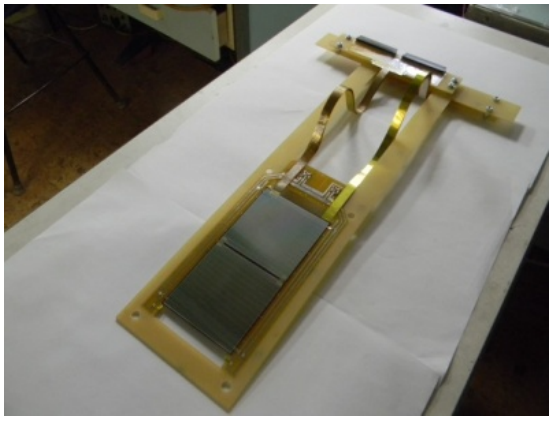

M3

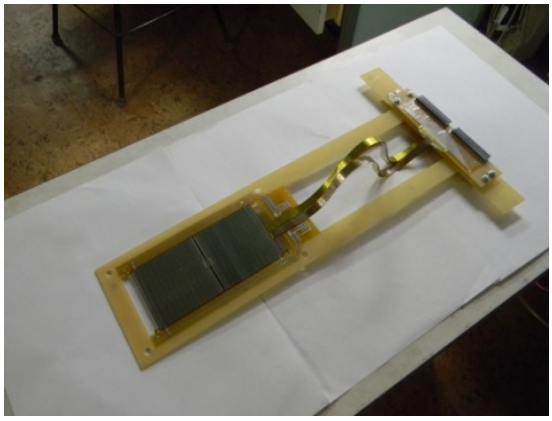

M4

Figure 1: Demonstrator modules assembled for delivery to GSI

In-beam test of prototype modules for the CBM Silicon Tracking System

T. Balog[1,2], *O. Bertini*[1], *J. Eschke*[3], *V. Friese*[1], *P. Ghosh*[4,1], *T. Heinz*[1], *J. Heuser*[1], *V. Khomyakov*[5], *P. Larionov*[4,1], *W. Niebur*[1], *C. Pauly*[6], *F. Uhlig*[1], *M. Singla*[4,1], *I. Sorokin*[4,1,7], *C. Sturm*[1], *A. Wolf*[1], *and P. Zumbruch*[1]

[1]GSI, Darmstadt, Germany; [2]Comenius University, Bratislava, Slovakia; [3]FAIR, Darmstadt, Germany; [4]Goethe-Universität, Frankfurt, Germany; [5]ITEP, Moscow, Russia; [6]Bergische Universität, Wuppertal, Germany; [7]KINR, Kiev, Ukraine

In December 2013 three groups of the CBM and HADES collaborations tested recently developed prototype detectors in the 2.8 GeV high-intensity proton of COSY, Research Center Jülich, Germany. The beam was provided within a week long shift block dedicated to FAIR detector tests. On the test bench in the JESSICA cave were several prototype modules of the CBM Silicon Tracking System, several prototypes of GEM detectors for the CBM muon detection system developed by the CBM groups at VECC, Kolkata, India, and GSI, and diamond detectors for the T0 determination in CBM and HADES developed by GSI and the Technical University Munich. The beam definition was made with the already approved scintillating fiber hodoscopes built at Wuppertal University.

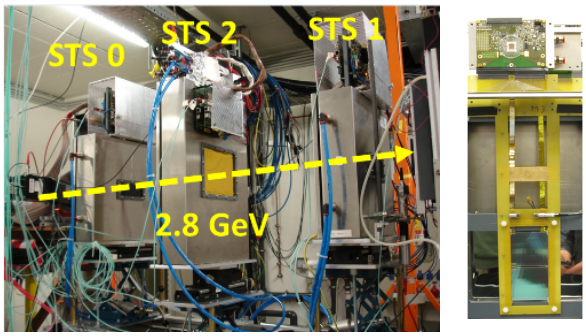

Figure 1: Prototype silicon tracking system in the JESSICA cave at COSY. Station STS 2 comprised the modules under test; one is shown in the right panel.

The modules were to demonstrate the charge collection properties of the recent full-size CBM prototype microstrip sensors CBM05, and the signal transmission to the front-end electronics with optimized micro cables. They were designed at GSI and assembled at SE SRTIIE (team now with LTU) in Kharkov, Ukraine. The read-out was performed with the established front-end boards based on the n-XYTER ASIC. This limited the number of read-out channels to 128 per side, one eighth of all sensor channels. Therefore, the modules were produced in four versions to probe different sensor regions. Two modules used a single CBM05 sensor, one attaching to the central long strips on either side, and another reading out strips of the sensor corners. Two further modules realized, for the first time, also the operation and read-out of daisy-chained sensors, as they will be deployed in the outer regions of STS stations where the track densities allow minimizing the number of read-out channels by using particularly long strips.

The STS set-up on the beam table is shown in the left panel of Fig. 1. Two reference stations (STS 0, STS 1) defined the particle trajectories for impact on station STS 2 comprising a module under test. Such a module, here with daisy-chained sensors and the 25 cm long read-out cable, is shown in the right panel of the figure.

The beam profile was adjusted to a diameter of about one centimeter. As the CBM05 microstrip sensors provide an active area of 6.2 cm by 6.2 cm, the middle station could be adjusted to probe certain sensor regions with beam. In addition to adjusting the horizontal and vertical position, also the impact angle of the beam was changed by rotating the station around the vertical axis. Several tens of runs with large statistics were taken for every module to study the charge collection properties as a function of various parameters, including bias voltage, strip length, signal path length, and beam incidence angle. Detailed analyses are being performed.

The performance of the modules shall be illustrated with charge spectra, here from a module with two daisy-chained CBM05 sensors operated in self-triggered read-out mode. The distributions show, for both the n and p sides of the sensor, the charge collected on all of the 128 channels, after transmission through the read-out cables. The small peak is residual noise, the large peak charge from transient protons.

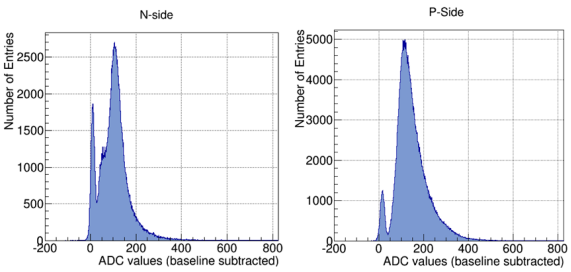

Figure 2: Charge spectra from both sides of a module

Threshold calibration of the n-XYTER readout ASIC

I. Sorokin[1,2,3] *and C. J. Schmidt*[1]

[1]GSI, Darmstadt, Germany; [2]Goethe-Universität, Frankfurt, Germany; [3]KINR, Kiev, Ukraine

The n-XYTER 1.0 front-end chip [1] has been widely used in various projects at GSI, including the CBM experiment, the GEM-TPC and others. The calibration of its threshold scale has however never been reported.

A threshold calibration was performed on two n-XYTER chips, operated on Front-End Board rev. D. Since in most applications the n-XYTER is used without prior threshold trimming, the threshold was not trimmed before calibration in this case either (all trim registers were set to 16). The `Vbfb` register was set to 50, `VBiasS` adjusted such that the baselines are at around 2000 ADC units, and all other settings were kept at the `roclib` (rev. 4174) default values.

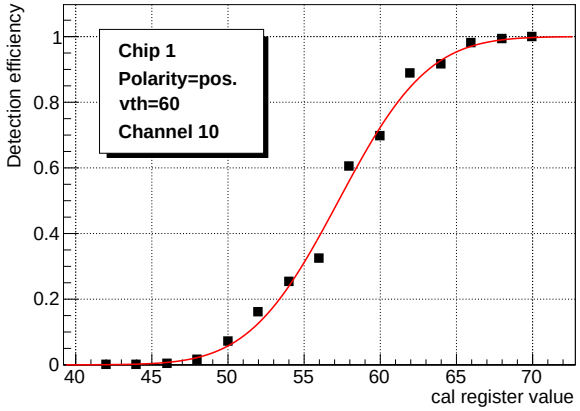

Figure 1: Example for the dependence of the detection efficiency vs. `cal` register setting

To determine the absolute value of the thresholds, pulses of the n-XYTER internal test pulser were injected in groups of 32 channels simultaneously. The number of the channels which the pulses were simultaneously injected to appeared to have no effect on the thresholds. A scan over pulse amplitudes (controlled through the `cal` register) was performed (Fig. 1). The threshold was considered to be equal to the pulse amplitude whenever the pulse detection efficiency was 50%. The corresponding amplitude, expressed in units of `cal`, was determined by fitting the scan data with an error function. Then a the calibration of the `cal` register gain was performed individually for each channel, at low thresholds: the pulse amplitude was measured in the n-XYTER slow lane, digitized with the on-board ADC and converted to the physical units using the calibration [2].

In Fig. 2 an example of the obtained threshold distributions for all channels of one chip, at three different `vth` register settings are shown. The mean thresholds as a function of `vth` for the two different chips are shown in Fig. 3 (the error bars are the variances). It can be seen that both the channel-to-channel as well as the chip-to-chip threshold variations are large (if no threshold trimming is done). In applications, where precise threshold setting is necessary, it is therefore recommended to perform the threshold trimming first, and then to redo the threshold calibration. The developed algorithms can be reused. For rough estimates the Fig. 3 can be used.

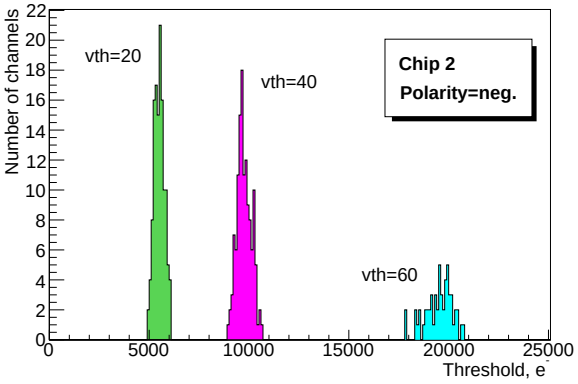

Figure 2: Example of the distributions of the thresholds of all channels in one chip at various `vth` settings

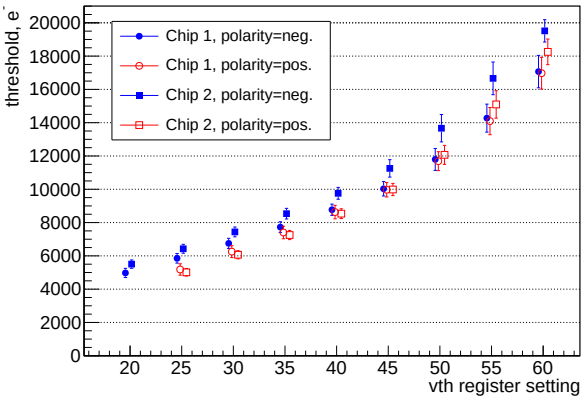

Figure 3: Threshold calibration plot. Points are shifted by $\pm$ 0.15, and $\pm$ 0.45 in x to improve visibility (initially they were at multiples of 5).

References

[1] A.S. Brogna et al., n-XYTER reference manual, unpublished, http://hipex.phys.pusan.ac.kr/drupal/sites/default/files/nXYTER.pdf

[2] I. Sorokin *et al.*, Nucl. Instrum. Methods **A 714** (2013) 136

Experience with TAB bonding of ASICs to front-end electronics boards

V. Borshchov[1], Yu. A. Murin[2], M. A. Protsenko[1], I. T. Tymchuk[1], N. F. Chernikova[1], L. V. Klimova[1], and D. Dementyev[2]

[1]LED Technologies of Ukraine (LTU) Ltd, Kharkov, Ukraine; [2]JINR, Dubna, Russia

Sixteen front-end electronics boards (FEB) comprising the n-XYTER 2.0 ASIC and microcables for their connection to the board, have been assembled at LTU and tested at JINR. The boards base on a design from GSI and were produced within a JINR project.

The spTAB-bonding technology was developed at LTU, Kharkov for double-layer microcable mounting of the ASIC to the PCB in attempt to simplify the FEB assembling procedures relevant to high density challenges of the CBM STS front end electronics. Advantages of the microcable using such ASICs connection were previously described in [1, 2]. The sequence of FEB assembly was the following:

- gluing of PCB to the primary heat-sink (using of heat-conductive paste)
- assembling of double-layer microcable (spTAB-bonding, glue-protection)
- assembling of ASIC with microcable (spTAB-bonding, glue-protection)
- assembling of ASIC with PCB (gluing, spTAB-bonding,glue-protection).

During the assembly of the FEBs technological regimes of spTAB-bonding were investigated (Fig. 1) for five variants of connections as given by Table 1. After assembly the FEBs were tested as depicted in Fig. 2.

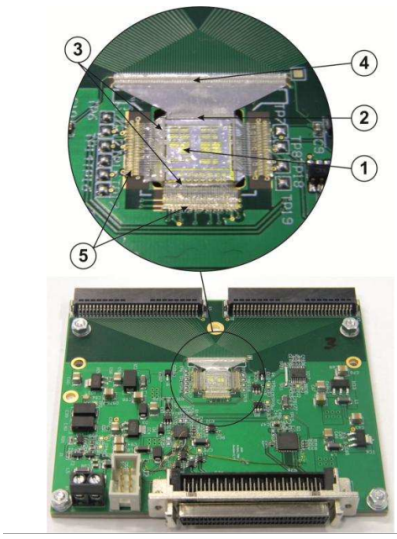

Figure 1: FEB with n-XYTER ASIC connected via microcable by spTAB-bonding

Table 1: Geometric parameters of the bonding areas

Area		# (Fig. 1)	Width of trace, um	Pitch of traces, um
Microcable (top to bottom layers)		1	100	not less than 400
Microcable to ASIC	input area	2	30	50,7
	output area	3	40	100
Microcable to PCB	input area	4	90	150
	output area	5	90	200

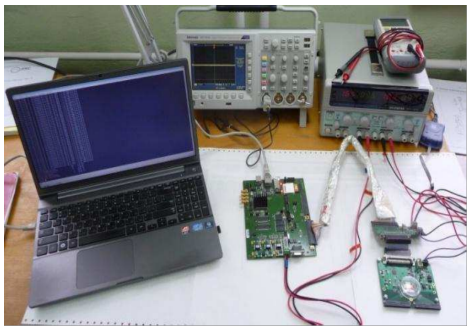

Figure 2: FEB under testing

The JINR FEB design is based on the GSI FEB rev. E schematics with a difference in the layout. The central part is the n-XYTER 2.0 ASIC with associated electronics and a newly introduced feature, the Atmel Atiny 88 MCU which is used to set registers of n-XYTER and ADC. First results of n-XYTER 2.0 tests were previously published [3]. FEBs were operated with SysCore V2.2 board and additional adapter board. Five FEBs were tested and found out to work fine (Fig. 3).

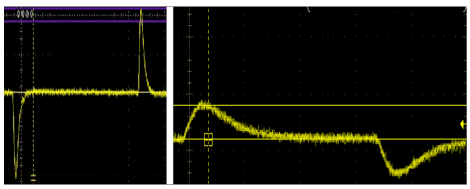

Figure 3: Samples of the signals from the fast (left) and slow (right) shapers of the ASIC test channel

References

[1] V. M. Borshchov *et al.*, CBM Progress Report 2010, p. 17

[2] V. M. Borshchov *et al.*, CBM Progress Report 2012, p. 16

[3] D. Dementyev *et al.*, CBM Progress Report 2012, p. 15

Status of STS-XYTER, a prototype silicon strip detector readout chip for the CBM Silicon Tracking System

K. Kasinski, P. Grybos, R. Kleczek, P. Otfinowski, and R. Szczygiel
AGH University of Science and Technology, Cracow, Poland

The STS-XYTER ASIC was fabricated in 2013 [1] as a 128+2 channel full-size prototype IC dedicated for silicon strip detector readout in the Silicon Tracking System of the CBM experiment. It contains the following functional blocks: a complete analog front-end (AFE) circuit, calibration pulse unit, band-gap circuit and biasing DACs supplied with a digital back-end based on CBMnet protocol and four 500 Mbit/s LVDS data links. The single AFE channel is built of an input stage (charge sensitive amplifier (CSA) and polarity selection circuit) and two different, parallel signal processing chains: the fast and slow. The fast path, optimized for determining an input charge arrival time, is built of: a fast shaper with the peaking time t_P = 40 ns, a discriminator, a pulse stretcher and a time stamp latch. The slow path, which is optimized for low noise, accurate energy measurement, is consisted of: a slow shaper with the peaking time t_P = 80 ns, a 5-bit flash ADC, and a digital peak detector.

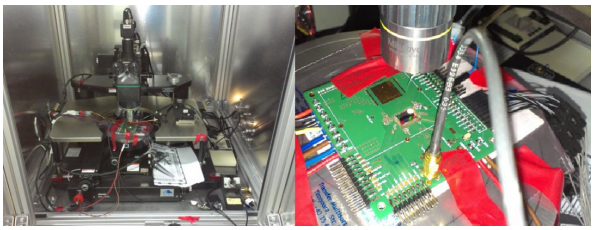

Figure 1: Test setup of the STS-XYTER

The measurements of the STS-XYTER ASIC are in progress. Preliminary tests were performed at AGH using a Cascade Microtech probe station, a NI PXI measurement system and the dedicated test PCB (Fig. 1). A summary of the measured parameters of the analog processing chain is presented in Table 1. The measured characteristics (Fig. 2) of the AFE circuit (recorded for test channel one and negative polarity of input charges) are in agreement with simulation results.

The digital part of the ASIC was partially verified (all configuration registers, behavior of all configuration DACs) by using the test interface. The tests of the CBMnet and LVDS links are also in progress [2]. The ASIC's documentation is continuously evolving [3] to cover all the aspects of the chip operation and performance. The tests revealed also a field for improvement in the next version of the ASIC.

The upcoming tests using the new designed PCBs hosting ASIC (FEB) and the interface system SysCore V3 will enable a complete characterization of the ASIC and verification of the implemented logic.

Table 1: Preliminary characterization of the STS-XYTER prototype ASIC summarized

Parameter	**Measured value**
CSA charge gain	10.4 mV/fC
Fast shaper gain	68 mV/fC for $Q_{IN} < 3$ fC
Slow shaper gain	49.5 mV/fC for $Q_{IN} < 10$ fC
ENC at fast shaper	513 e^- rms (no sensor)
ENC at slow shaper	327 e^- rms (no sensor)
Power consumption	0.52 W total
(AFE, no CBMnet)	4.03 mW/channel

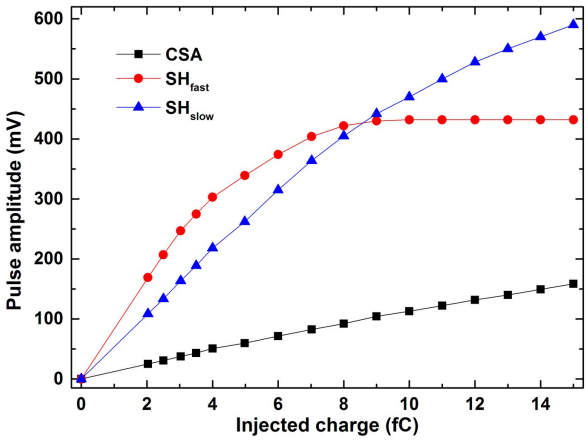

Figure 2: The measured characteristics of the AFE

Acknowledgment

We would like to thank the group from ZITI Heidelberg University and colleagues from GSI for the efforts towards testing of the digital part.

References

[1] P. Grybos *et al.*, CBM Progress Report 2012, p. 17

[2] F. Lemke *et al.*, *Status of the CBMnet based FEE DAQ readout*, this report

[3] STS-XYTER documentation v15a

A front-end electronics board to test the assembly procedure of modules for the CBM Silicon Tracking System

V. Kleipa, C.J. Schmidt, C. Simon, and D. Soyk
GSI, Darmstadt, Germany

For the Silicon Tracking System (STS) of the CBM experiment, about 2000 read out electronic boards (FEBs) have to be produced. They comprise eight readout ASICs of 128 amplifier channels each which will read the 1024 sensor channels on either side of a STS detector module [1]. So there is a need to prepare tools and assembly instructions for their serial production. In order to develop and verify the assembly procedures, a test board has been designed.

The assembly chain will start with the tab-bonding of the read-out micro-cables on the ASICs. Then the ASICs must be glued in spares of the FEB's printed circuit board. In a next step the ASICs will be connected to the supply, control and read-out lines with wire bond. The challenge is how to adjust the ASICs with the sensitive tab-bonded sensor-cables on the PCB and how to connect the ASÌCs further with bond wires to the main PCB.

In all these cases the hight of additional components on the PCB have to be respected. I.e. SMD capacitors and resistors or the globtop - which is protecting the bond wires, cause barriers for the second row of ASIC chips. It needs also to be verified, if embedded passive devices are required to be reduced in height.

Two ASIC footprints are prepared on the PCB for the different test purposes. One footprint needs to be generated with laser cavity technology. Here the bond wires can be connected directly to the inner layers of the PCB. The other footprint consists only of bond pads on the top layer. Some additional routing space will be required here too. Additional thermal cycling tests are planned to proof the safety of the tab and wire bond connections.

The front-end board designed to test the assembly procedure and the functionality of the pairs of ASICs and tab-bonded micro cables is shown in Figures 1 to 3:

- Figure 1 depicts the FEB layout for the assembly test.
- Figure 2 is a 3D rendering of a possible FEB PCB.
- Figure 3 depicts an assembly with FEB, ASICs and micro cables.

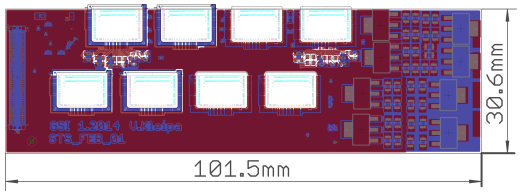

Figure 1: STS FEB8 test layout

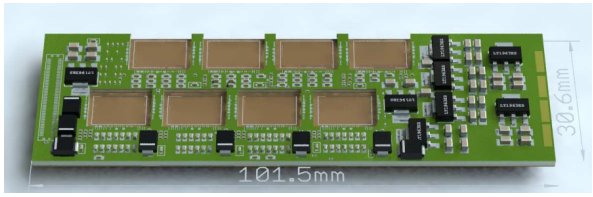

Figure 2: 3D View of equipped STS FEB Board

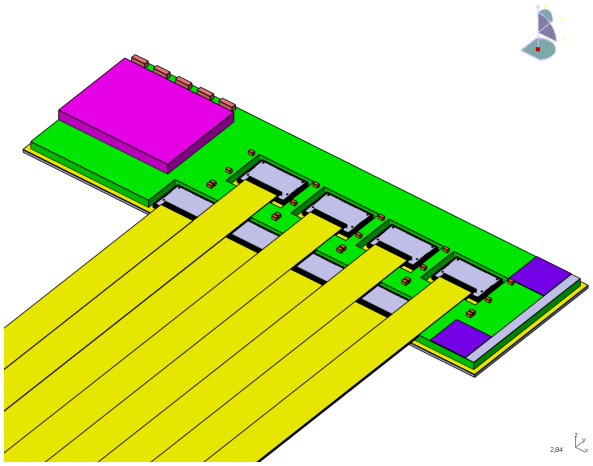

Figure 3: Assembly of sensor cables and FEB

References

[1] J. Heuser *et al.*, *Technical Design Report for the CBM Silicon Tracking System*, GSI Report 2013-4, `http://repository.gsi.de/record/54798`

Low and high voltage power supply for STS detector electronics

P. Koczoń, B. Ernst, and C. J. Schmidt
GSI, Darmstadt, Germany

The silicon tracking detector STS for the CBM experiment at FAIR will work inside a magnetic field of 1 T and will have to stand a radiation load of up to 10^{14} n_{eq}/cm^2 in the regions close to the beam pipe. It consists of more than 1200 double sided silicon sensors arranged in 8 planes covering a cone of the opening angle of ± 25 degrees, illustrated in Fig. 1 [1].

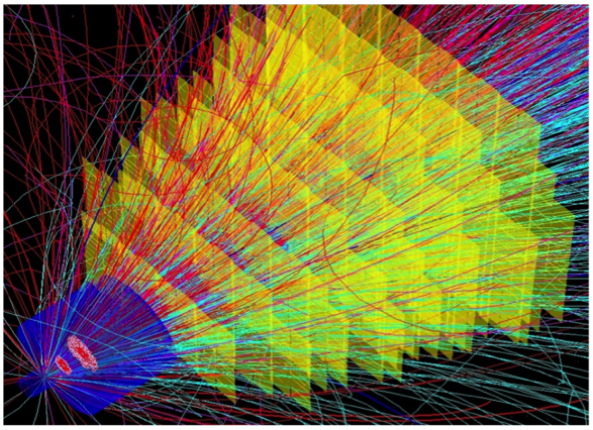

Figure 1: Silicon Tracking System with simulated tracks

The readout electronics should work floating what means that each side of every sensor has to be operated on electric potential of up to ± 250 V (sensor bias up to 500 V) and read out independently of each other.

Each side of each silicon sensor will be supplied with a half of the nominal biasing voltage to achieve full depletion and floating operation mode. Low leakage currents in the sensors allow sufficiently compact feed-through construction and off-the-shelf system for full control of the depletion voltages from outside of the STS thermal enclosure.

The electrical supply needs are a power of about 45 W per detector module at several voltages (1.2, 1.5, 3.3 V). These voltages have to be delivered for each side of every sensor separately. The sheer number of feed-throughs with pin cross sections allowing for currents of 1 - 3 A would exceed the available mounting surface. Cable power losses would require additional sensing wires and would heat-up the surrounding volume. Instead, DC/DC conversion inside the temperature controlled STS-container is proposed.

Several DC/DC converter ICs have been evaluated, both isolated discrete systems (like VICORS P048T048T24AL and B048F012T30) and non-isolated systems (Linear Technology LT3605, LT3610, LTM4619, Texas Instruments LM2596 or Yutaka Electric YSD812). All investigated buck (step-down) systems are equipped with an inductance driven by a pair of high-power transistors. An air-coil type inductivity can work in a magnetic field in contrary to ferrite coils which saturate and cause system malfunction.

Both isolated DC/DC converters appeared to break down already at 50 mT due to the failure of the built-in ferrite inductivity. Measurements of converters based on other chips proved that some of them can work in a magnetic field of up to 0.7 T (field strength at the STS periphery) with efficiency of 80 - 90 % (Fig. 2). Since the evaluation boards in test have been equipped with metal oxide coils there is still a room for efficiency improvement by using air coils.

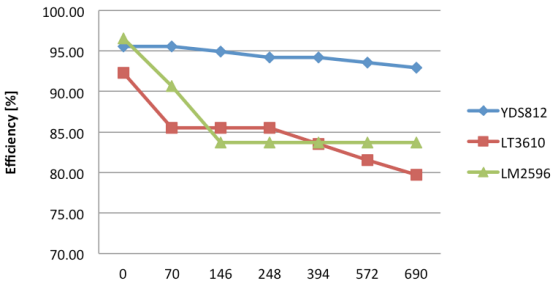

Figure 2: Converter efficiency as function of the magnetic field [mT]

Selected DC/DC converter chips have been tested for radiation hardness and results of these measurements are reported in [2] together with other electronic parts.

References

[1] J. Heuser *et al.*, *Technical Design Report for the CBM Silicon Tracking System*, GSI Report 2013-4, `http://repository.gsi.de/record/54798`

[2] S. Löchner *et al.*, *CBM proton beam test for electronic components*, this report

Status of the CBMnet based FEE DAQ readout

F. Lemke[1], *S. Schatral*[1,2], *and U. Brüning*[1]
[1]University of Heidelberg, Mannheim, Germany; [2]GSI, Darmstadt, Germany

In the past year, the CBM read-out data acquisition (DAQ) network capabilities based on the CBMnet protocol [1] have been extended. Currently, there are two FEE ASIC implementations which include the CBMnet module blocks. The first is the SPADIC V 1.0 [2] with functioning communication, which is currently in the process of commissioning. The second ASIC is the STS-XYTER [3] which provides twice the data bandwidth in back-end direction compared to the SPADIC. Therefore, the CBMnet has been extended to a four-lane core and a lot of improvements were implemented. The functional verification of the digital part has been done with two Spartan6 FPGAs in a long term test running more than 7 days. Hence, the FEE LVDS interconnect [4] has been proven as stable under laboratory conditions. To get more information about the status and error behavior of the LVDS link in the STS-XYTER, a CBMnet diagnostics core has been developed. With that, it is possible to get information about the link quality, read the status of the link initialization and collect statistics about bit-error rates and retransmissions of the active interconnect. The test setup of the STS-XYTER connected to a SysCore3 with HDMI cables is shown in figure 1. The Syscore3 firmware has been extended and now provides a full deterministic optical link.

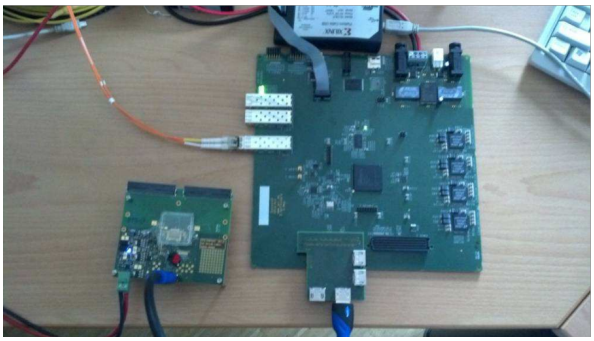

Figure 1: STSXYTER read-out setup

Further research has been done concerning the HUB ASIC to provide a hierarchical synchronized DAQ network [5]. In addition to controlling the FEEs, the focus was to achieve a high density and enable early multi-layered data aggregation capability. Thus, flexible build-up scenarios are possible, which are required due to varying amounts of data for different detector parts. The HUB will support up to 40 FEE links (500 Mb/s) and up to 4 back-end links (5 Gb/s). Besides high density, special difficulties include handling and deadlock avoidance for the traffic, radiation tolerance, and the design of a serializer/deserializer (SERDES) capable of 5Gb/s. A collaboration with the Indian Institute of Technology Kharagpur (IITKGP) was initiated to build this SERDES in partly full-custom design. A SERDES structure diagram is presented in figure 2. It depicts handling of the receive and transmit streams, including features such as clock data recovery (CDR) and eye measurement. Currently, a prototype ASIC is being designed with the focus on testing the SERDES and critical HUB functionality. Therefore, a miniASIC submission will be prepared in 2014 with the TSMC 65nm Europractice process.

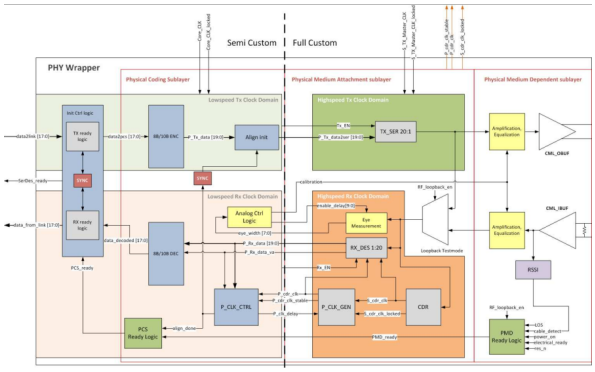

Figure 2: SERDES block-diagram for HUB ASIC

References

[1] F. Lemke and S. Schatral, *Design concepts and measurements of the CBM DAQ networ*, Deutsche Physikalische Gesellschaft EV (DPG13), Frühjahrstagung, March 4-8, Dresden, Germany, 2013

[2] M. Krieger and P. Fischer, *Commissioning of the SPADIC 1.0 Amplifier / Digitizer Chip*, this report

[3] K. Kasinski and R. Szczygiel, *Status of the STS-XYTER, a prototype silicon strip detector readout chip*, this report

[4] S. Schatral, F. Lemke and U. Brüning, *Design of a deterministic link initialization mechanism for serial LVDS interconnects*, TWEPP 2013 - Topical Workshop on Electronics for Particle Physics, Sept. 23-27, Perugia, Italy, 2013

[5] F. Lemke and U. Bruening, "A Hierarchical Synchronized Data Acquisition Network for CBM", IEEE Transactions on Nuclear Science (TNS), Journal Paper, VOL. 60, No. 5, Part II, Oct. 2013.

Development of a CO_2 cooling prototype for the CBM Silicon Tracking System

J. Sánchez[1], J. M. Heuser[1], W. Niebur[1], C. Sturm[1], H. R. Schmidt[2], A. Lymanets[2], P. Petagna[3], B. Verlaat[3], and L. Zwalinski[3]

[1]GSI, Darmstadt, Germany; [2]Eberhard Karls University, Tübingen, Germany; [3]CERN, Geneva, Switzerland

Nowadays the high energy physics detectors require ever more powerful cooling plants as well as a non-invasive piping. This means that the mass budget has to be as small as possible in order to not decrease the efficiency of the detector effective surface. We report on the development of a bi-phase CO_2 test cooling system, called TRACI-XL, that is based on the "2 phase accumulator controlled loop (2PACL)" concept and is carried out at GSI within the EU-FP7 project CRISP in cooperation with experts of the DT group at CERN, and the CBM group at Eberhard Karls University, Tübingen. TRACI-XL is the 1 kW prototype that will be used as a pre-plant design for the cooling of electronics in the CBM Silicon Tracking System STS. A design study of the system is depicted in Fig. 1.

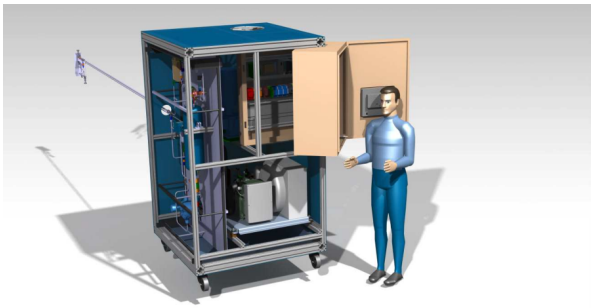

Figure 1: A CATIA model of TRACI-XL

Several fields of engineering have been addressed for the realization of this phase of the prototype design. Different areas as thermodynamics and its study of nucleate boiling, had to be carefully considered. Due to the complexity of this type of evaporative process only the experimental findings can provide more information for the design of the final plant to be installed in the CBM experiment.

Technical documentation like PID diagrams have been developed to be as clear as possible and being similar to some of the screens that were subsequently used in the HMI (Human Machine Interface) thus making TRACI-XL a user-friendly prototype in which a malfunction can quickly be detected. Considering it as one of the most important parts of the system, the secondary CO_2 line has been designed as rigorously as possible, taking into account the possibility of future upgrades to the plant, providing extra flexibility to implement in the future other functionality such as electrical valves to be fully controlled by PLCs. All this is achieved through the choice of high performance Swagelok VCR fittings with high life cycle where subsequently modules may include new parts.

The STS cooling system has to provide necessary cooling power for the front-end electronics at a given thermal load. For this reason, process variables have to be monitored and maintained at their desired values by communicating to the devices in the cooling plant, e.g., heaters, pumps, indicators, etc. The task is automated using Siemens modular programmable logic controllers (PLC). The PLC functionality includes sensor monitoring, device control, data logging and archiving. The system is controlled via a touch panel Human-Machine Interface (HMI). The software framework STEP 7 v11 (TIA Portal) communicates to the PLCs via PROFINET protocol, thus providing a compact automated solution for the TRACI-XL project. Figure 2 shows a test system including the PLC controller with sensor-specific modules (resistance temperature detector, thermocouple, analog input for pressure transmitter readout, etc.) Analog values and digital indicators are displayed on the touch panel.

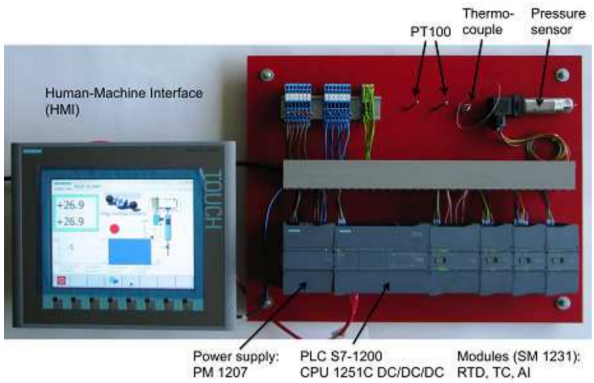

Figure 2: PLC-based test system with analog sensors and touch panel control

References

[1] B. Verlaat, International Conference of Refrigeration 2007, Beijing, China, ICR07-B2-1565

[2] R. W. Lockhart and R. C. Martinelli, Chem. Eng. Progr. **45** (1949) 39

Commisioning of the test CO_2 cooling system for the CBM Silicon Tracking System

E. Lavrik[1], *A. Lymanets*[1,2], *and H.-R. Schmidt*[1]
[1]University of Tübingen, Tübingen, Germany; [2]Kiev Institute for Nuclear Research, Kiev, Ukraine

The CBM Silicon Tracking System [1] is a compact detector that consists of double-sided silicon microstrip sensors comprising volume of about 1 m^3 defined by the aperture of the dipole magnet. The sensors have to be kept at a temperature of $-7°C$ during the in-beam operation in order to avoid thermal runaway and slow down the reverse annealing of radiation defects. The heat sources include self-heating of sensors due to leakage current and heat dissipated by the front-end electronics. The sensors produce about 1 W of power in the innermost region that can be removed using forced convection cooling, e.g. with dry N_2. The 2133k channels of the front-end electronics will dissipate up to 40 kW power localized at the periphery of the tracking stations. Particularly high heat density requires a cooling system with high volumetric heat transfer. Necessary cooling power can be achieved with bi-phase evaporative cooling [2].

A test system designed to dissipate about 200 W under realistic geometrical constraints has to verify the cooling efficiency. The heat generated by resistive thermal load will be dissipated in front-end board (FEB) box with $110\times70\times30$ mm^3 and removed by the integrated capillary with total length of about 2 m and about 2 mm diameter. For this test, an open-loop CO_2 cooling system has been assembled [3] and commissioned.

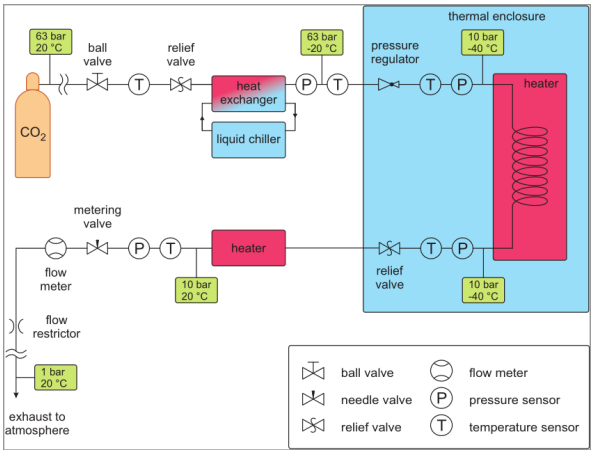

Figure 1: Conceptual scheme of the open-loop test CO_2 cooling system

The operation principle of the test system is sketched in Fig. 1. The liquid CO_2 is supplied from a gas bottle at room temperature and 63 bar pressure. By precooling the liquid down to $-25°C$ in the heat exchanger and expanding it behind the pressure regulator, the liquid is brought to the phase boundary at $-40°C$ and 10 bar from whereon the latent heat can be utilized for cooling. After passing the thermal load and leaving the thermal enclosure, the bi-phase mixture with about 50% dryout is evaporated in the water-based heater and exhausted into the atmosphere. A metering needle valve with flow coefficient up to 0.004 controls the gas flow. A flow restrictor at the end of the transport line prevents the overexpenditure of CO_2. Pressure, temperature and flow are controlled along the line in order to ensure the proper operating conditions.

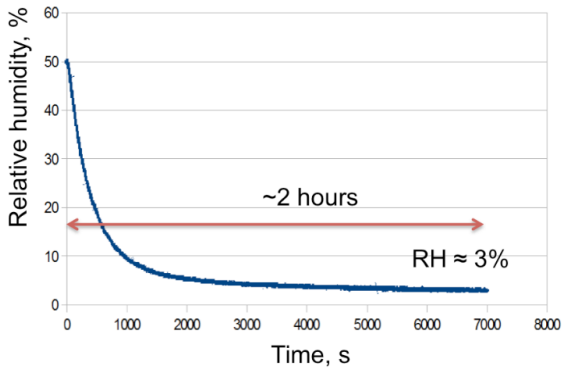

Figure 2: Relative humidity inside of the thermal enclosure that is being filled with N_2 as a function of time

Operation of the cooling setup at low CO_2 temperatures requires special care to be taken to prevent the ice formation. Thus, if cooling agent is at $-40°C$ and surrounding atmosphere in the enclosure is at room temperature, the relative humidity has to be below 0.5% for the dew point to be lower than $-40°C$ such that no ice is being formed. The vapour isolation of the thermal enclosure of the cooling system has been checked by filling it with dry nitrogen at a flow rate of 16 l_n/min. The resulting time dependence of relative humidity is shown in Fig. 2. The relative humidity saturates at the level of about 3% within 2 hours.

References

[1] J. M. Heuser *et al.*, Nucl. Instrum. Methods **A 568** (2006) 258

[2] B. Verlaat *et al.*, TWEPP'08, Naxos, Greece, 15-19 Sept. 2008, pp. 328-336

[3] E. Lavrik *et al.*, CBM Progress Report 2012, p. 20

First mock-up of the CBM STS module based on a new assembly concept

V. M. Borshchov[1], *C. J. Schmidt*[2], *Yu. A. Murin*[3], *I. T. Tymchuk*[1], *M. A. Protsenko*[1], *J. M. Heuser*[2], *R. A. Kushniruk*[1], *L. V. Klimova*[1], *and N. F. Chernikova*[1]

[1]LED Technologies of Ukraine (LTU) Ltd, Kharkov, Ukraine; [2]GSI, Darmstadt, Germany; [3]JINR, Dubna, Russia

The first mock-up of the CBM STS detector module based on a modified design and new assembly concept has been developed and manufactured by the Kharkov team at the newly created assembly site of LTU Ltd.

The initial module concept [1, 2] foresaw multi-layered cables comprising 512 traces at each signal layer. Based on the experience obtained in the prototyping stage and taking into account risk minimization and yield increase with the manufacture and assembly of components a new design and assembly concept was suggested [3]. The module mock-up was developed for verification of this concept. It includes the following components, similar as in real full-scale modules:

- dummy microstrip double sided sensor (1024 strips on each side at 58 um pitch, 7.5° stereo angle of strips);
- prototypes of multilayered connection microcables (1024 lines for one side of sensor);
- dummy chips with 128 input pads;
- dummy FEBs with 8 seats for chips.

A microcable consists of the following layers:

- eight multilayered microcables (128 lines for chip to sensor connection). Each multilayered cable includes two connecting layer (FDI-A-24, 64 traces at 113 μm pitch) and meshed spacers (Kapton 50 μm thick, fill factor about 40%).
- overall meshed spacer for all 8 multilayered microcables (Kapton 100 μm thick or two spacers 50 μm thick, fill factor about 40%).
- overall shielding layer for all 8 multilayered microcables (FDI-A-24) with glued meshed spacer (Kapton 50 μm thick, fill factor about 40%).

For the first detector module mock-up the following technological sequence has been developed:

1. Assembly (gluing) of multilayered components (connecting and shielding layers with spacers).
2. SpTAB bonding bottom connecting cables to chips, bond joints protecting.
3. SpTAB bonding top connecting cables to chips, bond joints protecting.
4. Aligning of sensor sides of the top and bottom cables and cables gluing (fixing precise aligned position one to each other).
5. Aligning of sensor sides of 8 assembled multilayered connecting cables to sensor.
6. Gluing of overall meshed spacer or shielding layer (depending on modules side).
7. Mounting (gluing, wire bonding, encapsulating) of assembled multilayered cable with chips to the FEB (first 4 chips than second 4 chips),
8. Multilayered cables (mounted on the FEB) SpTAB bonding to the sensor (bottom cables, then top cables), bond joints protecting,
9. Flipping the assembled half-module upside down,
10. Repetition of operations 7 and 8 for second side.

For the first module mock-up were developed and produced more than 10 types of component requiring more than 20 photomasks. As a result of abovementioned works the first half-module (only one sensor side connected, without wire bonding chip-to-FEB) was assembled (Fig. 1).

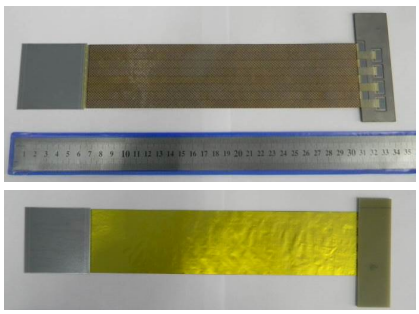

a)

b)

Figure 1: First mock-up of the CBM STS detector half-module a) top view, b) bottom view.

During the assembly of the first module mock-up only visual inspection were performed but for real detector modules after each bonding of connecting layers to sensors or chips need to be done electrical QA testing.
Results of development and assembling of the first mock-up of the CBM STS half-module confirm practical feasibility of suggested concept on detector modules creation.

References

[1] V. M. Borshchov *et al.*, CBM Progress Report 2009, p. 17

[2] Yu. A. Murin *et al.*, CBM Progress Report 2011, p. 19

[3] C. J. Schmidt *et al.*, CBM Progress Report 2012, p. 18

Development of a tool for CBM STS module assembly

D. Soyk, J. Kunkel, C. Simons, and C. J. Schmidt
GSI, Darmstadt, Germany

The assembly of a silicone strip sensor with microcable and the readout chip is called in the CBM STS collaboration a "module". To connect the double-sided CBM sensor with 1024 channels on each side via microcables to the CBM STS-XYTER chip the tab-bonding process was chosen. One microcable has 64 channels with a pitch of 116 μm and a lead width of 46 μm. The thickness of the aluminium lead is 14 μm and the thickness of the polyimide substrate is 10 μm. Consequently the microcable is easily floating, fragile and not easy to handle without tooling. For the assembly of the chip or of the sensor to the microcable, the microcable has to be moved in two translational and one rotational directions (see Fig. 1). Therefore

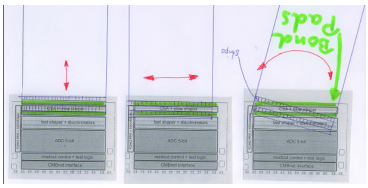

Figure 1: Degrees of freedom of the microcable

the assembly tool needs at least two translational and one rotational degree of freedom to assure a correct alignment of the microcable to the sensor or chip. To realize these three degrees of freedom the microcable can be fixed and the sensor, respectively the chip, can be movable. Alternatively the microcable is movable and the sensor, respectively the chip, is fixed. Finally the microcable as well as the sensor respectively the chip are movable. For the first test version the decision was taken to move only the microcable and keep the sensor, respectively the chip, on a fixed position.

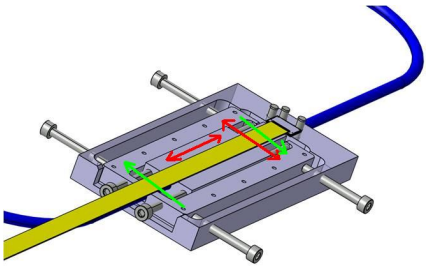

Figure 2: CAD model of assembly tool with chip and microcable (yellow). Red and green arrows indicate the different degrees of freedom

To fixate the sensor respectively the chip and the microcable on the assembly tool it is a good choice to use vacuum, because the microcable would be deformed by mechanical clamping, and the clamping tools for sensor respectively chip will reduce the accessibility of the bond pads.

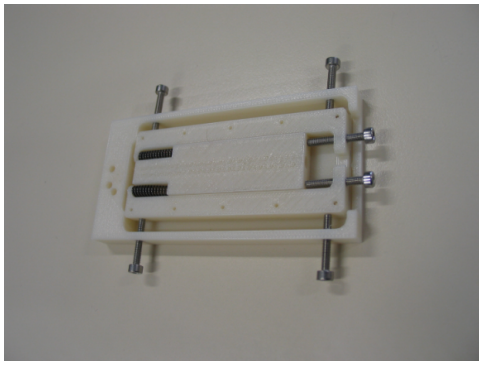

Figure 3: 3D model of the tool

To speed-up the development the 3D CAD data (see Fig. 2) were printed using a 3D plotter and tested by the bond experts before the final tool was machined out of aluminium. Due to the printing process some fine structures on the tool were not perfectly shown (see Fig. 3), but it was precise enough to decide about the handling properties of the tool. In Fig. 4 the final tool in aluminium is shown.

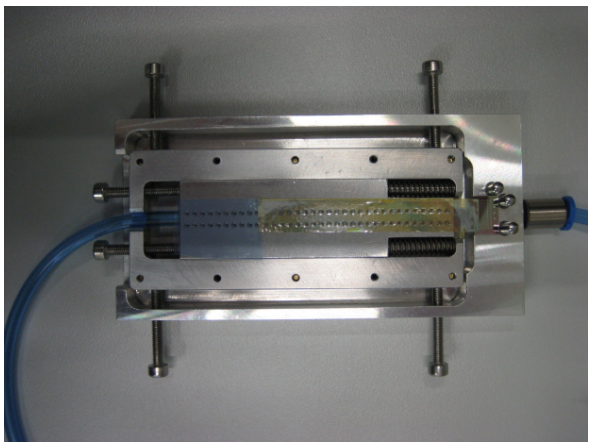

Figure 4: Final tool

While using the final version of the tool it turned out that it works well and fulfills all requirements.

A setup for adjustment of process parameters for CBM module production

D. Soyk[1], C. Simons[1], C. Schmidt[1], I. Tymchuk[2], M. Protsenko[2], and V. M. Borshchov[2]
[1]GSI, Darmstadt, Germany; [2]LTU, Kharkov, Ukraine

The sensor modules for the CBM STS comprise an STS microstrip sensor, 16 CBM STS-XYTER readout chips and 32 microcables of 64 leads each. The double-sided STS sensor has 1024 strips on each side. Consequently 2048 channels per module must be connected by means of 4096 bonds. It is obvious that the quality assurance of theses tab-bonds is a major ingredient to the yield of module production and reliability of the detector as a whole. Especially the large number (around 1000) of modules needed for the entire CBM STS requires to have a detailed look at the tab-bond process and its parameters, as potentially required repair actions on defective modules will be time consuming and adds the risk of additional inadvertent damage to the module. Therefore it is the best solution to improve and bring the tab-bond process to perfection before starting the serial production of modules for the CBM STS.

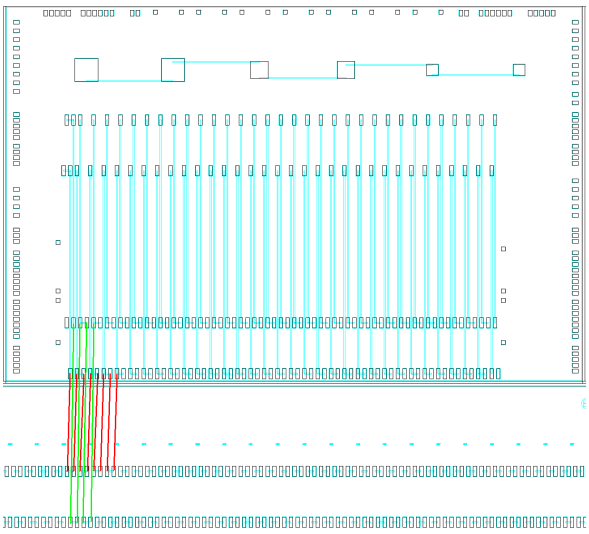

Figure 1: Dummy CBM STS-XYTER chip (up) and a partial plan of a CBM sensor dummy (down). The red lines are the connections via the microcable for the first row of bond pads. The green lines are the connections via a second microcable for the second row of the pads. In the upper part of the Dummy CBM STS-XYTER are the contact pads for the test equipment directly connected to the tab-bond pads in the lower part of the chip.

It is clear that for such process optimization no original full functional STS sensor and CBM STS-XYTER chip will be used or needed. The first reason is the costs of the original components and second reason is the missing of fast and easy ways to check the quality of the tab-bonds. For this reason, dedicated dummy-sensors as well as dummy-chips have been designed and manufactured. To check the quality of bonding two tests are necessary. One is the pull test to check mechanical adhesion of the aluminum lead of the microcable to the bond pad. The second is the electrical connectivity of the bond.

In order to make this test conclusive for the real module the microcable must the original, the surface and the material of the bond pads for dummy-sensors and chips must be identical to the material on the original sensors and chips. Also, the Silicone wafer material and thickness should be identical. If these requirements to the microcables, dummy sensors and chips are fulfilled, it is possible to transfer the process data to the serial production process.

To improve the test routines for the electrical contacts, additional pads for test needles and connections between the pads were added to the dummy-sensors and -chips. (These additional features will not be part of the layout of the final devices.) In Fig. 1 the scheme of electrical connections is shown with the layout of the dummy chip and sensor. On the dummy chip, each second pad of each row is electrically connected to a pad far away from the tab-bond area. (The first pad of a row is like the second also electrically connected to a shifted pad.) The non duplicated pad is electrically connected to its left neighbor. On the dummy sensor two neighboring pads of a row are electrically connected together.

The idea behind this set-up is to make an electrical connection between the pad of the test needle via the tab-bond on the chip, the microcable, the tab-bond on the sensor and back to the second test pad for each row. With this simple serial routing it is possible to check 4 tab-bond connections and two leads of the microcable with one single measurement. If the connection is good the first needle is kept on its starting position whereas the second needle is shifted to the next pad of the row. This daisy chaining now allows to check 8 tab-bonds and 4 leads of the microcable in one go. While continuing this daisy chaining it is possible to check numerous tab-bonds and microcable leads. If a broken lead or damaged tab-bond is found the first needle of the test set-up must be moved to the unconnected pad and the second needle can step further. With this test strategy we can reduce the number of single tests, because only broken leads or tab-bonds will cause a restart of the test procedure. Additionally the test procedure could be done automatically on a wafer prober.

At the moment the dummy chips and sensors have been delivered. We are now waiting for a sufficient number of sample microcables to start process optimization.

Productivity estimates of module and ladder assembly sites in the CBM STS project

V. M. Borshchov[1], *J. Heuser*[2], *Yu. A. Murin*[3], *M. A. Protsenko*[1], *and I. T. Tymchuk*[1]
[1]LED Technologies of Ukraine (LTU) Ltd, Kharkov, Ukraine; [2]GSI, Darmstadt, Germany; [3]JINR, Dubna, Russia

The CBM STS detector system consists of eight tracking stations depicted in Fig. 1 [1]. The total amount of ladders and modules is 106 (126) and 896 (1075), respectively, with the additional "spares" ones indicated in parentheses. Their distribution across the stations is shown in Table 1.

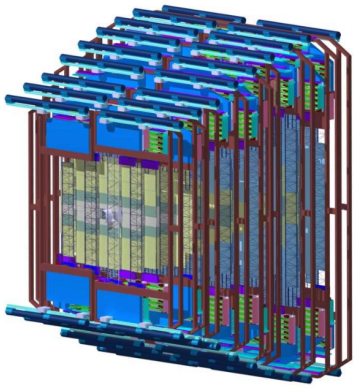

Figure 1: STS detector system

A typical module assembly site is assumed to have at least five workplaces with outfitted with the following equipment [2, 3, 4]:

1. workplace for preparation of mechanical parts,
2. workplace for modules and components assembly (automatic bonder for TAB-bonding),
3. workplace for bond joints protection and gluing (dry box, scales, oven),
4. workplace for modules and components testing,
5. workplace for chip-to-FEB wire bonding (semi-automatic bonder for wire-bonding).

Table 1: Composition of the STS stations

Station No.	Number of ladders	Number of modules
1	8 (9)	76 (91)
2	12 (14)	100 (120)
3	12 (14)	108 (130)
4	14 (17)	116 (140)
5	14 (17)	112 (134)
6	14 (17)	112 (134)
7	16 (19)	136 (163)
8	16 (19)	136 (163)

All working places must be equipped with microscopes and ionizers, and have storage space for in- and outgoing components foreseen. The clean rooms purity must correspond to the ISO 7 class with an area of not less than 35-40 m^2 (excluding technical areas). The staff working in the cleanroom needs to amount to at least four technical persons. Based on the performed estimations the site can ensure assembly productivity (during the production stage) of 15-16 modules per month.

A ladder assembly site must have at least three workplaces with requirements similar to the module assembly site [2, 3, 4]

1. workplace for ladder assembly (optical-mechanical system)
2. workplace for glue preparation (dry box, scales)
3. workplace for ladder testing.

The area of this site shall be not less than 15-20 m^2 (excluding technical areas). The working staff in the cleanroom at such site is at least three trained technicians. The estimate for the ladder assembly productivity (during the production stage) ranges at around 3 ladders per month. The ladder and module assembly can be performed at the same one site of sufficiently large area.

Taking into account the presented estimates it is reasonable to organize two assembling clusters (one in Germany and one in Russia). Each cluster must contain a center (for modules and ladders assembly) site and one or more satellites (for modules assembly) as follows:

- GSI (center) with Univ. Tübingen and KIT (satellites),
- JINR (center) with IHEP (satellite).

Such organization and structure of assembly sites will allow producing the required 1075 modules within 24 months and 126 ladders within 21 months.

References

[1] J. Heuser *et al.*, *Technical Design Report for the CBM Silicon Tracking System*, GSI Report 2013-4, `http://repository.gsi.de/record/54798`

[2] Workshop on module and ladder assembly for the CBM Silicon Tracking System, JINR, Dubna, Russia, 6-7 June 2013

[3] 22nd CBM Collaboration Meeting, JINR, Dubna, Russia, 23-27 September 2013

[4] Workshop on module and ladder components production and assembly for the CBM Silicon Tracking System, LTU Ltd, Kharkov, Ukraine, 14-17 January 2014

The layout of the CBM Silicon Tracking System

T. Balog and J. Heuser
GSI, Darmstadt, Germany

As the central detector in the Compressed Baryonic Matter experiment, the Silicon Tracking System (STS) is required to perform efficient charged-particle tracking with high momentum resolution. With feedback from the engineering activities, the detector's layout has been further optimized, in particular to minimize the number of modules, the component with most complex assembly and associated production risks and costs.

The STS will be located in the gap of the 1 T dipole magnet and will comprise 8 tracking stations between 30 and 100 cm distance downstream of the target. Its polar aperture, where minimal material budget is achieved, is 2.5-25°. The STS stations are built from detector ladders that are populated with detector modules. A detector modules is the functional unit of a single silicon microstrip sensor (or a pair of daisy-chained sensors), read out by two front-end electronics boards, and read-out cables between the sensoric part and the electronics. Eight or ten modules mounted onto a carbon fiber support structure form a ladder; the electronics is arranged at the top and bottom end of the ladder, reaching already out of the physics aperture. The ladders themselves are arranged on further support frames to form the stations of the STS. As an active material double-sided silicon sensors of 300 μm thickness and readout strip pitch of 58 μm will be used. The angle between front and back side is 7.5^o where only the strips of the p-side are tilted and n-side strips are vertically oriented. Different strip lengths are used for the different regions of the STS (short in inner region and long in outer areas). Such way the maximum occupancies are kept all over the tracker below few per cent. Sensors and read-out electronics will be interconnected via low-mass micro-cables.The total material budget in a station ranges from 0.3% X_0 (inner regions) to 1.2% X_0 (outer parts).

The recent optimization to the detector layout were made due to a paradigm change with respect to the component with most complex assembly. As this was previously the detector ladder, where the mechanical assembly had to be made with highest accuracy and involved costly machinery and survey time, the recent progress in the module development now revealed that the modules themselves present as the most work intensive objects. The ladders turned out to need less absolute mechanical precision, but stability and compatibility with mechanical survey for later alignment procedures with straight particle tracks and suitable software. An optimization of the population of STS ladders with modules of different strip length was possible since there was a reserve of unnecessarily high segmentation near the horizontal coordinate, a consequence of multiply deployed ladders of the same design.

The new layout of the STS stations reduces now significantly the absolute number of modules. The variety of modules increases, though, but only involving differently long read-out cables that can be accommodated in the assembly fixtures and leave the mechanical complexity unchanged. The stations were commuted into doublets, where four (almost) identical pairs of stations were introduced, increasing the number of identically populated ladders.

The STS breaks down into 106 ladders to be produced in 17 variations, i.e. that many different module combinations are to be arranged on carbon fiber supports. They realize a symmetrical granularity within the stations decreasing from their center to the outer edge. The total number of modules in the STS amounts to 896. The modules come in 18 varieties having differently long sensors and read-out cables in certain combinations. In the optimized layout requirements such as full acceptance coverage (including the innermost areas around the beam-pipe) have been considered. The layout of one pair of stations is shown in Fig. 1. The performance of the re-arranged detector system has been verified in simulation studies. The tracking efficiency of 97% for fast primary tracks and 90% for secondary tracks together with a momentum resolution of 1.3% were confirmed.

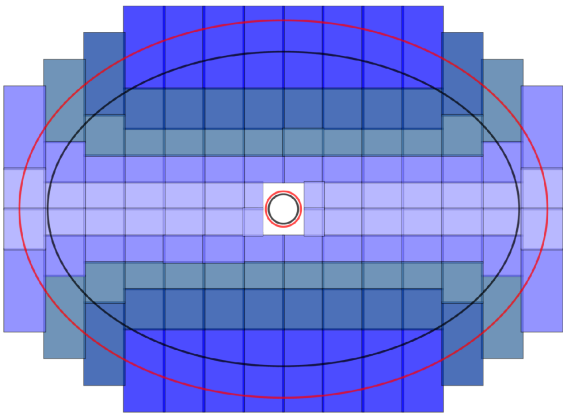

Figure 1: Layout of the second doublet of STS tracking stations. Black and red lines indicate the acceptance for stations number 3 and 4, respectively, including the horizontal enlargement for low-momentum tracks.

Application of the CBM Silicon Tracking System CAD model for integration studies

S. Belogurov[2], A. Kolosova[2], and J. Kunkel[1]
[1]GSI, Darmstadt, Germany; [2]ITEP, Moscow, Russia

Motivation

The high density of equipment inside the gap of the CBM dipole magnet requires special attention to the integration effort and, more generally speaking, to the system engineering of the set-up. In this report we discuss the current status of the system integration effort, the tasks to be solved and the methods in use.

CAD (Computer Aided Design) software is one of the major tools in complex system development. It is used to create a virtual model of the product in development. For the CBM STS detector system a virtual model of the whole system is created with CATIA, a software package for product development that covers the whole process from first sketches to final drawings for the manufacturing of components.

Status and tasks of the system integration

The STS detector system is designed in functional parts, such as main detector parts, mounting structures, enclosures and supply lines. The virtual model in the CAD software is set up in the same way. Since parts and assemblies are stored in separate files, collaborative work on different parts of the detector at the same time is possible.

One important integration task is to reserve space for various functional nodes. Currently we develop to arrange in space of the following items: Sensors, sectors, modules, ladders, data cables, C-shaped supporting frame for ladders, fixation for the ladders and for the cables, front-end-boards (FEB), FEB fixation and cooling boxes, cooling plates common for a unit (i.e. two neighboring half stations belonging to the two consequent stations), CO_2 cooling connections, power supply lines for FEBs, data transport lines from FEBs to data aggregation boards, voltage conditioners for the FEBs, optical links and cooling boxes for voltage conditioners, data aggregation boards and optical links. An overall view of the STS and a detailed view of one quarter of the 8th station are shown in Figs. 1 and 2, respectively. Generally, the design of the STS follows an onion logic from the innermost parts to the outer ones.

Space analysis allows to see the critical elements in the system. E.g. it has been demonstrated that the availability of single-channel radiation hard SFP optical links only causes a limitation on the total number of channels in the system. Any development towards higher granularity would require new radiation hard multichannel optical links.

Another task for the system integration is to study and to balance contradictory requirements of various origin. E.g. front-end electronics developers tend to insist on the shortest possible cables in any particular case, however the reasoning of the C-Shaped frame rigidity and cooling plate beauty forces us to use sometimes the cables a bit longer than absolute minimum. A further issue under investigation is the checking for all the possible dependencies, e.g. the thickness of cooling plates has influence on the space available for bending of cables, and the pad pattern on different sensors, staggering of the sensors in a ladder and spacing between the FEBs in the working position are connected to the reduction of the number of different types of cables.

Methods in use

For the integration studies a deeply parametrized model has been created using the CATIA VBA code called "STS creator". The tool arranges correctly in space all the components based on parametrized templates. The composition of the ladders can be modified later and all the parts like CF ladder support frames, C-shape unit frames and cooling plated will be adjusted automatically. The entire model can be checked for interferences, margins and free space. Using such a tool allows saving a lot of manpower and time since, for the CBM STS, the active detector part consists of several hundreds of parts.

For making design information available for further analysis each functional node has an *HTML* description accessible from CATIA. Cross links to descriptions of mother and daughter products are generated automatically. A data base for design solutions, options, versions, open questions and mutual dependencies is under development. Data retrieval from this base can be made available from the above mentioned *HTML* documentation.

Next steps

We plan to establish a CAD data exchange platform for efficient collaborative work on the project. Dedicated programs like Git and Subversion are available for software developers. Although CATIA files are binary such a tool could satisfy our needs for sharing data and revision control. Special programs for CAD data handling are under investigation, too. The design solution database mentioned above should be transferred from prototype to development status. The outer layers of the system, like connecting unit to the outside world, thermal enclosure and the mechanical super structure should be developed rather soon.

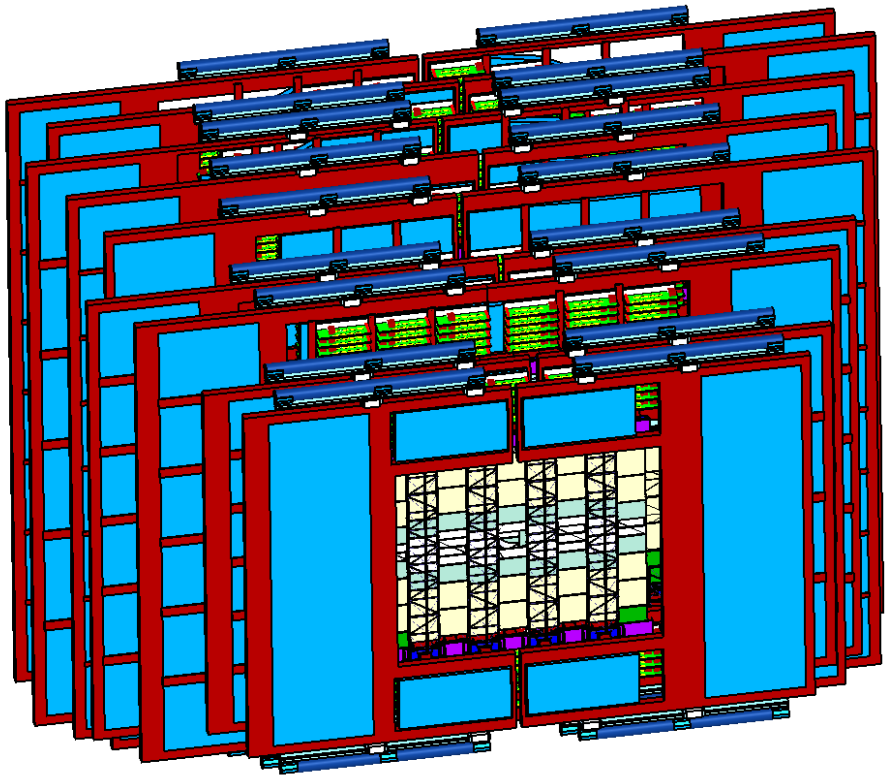

Figure 1: Overall view of all 8 STS stations

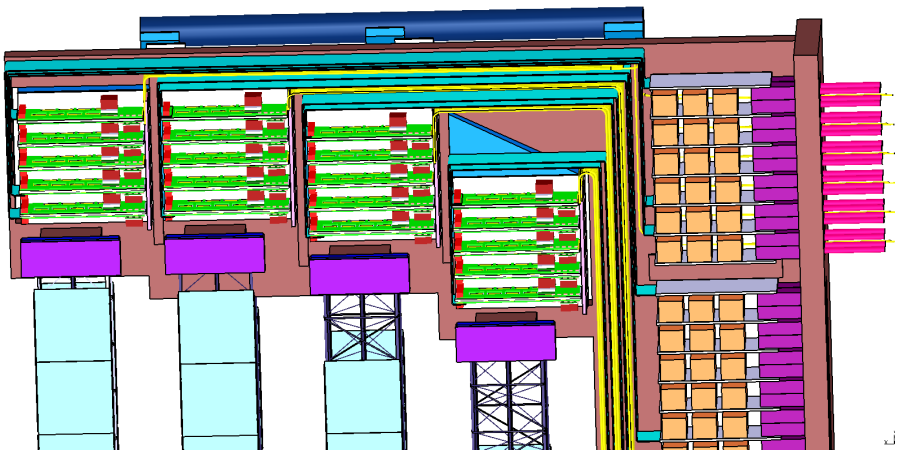

Figure 2: One quarter of station 8 including readout and data transfer electronics, power supply and cooling equipment

A mechanical model of an STS station for the study of cable routing

P. Koczoń, J. Kunkel, D. Soyk, and C. J. Schmidt
GSI, Darmstadt, Germany

The silicon tracking detector STS for the CBM experiment at FAIR poses an engineering challenge due to its compactness and requirements concerning signal density, signal-to-noise ratio, and efficiency. The restricted height of the magnet yoke opening together with the number of readout channels and requirement to geometrical acceptance, operating temperature and mass budget [1] leave very little room for the readout and data transfer electronics and needed power conversion electronics inside of the STS container (Fig. 1).

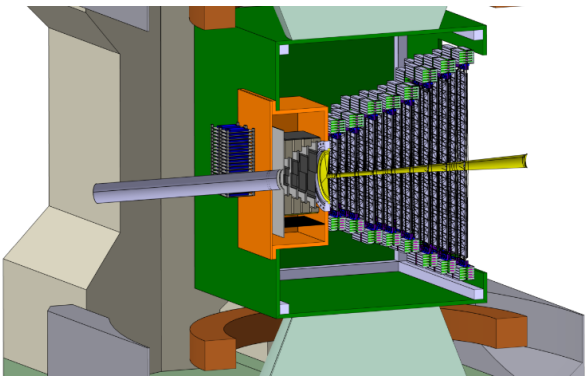

Figure 1: STS in the yoke of the dipole magnet

Under such restrictive conditions it is very critical to find proper mechanical, electronic and electrical solutions/components like very compact circuits of highest efficiency, fine-pitch flexible cables for analog and digital signals, corresponding connectors or bonding methods as well as thin and flexible cables of adequate lead cross section for power supply. Last but not least the positioning of the components and shape of the cooling bodies together with the topology of cable routing paths have to be defined.

In order to verify many of the posed questions and corresponding tentative answers a three-dimensional model of one STS station has been constructed. Axial symmetry of the STS allows to concentrate on one quarter of the most crowded station 7 of the STS (Fig. 2). The model has been constructed according to mechanical design drawings and fulfills requirements like parts' dimensions, cable thickness and flexibility. This mechanical mockup allows confirming methods elaborated for the handling of STS stations and its subsystems as well.

Figure 2: Mechanical model of one STS station

References

[1] J. Heuser *et al.*, *Technical Design Report for the CBM Silicon Tracking System*, GSI Report 2013-4, `http://repository.gsi.de/record/54798`

Ring-Imaging Cherenkov Detector

Comparison of various photon sensor devices in the RICH-prototype beamtest 2012 at CERN/PS

S. Reinecke[1], K.-H. Becker[1], C. Deveaux[4], V. Dobyrn[5], M. Dürr[2], C. Höhne[4], K.-H. Kampert[1], L. Kochenda[5], J. Kopfer[1], G. Krauss[2], P. Kravtsov[5], S. Lebedev[4], E. Lebedeva[4], T. Mahmoud[4], E. Ovcharenko[3], C. Pauly[1], J. Pouryamout[1], J. Rautenberg[1], Y. Riabov[5], E. Roshchin[5], V. Samsonov[5], J. Song[6], E. Vznuzdaev[5], M. Vznuzdaev[5], J. Yi[6], and I.-K. Yoo[6]

[1]Bergische Universität, Wuppertal, Germany; [2]Hochschule Esslingen, Esslingen, Germany; [3]ITEP Moscow, Russia; [4]Justus-Liebig-Universität, Gießen, Germany; [5]Petersburg Nuclear Physics Institute, St. Petersburg, Russia; [6]Pusan National University, Pusan, Korea

The analysis of the 2012 CERN/PS beamtime related to the CBM-RICH prototype ([1]) has been nearly finished showing different promising results (see also [2, 3, 4]). One main goal was the comparison of three photon sensor types for the RICH-camera, namely the Hamamatsu H8500 MAPMT, the Hamamatsu R11265 MAPMT and the Photonis XP85012 MCP. As a short reminder the camera with all different sensors can be seen in Fig. 1.

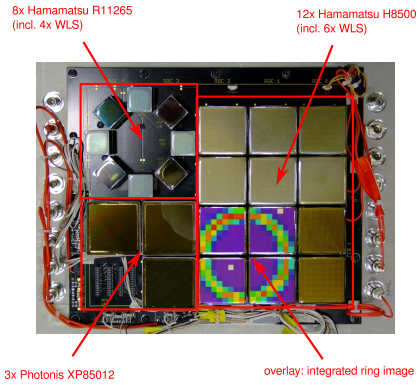

Figure 1: Photograph of photon detector tested in 2012, overlayed with one integrated ring image scaled to realistic size. The 3 × 4 MAPMTs on the right half are of type H8500, the 8 ring-shape arranged MAPMTs in the upper left corner of type R11265 and the 3 ones in the lower left corner are the Photonis XP85012 MCPs.

In order to compare the different sensors with respect to photon detection efficiency, first the individual crosstalk has to be estimated. Crosstalk is here defined as additional registered hits in neighbouring pixels, which are not directly derived from a photon. First estimations were already done from lab-measurements for several H8500 and R11265 MAPMTs [5]. In these lab results a systematic effect due to varying illumination intensity was discovered, which has now been treated properly in the analysis of the 2012 beamtime data. The resulting crosstalk can be seen in Fig. 2 for all 23 sensors for standard (hardware-) thresholds and high voltages.

The resulting crosstalk amounts of both MAPMT types meet our expectations, but the MCPs show a much worse behaviour. One reason for this is the relatively low threshold as with additional ADC cuts the crosstalk amount can be significantly reduced (but with a decent loss in efficiency). The R11265 show by far the smallest crosstalk owing to the small size and the single-photon optimization. In contrast to the old crosstalk measurements the new ones show more consistent characteristics and therefore seem more reasonable.

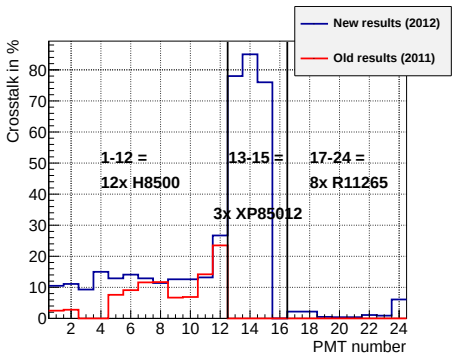

Figure 2: Crosstalk for all 23 used sensors (position 16 did not hold a PMT). For comparison, values from previous analyses were included for several H8500 MAPMTs (not available for PMT nos. 3 and 4).

By taking these crosstalk results into account one can now compare the crosstalk-corrected photon yields of the different sensor candidates. The most important aspect of this comparison is the number of detected photons per Cherenkov ring, which is influenced by temperature and pressure, by the different geometrical proportions and the amount of produced crosstalk of each individual photon sensor. Using dedicated runs this aspect could be studied in dependence on the used high voltage and threshold values. The results for different high voltages (with fixed threshold) and for different thresholds (with fixed HV) can be seen in Figs. 3 and 4, respectively.

As expected the R11265 PMT, in comparison to the other sensors, detects most Cherenkov photons because of its Super-Bialkali cathode (the others have only Bialkali) and its optimization for single-photon measurements. Even though the XP85012 MCP has a quartz window (compared to the UV-extended borosilicate window of both MAPMT types) and would therefore be expected to perform better

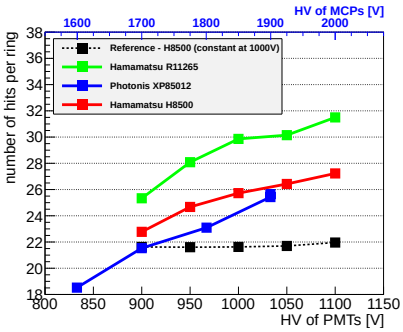

Figure 3: Number of detected photons per Cherenkov ring for different high voltages and fixed hardware thresholds

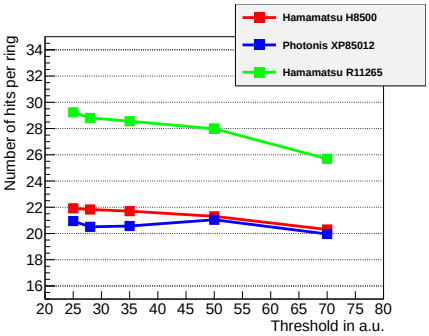

Figure 4: Number of detected photons per Cherenkov ring for different thresholds and fixed high voltages

(especially in the deep-UV region, matching the slope of the Cherenkov spectrum), the bad quantum efficiency and the high amount of crosstalk level out this advantage, resulting in a performance comparable to the H8500 PMT.

Another efficiency test involved a H8500 model with SBA cathode and only 8 dynode stages ("standard" is 12 stages) and was compared by the number of hits per half-ring. The results show that in total this PMT type detects more photons but only because of the higher quantum efficiency. When correcting for the QE the results are worse for this type compared to the 12-stage version with BA.

One question, which occured on several meetings and has also been proved for the CLAS12-RICH [6], is the influence of the dispersion of the CO_2 radiator on the ring sharpness which is most remarkable in the deep-UV region. Investigations were done by using two MAPMTs with borosilicate window (transmission cut-off at around 300 nm) and comparing the dR-distributions (distance between hit and fitted ring) for half-rings lying on these MAPMTs with the ones lying on standard MAPMTs (with UV-extended borosilicate window).

Figure 5 shows the width of the dR-distributions for several half-rings on different positions. There is indeed a small gain on ring sharpness when neglecting deep-UV photons (lower left position), but the size of this effect is too small to be of any relevance for the CBM-RICH, at

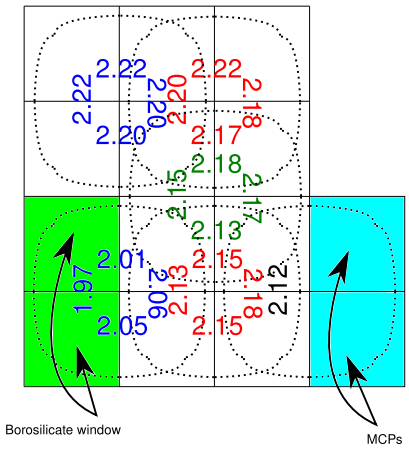

Figure 5: Width (in mm) of dR-distributions for several half-rings (left/right + top/bottom) on different positions with an additional ADC-cut on 20% of the single-photon peak. Each half-ring covers two PMTs. Different colours are only for better optical separation. Half-rings covering the same two PMTs should ideally have same dR-width.

least when comparing the homogeneity over all positions and when also considering a pixel granularity of 6.5 mm. Therefore CO_2 can be used without any concern in this respect.

Even though a final decision of the sensor type for the CBM-RICH camera would seem possible regarding the presented results, Hamamatsu recently developed a new sensor, the H12700, which should combine the size of the H8500 (and also its price) with the single-photon detection capabilities of the R11265 MAPMTs (also with SBA cathode). If future measurements confirm these statements, the H12700 will most probably be the sensor type of our choice.

As long as we can handle the magnetic stray field in the region of the camera, the MCPs will not be considered anymore as photon sensor because of their worse photon detection efficiency and especially the very high price. Also the high crosstalk amount would significantly increase the hitrate on the camera in the full CBM-RICH.

References

[1] S. Reinecke *et al.*, CBM Progress Report 2012, Darmstadt 2013, p. 30

[2] T. Mahmoud and C. Höhne, *Mirror displacement tests - simulation and beam time results*, this report

[3] J. Kopfer *et al.*, *Pion suppression with the CBM RICH prototype*, this report

[4] J. Kopfer *et al.*, *Cherenkov photon detection with WLS coated MAPMTs*, this report

[5] J. Kopfer *et al.*, CBM Progress Report 2012, Darmstadt 2013, p. 29

[6] R. A. Montgomery, Nucl. Instrum. Methods **A 732** (2013) 366

Cherenkov photon detection with WLS coated MAPMTs

J. Kopfer[1], *C. Deveaux*[2], *M. Dürr*[2], *J. Eom*[3], *C. Höhne*[2], *K.-H. Kampert*[1], *L. Kochenda*[4], *P. Kravtsov*[4], *S. Lebedev*[2], *E. Lebedeva*[2], *T. Mahmoud*[2], *Y. Nam*[3], *C. Pauly*[1], *S. Reinecke*[1], *Y. Riabov*[4], *J. Song*[3], *J. Yi*[3], *and I.-K. Yoo*[3]

[1]Bergische Universität, Wuppertal, Germany; [2]Justus-Liebig-Universität, Gießen, Germany; [3]Pusan National University, Pusan, Korea; [4]Petersburg Nuclear Physics Institute, St. Petersburg, Russia

The performance of wavelength shifting (WLS) films on the front windows of MAPMTs installed in the CBM RICH prototype camera was studied during the beam test campaign in 2012 [1]. Three types of MAPMTs were coated with WLS films of approximately 200 nm thickness, which has been shown to be the optimium thickness for the respective MAPMTs with UV-extended front window [2].

The WLS films were evaluated by first measuring Cherenkov rings on an array of two by two MAPMTs with WLS films, then cleaning these MAPMTs, and measuring a second time on the same MAPMTs without WLS coverage. A correction for variations of the refractive index due to temperature and pressure changes during the cleaning process was done by using the data recorded by the gas system [3].

The analysis shows an increased hit multiplicity, i.e. photoelectrons per electron ring after ring finding and ring fitting [4], for WLS coated MAPMTs. Figure 1 depicts the hit multiplicity distribution for coated and uncoated MAPMTs of the H8500D-03 type. When comparing different MAPMT types, the following result is obtained (see Table 1): The gain with WLS films is 21.2 % for H10966A-103 (size 2", SBA photocathode, UV-extended window), 18.2 % for H8500D-03 (size 2", BA photocathode, UV-extended window), and 18.0 % for R11265-103-M16 (size 1", SBA photocathode, UV-extended window). This hierarchy is also seen in full Monte Carlo simulations using the measured wavelength dependent quantum efficiency (*QE*) for the different MAPMT types. The larger gain in hit multiplicity of the H10966A-103 compared to the H8500D-03 type can be understood when considering that, in the case of SBA photocathodes, the UV photons are shifted to a wavelength range with higher *QE* when compared to BA photocathodes. The comparison between both SBA MAPMT types, H10966A-103 and R11265-103-M16, reveals that the thinner front glass of the 1" R11265-103-M16 is more UV transparent than the thicker glass of the 2" H10966A-103 and thus makes the use of WLS films less effective.

When using WLS films on the MAPMTs, in principle two effects can lead to a decrease of the ring sharpness. First, due to the isotropic fluorescence of WLS films, the majority of wavelength shifted photons pass the MAPMT front window under a more inclined angle than without WLS film. Since the window has a certain thickness, the photon will thus enter the photocathode at a different position compared to the point of incidence on the window surface and the ring sharpness is therefore expected to decrease. Second, since chromatic dispersion is more pronounced in the UV range, the enhanced UV sensitivity with WLS coating may lead to a decrease in ring sharpness. Here, the ring sharpness is quantified by the parameter *dR*, which is defined as RMS of the distribution of the distance between each hit and the circular ring fit.

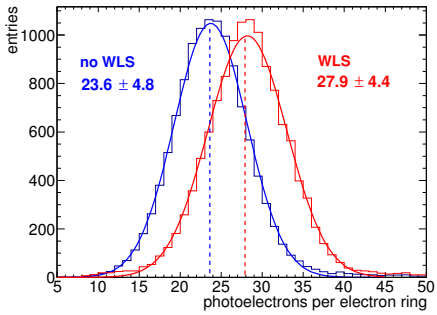

Figure 1: Number of photoelectrons per electron ring on H8500D-03 MAPMTs with WLS film in comparison to the same MAPMTs after film removal. Numbers show mean and sigma of gaussian fits to the distributions.

Table 1: Hit multiplicity gain due to WLS films on different MAPMT types in data and simulation.

MAPMT type	hit multiplicity gain data	hit multiplicity gain MC
H10966A-103	(21.2 ± 1.4) %	(23.1 ± 4.8) %
H8500D-03	(18.2 ± 1.5) %	(18.3 ± 4.7) %
R11265-103-M16	(18.0 ± 1.4) %	(14.8 ± 3.9) %

For H8500D-03 MAPMTs, the parameter *dR* has a value of 2.73 mm with WLS films and 2.42 mm without. The difference of $\approx$ 0.3 mm is small compared to the absolute value of *dR*. Given the pixel size of 6.125 mm and the resulting spatial resolution of the MAPMTs under test of $(6.125/\sqrt{12})$ mm $= 1.8$ mm, the effect on the ring sharpness is not significant.

References

[1] S. Reinecke *et al.*, CBM Progress Report 2012, p. 30

[2] T. Schweizer *et al.*, CBM Progress Report 2012, p. 34

[3] L. Kochenda *et al.*, CBM Progress Report 2012, p. 36

[4] S. Lebedev and C. Höhne, CBM Progress Report 2012, p. 37

Pion suppression with the CBM RICH prototype

J. Kopfer[1], C. Deveaux[2], V. Dobyrn[3], M. Dürr[2], J. Eschke[4], C. Höhne[2], K.-H. Kampert[1], L. Kochenda[3], P. Kravtsov[3], D. Kresan[4], S. Lebedev[2], E. Lebedeva[2], T. Mahmoud[2], C. Pauly[1], J. Pouryamout[1], J. Rautenberg[1], S. Reinecke[1], E. Roshchin[3], V. Samsonov[3], J. Song[5], E. Vznuzdaev[3], M. Vznuzdaev[3], J. Yi[5], and I.-K. Yoo[5]

[1]Bergische Universität, Wuppertal, Germany; [2]Justus-Liebig-Universität, Gießen, Germany; [3]Petersburg Nuclear Physics Institute, St. Petersburg, Russia; [4]GSI, Darmstadt, Germany; [5]Pusan National University, Pusan, Korea

For a clean identification of electron-positron pairs with the CBM RICH detector, the suppression of pions is of major importance. During the beam test with the CBM RICH prototype at the CERN PS in 2011 [1], the pion suppression factor could be measured as function of momentum using a mixed beam of single electrons and pions. The pion suppression factor is defined in the context of prototype measurements as the number of pions identified in two threshold Cherenkov counters and generating a ring in the prototype divided by the number of such pions identified as electrons in the RICH detector.

During the beam test, the particle momentum was varied between 2 GeV/c and 10 GeV/c in steps of 1 GeV/c. Figure 1 shows the reconstructed ring radius for both electrons and pions at 10 GeV/c. By using the two threshold Cherenkov counters, electrons and pions can be separated and are marked in blue and red respectively. An interval $\mu_e \pm k\sigma_e$ around the mean of the electron peak is marked with two vertical lines. The value for k is chosen such that the interval contains a certain fraction of all electrons. This fraction is the so-called electron efficiency e_{eff}. In Fig. 1, $e_{eff} = 95$ %, i.e. 95 % of all electrons have a radius within the cut. Pions within the cut are misidentified as electrons. The pion suppression factor is determined as ratio between the number of all pions and the number of pions misidentified as electrons.

In Fig. 2, the measured pion suppression factor is shown as function of momentum and for electron efficiencies between 93 % and 99 %. It can be observed that the pion suppresssion factor decreases with increasing momentum. Since electron and pion rings have more similar radii at large momenta, the separation gets more difficult and thus the pion suppression factor decreases. It can be also observed that the pion suppression factor drops with larger electron efficiency since a wider electron cut results in a lower separation capability between electrons and pions because more pions are lying under the electron peak.

Moreover, Fig. 2 shows the pion suppression factor from a full Monte Carlo simulation of the prototype in CbmRoot. It can be seen that simulation and data agree up to 9 GeV/c and $e_{eff} \leq 97$ %. The discrepancy at 10 GeV/c and electron efficiencies exceeding 97 % is due to muons in the pion data sample [2].

In conclusion, the agreement between data and simulation in terms of the pion suppression factor verifies the CBM RICH simulations done with CbmRoot.

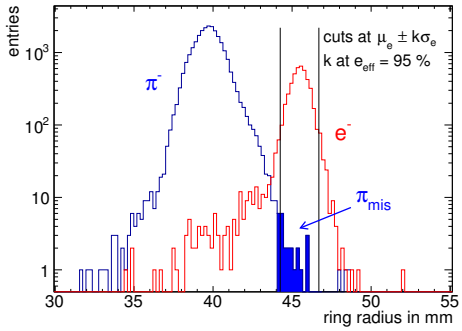

Figure 1: Radius distribution of electrons and pions at 10 GeV/c. PID is done with two external threshold Cherenkov counters. In the prototype, particles with a radius within the cut at $\mu_e \pm k\sigma_e$ are identified as electrons. Here, k is adjusted such that electrons within the cut add up to 95 % of all electrons The pion suppression factor is given by the ratio between the number of all pions and the number of misidentified pions.

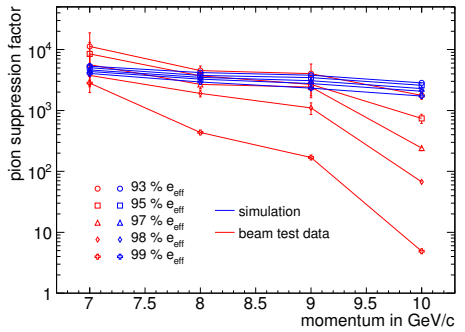

Figure 2: Comparison of simulated and measured pion suppression factor. The pion suppression factor below 7 GeV/c cannot be given due to limited statistics. Simulation and data are in agreement up to 9 GeV/c and $e_{eff} \leq 97$ %. Lines between the data points are drawn to guide the eye.

References

[1] J. Kopfer *et al.*, CBM Progress Report 2012, p. 27

[2] T. Mahmoud *et al.*, *The RICH detector of the CBM experiment*, submitted to JINST

Mirror displacement tests - simulation and beam time results

T. Mahmoud[1], C. Deveaux[1], V. Dobyrn[2], M. Dürr[1], J. Eschke[3], C. Höhne[1], K.-H. Kampert[4], L. Kochenda[2], J. Kopfer[4], P. Kravtsov[2], D. Kresan[3], S. Lebedev[1], E. Lebedeva[1], C. Pauly[4], J. Pouryamout[4], J. Rautenberg[4], S. Reinecke[4], E. Roshchin[2], V. Samsonov[2], J. Song[5], E. Vznuzdaev[2], M. Vznuzdaev[2], J. Yi[5], and I.-K. Yoo[5]

[1]Justus-Liebig-Universität, Gießen, Germany; [2]Petersburg Nuclear Physics Institute, St. Petersburg, Russia; [3]GSI, Darmstadt, Germany; [4]Bergische Universität, Wuppertal, Germany; [5]Pusan National University, Pusan, Korea

Misalignment of mirror tiles in the RICH detector can lead to displacing the hit position of a reflected photon on the detector plane (see Fig. 1). This corrupts the shape and properties of Cherenkov rings. To determine displacement tolerances this aspect was simulated and addressed within beam tests with the real-size RICH prototype, where the mirror system consists of four real-size mirror tiles. In a previous report, preliminary results of beam time data were presented [1].

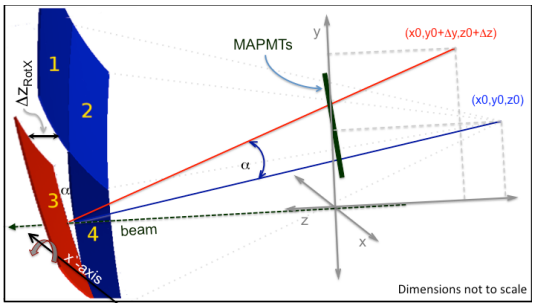

Figure 1: Displacement of the top side at mirror number 3, Δz_{RotX}. The blue (red) line connects the beam position on the mirror surface with the middle point of the sphere before (after) the rotation.

Study environment: The upper side of mirror number 3 was displaced backwards as illustrated in Fig. 1. This displacement is called Δz_{RotX} and corresponds to a rotation around the x'-axis by an angle α_X. Simulations and measurements were carried out with an electron beam with a momentum of 3 GeV/c. The beam center runs exactly between mirrors number 3 and number 4. The main focus was on the half major axis, A-axis, of an elliptic fit on reconstructed Cherenkov rings.

Results: The left panel of Fig. 2 shows simulated A-axis distributions as a function of Δz_{RotX}. Starting from the ideal case with Δz_{RotX}=0 mm, the mean value of the A-axis distribution increases with Δz_{RotX} and starts decreasing at Δz_{RotX}=1 mm. This behavior is easily understood when considering the half ring which is reflected on mirror number 3. It moves along the photon detector plane upwards as seen in Fig. 3. For small displacements the ring finder still finds one ring and the ring fitter fits it but with a larger A-axis. The larger the displacement the more pronounced is the splitting of both halves and consequently the A-axis grows more and more leading to wider distributions.

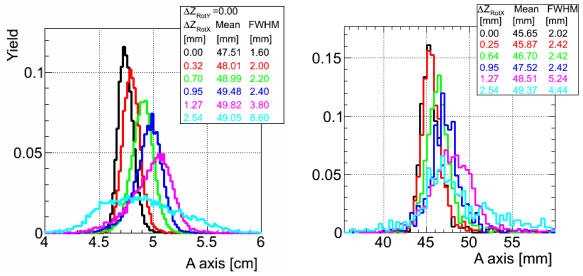

Figure 2: A-axis distributions for several Δz_{RotX} displacements. Left: simulations; right: measured data.

At $\Delta z_{RotX} \approx 1$ mm the splitting is pronounced enough such that the ring finder recognizes two rings as seen in Fig. 3. They can be fitted with more realistic values of the A-axis. This partial regeneration of the distribution shape is deceptive because we have two rings stemming from one electron. The right panel of Fig. 2 shows measured data. Within tolerances they agree well with simulations.

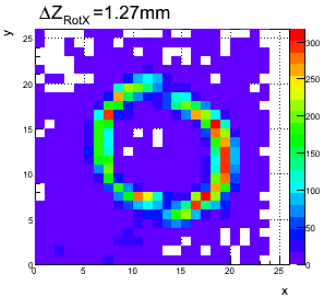

Figure 3: Measured Δz_{RotX} of 1.27 mm. At such a displacement the ring is splitted pronouncedly in two semi-rings.

Conclusions: The study shows that a displacement of Δz_{RotX}=0.32 mm, corresponding to an α_X of about 1 mrad is still tolerable. In this case A-axis values increase by about 1% only. Displacements in other directions lead to the same conclusion of tolerances of 1 mrad around any axis running along the surface of any mirror.

References

[1] T. Mahmoud and C. Höhne, CBM Prog. Report 2012, p. 38

Ronchi test for measurements for the mirror surface of the CBM-RICH detector

E. Lebedeva, T. Mahmoud, and C. Höhne
Justus-Liebig-Universität, Gießen, Germany

The CBM RICH detector will be operated with CO_2 radiator gas, MAPMTs (Multi-Anode Photo Multiplier) as photodetector and spherical glass mirrors as focusing element. Surface homogeneity is one of the important properties required for the single mirror tiles. The global homogeneity has been tested with the $D0$ measurement as reported earlier [1]. Local deformations e. g. by the mirror holding structure can be investigated with the Ronchi test method from which first results are discussed in this contribution.

The principle of the Ronchi test is quite simple. A grating, called Ronchi ruling, consisting of fine, opaque, equally spaced lines ruled onto a transparent substrate is projected onto the whole mirror surface. The shadows of these lines then appear on the face of the mirror under test and will be reflected back onto a camera. The shape and position of these bands is examined and interpreted to give information about the shape of the mirror's surface. Contrary to the $D0$ measurement the Ronchi test thus allows to get information on local mirror deformations which is of particular interest considering e g. inhomogeneities which may be caused by the mirror mounts.

The Ronchi test is inherently qualitative and needs detailed comparison to a computer model in order to assess possible distortions more quantitatively. The band shapes observed in the Ronchi test can be caused by many different mirror types, i. e. surface profiles. Therefore the pattern seen in the Ronchi test has to be compared with a virtual, perfect mirror copy of the mirror under test. However, the qualitative picture quickly achieved and presented in this contribution already reveals a lot of useful information about the mirror at a glance. It later may also be used for a fast semi-qualitative test which allows to quickly check the local mirror homogeneity in particular after gluing the mirror mounts.

Figure 1 shows the sketch of the experimental setup for the $D0$ measurement, which was used for the Ronchi test as well. The only difference is the usage of the Ronchi grating in front of the CCD camera (c) and the laser point source (b). The Source-Camera (SC) unit is located exactly at the mirror radius R. The active area of SC is located in the same plane orthogonal to the optical axis of the mirror. A mirror prototype with a curvature radius of 3 m from SLO Olomouc was tested. The mirror is flashed with light from the point source. If the mirror had an ideal spherical shape, the fringes seen on the camera would appear straight. Deviations from the spherical surface cause deformations of the fringes, but the measurement is only sensitive to changes of

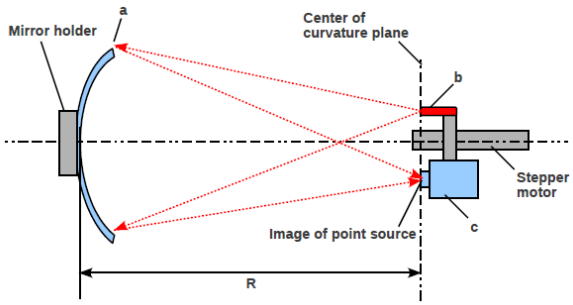

Figure 1: Experimental setup

the curvature radius perpendicular to the grating direction. In order to get a complete picture of a given mirror, several different grating orientations should be measured.

Figure 2 shows the image of a reflected light on the camera chip. The left Ronchigram was obtained at the distance of 3 m (nominal curvature), the right plot was obtained at 3.01 m. A possible interpretation of the deformed fringes in the center can be a depressed center of the mirror. The three dark sports correspond to local deformations due to the mount system [2]. Cutting the squared mirror tiles from the produced circular shapes in the manufacturing process can be the reason for the modification of fringes seen at the mirror edges. For further detailed understanding of the mirror surface the comparison with a computer model is under way.

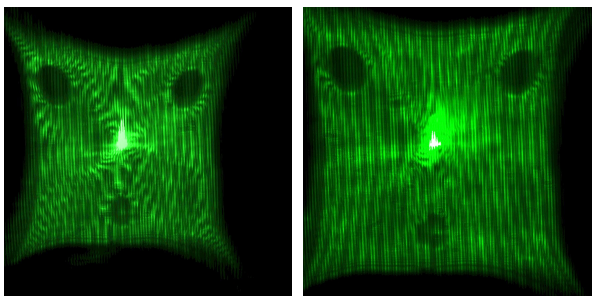

Figure 2: CCD camera view. Left: for R = 3 m. Right: for R = 3.01 m.

References

[1] E. Lebedeva, CBM Progress Report 2011, p. 37
[2] V. Dobyrn *et al*, CBM Progress Report 2011, p. 39

Single photon XY scans of various MAPMTs

C. Pauly[1], *K.-H. Kampert*[1], *J. Kopfer*[1], *S. Reinecke*[1], *and J. Adamczewski-Musch*[2]
[1]Bergische Universität, Wuppertal, Germany; [2]GSI, Darmstadt, Germany

Position resolved single photon efficiency scans provide valuable information for the performance evaluation of multianode photomultipliers (MAPMTs). Blue light (405 nm) from a pico-second pulsed laser source is coupled into a thin light fiber, the other end of the fiber with a pinhole collimator being attached to a XY stepper device in front of the MAPMT(s) under test. The light intensity is damped such that only in few percent of the laser pulses a photon is detected on the MAPMT. This ensures that only single photons with very small contribution of double photon pulses are produced. The stepper device is controlled via an EPICS control and user interface providing easy configuration of scans, and serving EPICS record variables which keep the actual stepper motor position and a special flag indicating whether the motors are moving or on fixed position.

The MAPMT is read out using the established self-triggered n-XYter+SysCore readout chain, DABC is used for DAQ. The SYNC-signal from the pulser is included in the data stream via SysCore AUX input and can be used in the offline analysis to define a time window around the expected time of laser correlated photon pulses. A special mechanism was implemented in DABC in order to include the actual position information in the data stream: The DABC continously (10x per second) polls the EPICS-flag indicating the motor activity. Every time a new measurement position is reached, the full EPICS record is read out and included in the data stream. In addition, a special SYS-message is inserted into the SysCore FIFO buffers via ROC messaging service to help synchronization in the offline analysis due to possible latency in including the EPICS subevent.

This combination of autonomous stepper scan control and fully self-triggered, asynchronous readout is the key to investigate many different MAPMT properties based on a single scan data file: Not only the relative detection efficiency (as fraction of Laser pulses with a corresponding photon being detected by the MAPMT), spatial resolution, cross talk, effective area, gain (mean single photon peak amplitude) and gain uniformity can be extracted, but also time-related quantities like dark rate (selecting a time window *before* the actual light pulse in the self triggered data stream) and afterpulsing can be evaluated based on the same data file. This provides an efficient tool also for series testing and classification of individual PMT characteristics, by simply archiving a single scan-data raw file for possible later re-analysis.

Some first results of such scans can be seen in Fig. 1, where single photon scans of three different MAPMT models are shown. The upper line of scans compares the relative photon detection efficiency by counting the fraction of laser events where *one or more* photons were detected. The (relative) efficiency index here is defined as average over the effective area. In the lower line of histograms, the fraction of events with *two or more* hits being detected is visualized, a measure for the MAPMT cross talk / charge sharing between neighbouring channels. It can be clearly seen that the new H12700 MAPMT exhibits significantly reduced cross talk compared to the H8500 MAPMT (same color scale on all plots).

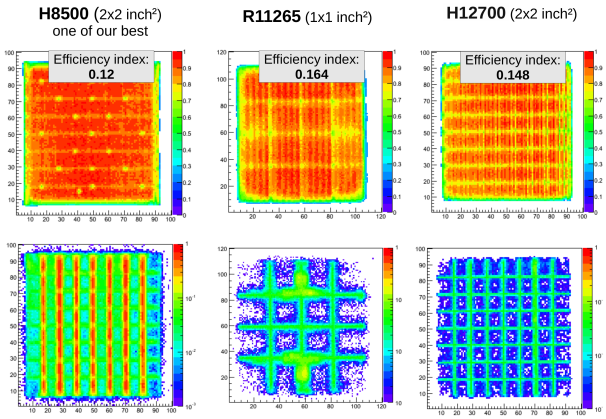

Figure 1: Single photon efficiency scans for different MAPMTs, showing the fraction of pulser events with ≥1 hit being detected (upper line) and ≥2 hits (lower line)

MAPMT type	relative efficiency	cathode blue index
H8500 #1	100%	10,7
H8500 #2	85%	9,37
H8500 #3	89%	10,1
R11265	133%	15,1
H12700	**121%**	**12,6**

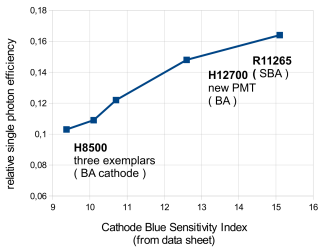

Figure 2: Relative comparison of single photon detection efficiency from scans, in relation to the blue sensitivity index from Hamamatsu data sheets

In Fig. 2, the relative detection efficiency is correlated to the blue sensitivity index taken from the MAMPT data sheet, a quantity closely related to the quantum efficiency. Obviously this number is a good indication for the detection quality of individual MAPMTs.

Development of a CBM RICH mirror frame prototype

N. Boldyreva[1], Ya. Berdnikov[4], A. Berdnikov[4], V. Dobyrn[1], C. Höhne[2], E. Leonova[1], N. Mifstahov[1], C. Pauly[3], Yu. Ryabov[1], V. Samsonov[1], O. Tarasenkova[1], and E. Vznuzdaev[1]

[1]PNPI, Gatchina, Russia; [2]Justus-Liebig-Universität, Gießen, Germany; [3]Bergische Universität, Wuppertal, Germany; [4]SPbSPU, St.Petersburg, Russia

Electron identification in the momentum range up to 10 GeV/c is the main goal of the CBM RICH detector. Its design follows the classical scheme of a gaseous RICH detector with focusing mirror. The RICH detector mirror surface consists of two parts, each of them divided into 36 individual tiles [1]. These tiles consist of spherical glass mirrors of 6 mm thickness with a reflective $\mathrm{Al+MgF_2}$ coating. The mirror has a total surface area of 13 $\mathrm{m^2}$, with gaps between individual mirror tiles of only 3–4 mm. In the CBM setup, the RICH detector shares its detector position with the muon detector (MUCH); both will be interchanged on a periodical basis using a crane.

The main challenge in the RICH mechanical design is the development of the mirror support frame. On the one hand, the frame has to provide sufficient rigidity to ensure (long term) stability of the optical focusing properties of the mirror, and to prevent damage of the fragile glass mirror tiles, especially during the crane operations. On the other hand, in the CBM detector setup the RICH is located right behind the magnet, in front of further sub-detectors like TRD and TOF. It is vital to minimize the amount of material within the detector acceptance in order to reduce the impact on the performance of the detectors installed downstream, behind the RICH.

Figure 1: Photo of the real mirror supporting frame prototype

A light-weight mirror support frame was developed with the goal to provide the optimum compromise between the conflicting requirements of structural strength and minimization of material budget. This concept was successfully tested using ANSYS simulations. In order to crosscheck these simulations, it was decided to build a prototype of the mirror support frame with a size of 3 x 4 tiles (see Fig. 1). Building such a prototype provides many valuable information: development of assembly technology, estimation of convenience of assembly and adjustment possibilities, identifying possible problems and fixes. We plan to perform stress tests, mechanical response (shaking, acceleration) tests, and to check the long-time behavior.

Work on the prototype has begun in the end of 2013. The base frame and places for mirrors were manufactured and assembled (see Fig. 1). At the moment, a special structure for imitation of load from mirrors is under preparation. This structure includes imitation of mounts and mirror tiles [1]. One of the variants is shown in Fig. 2.

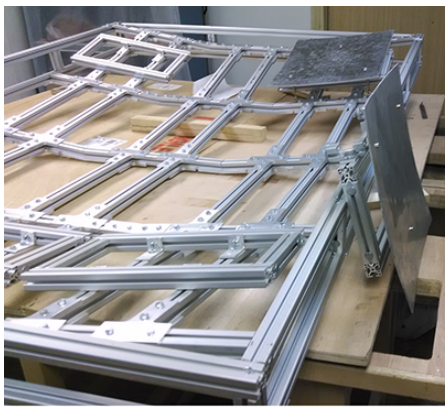

Figure 2: Mirror supporting frame prototype and tools for imitation of the load from mirror weight

According to our first impression this design provides the needed rigidity, but we have to wait for measurement results. As a next step, we plan to measure deformation of the frame in different positions in accordance with the test plan.

References

[1] V. Dobyrn *et al.*, CBM Progress Report 2012, Darmstadt 2013, p. 40

Muon Detection System

Building and testing a large-size GEM detector

A. K. Dubey, J. Saini, S. Chattopadhyay, and G. S. N. Murthy
VECC, Kolkata, India

As part of GEM R&D related to the CBM MUCH, we have so far reported studies and investigations carried out using $10\,\mathrm{cm} \times 10\,\mathrm{cm}$ GEM detector prototypes [1, 2]. However, the actual layout option of the CBM detector consists of large, sector-shaped chambers. In this report we present our first attempt towards building and testing a $31\,\mathrm{cm} \times 31\,\mathrm{cm}$ large triple GEM detector.

Stretching and framing of GEM foils

Large-area, single-mask GEM foils of $31\,\mathrm{cm} \times 31\,\mathrm{cm}$ were procured from CERN along with separate edge frames. The top surfaces of each of the foils were segmented into 12 strips to reduce the overall capacitance of the foils. The foils being 50 μm thin need to be stretched and framed to make them usable. The thickness of these frames provide the transfer gaps between any two consecutive GEM planes. Stretching of foils and gluing of edge frames is a delicate and complex process and needs several iterations in order to perfect the production techniques.

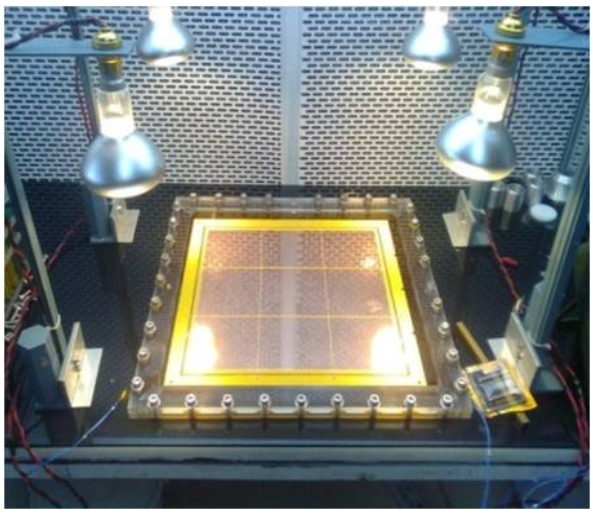

Figure 1: Stretching and framing of large-size $31\,\mathrm{cm} \times 31\,\mathrm{cm}$ GEM foils at VECC

The foil clamped in a suitable jig can be stretched either mechanically or by using thermal techniques. Each of these procedures has its own advantages and disadvantages. The chances of mechanical sagging increase as the area of the foils increase. This is prevented by ensuring that there is no under-stretch during stretching and also by using edge frames with thin supporting cross ribs which have minimum dead area. The edge frames being 1 mm thick and typically 1.5 cm wide, care has to be taken that there is no overstretch either, otherwise it causes the opposite corners to bend.

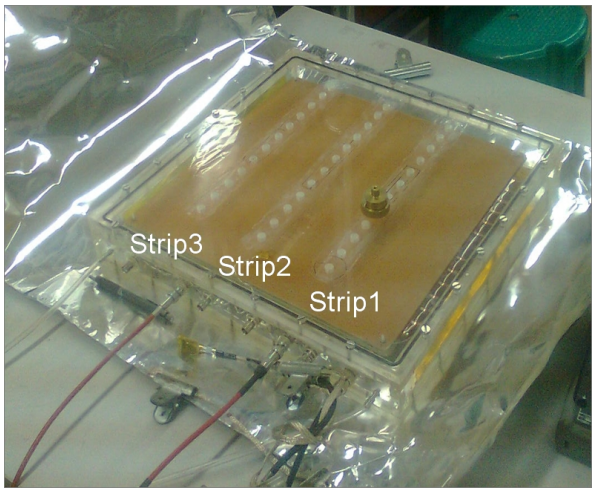

Figure 2: A single large-size GEM under test with a ^{55}Fe source

Membrane creeps that can occur in mechanical stretching can be avoided if one follows the thermal stretching techniques, which though consuming relatively more time are in fact relatively simpler to adopt. Such a technique has been followed by several groups in the world [3, 4]. At VECC, we followed a thermal stretching technique as our first attempt to stretch and frame large-size GEMs. The goal is to arrive at a production procedure for assembling large-size GEM modules. As shown in Fig. 1, the GEM foil was clamped inside a Perspex jig of appropriate dimensions and was made to stretch using heating lamps. Once stretched, a thin layer of glue was then applied manually on the surface of the FR4 based edge frame which was then gently placed over the stretched foil. The entire assembly is then left undisturbed for at least 20 hours for the glue to settle and fix. It is very important to control the temperature of the frames to prevent overstretching. The jig was kept at a temperature of about $(45 \pm 2)\,^{\circ}\mathrm{C}$. We built appropriate temperature controllers to maintain the temperatures within permissible limits. Three such foils were stretched and framed. The results of the lab test are discussed in the next section.

Test results

Each of the framed large-size GEMs was first tested individually in a specialized Perspex based test chamber as shown in Fig. 2, using radioactive sources and in a $Ar/C0_2$ $(70:30)$ gas mixture at a $\Delta V_{\rm gem}$ of about 525 V. The tests were carried out using conventional NIM electronics. The signal was readout via three strips (each 2 cm wide) as indicated in the figure.

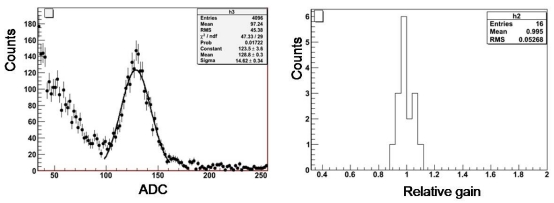

Figure 3: ^{55}Fe pulse height spectra (left) and relative gain distribution (right) for a single GEM at $\Delta V_{\rm gem} = 525$ V

Appropriate provisions were made to allow ^{55}Fe X-rays to pass through. Data were collected with the source placed at several locations on the chamber to estimate the gain variation. Shown in Fig. 3 (left) is the pulse height spectrum corresponding to the ^{55}Fe source for a single large GEM, with the major peak representing the 5.9 keV X-ray energy. A gain scan was performed at 16 different positions on the GEM surface in order to test the uniformity of the holes and construction issues, if any. A gain variation at the level of 6 % is observed as seen from Fig. 3 (right).

A triple GEM assembly of such locally stretched and framed large-size GEMs was also made and tested in the same test chamber with strip readout. A resistive chain was used to bias the drift plane and the three GEMs. The first signal from this large-size triple GEM using the ^{55}Fe source is shown in Fig. 4 (left), where the major peak of the pulse height distribution fitted to a Gaussian corresponds to the 5.9 keV X-rays. Shown in Fig. 4 (right) is the relative gain distribution as obtained from a position scan of 19 points and this variation is seen to be below 10 %. It needs to be mentioned that the gain-scan measurement has to carried out at more locations over the entire area and more of such foils need to be tested. With these measurements, the idea was to setup a quality-assurance mechanism when we go for large-size production of GEM chambers.

Fabrication of a triple GEM prototype having sector readout

The next step was to build a large-size triple GEM detector with realistic pad geometry for tests with high energy proton beams. For the first time, a readout PCB having a sector-shaped active region as shown in Fig. 5 has been fabricated. It consisted of progressively increasing pad sizes the dimension of which were determined based on realistic tracking simulations. Consisting of about 1200 pads, the

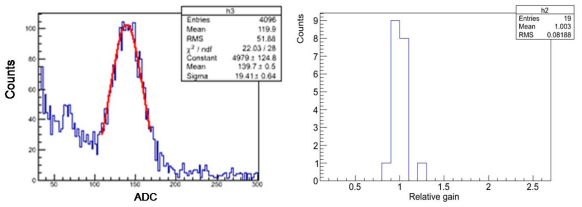

Figure 4: ^{55}Fe Pulse height spectrum (left) and relative gain distribution (right) from the $31\text{cm} \times 31\text{cm}$ triple GEM detector at $\Delta V_{\rm gem} = 354$ V

smallest pad in the PCB was of 3 mm × 3 mm in size and the largest one was $1\,\text{cm} \times 1\,\text{cm}$. Using a six layer PCB, the readout tracks were fanned outwards onto the three sides of the bottom plane as shown in the picture.

Arrangements for HV connections using a resistive chain were provided on one of the sides as shown. Protection resistances of $10\,\Omega$ each were soldered to all pads. G10 frames of 10 mm thickness was glued on this PCB, and a triple GEM stack was then assembled inside the chamber volume. Protection resistance of $1\,\text{M}\Omega$ was provided across each top segment of all the three GEM foils. The test results of such a prototype are discussed in [5].

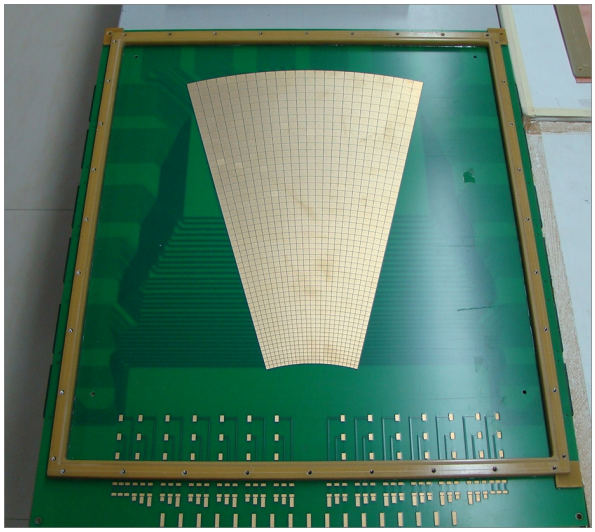

Figure 5: Large-size sector-shaped readout PCB

References

[1] A. K. Dubey *et. al.*, Nucl. Instrum. Methods **A 718** (2013) 418

[2] A. K. Dubey *et. al.*, CBM Progress Report 2010, p. 36

[3] M. Villa *et al.*, *Progress on large area GEMs (VCI 2010)*, arXiv:1007.1131 [physics.ins-det]

[4] M. Staib *et al.*, *Thermal stretching of Large-Area GEM Foils Using and Infrared Heating Method*, RD51 note 2011-004

[5] R. Adak *et al.*, *Test of a* $31\,\text{cm} \times 31\,\text{cm}$ *GEM chamber at COSY*, this report

Test of a 31 cm × 31 cm GEM chamber at COSY

R. P. Adak[1], *A. K. Dubey*[2], *J. Saini*[2], *V. Jain*[2], *S. Chattopadhyay*[2], *S. Das*[1], *U. Frankenfeld*[3], *J. Henner*[3], *W. Niebur*[3], *I. Sorokin*[3], *T. Balog*[3], *F. Uhlig*[3], *V. Friese*[3], *P. Ghosh*[3], *and J. Heuser*[3]

[1]Bose Institute, Kolkata, India; [2]VECC, Kolkata, India; [3]GSI, Darmstadt, Germany

Operation of the CBM-MUCH at high interaction rates requires a detector with large acceptance, high granularity and high rate capability. In this direction, we have conducted a beam test of triple GEM detectors at COSY using 2.36 GeV/c proton beams. Our goal was to study the response of the detector with high intensity beams using nXYTER-based self-triggered readout electronics and also to test for the first time the performance of a large-size triple GEM detector. In this study, we compare the results at different peak intensities in a typical beam spill. The highest intensity as calculated from the spill structure is ∼565 kHz/cm^2, which is close to the peak intensity expected by the first MUCH detector station.

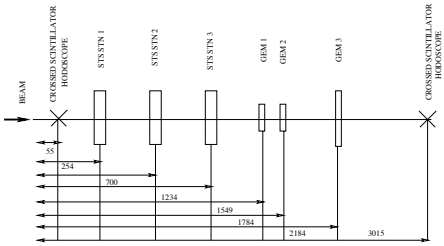

Figure 1: Experimental Setup at COSY

The schematic layout of the test setup is shown in Fig. 1. Out of the three GEM detectors tested, the first two (GEM1 & GEM2) are of $10 \times 10\,\mathrm{cm}^2$ size with square readout pads of sizes $3 \times 3\,\mathrm{mm}^2$ and $6 \times 6\,\mathrm{mm}^2$, respectively. The drift, transfer and induction gaps of GEM1 are 3 mm, 1 mm and 1.5 mm; the corresponding values for GEM2 are 3 mm, 2 mm and 2 mm. The third detector (GEM3) is made out of large GEM foils of $31 \times 31\,\mathrm{cm}^2$ size with trapezoidal readout pads of radially increasing size [1]. The drift, transfer and induction gaps of the chamber are 3 mm, 1 mm and 1.5 mm. A premixed gas mixture of Ar and CO_2 mixed in the ratio of 70:30 by mass was used for all the GEMs. Data were acquired by a DABC-based DAQ system. GEM1 and GEM2 were read out using two nXYTERs and one ROC while GEM3 was read out using 8 nXYTERs and 4 ROCs. In this test beam, the feedback parameter $v_b f_b$ of the nXYTER was set to the high frequency requirement as reported in [2]. All the hits above a predefined threshold and time-correlated with the trigger were used for analysis.

The beam spots of GEM2 and GEM3 are shown in Fig. 2. We do not observe any structure inside the beam spot as was the case in the earlier beam tests at higher intensities. The ADC spectra are obtained by assuming a baseline value of 2000 ADC for all nXYTER channels. The pulse height distributions for GEM2 and GEM3 for both low and high intensity fitted by a Landau distribution are shown in Fig. 3, corresponding to the pad with highest ADC taken event by event.

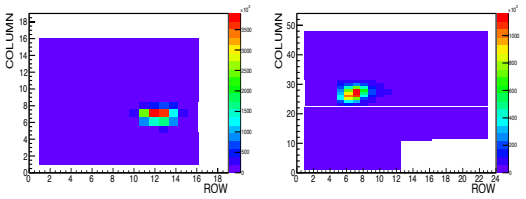

Figure 2: Beam spot of GEM2 (left) and GEM3 (right) at high intensity

The MPV of the ADC spectra at low and high intensities are 124.85 and 122.53 for GEM2 and 240.0 and 227.0 for GEM3, respectively, for given sets of high voltage. They differ between GEM2 and GEM3 because of the different detector configurations mentioned above. For both detectors, the MPV is nearly the same at high and at low intensity. Preamplifier saturation effects as observed in earlier beam tests are no longer present owing to the choice of appropriate $v_b f_b$ values. Further analysis of the data is in process.

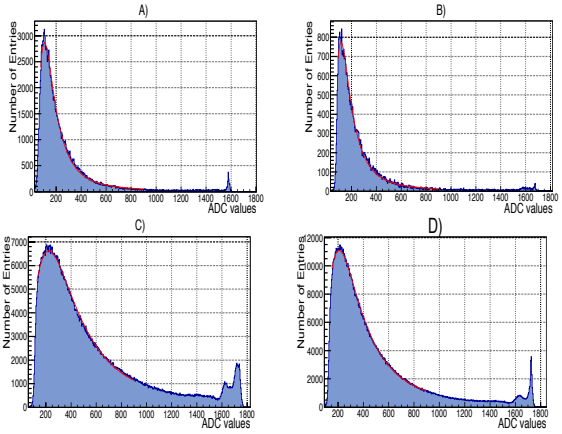

Figure 3: Pulse height spectra for GEM2 (A,B) and GEM3 (C,D) for ΔV_{GEM}= 359.06 V. The peak intensities corresponding to (A), (B), (C), (D) are 30 kHz, 253 kHz, 25.23 kHz and 357 kHz, respectively.

References

[1] A. K. Dubey *et al.*, Building and Testing a Large Size Triple GEM Detector, this report

[2] J. Saini *et al.*, CBM Progress Report 2012, p. 47

Test of a triple GEM chamber with neutrons using an alpha beam at the VECC cyclotron

A. K. Dubey[1], *J. Saini*[1], *R. Ravishankar*[2], *T. Bandopadhyay*[2], *P. P. Bhaduri*[1], *R. Adak*[3], *S. Samanta*[3], *S. Chattopadhyay*[1], *G. S. N. Murthy*[1], *Z. Ahammed*[1], *S. A. Khan*[1], *S. Ramnarayan*[1], *S. Muhuri*[1], *P. Ghosh*[1], *S. K. Pal*[1], *T. K. Nayak*[1], *and Y. P. Viyogi*[1]

[1]Experimental High Energy Physics and Applications Group, VECC, Kolkata, India; [2]Health Physics Group,VECC, Kolkata, India; [3]Bose Institute, Kolkata, India

A high hadronic environment and the thick iron absorbers of the CBM MUCH contribute to a high neutron background. As per FLUKA calculations, it is estimated that the MUCH detectors will have to cope with a neutron dose of $\approx 10^{13}\,\mathrm{n_{eq}/cm^2}$/year. It is therefore necessary that the GEM detectors being developed for MUCH [1] are tested in a comparable neutron environment. The aim of the neutron tests is to measure the neutron hits as recorded by the detector so as to have an idea of the number of background hits per event on the GEM detector and also to study the response of the detector before and after neutron irradiation, in terms of relative change in gain, or in terms of any physical damage due to irradiation. In this direction, we conducted a first such test of a triple GEM chamber in the VECC cyclotron. As shown in Fig. 1, a 40 MeV α beam hitting a 0.5 cm thick tantalum target produces neutrons and gammas as end products. A Pb shield of 10 cm is placed in front of this target for screening the gammas. The triple GEM chamber was placed at about 80 cm from the Tantalum target and was operated at $V_{\mathrm{gem}} \approx 340$ V across each GEM layer. The gas mixture consisted of Ar/CO_2 mixed in the ratio 70:30. The GEM signal was read out using standard Ortec NIM electronics coupled to an MCA. Data corresponding to different beam currents (which corresponded to different neutron intensities) were taken with and without the Pb shielding. The neutron flux was measured with BF_3 counters for current ranges from 50 – 500 nA for both with and without Pb shield.

Figure 1: Photograph of the neutron test setup

Fig. 2 (top) shows the pulse height spectra from the detector for four different beam currents (neutron intensities) without Pb shielding. The highest neutron flux corresponding to a beam current of 4 μA as obtained from the calibrated fit of BF_3 data was about $\approx 10^5$ neutrons/cm^2/s. For every current setting, three sets of data were taken, and the number of GEM hits for each of these sets were estimated. Fig. 2 (bottom) shows the number of hits as function of the beam current. About 350 hits/$\mathrm{cm^2/s}$ are seen, corresponding to a maximum neutron flux of $\approx 10^5/\mathrm{cm^2/s}$. The expected neutron rate in the CBM experiment is 10^5/s resulting from a collision rate of 1 MHz.

The test results indicate that the background hits per event in the GEM detector due to neutrons would be insignificant, thereby ruling out any tracking issues due to neutron hits. The prototype detector was exposed to neutron radiation for about four days, with an integrated dose of exposure of about $10^{11}\mathrm{n_{eq}}$ over 100 $\mathrm{cm^2}$. No visible damages were observed after this irradiation. It is planned to conduct more such tests in future at higher beam intensities and at higher overall dose of neutron exposure to investigate the detector response in detail.

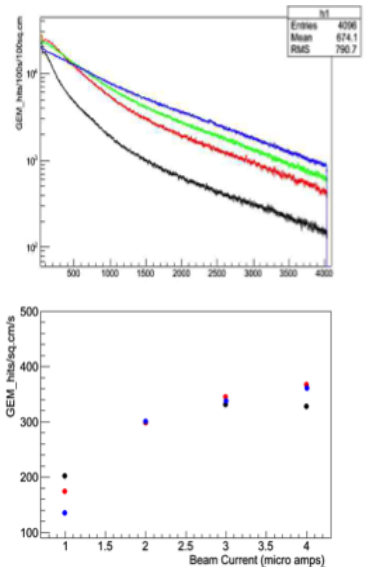

Figure 2: Top: Neutron fluence vs. beam current as measured by the BF_3 counter; bottom: Number of GEM chamber hits per $\mathrm{cm^2}$ and second vs. beam current

References

[1] A. K. Dubey *et al.*, Proc. DAE Symp. Nucl. Phys. **55** (2010) 692; A. Kiseleva *et al.*, Indian J. Phys. **85** (2011) 211

Procedure of fabrication and assembly of GEM chambers in MUCH

A. K. Dubey[1], *G. S. N. Murthy*[1], *T. Ghosh*[2], *S. Bajirao*[2], *J. Saini*[1], *and S. Chattopadhyay*[1]
[1]Experimental High Energy Physics and Applications Group, VECC, Kolkata, India; [2]Mechanical Engineering Group, VECC, Kolkata, India

In this report, we discuss the procedure of assembly of large GEM chambers and their mounting scheme to form the layers. The mounting of the layers onto the superstructure is still under discussion and is not a part of this report. This writeup is as per the presentation in the MUCH TDR submitted to FAIR [1].

Fabrication of large GEM chambers

In the actual MUCH layer design, the annular region of each layer is to be achieved by overlapping back-to-back the trapezoidal shaped GEM chambers so that the active region of each GEM chamber seamlessly covers the required annular area. Though the GEM foils required can be made with large (≈1–1.5 m) length, the width has a limitation of around 600 mm due to the available maximum roll width of the copper clad polyimide foil. Thus the outer side of each trapezoidal chamber should not be more than around 500 mm active width. With this design constraint, the number of trapezoidal sectors needed for the annular coverage has to be optimized. The construction concept of large GEM chambers has evolved over the years. We have considered three possible ways of building these chambers. The design drawing of one sector is shown in Fig. 1.

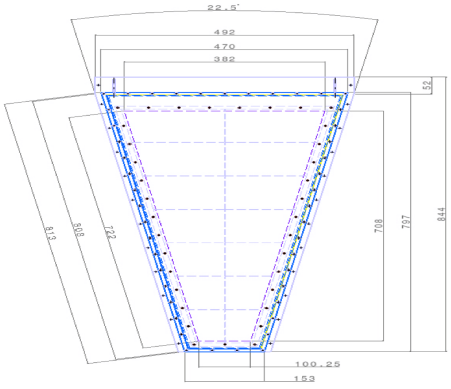

Figure 1: Mechanical drawing by CATIA of one sector

Glue-all layers approach. In this method trapezoidal GEM foils are first stretched over spacer grid-frames using thermal or mechanical stretching means. A thicker (≈2–2.5 mm) drift plane PCB serves as a rigid base, over which all layers are assembled and glued together. The width of the GEM and spacer frames thus becomes the outer wall of the gas tight chamber. The HV tails for GEM foils come out of the chamber walls, so that HV dividers can be mounted outside. Alternately HV dividers can also be placed inside if required. Provision for gas in/out feeds are also made in the frame wall by appropriate machining. Early prototypes of CMS high-η upgrade chambers followed this procedure. Though it works for test prototypes, for bulk production and maintenance the procedure has several drawbacks as itemized below.

- Thermal stretching is time consuming and severely limits the production rate of chambers.
- Gluing all frames together and oven curing is also a long procedure.
- GEM foils cannot be replaced if defective. Thus the entire chamber has to be rejected (cost burden).

O-ring sealed chamber. The modified construction method by introducing an additional O-ring sealed chamber frame is shown in Fig. 2.

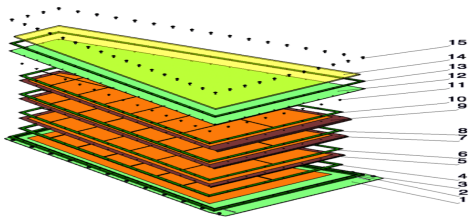

Figure 2: Exploded view of the O-ring sealed chamber. 1) drift PCB; 2) gas tight outer frame; 3) O-ring seal; 4) drift gap spacer; 5) bottom Gem foil; 6) bottom spacer grid frame; 7) middle GEM foil; 8) middle spacer grid frame; 9) top GEM foil; 10) top spacer grid frame; 11) GEM frame fasteners; 12) readout PCB; 13) edge frame; 14) top honeycomb board; 15) outer frame fasteners.

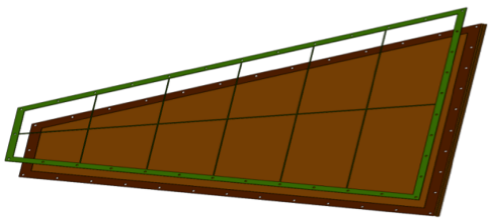

Figure 3: GEM foil with gridded spacer frame

The chamber frame is mounted on the rigid drift plane PCB and serves as a gas tight chamber housing. The three

GEM foil layers, thermally (or mechanically) stretched over FR4 spacer grid-frames (Fig. 3) are assembled over the drift plane with a 3 mm drift spacer frame using nylon fasteners. HV segment resistors are soldered at the outer edge of each GEM foil and only the HV tails come out of the chamber through the printed tracks on the drift plane PCB (Fig. 4).

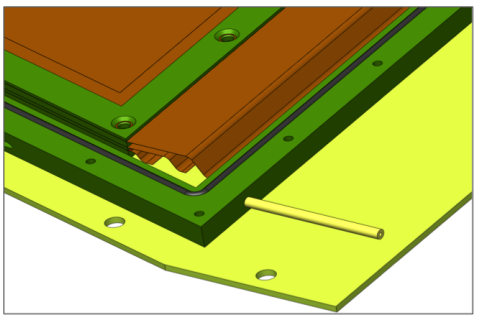

Figure 4: HV tails on HEM foils inside the O-ring sealed chamber

The pad plane PCB on top extends over the O-ring outer frame and can be press fitted over the frame by several fasteners. We plan to use O-ring seals both on top and bottom sides of the outer frame, to eliminate the time consuming gluing procedure. This method of construction gives access into the chamber interior for service and thus reduces the long-term maintenance costs. However the assembly with pre-stretched GEM foils is still a part of this procedure and the associated issues cannot be avoided. The exploded view of the chamber is shown in Fig. 4.

Fig. 5 shows a fully assembled sector. The thickness of the whole chamber will be dependent on the gas thickness of the chamber. At present the space available (30 cm) for assembly of three layers seem to be sufficient keeping a gap of 3 mm in between layers.

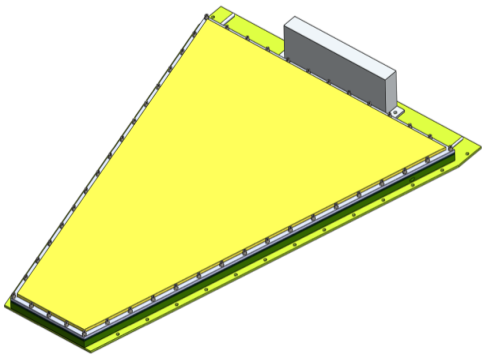

Figure 5: One sector after full assembly

Assembly of sectors to form a layer

The design has been performed using CATIA V5 R21 package. Fig. 6 shows the assembly of the sectors on a frame to build a station consisting of three layers. Each layer has chambers on two sides with overlap along the edges of the chambers to cover the dead areas. The sectors will be assembled on two sides of two support half-plates. Each two half plates when joined form a full layer. The half-plates could be moved in transverse direction for service etc. HV, gas and water connections will be taken out from the periphery. The chambers are assembled on the support structure at alternate positions on both sides of the plane. 16-chambers, as obtained for the first station in both the SIS-100 and SIS-300 setups, eight on each side of the support plane, are shown in the figure.

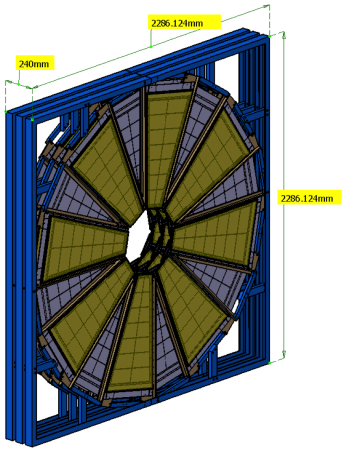

Figure 6: A station with 3 layers each of 16-sectors shown after assembly of chambers on one side. For the chambers on other side there will be overlap.

Once the sectors are mounted on the frame to form (half) layers, they need to be assembled on a stand. Fig. 7 shows a view of the assembled layers. The figure shows the mounted layers when separated in the transverse plane. The details of the movement mechanism will be installed later.

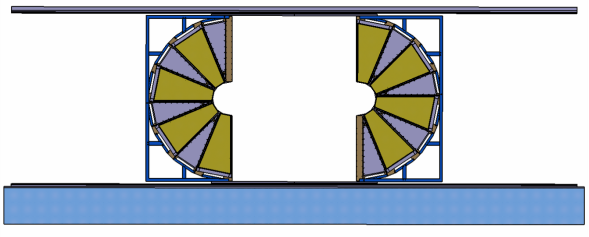

Figure 7: One view of the sectors mounted on support plane and on stand. Each half can be serviced separately.

References

[1] The CBM collaboration, *Technical Design Report for the CBM Muon Chambers*, December 2013, in press

Readout PCB design for CBM-MUCH

J. Saini, A. K. Dubey, S. R. Narayan, G. S. N. Murthy, and S. Chattopadhyay
Experimental High Energy Physics and Applications Group, VECC, Kolkata, India

The Muon Chamber (MUCH) will be designed to have an angular acceptance of 5° to 25°. The density of the particles hitting the detector decreases with radial distance r as 1/r. Hence a progressive sector geometry is chosen for the final design of the MUCH chambers.

The size of the first chamber is around 800 mm in height and 450 mm in width. As the design is very dense in the inner region of the detector, the PCB requires a multilayer design to route all pads to the connectors. For such big a PCB, most of the vendors are unable to process the design. Thus, the design has to be split in two PCBs, which must be joined by glue. Since the pad layout and tracking are very complicated, we plan to make the active area in one PCB and glue the side extender PCB to meet the requirements.

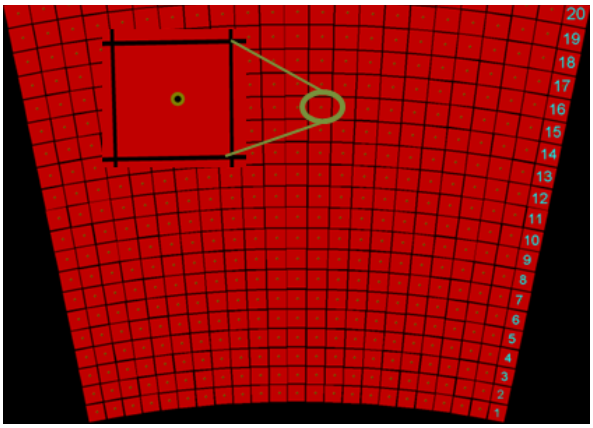

Figure 1: Small section of top copper of the PCB. The inset shows a zoom-in onto one pad.

The design is implemented using trapezoidal pads over conventional square pads to minimize the dead space between the pads. The design has a pad size of approximately 4.36 mm × 4.36 mm in the innermost region and 17.48 mm × 17.48 mm at the outermost ring. The pads are designed by 90.5 ° at two sides to make it trapezoidal and to fit to the design of 1° segmentation (see Fig. 1).

The following design considerations were taken into account:

- **Noise considerations.** As per the experience of a chamber of size 30 cm × 30 cm, it was found that long tracks give more noise as compared to short tracks even with lowest size of pads [**?**]. Our design is made to have connectors just at the back of the pads to get the shortest track size. Earlier designs had connectors at the edges and routing required longer track lengths.
- **Radiation considerations.** As the innermost region faces the highest radiation dose, this design was made to put the FEE boards at least 10 cm away from the first ring to minimize the dose on the FEE boards.
- **Grounding considerations.** With the past experience it was found that the HV and LV rigid grounding creates a lot of noise in the self-triggered system. In addition, if there is no ground plane below the HV components, then this will also introduce additional noise. Hence for this PCB we have introduced a ground plane for the full chamber, but the HV input cable will be connected to LV ground through a resistor.
- **Mechanical considerations.** As this chamber PCB is very big, and there is no mechanical support in the center of the PCB, the FEE connector is not placed in the center but near to the edges to get the necessary mechanical strength while plugging in the FEE board. At the same time, flexible PCBs, which would lead to noise, are avoided.

References

[1] R. P. Adak *et al.*, *Test of a 31 cm × 31 cm GEM chamber at COSY*, this report

Design and development of a low-voltage distribution for CBM-MUCH

V. Jain, S. K. Pal, S. R. Narayan, J. Saini, and S. Chattopadhyay
VECC, Kolkata, India

The Muon Chamber (MUCH) will be amovable system; thus, a careful design of low voltage distribution is needed for optimized performance and less cable count for ease of operation. To minimize the cable load, 48 V is planned to be taken as the input to a low voltage distribution board which will be located near the detector. There are no additional cooling arrangements made for this board, and hence power consumption is a major issue to address.

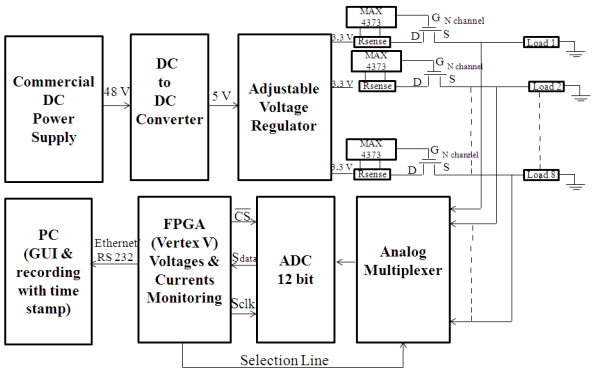

Figure 1: Block diagram of the low voltage distribution board

One low voltage distribution board can feed 8 channels, and with each channel it can provide 3.3 V / 1.8 V and 15 A of maximum current. The distribution board has over-current protection and remote monitoring facility of voltage and current for each channel. The block diagram of the distribution board is shown in Fig. 1. This distribution board steps down 48 V to 5 V using a DC to DC SMPS type converter. The reason for choosing the SMPS is its reduced size and associated low power loss which avoids excess heat generation on the board. The prototype design has been tested for two channels. The number of channels for each distribution board may vary depending on the final requirement. On an event of over-current of a channel, it will be shut down keeping the rest of its channels in a working state. This minimizes the data loss due to unexpected glitches in the system.

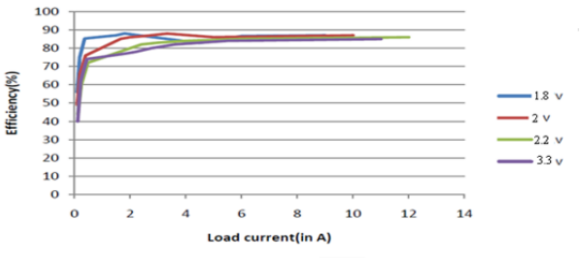

Figure 2: Load current vs. efficiency

In the distribution system we use a DC to DC converter (PTH05010) as voltage regulator. The test results of this voltage regulator are shown in Fig. 2. The LVDB shows a DC to DC conversion efficiency of nearly 90 % even at 1.5 A of current, which is expected to be the current required from a typical board in the MUCH readout chain.

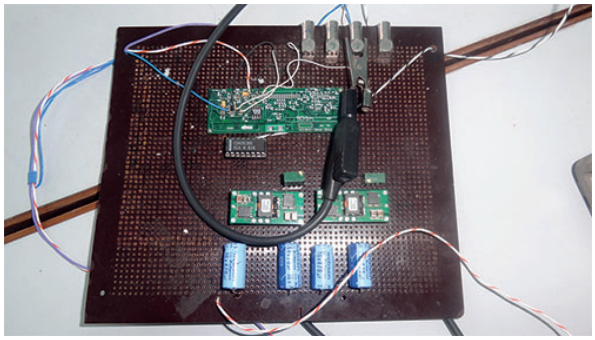

Figure 3: Two-channel prototype low voltage distribution board

To monitor voltage and current, we use a ML505 FPGA Board. We made a two-channel prototype as shown in Fig. 3. We used an analog multiplexer (CD4053B) to select the channel and an ADC (AD7476) to read the voltage or current of the selected channel. This digital data were read through RS232 via the FPGA board as shown in Fig. 4.

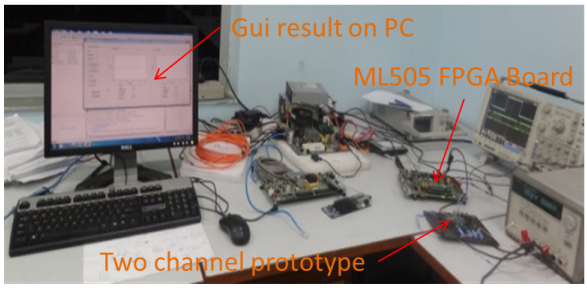

Figure 4: PC based experimental setup of the low voltage distribution board using the ML505 FPGA board

GEM demonstrator based on FEE ASIC for MUCH

E. Atkin[1], *V. Ivanov*[2], *E. Malankin*[1], *E. Roshchin*[2], *V. Samsonov*[1,2], *V. Shumikhin*[1], *and A. Voronin*[1,3]
[1]National Research Nuclear University "MEPhI", Moscow, Russia; [2]Petersburg Nuclear Physics Institute, NRC Kurchatov Institute, Gatchina, Russia; [3]Moscow State University, Moscow, Russia

The first lab test results of the FEE ASIC for MUCH were presented last year [1]. During 2013 there was developed a new demonstrator setup for chip testing with GEM prototypes. The test box (GEM detector and its electronics) is shown in Fig. 1. The chamber on the basis of the triple GEM, filled with Ar/CO_2 was used. The anode structure was adapted to the CBM muon detector. Pad area was 5x5 mm^2 and its capacitance – 12 pF.

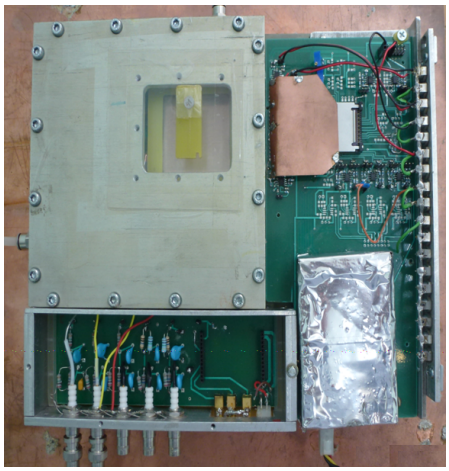

Figure 1: GEM test setup, based on the FEE ASIC

The measurements were carried out with the Fe-55 source and pulse generator. Both the spectrum from Fe-55 X-ray source and the shaper output are shown in Fig.2.

The test results are presented in Fig.3 and demonstrate sufficient amplitude resolution, linearity and dynamic range. In order to perform an accurate noise measurements an updated version of the chip test board was developed (see bottom left of Fig.3). The measured noise of 1000 electrons at a low input capacitance increases up to 2500 electrons at input capacitance of 100 pF.

Based on the test results of prototypes, we have enlisted below the points, related to the design of FEE ASIC for MUCH : a) the input signals are negative; b) the charge is distributed according to Landau distribution, the dynamic range is of the order of 50-100 fC; c) the signal shape is lumpy with a typical charge collection time of 50 ns. The input capacitances vary from 10 pF for small sectors up to 40 pF for large ones. Although the discharge and breakdown phenomena are greatly reduced comparing to the previous generation of gas detectors, it is still necessary to use a spark protection circuit at the input of FEE chip. An important feature of MUCH is a high rate environment: instant rate in its central part is about 10^6 counts per second, rapidly decreasing in its peripheral zone. This sets the requirements of a very high ASIC throughput and physical density in the inner region of the detector and it is not important at the chamber ends.

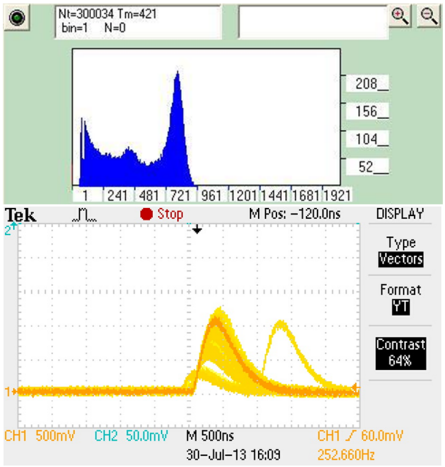

Figure 2: Spectrum from Fe-55 X-ray source (top) and the shaper output pulse (bottom)

Gain	6 mV/fC
Input signal range	1.5-100 fC
Maximum channel rate	2 MHz
Power consumption	1.2 mW
ENC Cdet = 1p	875e
Cdet = 100p	2427e
Chip area	1050 x 100 μm²

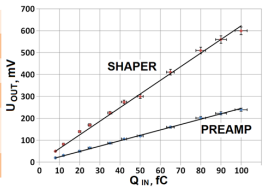

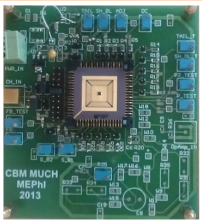

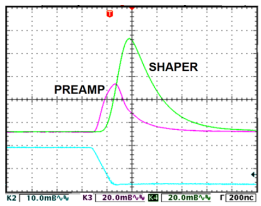

Figure 3: Test results summary (top left), transfer function (top right), ASIC test board (bottom left) and signal responses of preamp and shaper (bottom right)

References

[1] E. Atkin *et al.*, CBM Progress Report 2012, p. 52

Transition Radiation Detector

Construction and first performance studies of a CBM TRD prototype with alternating wires developed in Frankfurt

S. Gläßel, W. Amend, A. Arend, C. Blume, P. Dillenseger, and F. Roether
Institut für Kernphysik, Goethe-Universität, Frankfurt am Main, Germany

The Transition-Radiation Detector (TRD) for the Compressed Baryonic Matter (CBM) experiment at the Facility for Antiproton and Ion Research (FAIR) has to deliver electron identification and tracking performance in a high particle-density environment. To deliver the required fast detector response for the expected high signal rates, a thin Multi-Wire Proportional Chamber (MWPC) without drift region was developed [1].

One key challenge of this setup is the sensitivity of the field geometry to deformations of the cathode planes. With a thin foil as front cathode, even minor internal pressure variations can affect the gas gain [2]. In order to minimize this effect, the robust field geometry of an alternating wire structure, as proposed for the ALICE VHMPID [3], was explored. Field wires are introduced between the sense wires to generate field lines from the field to the sense wires that are independent of the front cathode. Consequently, the electrical field in the sensitive area near the entrance window becomes significantly lower.

To study the effects of an alternating wire setup on the gas gain, a small aluminium prototype with dimensions of 21,8 x 21,8 cm^2 was built. Thin sense wires (gold-plated tungsten, 20 μm) and thicker field wires (copper, 79 μm) are arranged on the anode plane with a pitch of 2.5 mm. A thin aluminized Mylar-foil (19 μm) serves as front cathode and entrance window at the same time. A pad plane with 15 read-out pads is used as rear cathode. Both front and rear cathode have a distance of 4 mm to the anode plane, leading to a total gas gap of 8 mm (see Fig. 1).

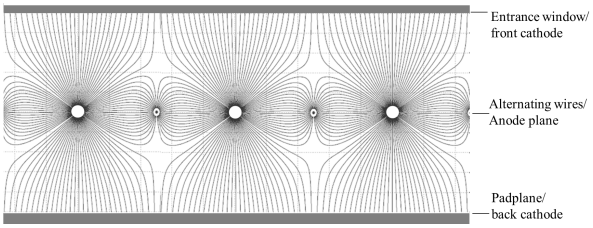

Figure 1: Schematic profile with field lines of the new prototype with alternating wires

First measurements in a laboratory environment were performed with an ^{55}Fe source. The sense wire current was measured for different positions at various differential pressures. Field wires were on ground potential. A standard prototype without field wires and with similar dimensions was employed for reference measurements.

The first tests give a clear indication for a superior performance in terms of gas gain stability for the new prototype. The effect that the gas gain shows variations up to 60 % in the case of internal overpressure, as seen for the standard setup, is drastically reduced for the setup with alternating wires (variations are below 10 %, as shown in Fig. 2).

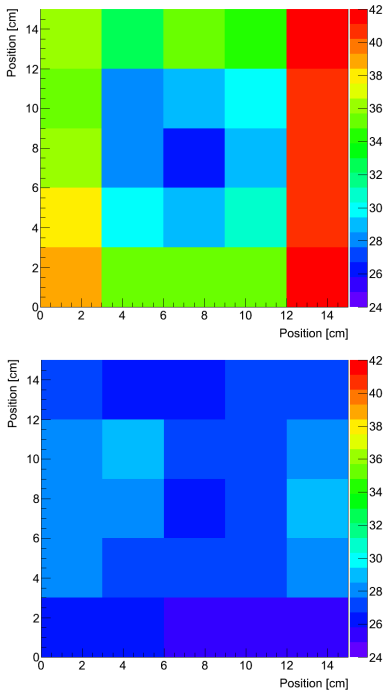

Figure 2: Gas gain as function of position at 0.5 mbar overpressure for standard (top) and new prototype (bottom)

The superior performance of the new prototype will be further investigated to confirm it on a quantitative level. Measurements with different field wire potentials and of the energy resolution will be performed.

A second prototype with alternating wires and an asymmetric structure, i. e. the wire plane being moved towards the readout cathode, has been built and will be tested as well.

References

[1] P. Dillensegger *et al.*, CBM Progress Report 2012, p. 58
[2] E. Hellbär *et al.*, CBM Progress Report 2012, p. 54
[3] D. Varga *et al.*, Nucl. Instrum. Methods **A 698** (2013) 11

e/π Discrimination and position resolution of a real-size CBM-TRD prototype

M. Târzilă[1], J. Adamczewsky-Musch[2], V. Aprodu[1], D. Bartoş[1], A. Bercuci[1], G. Caragheorgheopol[1], V. Cătănescu[1], F. Constantin[1], S. Linev[2], M. Petriş[1], M. Petrovici[1], L. Prodan[1], A. Radu[1], and V. Simion[1]

[1]NIPNE, Bucharest, Romania; [2]GSI, Darmstadt, Germany

A high-granularity real size TRD prototype, designed to fulfil the requirements of the innermost zone of the first CBM-TRD station of 1 cm^2 readout cell area, combines a multi-wire proportional chamber with a 2×4 mm amplification region and a drift zone of 4 mm. Architectural details of this type of TRD prototype were described in [1]. The e/π discrimination obtained with other types of radiators than those the performances of which were already reported in [1] and the position resolution will be the focus of the present contribution.

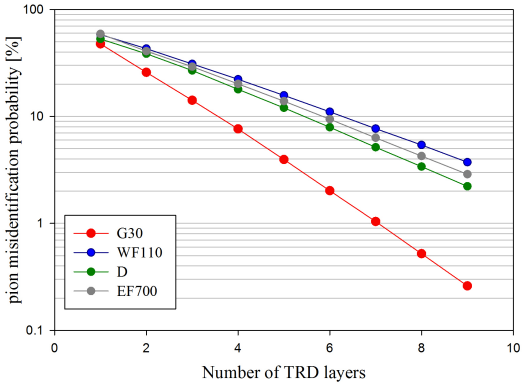

Figure 1: Pion misidentification as a function of the number of TRD layers for different types of radiators

The chamber was tested with a mixed beam of electrons and pions of 2 - 8 GeV/c particle momenta at the T9 beam line of the CERN-PS. A 80%Xe+20%CO_2 gas mixture was flushed through the chamber, operated at 2000 V anode and 800 V drift voltages. Several types of radiators were tested. The signals from three consecutive rows of 16 triangular pads each were processed by FASP V0.1 front-end electronics [2, 3].

The pion misidentification probability for 90% electron efficiency as a function of the number of TRD layers was obtained with a Monte Carlo simulation using the likelihood method based on the measured pulse height spectra of electrons and pions. The particles were identified and selected based on the information delivered by a Cherenkov detector and a lead-glass calorimeter positioned in front and at the end of the beam line, respectively. A pion misidentification probability of ≈1 % was obtained with a regular foil radiator (20 μm foil thickness, 250 μm gap, 220 foils) [1]. Fig. 1 presents the performance of the chamber with other types of radiators: G30 (fiber radiator made from 16 mats of pure LRP 375 BK polypropylene fibers), D (5 PE foam plates thermally glued to a block), WF110 (30 mm Rohacell plate) and EF700 (50 mm PE foam plate).

The position reconstruction is based on the charge sharing among consecutive rectangular and tilted pads obtained by the corresponding pairing of the triangular pads of the three operated rows. It was determined from the standard deviation of a Gauss function fitted to the difference between the positions reconstructed with two identical chambers (Fig. 2). A position resolution of $(385 \pm 0.02)\,\mu$m across the pads and of (1.6 ± 0.2) mm along the pads was achieved considering equal contributions of the two identical chambers.

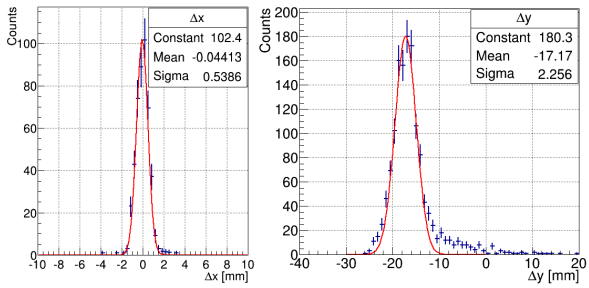

Figure 2: Difference between the hit position across the pads (left) and along the pads (right) reconstructed with two identical detectors, both fitted with a Gauss function

The support of the drift electrode of this prototype was made from a 9 mm honeycomb plate sandwiched between 2 Rohacell HF71 plates of 3 mm thickness. The measured transmission of such a structure for 5.9 keV X rays of ^{55}Fe is ≈43.77 %. This could be improved by ≈10 % if the Rohacell plates are replaced by aluminized carbon foil of ≈300 μm. A future TRD prototype will be built using this new drift electrode structure. These very good results in terms of e/π discrimination and position resolution will be further improved using a new version of FASP where the signals delivered by triangular pads will be paired inside the chip, such that the effect of the large dynamical range caused by triangular pads will be drastically reduced.

References

[1] M. Târzilă *et al.*, CBM Progress Report 2012, p. 60

[2] V. Cătănescu *et al.*, CBM Progress Report 2009, p. 47

[3] A. Caragheorgheopol *et al.*, CBM Progress Report 2010, p. 46

Commissioning of the SPADIC 1.0 Amplifier / Digitizer Chip

M. Krieger and P. Fischer
ZITI, University of Heidelberg, Germany

The SPADIC chip was developed for the readout of the CBM TRD. The latest version SPADIC 1.0 has 32 channels on an area of $5 \times 5\,\mathrm{mm}^2$. The chip is fully functional and was extensively tested in 2013.

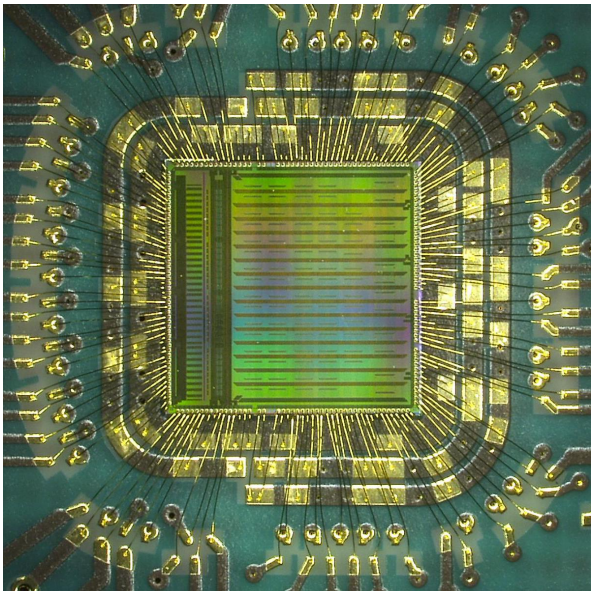

Figure 1: SPADIC 1.0 chip bonded to the readout PCB

SPADIC 1.0 contains 32 identical channels on a die of $5 \times 5\,\mathrm{mm}^2$ size. It is fabricated in the 180 nm technology from UMC. The digital part uses custom made mixed mode standard cells and 44 SRAM blocks for data buffering. Each channel contains:

- A charge amplifier / first order shaper ($\tau = 80\,\mathrm{ns}$) for positive input pulses with a noise of $\approx 800\,\mathrm{e}$ at $C_{in} = 30\,\mathrm{pF}$. This part consumes $\approx 5\,\mathrm{mW}$. In addition an experimental frontend for negative pulses is available.
- A $25\,\mathrm{MHz}$, $4.8\,\mathrm{mW}$ pipeline ADC with 9 bit output and an ENOB of > 8 Bit.
- A fully programmable digital IIR filter with 4 first order stages (16 bit processing, 6 bit coefficients).
- A sophisticated hit detection logic with differential threshold option for double hit detection and forced 'neighbor' trigger from channels on the same chip or even from different chips.
- A unit to pick an arbitrary set of amplitude samples from each pulse.
- A time ordered derandomization FIFO.
- Various error detection and recovery features (mainly for full buffers).

The data link backend implements for the first time the CBMnet protocol on an ASIC. It sends out the agglomerated hit data in a compact data format over two serial LVDS links running at up to 500 Mbps. In order to simplify the system design as much as possible, SPADIC 1.0 contains all further required infrastructure (current reference, bias DACs, monitoring busses, test pulse injectors) required to operate the chips with a minimum of external components and signals. For simplified assembly of detector readout modules, some chips have been packaged in QFP176 carriers of $26 \times 26\,\mathrm{mm}^2$ size.

The chip is bonded to an adapter board (Fig. 1) which is connected to a custom FPGA board holding a CBMnet receiver firmware. The FPGA is accessed through USB2.0 using multi threaded Linux applications allowing for configuration of all chip settings, injections and data readout.

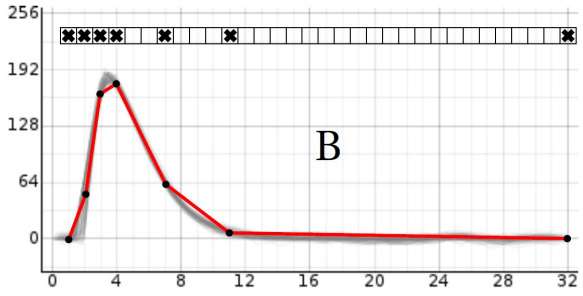

Figure 2: Samples sent out for a pulse using a selection mask

All features of the chip were operated successfully. Only few minor bugs were identified which do not prevent chip operation on detectors. As just one example, Fig. 2 shows how interesting samples in one pulse can be picked using a freely programmable mask.

References

[1] M. Krieger, *Self-triggered charge pulse processing ASIC*, Proc. TWEPP 2013, to be published in JINST

[2] T. Armbruster *et al.*, *Multi-Channel Charge Pulse Amplification, Digitization and Processing ASIC for Detector Applications*, IEEE-NSS/MIC **2012** 697

[3] `http://spadic.uni-hd.de/`

Design of new SPADIC front-end boards for TRD readout

M. Krieger
ZITI, University of Heidelberg, Germany

The design of the TRD subsystem foresees the use of different types of modules and front-end boards (FEBs). In order to keep the hit rates per channel within controlled limits across the detector, the modules and FEBs cover a range of different channel densities.

This means that between 4 and 10, or even more, SPADIC chips must be assembled on one FEB of approximately 50 cm length. For testing the type of FEB with the lowest SPADIC density, for 2014 a prototype FEB is designed that connects one SPADIC every 114 mm.

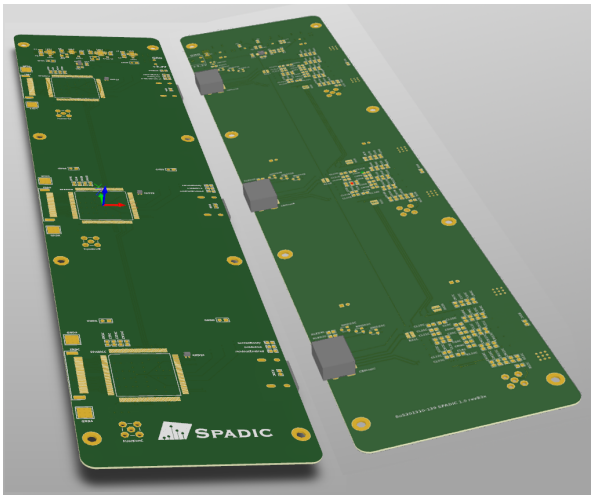

Figure 1: Rendered view (front and back side) of the new FEB for 3 packaged SPADIC 1.0 chips

As the first prototype of such a multi-chip FEB, a new PCB holding 3 SPADIC chips with this pitch has been designed (Fig. 1). It contains voltage regulators and power-on sequencing logic shared by all SPADICs, and for each SPADIC individually a TRD input connector, decoupling capacitors, charge injection, and an HDMI connector for CBMnet data links. Neighboring SPADICs are connected to allow exchange of trigger signals. Additionally, a smaller version of the FEB containing only one SPADIC has been designed (Fig. 2b).

For the evaluation of integration options and a simplified FEB assembly, most of the remaining SPADIC 1.0 chips were cased into ceramic quad-flat packages with 176 pins (QFP176, Fig. 2a) and 23 mm×23 mm in size. This allows saving space by placing the decoupling capacitors on the opposite size of the PCB directly beneath the package, as shown in Fig. 3.

This new 3-SPADIC FEB has a size of 83 mm×339 mm

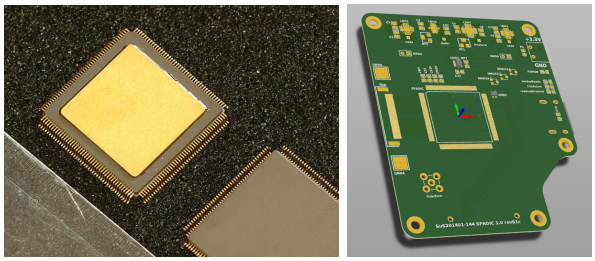

Figure 2: (a) SPADIC 1.0 chip assembled in QFP176 package. (b) The smaller version of the new FEB for only one SPADIC 1.0 chip allows easier testing.

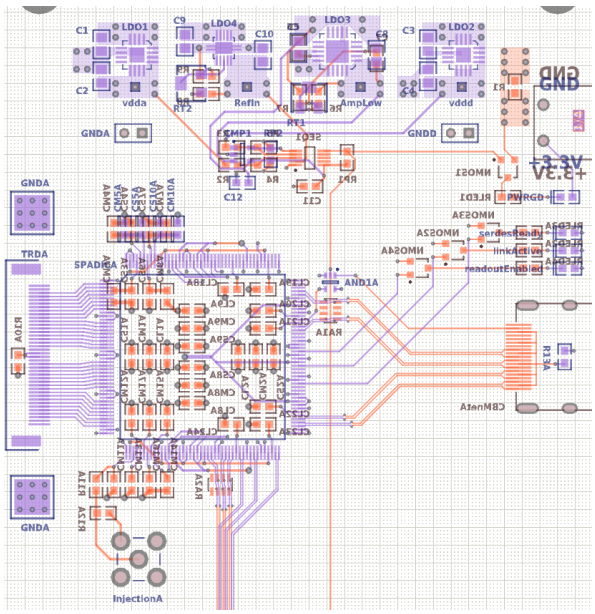

Figure 3: Layout of the top third of the new PCB, containing the voltage regulators and one of three SPADIC chips

and requires 4 layers. Using the same layout, the SPADIC pitch could be reduced to approximately 60 mm.

References

[1] M. Krieger and P. Fischer, *Commissioning of the SPADIC 1.0 Amplifier/Digitizer Chip*, this report

[2] D. Emschermann, *Development of the Münster CBM TRD prototypes and update of the TRD geometry to version v13a*, CBM Progress Report 2012, p. 53

[3] F. Lemke *et al.*, *Status of the CBMnet based FEE DAQ readout*, this report

Development of an online feature extraction pre-processing stage for the TRD based on SPADIC 1.0

C. Garcia and U. Kebschull
Infrastructure and Computer Systems for Data Processing (IRI), Goethe University, Frankfurt/Main, Germany

One of the main challenges for the data acquisition of the Transition Radiation Detector (TRD) for the Compressed Baryonic Matter experiment (CBM) is to efficiently process the high data rate produced by the front-end electronics operating in a free-streaming data acquisition mode. In this scenario, the TRD detector is read-out by the front-end mixed-signal SPADIC 1.0 chip [1]. The SPADIC 1.0 delivers 32 autonomous read-out channels with a large set of meta-information attached to the generated messages. In order to fulfill the processing requirements for the TRD, a feature extraction online pre-processing stage has been proposed [2]. The aim of the feature extraction is to do an online pre-processing of the front-end electronics data, in order to reduce it by means of parameter extraction and clustering. The feature extraction pre-processing stage would be integrated within the functionality of the Data Processing Board (DPB) [3].

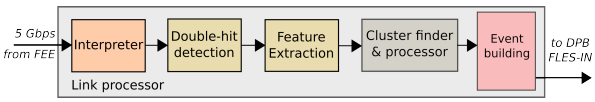

Figure 1: Block diagram of the internal architecture of the feature extraction core

As seen in Fig. 1, the internal processing logic of the feature extraction firmware would allow to instantiate multiple "link processors" in parallel in order to handle the data from different data-input optical links. However, the maximum number of link processors would be constrained by the FPGA resources available.

The internal architecture of the feature extraction core is based on the following processing stages: first, a message interpreter module decodes the incoming SPADIC 1.0 event words wrapped around the CBMnet 2.0 headers and delivers the full time-bin RAW data, as well as useful metadata attached to the hit message (e. g., timestamp, channel id, group id, hit type, etc.). This decoded data is then handled by the double-hit detection logic. The double-hit logic works in two configurable modes: first, in conjunction to the double-hit detection logic implemented in the SPADIC 1.0 chip and second, as a stand-alone detection logic. In the first case, the double-hit logic compares the hit-message flags set by the SPADIC 1.0 that tell whether a double hit was detected or not. In the second case, as a stand-alone detection mode, the logic compares the signal charge with different virtual thresholds at different time bin positions. A parallel running module finds the peaks and valleys in the signal evolution. These information is used by a later logic that splits the message between two maxima, when a valley has been found.

The second processing stage consists mostly of two parallel processes, a total charge integrator (Qtot) and a temporal center of gravity calculator (COG). The Qtot module delivers an amplitude vs. time integration from a region of interest or from all the time bins included in the event. On the other hand, the COG calculates the center of gravity of the signal in time direction. In order to save FPGA resources, the feature extraction can be configured to use only one of the before mentioned cores. Further beam test analysis will show which processing module gives better results for the event reconstruction. A final processing stage is called cluster finder and processor. This module finds clusters from events that share similar characteristics, e. g. contiguous fired pads, events with a timestamp that falls within a certain threshold and also by comparing the neighbor trigger matrix flags generated by the SPADIC 1.0. Finally, after a cluster has been completed, the data from each event that belongs to the found cluster is processed by a Center of Gravity (COG) algorithm that provides a temporal resolution of the hit position within the found cluster. In the end, the event building logic wraps the hit-message into CBMnet 2.0 containers in order to be shipped to later DPB processing stages.

Currently, most functionality of the feature extraction firmware has been developed and is under continuous testing in a laboratory setup. In 2014, a TRD beam test will be performed in order to test and provide consistent results about performance and FPGA resource consumption.

References

[1] T. Armbruster *et al.*, *SPADIC 1.0 – a self-triggered amplifier/digitizer ASIC for the CBM-TRD*, CBM Progress Report 2012, p. 55

[2] C. Garcia *et al.*, *Beam test results of the CBM-TRD feature extraction using SPADIC v1.0*, CBM Progress Report 2012, p. 59

[3] J. Gebelein *et al.*, *SysCore3 – A universal Read-Out Controller and Data Processing Board*, CBM Progress Report 2012, p. 87

Time-of-Flight Detector

Hybrid Al_2O_3 and Si_3N_4/SiC ceramic RPCs

A. Laso Garcia[1], A. Akindinov[2], J. Hutsch[1], B. Kämpfer[1], M. Kaspar[1], R. Kotte[1], D. Mal'kevich[2], L. Naumann[1], A. Nedosekin[2], V. Plotnikov[2], M. Sobiella[1], D. Stach[1], R. Sultanov[2], K. Voloshin[2], C. Wendisch[1], and J. Wüstenfeld[1]

[1]Helmholtz-Zentrum Dresden-Rossendorf, Dresden, Germany; [2]ITEP, Moscow, Russia

RPCs with ceramic electrodes are proposed to cover the low angle regions of the CBM-ToF wall. The purpose of this coverage is to determine the reaction plane in heavy ion collisions as well as to provide a start time for the rest of the wall. The proposed RPCs use Al_2O_3 and Si_3N_4 ceramic electrodes. Al_2O_3 is a high-resistive ceramic with a bulk resistivity in the order of $10^{14} - 10^{15}\,\Omega\,$cm. A thin layer of Chromium, about 90 nm thick, is deposited through evaporation on the surface of one side of the plate. This metallic layer is used for high voltage supply and signal readout. A groove carved into the plate smoothly separates the metallic layer from the edge of the ceramic plate. Thus fringe electric fields due to edges are suppressed. The Al_2O_3 ceramic plate has dimensions $5\times5\times0.2\,$cm^3. The Si_3N_4/SiC ceramic plate is of the same composition as the one used in large HZDR prototypes (dimensions of $5\times5\times0.2\,$cm^3). A two-gap structure is formed by two Al_2O_3 electrodes on the outside and a Si_3N_4/SiC electrode in the middle. The spacers are 250 μm thick made of Al_2O_3. A full RPC module is comprised of three such structures having in total 6 gaps. A photograph of one of such "sandwiches" is shown in Figure 1. Three such prototypes were tested, one with floating electrodes with a bulk resistivity of $10^8\,\Omega\,$cm (ITEP 8) and two other with bulk resistivity of $10^{10}\,\Omega\,$cm (ITEP 1, ITEP 2). The signals were read at one corner of the electrodes. The combined charge of the six gaps was read out by custom-made amplification electronics based on the MAXIM 3760 chip.

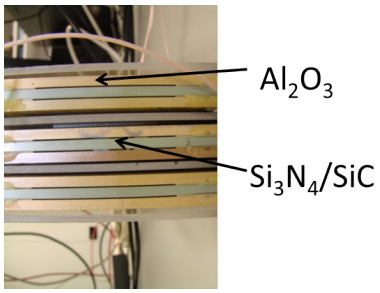

Figure 1: Sandwich of 3 stacks of 2 gap-modules

These prototypes were tested at the electron accelerator ELBE at HZDR in June and November of 2013. The goals were: i) to determine the influence of the floating electrode bulk resistivity on the performance of the RPC, ii) to test the stability of such detectors and their recovery from streamers, iii) to check the effects of a mixture without i-butane and iv) to estimate the efficiency and time resolution of these prototypes. Our previous tests in 2012 showed that the dark current in these RPCs is negligible. Tests showed a current less than 10 nA up to field strengths of 90 kV/cm. Also, the polymerization of whiskers in the cathode was eliminated after taking out the i-Butane from the gas mixture [1].

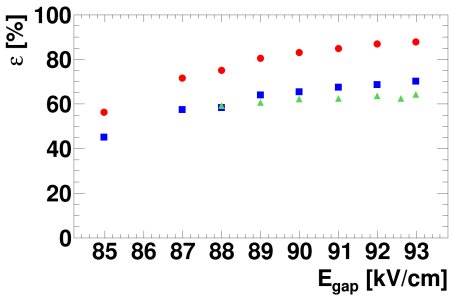

Figure 2: Comparison of efficiency ε as a function of the electric field strength in the gas gap $E_{\rm gap}$ for ITEP 1 and ITEP 2 under two different trigger conditions. The red bullets, •, represent the efficiency for ITEP 1 under Trigger + All Sinctillator condition, the blue squares, ■, and green triangles, ▲, correspond to ITEP 1 and ITEP 2 under Trigger + S6, respectively.

In summer 2013, the RPCs were exposed to 30 MeV electrons at ELBE. The performance of the detector was evaluated by means of voltage and rate scans under different trigger areas. A trigger area of $2\times2\,$cm^2 is defined by two plastic scintillators read out by PMTs placed 30 cm before and after the RPC plus a scintillator immediately after the RPC with dimensions $4\times4\,$cm^2. This trigger is denominated "Trigger + S6". The second trigger condition uses two additional $0.5\times0.5\,$cm^2 scintillators located on the anterior wall of the RPC box. These two scintillators were placed next to each other defining a trigger area of $1\times0.5\,$cm^2. This trigger is named "Trigger + All Scintillator". Due to the low angle scattering of the electrons when traversing the scintillators and the ceramic plates, the efficiency estimated with the two trigger conditions varies significantly. This geometrical effect can be observed through the comparison of the efficiencies under different trigger conditions for one chamber as plotted in Fig. 2. The effi-

ciency is calculated as the fraction of hits in the RPC timing spectrum window with respect to the number of triggers. The red bullets represent the effiency for ITEP 2 at the more stringent trigger condition while the blue squares and green triangles represent the efficiency for ITEP 2 and ITEP 1 at the lax trigger condition, respectively. The rate scan was analyzed under the Trigger + S6 condition. Due to time limitations, only one of the RPCs was operated during this scan. The results are shown in Fig. 3. The efficiency remains constant at approximately a value of 60 % up to fluxes of $125\times10^3\,\mathrm{cm}^{-2}\,\mathrm{s}^{-1}$. However, as shown in Fig. 2 with a narrower trigger this efficiency is expected to be 90 %.

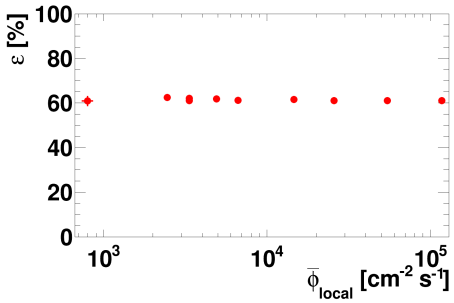

Figure 3: Efficiency ε as a function of the local particle flux $\overline{\phi}_{local}$ for ITEP 1 under Trigger + All Scintillator condition

Simulations done with the SHIELD generator and CBMRoot at ITEP show that the particle flux can reach $250\times10^3\,\mathrm{cm}^{-2}\,\mathrm{s}^{-1}$ at the border of a 40 cm wide beampipe. Therefore the bulk resistivity of the material should be lower than $10^{10}\,\Omega\,\mathrm{cm}$.

The effects of a lower bulk resistivity were studied during autumn 2013. The same trigger scheme, "Trigger + All Scintillator" was used in this beamtime. Figure 4 shows the efficiency ε as a function of the electric field strength in the gas gap E_{gap} for two prototypes. The RPC with lower bulk resistivity presents an increase in efficiency for lower electric field strength than the one with the higher resistivity, as was expected. Both prototypes do not show a clear plateau in efficiency, most probably due to the electric field strength not being high enough. ITEP 8 had an efficiency of 80 % at $E_{\mathrm{gap}} = 84\,\mathrm{kV/cm}$. Due to the low resistivity, $\rho \sim 10^8\,\Omega\,\mathrm{cm}$, it is not possible to operate the RPC at higher electric fields with low streamer probability. ITEP 1 has an estimated efficiency of near 90 % at $E_{\mathrm{gap}} = 93\,\mathrm{kV/cm}$, a result compatible to the one obtained in summer. The time resolution was in the order of 300 ps after time-walk correction. As can be observed in Fig. 5, the electronics introduce a large walk of around 4.8 ns. This is due to the non-matching of the electronics to the capacitance of the RPC.

The goals for next year include i) testing single cells with appropiate bulk resistivity (between 10^8 and $10^{10}\,\Omega\,\mathrm{cm}$), ii) improving groove carving to reach higher electric field strengths without edge effects as seen in Figure 6, and iii) finding suitable electronics to improve time resolution. The final milestone for next year will be to operate an RPC at $250\times10^3\,\mathrm{cm}^{-2}\,\mathrm{s}^{-1}$ with an efficiency over 90 % and minimal admixture of streamers. Beamt-tests at ELBE at HZDR and T10 at CERN are planned in order to achieve this goals.

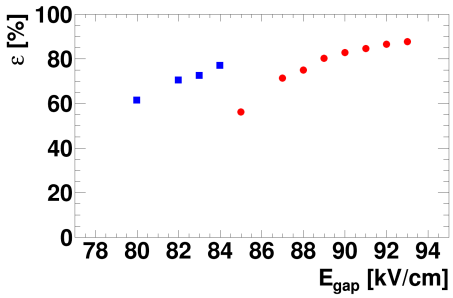

Figure 4: Efficiency ε as a function of the electric field strength in the gas gap E_{gap}. Red bullets (●) correspond to ITEP 1 and blue squares (■) to ITEP 8.

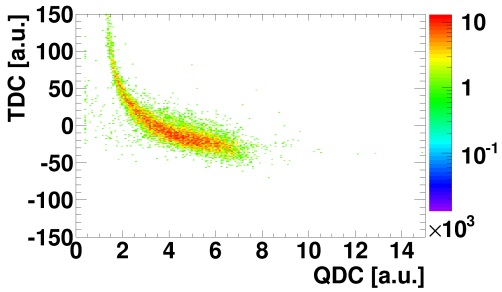

Figure 5: Time walk due to the electronics for ITEP 1. Each TDC unit corresponds to a time of 24.41 ps.

Figure 6: Improved grooved carving method on a Si_3N_4/SiC ceramic plate

References

[1] A. Laso Garcia *et al.*, CBM Progress Report 2012, p. 73

High counting rate test of the basic structure for the inner zone of the CBM RPC-TOF

A. Bălăceanu[1], V. Aprodu[1], D. Bartoş[1], G. Caragheorgheopol[1], F. Constantin[1], I. Deppner[2], V. Duţă[1], N. Herrmann[2], P. Loizeau[2], M. Petriş[1], M. Petrovici[1], L. Prodan[1], A. Radu[1], L. Rădulescu[1], V. Simion[1], and C. Simon[2]

[1]NIPNE, Bucharest, Romania; [2]Physikalisches Institut der Universität Heidelberg, Germany

A basic structure for the inner zone of the CBM-TOF wall using multi-strip multi-gap low resistivity glass RPCs was designed, built and successfully tested in terms of time resolution and efficiency [1]. The performance as a function of counting rate was tested exposing the counter in high intensity proton beam of 2.5 GeV/c at COSY-Jülich on a rather limited surface corresponding to the size of the beam spot [2]. In the present contribution we report for the first time results obtained exposing the whole detector surface at counting rates up to 10^4 particles/(cm^2·s).

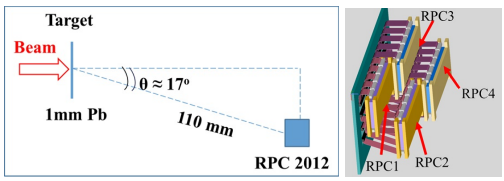

Figure 1: Left side - experimental geometry. Right side - the architecture based on four RPC cells

The in-beam test was performed at the SIS18 accelerator of GSI-Darmstadt. The RPC prototype was exposed to charged particles produced by colliding 1.7A GeV Ni ions with a 1 mm thick Pb - target at the highest intensity per spill delivered by SIS18. Fig. 1 shows the geometry of the experiment (left side) and the staggered structure of the 4 RPC cells (right side). The spill length was varied between 5 s and 2.5 s. The analysis is based on ROOT [3] and Go4 [4]. The detector was operated in a standard gas mixture of 85% $C_2F_4H_2$+10% SF_6+5% iso C_4H_{10} and at an electric field strength of 157 kV/cm. Signals of 16 strips of each cell were processed by NINO fast amplifiers [5], their differential outputs being converted by FPGA TDCs [6]. The

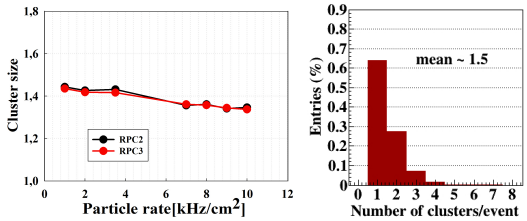

Figure 2: Left side - cluster size as a function of counting rate. Right side - number of clusters per event for a counting rate of 8x10^3 part/(cm^2·s) .

number of simultaneously recorded signals (calles cluster size) is shown in Fig. 2, left side as function of the counting rate. A decrease of about 7 % is observed. On the right side of Fig. 2 the number of clusters per event is represented for one of the RPC cells.

The time resolution was obtained using the time difference between two RPC cells overlapped along the strips, i. e. RPC2-RPC1 or between two RPCs overlapped across the strips, i. e. RPC1-RPC3. For the first case, where the overlap is at the edge of the strip, some influence of edge effects is not excluded. After walk correction, a time resolution of ≈70 ps was obtained, including electronic resolution and considering an equal contribution of the two RPC cells. For the overlap across the strips a time resolution of ≈60 ps was obtained. The corresponding time difference spectrum for a flux of 10^4 part/(cm^2·s) is presented in Fig. 3, left side. The non-Gaussian tails are at the level of 1-2%. The time resolution as a function of counting rate is shown in Fig. 3, right side. A slight deterioration of the time resolution of about 5 % is observed up to 3·10^3 particles/(cm^2·s) counting rate followed by a levelling off, within the error bars, up to 10^4 particles/(cm^2·s), the highest counting rate accessed in the experiment.

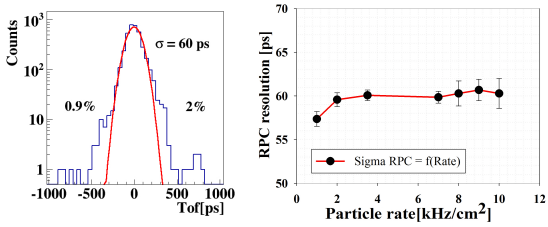

Figure 3: Left side - time difference between two overlapped strips of RPC1 and RPC3 cells. Right side - time resolution as a function of particle rate.

These results together with the previous reported ones [1, 2] show that such RPC architecture, based on low resistivity glass electrodes conserves their excellence performance in counting rates up to 10^4 particles/(cm^2·s) on the whole area of the detector. Such tests will continue at even higher rates and longer exposure periods in order to confirm that these type of RPCs can be used even for the most forward regions of the CBM-TOF wall with negligible ageing effects.

References

[1] M. Petris *et al.*, CBM Progress Report 2012, p. 68

[2] M. Petrovici *et al.*, JINST **7** (2012) P11003

[3] R. Brun and F. Rademakers, Linux Journal 1998 Issue 51

[4] J. Adamczewski *et al.*, IEEE TNS **51** (2004) 565

[5] F. Anghinolfi *et al.*, Nucl. Instrum. Meth. **A533** (2004) 183

[6] J. Frühauf *et al.*, CBM Progress Report 2012, p. 71

100 Ω transmision line multi-strip multi-gap high counting rate RPC prototype

V. Aprodu, D. Bartoş, A. Bălăceanu, G. Caragheorgheopol, F. Constantin, V. Duţă, M. Petriş, M. Petrovici, L. Prodan, A. Radu, L. Rădulescu, and V. Simion
NIPNE, Bucharest, Romania

A basic structure for the inner zone of the CBM-TOF wall using multi-strip, multi-gap low resistivity glass RPCs showed excellent performance in terms of time resolution and efficiency [1] up to local counting rates of 10^5 particles/(cm^2·s) [2] and up to 10^4 particles/(cm^2·s) all over the counter surface [3]. The differential read-out of the RPC cells had 50 Ω impedance and therefore using fast NINO amplifiers [4] of 100 Ω input impedance, an impedance matching was required at the level of mother-boards. In order to circumvent this aspect and at the same time to have a solution for the higher granularity required for the most inner zones of the CBM-TOF, a new RPC prototype was designed and built. The strip structure of the readout and high voltage electrodes was decided based on APLAC simulations such to obtain a differential readout impedance as close as possible to 100 Ω. The measured value of the glass permitivity was used in the simulation. The central read-out electrode was considered as a single layer strip structure sandwiched between two thin layers of FR4. For the standard structure of the RPC cells developed by us [1], in order to obtain a 100 Ω impedance for the transmission line, a pitch of 4.19 mm (2.16 mm strip width and 2.03 mm gap) is required.

The simulated signals on the anode and cathode electrodes read-out on 50 Ω load resistors and the differential one can be seen in Fig. 1. They were obtained with APLAC injecting in the transmission line pulses of ±1 V with a 100 ps rise time and 600 ps fall time through a 50 Ω resistor.

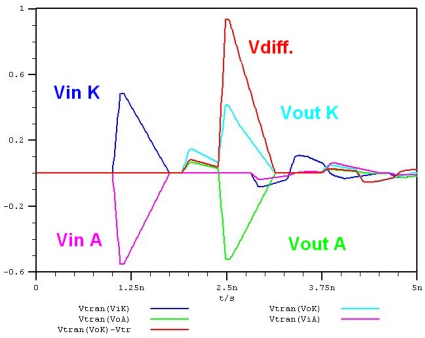

Figure 1: The signals on the anode and cathode electrodes and the differential one obtained with APLAC

The active area of the new prototype is 283 x 200 mm^2. A photo of the assembled RPC structure on the back flange and closing box is presented in Fig. 2 (left). The PCB with the structure of the read-out electrodes can be seen on the right side of Fig. 2.

The prototype based on such strip characteristics was

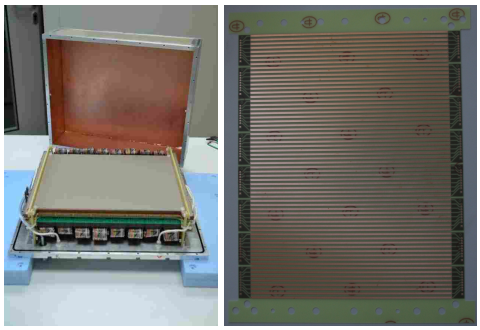

Figure 2: Left side: A photo of the assembled RPC structure on the back flange and closing box. Right side: the PCB with the structure of the read-out electrodes.

built and the results in terms of the differential and the anode and cathode signals, respectively, obtained directly from the RPC with a ^{60}Co source can be followed in Fig. 3.

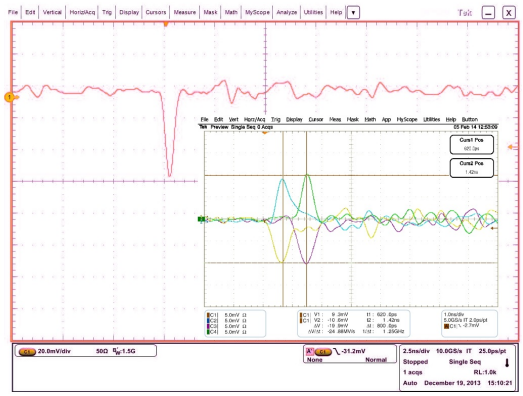

Figure 3: The differential and the anode and cathode signals at the two ends of a strip

As can be seen, the APLAC predictions are rather well confirmed by the real signals delivered by the RPC.

Detailed cosmic ray tests are in progress and in-beam tests are foreseen in the near future.

References

[1] M. Petriş *et al.*, CBM Progress Report 2012, p. 68

[2] M. Petrovici *et al.*, JINST **7** (2012) P11003

[3] A. Bălăceanu *et al.*, *High counting rate test of the basic structure for the inner zone of the CBM RPC-TOF*, this report

[4] F. Anghinolfi *et al.*, Nucl. Instrum. Methods **A 533** (2004) 183

RPC prototype test with cosmic irradiation

C. Simon[1], I. Deppner[1], N. Herrmann[1], P.-A. Loizeau[1], J. Frühauf[2], C. Xiang[1,3], and the CBM-TOF working group

[1]Ruprecht-Karls-Universität Heidelberg, Germany; [2]GSI, Darmstadt, Germany; [3]Central China Normal University, Wuhan, China

Following the proposal to construct the outer ToF wall based on fully differential multi-strip MRPCs [1] the response of a new prototype RPC designed in Heidelberg to cosmic irradiation was measured throughout the year 2013. In particular, a focus was put on compatibility with the read-out electronics, i.e. PADI-6 preamplifier cards [2] and VFTX FPGA-TDC modules [3], and on refinement of the existing calibration and correction algorithms [4].

The RPC prototype implements an 8-gap single-stack configuration with a gap width of $220\,\mu$m. It features 56 read-out electrodes of length $53\,$cm and pitch $9.4\,$mm that add up to an active area of about $2800\,\mathrm{cm}^2$. As RPCs in the outer wall region do not have to stand incident particle fluxes larger than $1\,$kHz, the prototype is equipped with float glass of resistivity $10^{12}\,\Omega$cm. The working voltage of the counter amounts to $\pm 11\,$kV. The preamplifier cards are placed inside the gas volume (Fig. 1, right) and connected directly to the read-out electrodes.

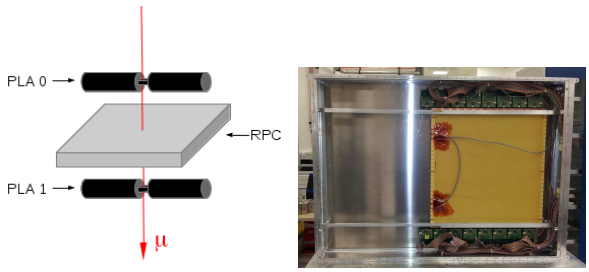

Figure 1: Sketched arrangement (left) of two plastic scintillators with respect to the RPC prototype (right) to measure its response to cosmic irradiation

The test setup in the lab comprises—besides the RPC prototype—two plastic scintillators (PLA) of dimensions $8\times2\times1$ and $11\times4\times2\,\mathrm{cm}^3$ which are each read out on two sides by photomultipliers. One PLA counter is placed above, the other one below the RPC (Fig. 1, left). From the coincidence of signals in both scintillators a trigger is built that is used to read out the RPC.

To evaluate the characteristic RPC parameters time resolution and detection efficiency of the prototype a calibration algorithm needs to process the TDC raw data. In this way, fixed time offsets due to different runtimes of the signals inside the TDCs and the cables connecting the RPC and the PLA counters with the TDCs can be accounted for. Also, systematic effects varying from event to event are corrected for, like charge walk, the velocity spectrum of the incident cosmic muons, and their angular distribution in the test arrangement. After applying all corrections to the raw data the algorithm proceeds with clustering RPC signals on neighboring read-out electrodes that show correlations in time and space. Here, the idea is that an avalanche triggered by a single charged particle traversing the RPC prototype can induce mirror charges on more than one read-out electrode. A typical cluster size for the prototype is 1.3 strips.

In the cosmic muon setup, i.e. for the section of the counter surface affected by the PLA coincidence (cf. Fig. 2, right), a detection efficiency of $98.5\,\%$ and a system time resolution of $67\,$ps were found. The term system time resolution refers to the Gaussian standard deviation σ of the time difference spectrum between the RPC and the PLA counters (Fig. 2, left). With a resolution of $55\,$ps for the plastic reference system, this allows for an estimate of the counter time resolution—still including the electronics resolution—of about $40\,$ps. An in-beam test of the prototype in April 2014 at GSI/SIS-18 will demonstrate if these very promising results also hold under heavy-ion load.

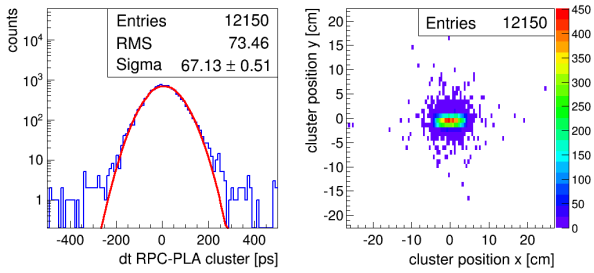

Figure 2: Time resolution of the PLA-RPC system (left) obtained in the trigger spot on the counter surface (right) requiring coincidence of the plastic scintillators

References

[1] I. Deppner *et al.*, CBM Progress Report 2012, p. 64

[2] M. Ciobanu *et al.*, CBM Progress Report 2012, p.72

[3] J. Frühauf *et al.*, CBM Progress Report 2012, p. 71

[4] C. Simon *et al.*, CBM Progress Report 2012, p. 65

A thin glass MRPC developed for the outer region of CBM-TOF wall

Zhu Weiping, Wang Yi, Wang Jingbo, Huang Xinjie, and Shi Li
Department of Engineering Physics, Tsinghua University, Beijing, China

Multi-gap Resistive Plate Chambers (MRPC) made out of float glass are proposed to be used in the outer region of the time of flight (TOF) system of CBM. Usually MRPC is assembled with common glass thicker than 0.5 mm, yielding a rate capability that is lower than the CBM requirement(1.5 kHz/cm^2) [1]. There are two ways to improve the rate capability; the first way is to reduce the resistivity of the glass plate and second to reduce the thickness of glass. Tsinghua University has made big progress in the development of low resistive glass and high rate MRPC [2]. For this contribution three MRPCs were produced with different glass thicknesses of 0.7 mm, 0.5 mm and 0.35 mm, respectively. Cosmic ray and X-ray test were preformed in our lab. The results show that the thin float glass MRPC can work well and has the potential to meet the demands of the CBM-TOF outer region. Further studies were performed by using a continuous deuterium beam of 1.5 GeV at the Nuclotron accelerator at the Joint Institute for Nuclear Research (JINR). Time resolutions of about 70 ps and efficiency higher than 90 % were obtained for flux densities up to 3 kHz/cm^2, which can fully cover the demand of the outer region of CBM-TOF [3].

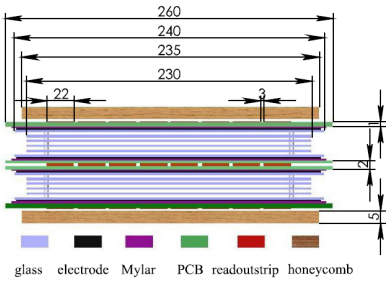

Figure 1: The structure of thin float glass MRPC

The structure of the MRPC is shown in Fig. 1. It is an eight strip counter, the size of each strip is 2.2 cm×12.5 cm. There is an 3 mm interval between each strip. The total active area is 20 cm×12.5 cm. It is a double stack device consisting two 5 gap stacks, the thickness of the gas gap being 250 μm. The three MRPC were tested at the Nuclotron in JINR at Dubna in March 2013. Deuteron beams were provided for our experiment at the energy of 1.5A GeV. Two Cherenkov detectors FFD1 and FFD2 provide the reference time of the system with a measured time resolution of around 30 ps.

Fig. 2 shows the efficiency plateau. All the modules achieved 95 % efficiency at high voltage and the efficiency of 0.35 mm MRPC is always higher than the one of the other two modules. Results of efficiency and time resolution measured under different fluxes in the range of 50 to 3200 Hz/cm^2 are summarized in Fig. 3. With the increase of the flux, the time resolution does not change too much, and the resolution of the modules is better than 75 ps. However, the efficiency of the counters decreases almost linearly. For the 0.7 mm MRPC, the detection efficiency drops below 90 % for fluxes above 500 Hz/cm^2. This result shows that the rate capability of this module is limited to 500 Hz/cm^2 at most, which is consistent with previous studies. Using the same criterion, the rate capability of the 0.5 mm MRPC and 0.35 mm MRPC are 1 kHz/cm^2 and 3 kHz/cm^2, respectively.

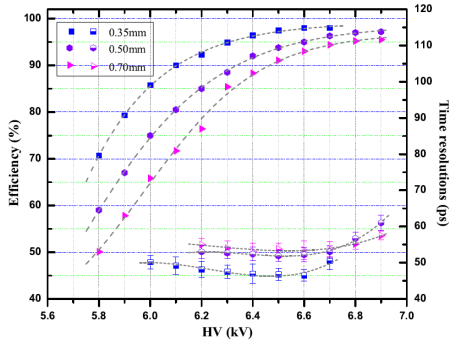

Figure 2: Efficiency and time resolution of the three modules as a function of the high voltage.

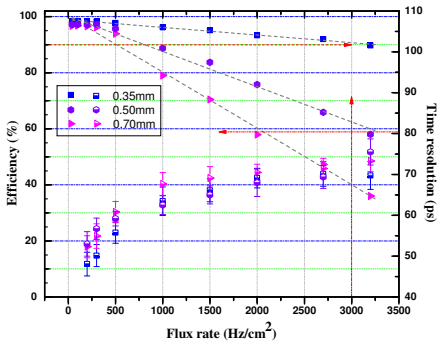

Figure 3: Efficiency and time resolution as a function of particle flux

References

[1] I. Deppner *et al.*, Nucl. Instrum. Meth. **A 661** (2012) S121
[2] J. Wang *et al.*, Nucl. Instrum. Methods **A 713** (2013) 40
[3] W. Zhu *et al.*, Nucl. Instrum. Methods **A 735** (2014) 277

TOF occupancy at SIS-100 and SIS-300

R. I. Sultanov
ITEP, Moscow, Russia

In this paper we present results of simulations performed to estimate the TOF wall occupancy and suitability of TOF granularity for two experiment set-ups: SIS-100 and SIS-300. In the SIS-100 set-up, containing STS and RICH in front of TOF and adapted for the beam energy of 10A GeV, the TOF wall is placed 6 m away from target. In addition to that, the SIS-300 configuration designed for the beam energy of 25A GeV includes the full TRD, while the TOF wall is positioned 10 m away from the target.The geometry versions of STS, RICH and TRD used in the simulations were v13c, v08a and v13c, respectively. For all configurations, the standard CBM magnetic field was used.

Data for the simulations was produced with the SHIELD generator which was chosen as providing a more "realistic" fragmentation compared to the commonly used UrQMD generator. Contrary to SHIELD, the latter does not include nuclear fragments and spectators in the output. A total of 10^4 minimum bias events, both at 10A and 25A GeV, were analyzed. To propagate generated events through experimental environment, `CBMROOT` and `GEANT4` were used.

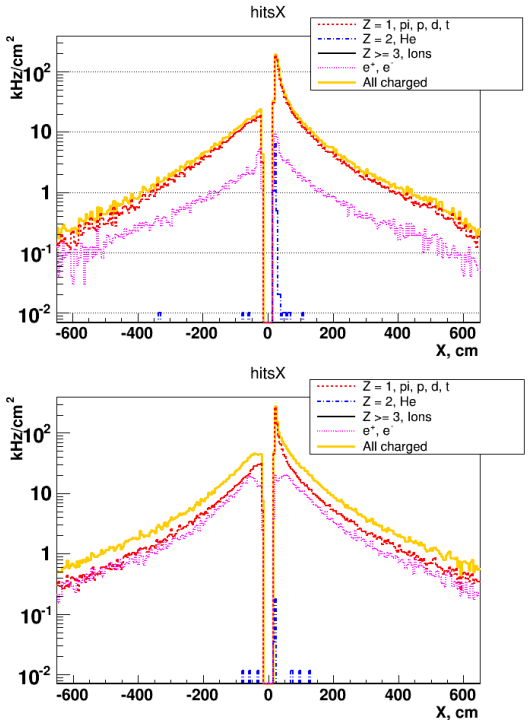

Figure 1: Particle flux along the x axis for the SIS-100 (top) and SIS-300 (bottom) configurations

Figure 1 shows the particle flux for SIS-100 and SIS-300 set-ups. Different lines correspond to different charges of particles and fragments. Fluxes are shown for the x axis only since it is more occupied. The plots correspond to a band in the center of the wall ($-10\,\mathrm{cm} < y < 10\,\mathrm{cm}$). The interaction rate is assumed to be equal to 10 MHz. One can see that the flux reaches 250 kHz/cm^2 in the peak next to the beam pipe. The flux almost entirely consists of primary particles with charge Z = 1 ($\pi^{\pm}, p, \bar{p}, d, t$). About 5 % of the flux in SIS-100 and 8 % in SIS-300 come from the secondary electrons produced in the material in front of the TOF. Fraction of fragments with Z = 2 reaches 5 % at the border with the beam pipe in SIS-100, while in SIS-300 it is less than 1 %.

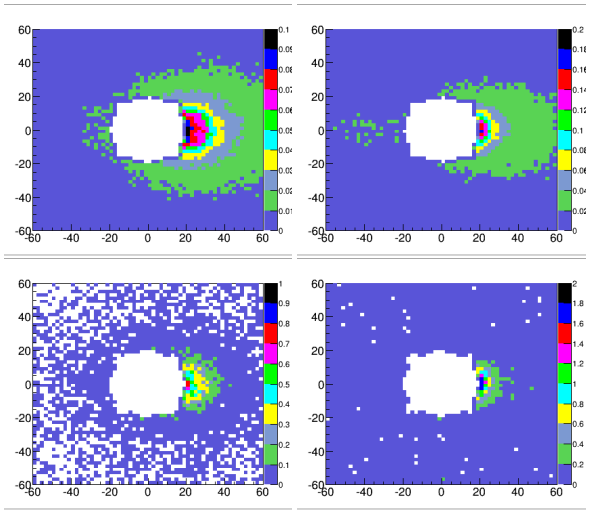

Figure 2: Top: hits density (hit/cell/event), bottom: double hit probability (%). Left: SIS-100, right: SIS-300. Central region $120 \times 120\,\mathrm{cm}^2$, cell size $2 \times 2\,\mathrm{cm}^2$.

In order to evaluate how the TOF design meets the requirements of the experiment, simulations were performed with a simple wall model with the cell size of $2 \times 2\,\mathrm{cm}^2$ and the hole for the beam pipe sized $40 \times 40\,\mathrm{cm}^2$. Figure 2 shows hits density and double hit probability for most central part of the TOF, called Beam Fragmentation T0 Counter (BFTC). It may be seen that the double hit probability is less than 1 % in SIS-100 and 2 % in SIS-300 configurations in the region of the most hit density.

Such results manifest that for considered TOF design, the double hit probability is low even at high occupancy and RPCs should be able to operate at particles flux of up to 250 kHz/cm^2.

Characterization of the GET4 v1.0 TDC ASIC with detector signals

P.-A. Loizeau[1], N. Herrmann[1], I. Deppner[1], C. Simon[1], C. Xiang[1,2], M. Ciobanu[3], H. Deppe[3], H. Flemming[3], J. Frühauf[3], M. Kiš[3], K. Koch[3], S. Linev[3], S. Manz[4], and the CBM ToF working group

[1]Physikalisches Institut, Universität Heidelberg, Germany; [2]Institute of Particle Physics, Central China Normal University, China; [3]GSI, Darmstadt, Germany; [4]IRI, Goethe-Universität, Frankfurt, Germany

A free-streaming readout chain is planned for the CBM Time-of-Flight (TOF) wall. The first element in this readout chain with a difference to usual triggered systems is the Time to Digital Converter (TDC). The GET4 ASIC is a free-streaming TDC developed for the CBM TOF wall. After tests with a first version called GET4 *Proto*, the GET4 v1.0 became available at the end of 2012 [1]. It was tested with pulser first alone [3] and then in conjunction with the PADI-6 pre-amplifier and discriminator ASIC [2].

Another interesting option for the TDC in the CBM TOF readout chain is the development of FPGA-TDCs. A first prototype for those is the VFTX board. A cosmic irradiation test campaign was performed throughout 2013 in Heidelberg using our last MRPC prototype, PADI-6 cards and VFTX boards to validate the detector design and this TDC option. Two plastics scintillators readout on both ends by photo-multipliers provide the efficiency and time reference. Results of the VFTX readout chain are presented in [5]. In the current VFTX readout chain, splitter boards are used between the PADI output and the VFTX input to ensure proper LVDS levels of the signals. As pictured in Fig. 1, the GET4 readout chain was connected in parallel for some of the data taking periods using the second output of the splitters. The GET4 readout chain is composed of 8 GET4 v1.0 chips, a Syscore v2 Readout Controller and an ABB PCI-E board for the optical readout. The analysis chain in software is the same as in the VFTX case.

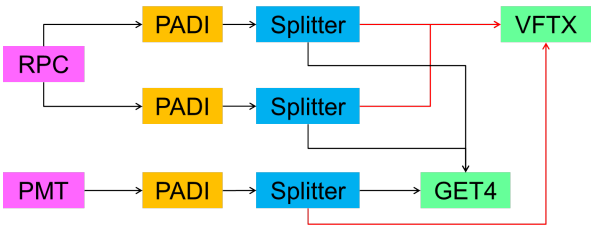

Figure 1: Connection scheme of the setup used for the cosmic rays test of GET4 v1.0

A measurement was done with the systems running in parallel at an RPC High Voltage of 11.5 kV. At this high voltage, the RPC efficiency relative to coincidences of the plastic scintillators reaches 97.5 % in the GET4 system. The system time resolution obtained after all calibrations is 82 ps. This can, however, be separated into two classes of events: those with multiple TDC hits on at least one RPC channel, for which the resolution is 90 ps, and those with only single TDC hits, for which the resolution is 76 ps. This stresses the importance of a proper matching between the components in a free-streaming TOF system to reduce fake data from reflexions, noise and cross-talk. When taking only single hit events, a time resolution of 49 ps can be extracted for the RPC and its electronics, by subtracting the contribution of the reference system. Similar results were obtained both when using a synchronization signal from the triggered system and in free-streaming mode.

In parallel to the trigger on coincidences of the two plastics, triggers on the OR of the PMTs and on the OR of the RPC strips were used to prevent buffer overflows in the VFTX system. This provides the opportunity to extract the time resolution of the GET4 system in real conditions with quite good statistics. As the time resolution of the VFTX systems and of the splitter boards are known, this can be done by comparing the time measured in the VFTX system to the one measured in the GET4 system. As the time frames of the two systems are independent, one actually needs to compare the value of time differences measured in both the VFTX and GET4 systems (Eq. 1).

$$\Delta t = (t_A - t_B)_{GET4} - (t_A - t_B)_{VFTX} \qquad (1)$$

Assuming the jitters of the VFTX, GET4 and splitter are independent and Gaussian, the GET4 resolution can be extracted for each pair (A,B) of signals (Eq. 2). This procedure was done for the left-right time differences of both plastics and of the equipped RPC strips. The counts for each left-right pairs are used to obtain a mean time resolution. The values of time resolution for the other elements are $\sigma_{\mathrm{VFTX}} = 12$ ps [4] and $\sigma_{\mathrm{Splitter}} = 10$ ps. The mean time resolution for GET4 v1.0 channels on different daughter boards and with RPC signals is then $\sigma_{GET4} = 24$ ps.

$$\sigma_{\mathrm{GET4\ channel}} = \sqrt{\frac{1}{2}\sigma^2_{\Delta t} - \sigma^2_{\mathrm{VFTX}} - \sigma^2_{\mathrm{Splitter}}} \qquad (2)$$

These value are within the CBM TOF specifications, but need to be tested with higher particle fluxes.

References

[1] H. Flemming *et al.*, CBM Progress Report 2012, p. 70

[2] P.-A. Loizeau *et al.*, CBM Progress Report 2012, p. 66

[3] J. Frühauf *et al.*, CBM Progress Report 2012, p. 67

[4] J. Frühauf *et al.*, CBM Progress Report 2012, p. 71

[5] C. Simon *et al.*, *RPC prototype test with cosmic irradiation*, this report

PADI-8 – a new ASIC prototype for the CBM ToF Wall

M. Ciobanu[1], *N. Herrmann*[2], *K. D. Hildenbrand*[3], *M. Kiš*[3], *A. Schüttauf*[3], *H. Flemming*[3], *H. Deppe*[3], *J. Frühauf*[3], *S. Löchner*[3], *I. Deppner*[2], *P.-A. Loizeau*[2], *and M. Träger*[3]

[1]ISS, Bucharest, Romania; [2]Physikalisches Institut, Universität Heidelberg, Germany; [3]GSI, Darmstadt, Germany

For the CBM ToF Wall we have designed and produced a new version of the PreAmplifier-DIscriminator (PADI) ASIC which is going to be used as the front-end electronics for the readout of Resistive Plate Chamber (RPC) detectors. The low-power PADI chip can be used for different flavours of RPC's, namely with both strip- and pad-like electrode structures. Timing RPC's have a signal rise time of the order of $t_R < 300$ ps and primary charges in the range of 10 to 500 fC, which implies a preamplifier-discriminator stage with an intrinsic electronic resolution of $\sigma_{t_E} < 15$ ps. We have developed and tested different 4-channel prototypes produced in CMOS 0.18 μm technology [1, 2, 3]. Because of the higher granularity in the inner region of the CBM ToF Wall, the PADI-8 (version 8) chip with 8 channels was designed; the bonded chip is shown in Fig. 1. The measured time resolution between two channels of a PADI-8 chip is comparable to the results obtained with PADI-6 and PADI-7 [3].

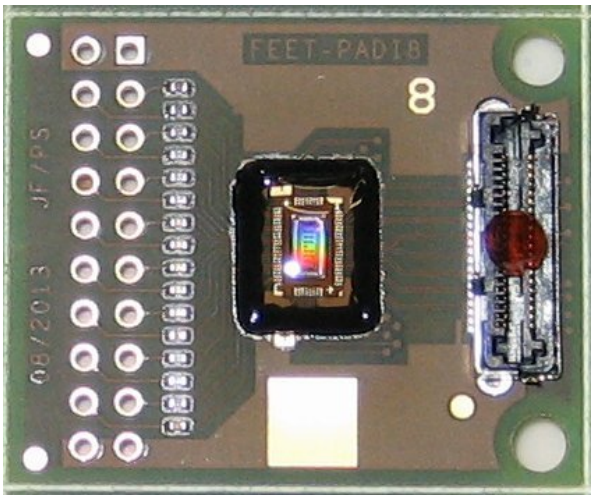

Figure 1: The test PADI-8 PCB; the PADI-8 chip is bonded directly on the PCB and protected with a transparent epoxy glob-top.

Another important feature, the uniformity of the channels on a single chip, is depicted in Fig. 2, showing the two-channel time resolution for seven channel pairs on one PADI-8 chip. At the reference threshold voltage (-124 mV), all channels are at the discrimination limit for the smallest test pulse amplitude (attenuation -50 dB is equivalent to 0.79 mV). All channels exhibit a similar behaviour. There is a small gradient (increase up to 13 %) which we correlate with a gradient in the DC voltages measured at the input ports of the channels on the same chip; we assign this gradient to the non-uniformity of the power distribution inside the chip.

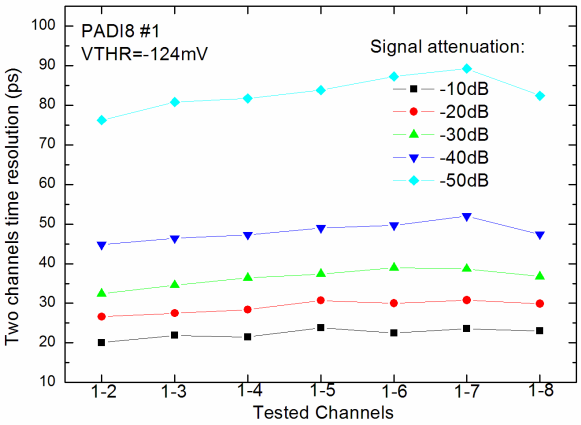

Figure 2: The time resolution uniformity is measured for different channel pair combinations on a single chip using a first channel as a reference. The test pulse (0.25 V amplitude and 3 ns width) is attenuated by the specified value (see text for details).

An evaluation of the channel noise in this case is difficult because only the discriminated signals are accessible. We have tried to determine the threshold-voltage limits for the discrimination of noise signals. For a single channel we find these limits at $\pm$36.9 mV for one discrimination in a period of $\approx$ 10 s. If we evaluate this rate for a normal distribution to 6σ, the related noise value is 6.15 $\mathrm{mV_{RMS}}$, which is close to the simulated value of 5.5 $\mathrm{mV_{RMS}}$. If we set the same threshold to all channels on a single chip and look to the OR output, we find new limits at $\pm$40.4 mV. This demonstrates that all eight channels have comparable noise properties and also a low dispersion of the DC baseline offset (the simulated σ of the offset is 1 mV).

References

[1] M. Ciobanu *et al.*, IEEE NSS Conf. Rec. **N30-18** (2008) 2018

[2] M. Ciobanu *et al.*, IEEE NSS Conf. Rec. **N13-44** (2009) 401

[3] M.Ciobanu *et al.*, CBM Progress Report 2012, p. 72

DAQ and Online Event Selection

Status of the CBMnet based FEE DAQ readout

F. Lemke[1], *S. Schatral*[1,2], *and U. Brüning*[1]
[1]University of Heidelberg, Mannheim, Germany; [2]GSI, Darmstadt, Germany

In the past year, the CBM read-out data acquisition (DAQ) network capabilities based on the CBMnet protocol [1] have been extended. Currently, there are two FEE ASIC implementations which include the CBMnet module blocks. The first is the SPADIC V 1.0 [2] with functioning communication, which is currently in the process of commissioning. The second ASIC is the STS-XYTER [3] which provides twice the data bandwidth in backend direction compared to the SPADIC. Therefore, the CBMnet has been extended to a four-lane core, and a lot of improvements were implemented. The functional verification of the digital part has been done with two Spartan6 FPGAs in a long term test running more than 7 days. Hence, the FEE LVDS interconnect [4] has been proven as stable under laboratory conditions. To get more information about the status and error behaviour of the LVDS link in the STS-XYTER, a CBMnet diagnostics core has been developed. With that, it is possible to get information about the link quality, read the status of the link initialization and collect statistics about bit-error rates and retransmissions of the active interconnect. The test setup of the STS-XYTER connected to a SysCore3 with HDMI cables is shown in Fig. 1. The Syscore3 firmware has been extended and now provides a full deterministic optical link.

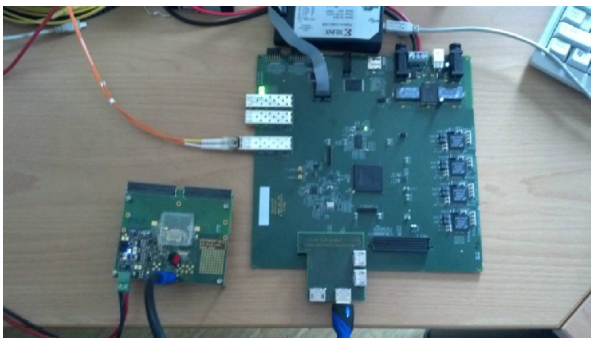

Figure 1: STSXYTER read-out setup

Further research has been done concerning the HUB ASIC to provide a hierachical synchronized DAQ network [5]. In addition to controlling the FEEs, the focus was to achieve a high density and enable early multilayered data aggregation capability. Thus, flexible build-up scenarions are possible, which are required due to varying amounts of data for different detector parts. The HUB will support up to 40 FEE links (500 Mb/s) and up to 4 backend links (5 Gb/s). Besides high density, special difficulties include handling and deadlock avoidance for the traffic, radiation tolerance, and the design of a serializer/deserializer (SERDES) capable of 5 Gb/s. A collaboration with the Indian Institute of Technology Kharagpur (IITKGP) was initiated to build this SERDES in partly full-custom design [6]. The SERDES structure is presented in Fig. 2. It depicts handling of the receive and transmit streams, including features such as clock data recovery (CDR) and eye measurement. Currently, a prototype ASIC is being designed with the focus on testing the SERDES and critical HUB functionality. Therefore, a miniASIC submission will be prepared in 2014 with the TSMC 65nm Europractice process.

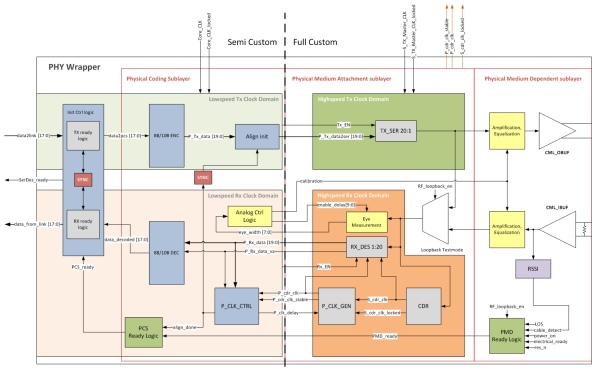

Figure 2: SERDES blockdiagram for HUB ASIC

References

[1] F. Lemke and S. Schatral, *Design concepts and measurements of the CBM DAQ network*, Deutsche Physikalische Gesellschaft EV (DPG13), Frühjahrstagung, March 4-8, 2013, Dresden, Germany

[2] M. Krieger and P. Fischer, *Commissioning of the SPADIC 1.0 Amplifier / Digitizer Chip*, this report

[3] K. Kasinski *et al.*, *Status of the STS-XYTER, a prototype silicon strip detector readout chip*, this report

[4] S. Schatral, F. Lemke and U. Brüning, *Design of a deterministic link initialization mechanism for serial LVDS interconnects*, Proc. TWEPP 2013 - Topical Workshop on Electronics for Particle Physics, Sept. 23-27, 2013, Perugia, Italy

[5] F. Lemke and U. Brüning, IEEE Trans. Nucl. Sci. **60** (2013) 3654

[6] T. K. Bhattacharyya *et al.*, *5 Gbps 20 bit serializer and deserializer in TSMC 65 nm technology for the Hub ASIC*, this report

5 Gbps 20 bit serializer and deserializer in TSMC 65 nm technology for the Hub ASIC

T. K. Bhattacharyya, I. Som, P. Som, S. Sarangi, P. Mahata, A. Rakesh Kumar, P. Pramanik, and A. Ghosh

E&ECE Department, Indian Institute of Technology, Kharagpur, India

The extension of the CBM net based readout circuit [1] along with the need for limited power, space, and material budget dictates the use of high-speed optical links and eventually, fast LVDS analog serializers and deserializers (SerDes) while implementing a four lane semi-custom ASIC core. The complete four-lane SerDes core shares a CMU (Clock Multiplier Unit) to generate high frequency and low jitter clock (2.5 GHz) for synchronization of data and clock of the SerDes block.

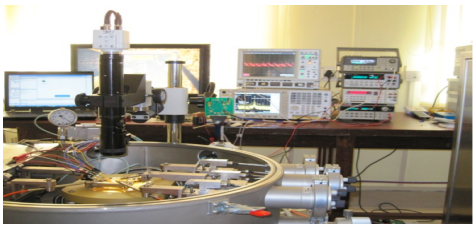

Figure 1: Test setup for the CMU

Figure 1 shows the test setup for the already fabricated 2.5 GHz prototype CMU in the 180nm process. Differential LC VCO topology has been adopted to synthesize a high quality clock signal with both fine and coarse control (digital) binary-weighted switches to accommodate the tolerance against the process-related variations. Figure 2 shows the layout implementation of the complete CMU in the 65nm process. Each ASIC hub lane runs with its own transmitter/receiver module implemented by its own serializer and deserializer synchronized with the CDR (clock and data recovery)-generated serial/parallel clock.

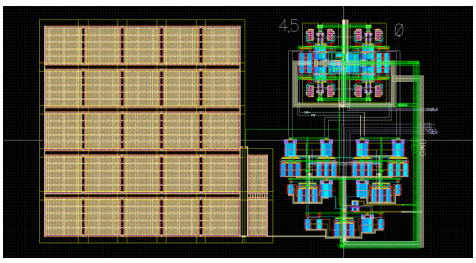

Figure 2: Layout of the CMU ($927\,\mu\mathrm{m} \times 650\,\mu\mathrm{m}$)

The SerDes architecture includes CML-CMOS mixed mode tree topology [2] to accommodate the stringent optimization between the silicon area and power without compromising its input-output data rate of 250 Mbps and 5 Gbps (and vice versa) with a limit of 0.1 UI of peak-to-peak jitter generation. Generation of serial (2.5 GHz) and associated parallel clock (250 MHz) from the input serial LVDS data stream along with the requirement of lower power and area requires the CDR to be implemented using a differential ring VCO with multiphase clock generation scheme and half-rate architecture [3] to mitigate the poor phase-noise performance. Figure 3 shows the complete CDR layout.

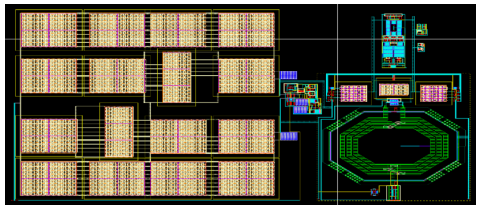

Figure 3: Layout of the CDR ($650\,\mu\mathrm{m} \times 450\,\mu\mathrm{m}$)

A robust digitally controlled low-voltage current reference generator tolerant of process and temperature variations has been implemented in TSMC 65nm process for biasing the different modules. The TC for core current for the worst case corner (with 10 % lower power supply) is less than 80 ppm/oC, after the post-layout simulation. The complete layout is shown in Fig. 4.

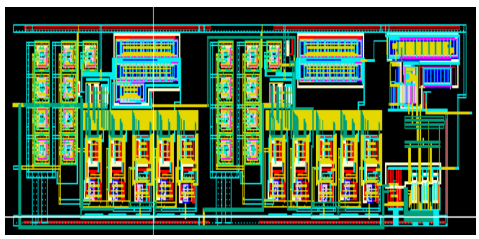

Figure 4: Layout of the BGR ($550\,\mu\mathrm{m} \times 120\,\mu\mathrm{m}$)

References

[1] F. Lemke, S. Schatral and U. Brüning, *Status of the CBMnet-based FEE DAQ readout*, this report

[2] D. F. Tondo, Ra. Lopez and Ro. Lopez, *A Low-Power, High-Speed CMOS/CML 16:1Serializer*, Proc. Argentine School of Micro-Nanoelectronics, Technology and Applications 2009, p. 81

[3] J. Savoj and B. Razavi, *Design of half-rate clock and data recovery circuits for optical communication systems*, Proc. Design Automation Conference 2001, p. 121, doi:10.1109/DAC.2001.156120

SysCore v3.1 – A universal Read Out Controller and Data Processing Board

J. Gebelein[1], *G. May*[2], *and U. Kebschull*[1]

[1]Infrastructure and Computer Systems for Data Processing (IRI), Goethe-Universität, Frankfurt, Germany; [2]GSI, Darmstadt, Germany

The universal SysCore architecture was announced in 2007 to provide an optimum balance between fixed requirements and flexibility. The first instance of boards following this principle, acted as development platform for FEE (Front End Electronic), especially the nXYTER with ADC (Analog Digital Converter) and ROC (Read Out Controller). The second slightly modified instance came into operation in several sub-detector systems of the CBM experiment, especially as ToF (Time of Flight) ROC where it is used for years now. To extend the usability spectrum, whilst keeping the re-usability approach, a completely new and improved version three of the SysCore architecture board has been developed [1]. It enables the CBM detector groups to additionally evaluate DPB (Data Processing Board) capabilities for an optical readout of the FEE. The initial prototype has been extensively tested and all results have contributed to build the current version 3.1 (see Fig. 1), which is currently distributed to the detector groups.

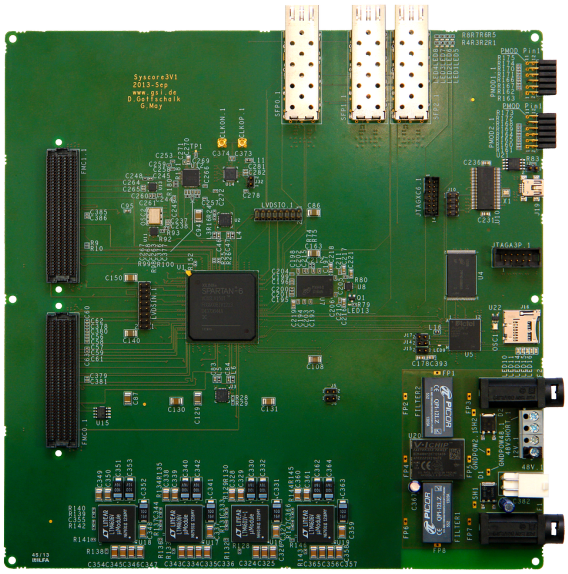

Figure 1: PCB top view of the SysCore v3.1

Implementing all specified requirements, the board features an inexpensive Xilinx Spartan-6 SRAM FPGA with 6-in LUTs, two partially populated HPC FMC connectors for efficient FEE data acquisition, three SFP connectors for up to 3.2 Gbps communication (limited by FPGA GTP speed), a jitter cleaner for clock distribution across multiple boards, a miniUSB interface for programming and data transfer, 128MB DDR3 memory, 12V/48V power supply, two Pmod connectors for quick module plugging, a JTAG connector as well as plenty of LVDS I/O pins.

The SysCore architecture is specified to provide fault tolerance for SRAM FPGAs, which is required to operate such chips in a radiation environment as it is proposed for the ToF ROC [2]. But this feature can only be realized if all components on the board are working together. Spartan-6 Configuration Scrubbing is performed by a simple Microsemi ProASIC3 Flash FPGA which is connected to a 512MB Micron SLC NAND Flash Memory with durable charge pumps [3]. Firmware updates of this controller are available via JTAG or Spartan-6. Moreover, the power supply utilizes Linear Technology POL (Point of Load) converters.

Due to the FMC HPC connectivity feature, it is possible to connect a variety of already existing adapter cards. It is even possible to develop individual ones. Figure 2 for example shows an implementation of such a mezzanine card, designated for the STS XYTER and TRD SPADIC readout using the SysCore3.

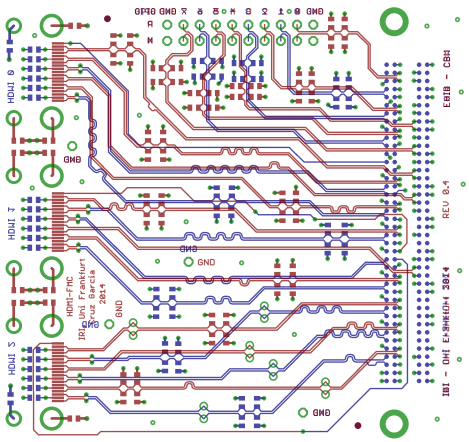

Figure 2: PCB Layout (Top/Bottom) of an FMC

References

[1] N. Abel *et al.*, CBM Progress Report 2011, p. 63

[2] N. Abel *et al.*, CBM Progress Report 2010, p. 62

[3] F. Irom and D. N. Nguyen, *Radiation Tests of Highly Scaled High Density Commercial Nonvolatile NAND Flash Memories*, JPL Publications 11-8 10/11

Firmware Development for the SysCore v3.1 Configuration Controller

A. Oancea, J. Gebelein, S. Manz, and U. Kebschull
Infrastructure and Computer Systems for Data Processing (IRI), Goethe-Universität, Frankfurt, Germany

The universal read-out controller implementing the SysCore architecture is used in various applications in the development phase of the CBM experiment. Due to the FPGA being the core component, and its various interfaces (optical links, USB, FMC, Pmod), it provides a high flexibility and adaptability to a wide range of functions. Therefore, it is found in different stages of the overall CBM data acquisition hierarchy, e.g. as read-out controller for the GET4 chip or as data processing board further upstream among other applications [1]. The second FPGA on the board is flash memory based, and acts as a configuration controller. It makes the board deployable in the radiation environment close to the Time-of-Flight detector, since it is immune to single event upsets. Consequently, it can be utilised to autonomously monitor and reset the read-out controller if necessary.

The first ten boards of the new SysCore iteration 3.1 have already been manufactured. They have been tested at IRI and are ready for delivery to the first users.

With the transition from one SysCore version to the next, the firmware development is also undergoing a substantial change towards finer modular granularity and interconnection through a Wishbone bus. Firmware porting is already in progress and successfully done for the GET4-ROC [2].

A fault-tolerant configuration and scrubbing chain has been implemented and tested for the previous SysCore version 2 [3]. The firmware for the configuration controller has been ported in a first version, providing the basic functionalities of flash memory communication and full configuration of the Spartan 6 FPGA (see Fig, 1).

The current firmware allows to transfer a bitfile of choice into the flash memory. This default firmware can then be loaded into the Spartan 6 FPGA after power-up or manual reset. For now, the configuration engine is controlled by two jumpers on the board, which is suitable for a laboratory setup with just a few boards. The file transfer is implemented with a ROOT script, through an optical link to the SysCore v3.1 board. The firmware interfacing the ProASIC3 FPGA is modularized into a Wishbone master at the optical link, and a Wishbone slave. Therefore, it is easily incorporated into any future firmware using any other means of communication, as long as the modular structure and the Wishbone bus is preserved.

On the new board, there is a connection between the Spartan 6 FPGA and the configuration interface of the ProASIC3 FPGA. This will allow for in-field updates of the configuration engine. Thus, the next step is to implement a

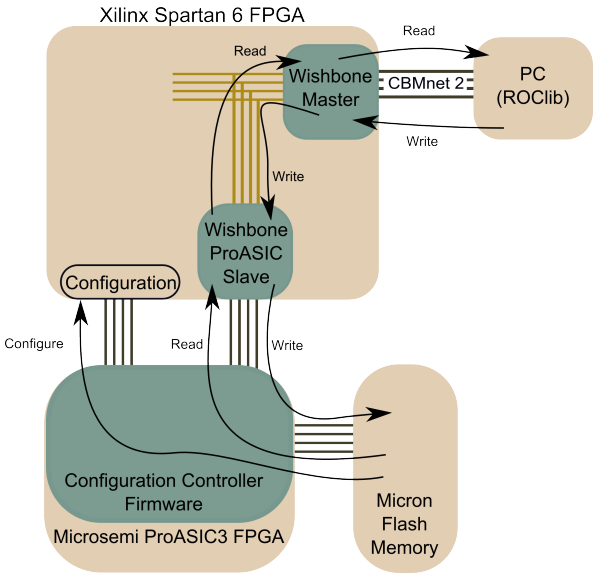

Figure 1: Current state and mechanisms of the configuration chain for the SysCore v3.1

Wishbone slave module interfacing the configuration pins of the Microsemi FPGA.

This module will then facilitate the major firmware updates for the configuration controller, which will furnish the flash memory with a file system allowing for several configuration files to be stored and selected, as well as the implementation of configuration scrubbing for deployment in areas with heightened radiation levels.

References

[1] J. Gebelein, D. Gottschalk, G. May and U. Kebschull, *SysCore3 - A universal Read Out Controller and Data Processing Board*, CBM Progress Report 2012, Darmstadt 2013, p. 87

[2] S. Manz, J. Gebelein, A. Oancea, S. Schatral and U. Kebschull, *GET4-ROC - Research and Development in 2013*, this report

[3] A. Oancea, S. Manz, H. Engel, J. Gebelein and U. Kebschull, *Development of a fault-tolerant Configuration- and Scrubbing-Chain for the CBM Read-Out Controller (ROC)*, DPG Conference, HK 34.5, Dresden, Germany, March 2013

GET4-ROC - Research and Development in 2013

S. Manz[1], *J. Gebelein*[1], *U. Kebschull*[1], *A. Oancea*[1], *and S. Schatral*[2]
[1]Infrastruktur und Rechnersysteme in der Informationsverarbeitung (IRI), Goethe-Universität, Frankfurt, Germany;
[2]Institut für Technische Informatik (ZITI), Heidelberg University, Mannheim, Germany

Irradiation Tests at COSY/Jülich

In June/July 2013 we continued our irradiation test from last year [1]. This year we also included the whole optics block (including the CBMNet core from ZITI) in the firmware under test. This means that not only a realistic logic block taken but a fully complete read-out firmware, as it would operate in the detector, was tested in-beam.

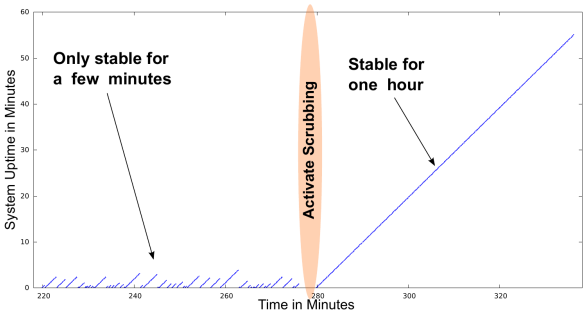

Figure 1: The plot shows the time since the last full reset of the setup, every return-to-zero of the blue plot refers to an unrecoverable failure of the setup caused by radiation. Scrubbing was disabled in the first hour and the system was only stable for a few minutes. Enabling scrubbing led the system to be stable for the remaining hour.

Figure 1 shows the results of the beamtest. We could repeat last year's promising results, this time with the transport logic included.

Porting to new Hardware

The read-out controller for the GET4 chips [2] was ported to the new hardware, the SysCore V3 [3]. With more fabric resources available, we could increase the number of supported GET4 chips from 16 to now 57 GET4s in single data line mode and 38 GET4s in double data line mode.

The port of the firmware for single data line mode is complete and the port to double data line mode is almost complete. Tests on real hardware will follow as soon as the referring FMC adapter boards are available.

Finer Granularity of Modular ROC

The successful 2-modules concept was improved for easier code sharing. As a first step, a 3-module concept was developed, concentrating common functionality in an separate module. This allowed the usage of this common logic in the STS-XYTER read-out controller [4].

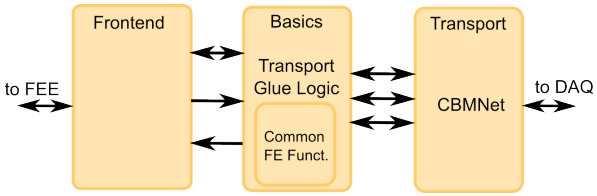

Figure 2: Illustration of the 3 module concept

As a next step, the modularization will be developed towards an even finer granularity. For 2014 the firmware of the GET4-ROC, as well as the firmware of other CBM related FPGA projects will consolidate to a common controls bus. This will allow the usage of logic in multiple designs, not only in read-out controller designs but also for example in the *First Level Event Selector Interface Board* [5].

References

[1] S. Manz *et al.*, *ToF-ROC FPGA Irradiation Tests 2012*, CBM Progress Report 2012, Darmstadt 2013, p. 69

[2] H. Flemming and H. Deppe, *The GSI Event driven TDC GET4 V1*, CBM Progress Report 2012, Darmstadt 2013, p. 70

[3] J. Gebelein, D. Gottschalk, G. May, and U. Kebschull, *SysCore3 - A universal Read Out Controller and Data Processing Board*, CBM Progress Report 2012, Darmstadt 2013, p. 87

[4] F. Lemke, S. Schatral, S. Schenk, and U. Brüning, *Status of CBMnet integration and HUB design*, CBM Progress Report 2012, Darmstadt 2013, p. 84

[5] J. de Cuveland, D. Hutter, and V. Lindenstruth, *Status of CBM First-level Event Selector Prototype Developments*, CBM Progress Report 2012, Darmstadt 2013, p. 89

FPGA based free running mode acquisition for high counting rate TRD

F. Constantin
"Horia Hulubei" National Institute for Physics and Nuclear Engineering, Bucharest, Romania

Two free running mode acquisition systems were developed for in-beam tests of the TRD prototypes. The first one is based on the Virtex®-6 FPGA ML605 Evaluation Kit (see Fig. 1). This activity is a continuation of the one presented in the previous report [1], aiming for a secure synchronization with MBS DAQ system. The signal from the TRD amplified by a FEE based on FASP ASIC [2] is transported via twisted pair cable to a fast MAX1434 ADC, a 10-bit analog-to-digital converter which features fully differential inputs, a pipelined architecture, and digital error correction incorporating a fully differential signal path. The MAX1434 offers a maximum sample rate of 50 Msps. The sync signal from MBS was used to correlate the information delivered by the MAX1434 ADC data with the other Read Out Controllers (mainly with the QDC operated in the VME crate used for lead glass and Cherenkov detectors). The information from the ML605 board was also made available to the general acquisition system which delivered to the Go4 environment used to monitor the whole system during data taking. Figure 2 shows the electron / pion separation using a fibre radiator and one of the TRD prototypes of the Bucharest group based on a MWPC architecture with 2×4 mm amplification zone and 4 mm drift region [3]. Electrons and pions were selected using the information from a Cherenkov detector and a lead glass calorimeter [4]. Although quite preliminary, the results show that the information delivered by high counting rate prototypes developed for CBM and amplified by FASP could be processed by the free running mode architecture, conserving their performance.

Figure 1: General view of the first acquisition system

The second new acquisition system was developed in order to acquire the data from 64 pads; it is a more dedicated system with a lower sample rate of 2 Msps and 12 bits ADCs. It is based on a Spartan 6 based SP601 evaluation board and a custom designed board for analogue conversion with MAX 11105 converter. (see Fig. 3). It is a cheaper solution and more suited for large TRDs. The new system is scheduled to operate our TRD for the next in-beam tests.

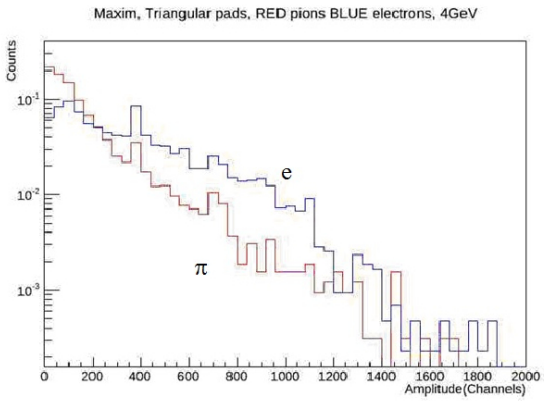

Figure 2: Electron/pion separation

Figure 3: General view of the second acquisition system

References

[1] F. Constantin and M. Petcu, CBM Progress Report 2011, p. 53

[2] V Catanescu, 10th CBM Collaboration Meeting, Sept. 25-28, 2007, Dresden

[3] M. Petris *et al.*, CBM Progress Report 2012, p. 61

[4] D. Emschermann *et al.*, CBM Progress Report 2012, p. 80

CBM First-level Event Selector data management developments

J. de Cuveland, D. Hutter, and V. Lindenstruth
FIAS Frankfurt Institute for Advanced Studies, Goethe-Universität, Frankfurt am Main, Germany

The First-level Event Selector (FLES) is the central event selection system in the CBM experiment. Its task is to select data for storage based on online analyses including a complete event reconstruction. To do so, the FLES timeslice building has to combine data from all input links to time intervals and distribute them via a high-performance network to the compute nodes. Data rates at this point are expected to exceed 1 TByte/s.

The FLES system consists of a scalable supercomputer with custom FPGA-based input interface cards and a fast event-building network (Fig. 1). Constructed largely from standard components, it will be situated at the new FAIR data center.

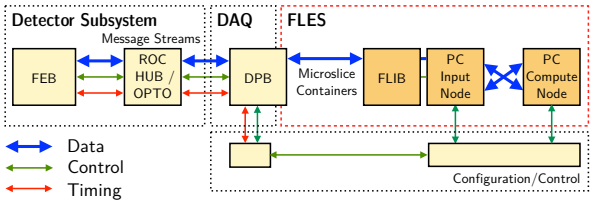

Figure 1: The First-level event selector (FLES) in the CBM read-out data path

A *timeslice* is the fundamental data structure that manages access to all detector raw data of a given time interval. It provides random access to *microslices*, each containing data from a small amount of time and a single input detector link (Fig. 2). By duplicating a small number of microslices at the border of a timeslice (*overlap region*), differences in detector readout timing performance can be accomodated, and it is ensured that every timeslice can be processed independently.

These data structures and a timeslice-based API for the following online data processing have been developed and optimized such that computer memory access (e. g., required by additional copy operations) can be minimized.

For data transfer between the FLES nodes, it has proven practical to use an InfiniBand network. A prototype software for efficient timeslice building based on InfiniBand Verbs has been developed, especially addressing questions regarding data structures and buffer management. It implements the full data structures as intended for the final setup. The feasibility of employing a more high-level interface to the network hardware, like MPI, is currently under investigation.

Efficient Timeslice building over a state-of-the-art InfiniBand FDR network has been successfully demonstrated on a small scale on the Micro-FLES cluster installed at GSI.

The CBM detector data enters the FLES system through

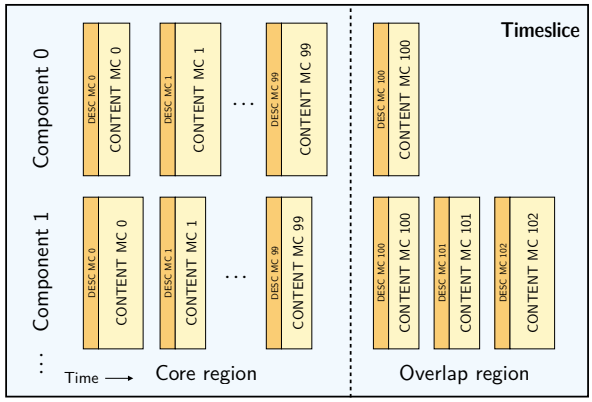

Figure 2: The FLES timeslice data structure provides indexed access to detector raw data packaged in microslices.

custom add-on cards in the FLES PCs. These FLES Interface Boards (FLIBs) require high-speed optical inputs to receive the data from the CBM readout electronics, a high-performance interface to the host PC, and a large buffer memory. A specially developed FPGA-based card with a PCIe interface at the maximum achievable rate will be employed here.

The FPGA design implements the DAQ protocol for receiving the data, manages the buffer memory, and controls the PCIe transfer. In contrast to the final system, early prototype setups lack the DPB layer (Fig. 1) and do not support the creation of microslices. The current prototype firmware therefore includes a mockup of the foreseen DPB design and is capable of directly receiving CBM-Net messages as delivered by the CBM front-end electronics.

The FPGA design has been ported to the Xilinx Kintex-7 family of FPGAs, as the current standard readout chain for CBM detector development employs a prototype board with this device. The prototype firmware, implemented in a total of 9700 lines of VHDL code, has been completed and successfully tested in a readout setup. In the future, further optimization of the DMA architecture including the software device driver will have to be performed to minimize memory access operations on the host PC.

Both aspects, input interface and timeslice building over Infiniband, have been intergrated in a common data management software project. This allowed to set up and successfully demonstrate the FLES data chain from data generating boards connected to the FLIB optical inputs to substitute analysis code on a FLES compute node after complete timeslice building.

High-level data flow description of FPGA firmware components for online data preprocessing

H. Engel, F. Grüll, and U. Kebschull
IRI, Institut für Informatik, Goethe-Universität, Frankfurt, Germany

FPGA firmware for detector read-out is commonly described with VHDL or Verilog. Data processing on the algorithmic level is a complex task in these languages and creates code that is hard to maintain. There are high level description frameworks available that simplify the implementation of processing algorithms. A sample implementation of an existing algorithm and the comparison with its VHDL equivalent show promising results for future online preprocessing systems.

Field Programmable Gate Arrays (FPGAs) are widely used in high energy physics detector read-out chains due to their flexibility. The protocols and interfaces are usually implemented with hardware description languages like VHDL or Verilog. With FPGAs getting bigger and faster they become more and more suitable for performing complex data processing tasks. This can reduce the data volume and significantly ease demands on later software based processing steps. The drawback of the commonly used hardware description languages is that they are mostly working on the Register Transfer Level. This is perfect for high performance protocol and low level interface implementations. However, using these languages to implement data processing on an algorithmic level requires experienced developers and usually involves customized IP cores and latency matching of components. This creates a rather complex and static design. There are several high level hardware description frameworks available that provide their own languages to describe data processing steps on an algorithmic or data flow level. Some of them also come with an own framework including building blocks for PCIe or DRAM interfaces. This significantly speeds up the development compared to a description in plain VHDL or Verilog.

The underlying framework of this work is made by Maxeler Technologies. The platform generates a pipelined version of the algorithm after its data flow graph has been described in a Java-like programming language [1]. The compiler manages the scheduling of the design, inserts latencies in the generated pipelines wherever needed to keep the data in sync, and instantiates interfaces to PCIe or DRAM if required. A software environment with a device driver and C API provides easy to use stream interfaces to the hardware. The compiler translates the data flow description into VHDL code which is then run through the vendor tools.

The algorithm described in this way is the FastClusterFinder that was used as a VHDL core in the readout of the ALICE Time Projection Chamber during LHC run period 1 [2]. A simplified overview of the algorithm is shown in Fig. 1. The incoming raw data is decoded into a data stream with time and location information. The center of gravity and the deviation of peaks are calculated in time direction. In a second step neighboring cluster candidates are merged to get the center of gravity and the deviation of the full cluster in pad direction. The last step is a floating point division. The VHDL implementation is a rather complex design due to its data flow control structures and the number of fixed point and floating point arithmetics.

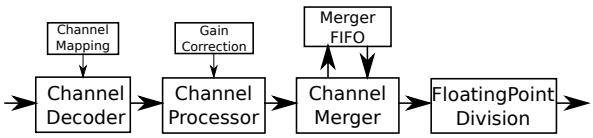

Figure 1: Schematic picture of the ALICE TPC FastClusterFinder algorithm

A functionally identical version of the FastClusterFinder algorithm has been described with the Maxeler data flow description language. The behavior of this implementation has been verified in simulation using recorded detector data from ALICE TPC. The output of the data flow simulation is directly compared to the output of a Modelsim simulation of the original VHDL code. In comparison to the VHDL implementation the number of lines of code is significantly reduced for the data flow description. Especially the computing intensive parts of the design are very easy to understand and to maintain. The resource usage of the generated design in its current state is slightly different in details but overall in the same order of magnitude as the VHDL implementation.

This implementation shows that there are tools available to describe processing algorithms on an algorithmic or data flow level that are able to generate hardware with comparable resource usage but significantly reduced code volume. This greatly improves maintainability of the code. A next step will be to implement and test the code in actual hardware. Furthermore, the generation of VHDL code out of the data flow description allows the processing elements to be extracted from the vendor framework and integrated as IP core into an own firmware environment.

References

[1] Maxeler Technologies, *Programming MPC Systems*, White Paper, June 2013

[2] T. Alt and V. Lindenstruth, *Status of the HLT-RORC and the Fast Cluster Finder*, GSI Scientific Report 2009

CBM proton beam test for electronic components

S. Löchner[1], J. Frühauf[1], H. Graf[2], J. Hoffmann[1], P. Koczon[3], S. Manz[4], and M.Witthaus[2]
[1]GSI Darmstadt, Experiment Electronics (CSEE); [2]GSI Darmstadt, Beam Instrumentation (LOBI);
[3]GSI Darmstadt, FOPI; [4]Goethe-Universität, Frankfurt am Main, IRI

Radiation damages to electronic components are an important issue for the CBM experiment and the used equipment there. Within the CBM collaboration a Single Event Effect (SEE) test with 2 GeV protons was realised in July 2013 at the particle accelerator COSY at Jülich [1]. Different components like power regulators, FPGAs, microcontrollers (MCU), Application Specific Integrated Circuits (ASIC) as well as a new electronic readout system (POLAND) [2] for beam diagnostic devices were tested.

The parts involved in the test are classified into three different groups. First in Commercial Off-The-Shelf (COTS) components for which no influence can be made to the internal structure (here tested: voltage regulator LTC 3605 and LTC 3610, micro-controllers PIC 18F4520, Propeller and TMS 570 MCU). The next group consists of devices that can modify the state of the circuit by programming (here tested: FPGA Xilinx Virtex4). Finally, the last group are devices in which the circuit can be improved accordingly to the test results. Here the designer has full control over the layout and special requirements of the later operation (here tested: QFW, PADI and Get4 ASIC). For the CBM experiment one of the preferred technology for ASIC developments is the 180 nm UMC CMOS process. The results of former tests showed a high intrinsic hardness to radiation for this process [3]. Two pictures of the COSY beam setup are shown in Fig. 1.

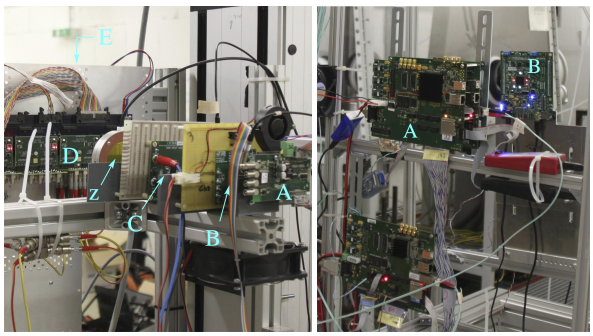

Figure 1: SEE beam test system. Left: A) QFW ASIC, B) LTC 3605, C) LTC 3610, D) PADI ASIC, E) Get4 ASIC (backside), z) Ionisation Chamber. Right: A) Syscore FPGA board, B) TMS 570 MCU.

For the SEE cross section measurement it is essential to know intensity, profile and position of the particle beam. The number of proton particles is measured via an ionising chamber (Fig. 1), read out with a Charge to Frequency Converter ASIC (QFW) [4]. An online measurement of the proton beam profile and position is done with a SEM grid device and readout via the new POLAND system.

Within the 2013 CBM test beam all devices were placed directly into beam. At a proton energy of 2.0 GeV, the total measured fluence was $3.88 \cdot 10^{12}$ p/cm^2. A typical 3D measurement of a time-resolved beam profile is shown in Fig. 2.

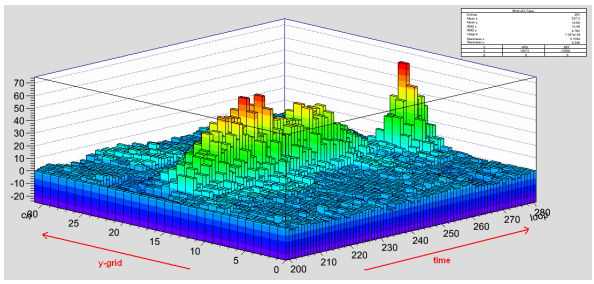

Figure 2: Time-resolved vertical beam profile measured at the 2013 COSY proton beam test. The beam extraction time was 7 s with an "extra" short pulse at the end of the extraction.

All tested devices survived the two days of beam operation, except the voltage regulator LTC 3605, which "died" after $0.77 \cdot 10^{12}$ p/cm^2. The Propeller MCU stopped its operation immediately after beam extraction where as the PIG last for several minutes. Both MCUs could be reactivated to operation after a power-cycle.

Other components, especially those that will be used in critical areas, will be tested in further radiation campaigns in 2014.

References

[1] Forschungszentrum Jülich, Institut für Kernphysik (IKP), Cooler Synchrotron (COSY), `http://www.fz-juelich.de`

[2] S. Löchner *et al.*, *POLAND - Low Current Profile Measurement Readout System*, GSI Scientific Report 2013

[3] S. Löchner, *Radiation Studies on the UMC 180 nm CMOS Process*, GSI Scientific Report 2009, p. 329

[4] H. Flemming and E. Badura, *A High Dynamic Charge to Frequency Converter ASIC*, GSI Scientific Report 2004, p. 341

Computing

An improved detector response simulation for the Silicon Tracking System

H. Malygina[1,2], *V. Friese*[3], *and J. Heuser*[3]
[1]Goethe-Universität, Frankfurt, Germany; [2]KINR, Kyiv, Ukraine; [3]GSI, Darmstadt, Germany

To achieve realistic simulation results, the response of the silicon strip sensors should be precisely included in the digitizer, which simulates a complete chain of physical processes caused by a charged particle traversing the detector, from charge creation in the silicon to the digital output signal. In the CBMROOT software, the current version of the STS digitizer [1] does not include all the processes required to obtain results with sufficient accuracy. It assumes a uniform energy loss distribution along the incident particle track and accounts for the Lorentz shift and effects of the read-out electronics such as threshold, random noise, charge collection inefficiency, and channel dead time. We considered the following improvements to the digitizer: non-uniform energy loss distribution, thermal diffusion, and charge re-distribution over the read-out channels due to interstrip capacitances (the so-called "cross-talk"). There are several possibilities to model each process with a different level of detail. We suggest the following procedure:

- to divide the incident particle trajectory into thin layers (3 μm) and to calculate the deposited energy in each layer according to the Urban method [2];
- to estimate the charge broadening due to thermal diffusion according to a Gaussian distribution for the charge in each layer [3];
- for each fired strip to calculate the charge sharing due to cross-talk, to add random noise distributed Gaussian-like with $\sigma = ENC$ (Equivalent Noise Charge);
- to convert the charge in each strip into ADC channel number; to apply a threshold and other effects of electronics.

We verify the new procedure by choosing tracks with random impact and inclination from $-45°$ to $45°$ and utilizing the center-of-gravity algorithm [4] to reconstruct clusters. From the obtained results we conclude that the most significant effect is the non-uniform energy loss along the incident particle track. Figure 1 shows a comparison between experimental data from the LHCb and our simulation. The experimental data agrees better with the new procedure. The current digitizer predicts the most probable amplitude loss for perpendicular tracks to be 0 %, whereas the improved version yields 10 %. The measured value is yet higher, demonstrating the advance in development of the digitizer.

Several STS prototype modules based on CBM05 prototype sensors were operated during an in-beam experiment at COSY in December 2013. Figure 2 shows a comparison between the simulated data and the data obtained during the experiment, in the external triggering mode at different track inclinations. The threshold was set to 9375 electrons for perpendicular tracks and to 6250 electrons for tracks at 20° inclination. As our simulation does not produce noise separately, but only adds random noise to the signal, a slight underestimation of small clusters as seen for inclined tracks is acceptable. We reproduce, however, the general behaviour of the measured cluster size distributions. Although the differences are small, we find in general a better agreement with experiment for the improved digitizer.

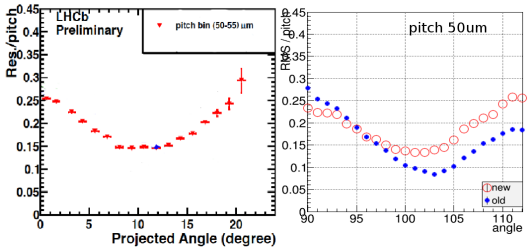

Figure 1: RMS of the hit position residuals distribution vs. track inclination. Left: LHCb VELO data [5]; right: CBM STS digitiser (open symbols: new version, full symbols: old version). Perpendicular tracks correspond to 0° in the left panel and 90° in the right one.

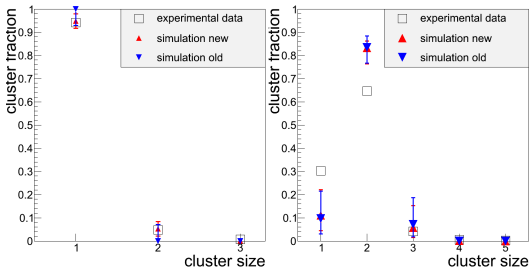

Figure 2: Cluster size distribution for perpendicular tracks (left) and for tracks at 20° (right). Squares denote measurements, red triangles results of the new digitizer, blue triangles results of the old one. The error bars show the uncertainty in angle determination.

References

[1] A. Kotynia and J. M. Heuser, CBM Prog. Report 2011, p. 14
[2] K. Lassila-Petini and L. Urban, Nucl. Instrum. Methods **A 362** (1995) 416
[3] M. Brigida *et al.*, Nucl. Instrum. Methods **A 533** (2004) 322
[4] R. Turchetta, Nucl. Instrum. Methods **A 335** (1993) 44
[5] E. Rodrigues, PoS(Vertex 2013)003

Parameterized geometric model of the updated CBM RICH detector

E. Ovcharenko[1], S. Belogurov[1], C. Höhne[2], S. Lebedev[2], T. Mahmoud[2], and V. Schetinin[1,3]
[1]ITEP, Moscow, Russia; [2]Justus-Liebig-Universität, Gießen, Germany; [3]BMSTU, Moscow, Russia

The original CAD model of the CBM RICH includes principal functional elements along with complex frames and structures. The process of creating a Monte Carlo (MC) model basing on such a detailed CAD model is very time consuming. However, a parameterized geometry description (in terms of e. g. mirror angle and radiator length) would allow to quickly change the model and thus provide great benefit for efficient testing and optimization of the RICH geometry. Implementation of parameterization and volume-assembly functionality into the "CATIA-GDML geometry builder" [1] opened the possibility to create a parameterized Monte Carlo geometrical model of the up-to-date CBM RICH as detailed and close to the engineering design as requested by physicists.

Following requests from the MC simulation side it was made possible to change the geometry quickly and easily using standard tools. A new volume hierarchy and a list of parameters were formed.

The full version of the geometry is shown in Fig. 1 and has the following volume hierarchy. The top volume, a volume-assembly which is skipped on importing into CbmRoot, contains:

- rich1 (air, box+trapezoid)
  - covering (aluminium)
  - pipe (aluminium)
  - gas (RICHgas_CO2_dis, box+trap-pipeshape)
    - main frame (volume-assembly)
      - numerous pillars (aluminium)
    - small frame (volume-assembly)
      - numerous pillars (aluminium)
    - photodetectors (CsI)
    - mirrors (volume-assembly)

There are 4 photomultiplier planes (photodetectors) represented by 4 boxes, but the user has to specify the position and rotation for only one of them. The other boxes are positioned automatically based on symmetry constraints.

Some of the parameters are supposed to be changed only by the advanced user – those are so-called "tuning" parameters. All the other parameters directly change the setup – detector size, mirrors position, photodetectors position, etc. Within the GDML file, the user can change the values of parameters in the "define" section. Parameters are grouped into sections, and there are comments for each section. Some geometrical values like sizes, angles or positions depend on the listed parameters. Computation of exact values is done during export of GDML file into ROOT. This means that the user only needs to change the GDML file and restart simulation which usually has the geometry import among the first steps.

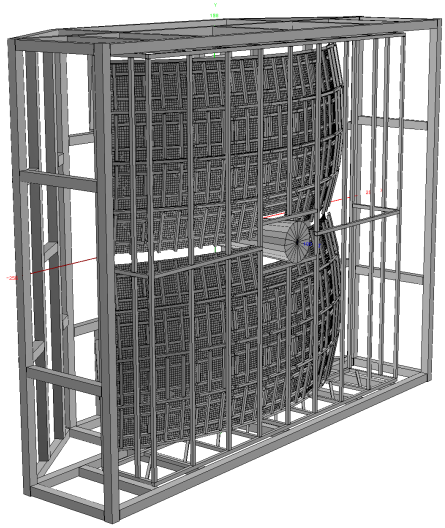

Figure 1: Full version of the Monte Carlo geometry

Based on the full geometric model, three more simplified models have were built to give the user even more flexibility. In these simplified models some elements are skipped w. r. t. the full model. This allows to have bigger possible ranges for the parameters, but the material budget in such models is underestimated. As an example, the simplest model has no frames (fixed elements), leaving only parameterized elements allowing to change all the sizes of the detector.

Altogether, four versions of RICH geometry were developed and integrated into the CBMROOT repository:

1. Full model;
2. Model without small frame;
3. Model without small and main frames;
4. Model without any support structures.

References

[1] S. Belogurov *et al.*, *Development and application of CATIA-GDML geometry builder*, to appear in J. Phys. Conf. Ser., `http://web-docs.gsi.de/~achernog/BelogurovCHEP13rev-builder.pdf`

[2] V. Dobyrn *et al.*, CBM Progress Report 2012, Darmstadt 2013, p. 40

First simulation results of the new RICH geometry including realistic material budget

S. Lebedev[1,2] *and C. Höhne*[1]
[1]Justus-Liebig-Universität, Gießen, Germany; [2]LIT JINR, Dubna, Russia

A new realistic geometry of the Ring Imaging Cherenkov detector (RICH) based on a CAD model as developed for the RICH TDR was implemented. In this report first results obtained with the new geometry are presented.

The geometry is implemented in ROOT and GDML formats differently to the obsolete ASCII format for the old geometry (v08a). The RICH software was updated to enable support of the new formats, at the same time ensuring backward compatibility for the ASCII format. The implementation only requires the RICH geometry file name to be used and will adopt all other settings accordingly thus allowing an easy change between formats.

The new geometry (v13c) as it is implemented in the CBMROOT simulation is presented in Fig. 1. The RICH detector was shifted by 20 cm from the target now being located at 180 cm. This shift was necessary due to the new dimensions of the CBM magnet; the integrated magnetic stray field along the beam axis in the RICH detector is 0.035 Tm. The RICH now contains a large support frame and also realistic mirror support structures at the back side of the mirrors. For tracks running parallel to the beam axis the integrated material budget would amount to 15 % to 50 % radiation length depending on how many support structures are on the way. The dimensions and rotation angles of the photon detectors and mirrors are still the same as for the previous geometry (v08a) and will be optimized in a second step. Due to the overall shift of the RICH detector the geometrical acceptance slightly reduces (see Table 1).

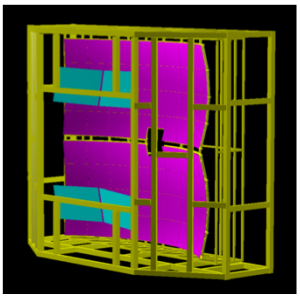

Figure 1: RICH geometry v13c as implemented in the simulation

In a first step the new geometry was tested with events containing one primary $e^{\pm}$ generated with uniform distributions of p_t, θ, ϕ. Fig. 2 shows the geometrical acceptance of the RICH which is defined as the number of $e^{\pm}$ rings with at least 7 hits divided by the number of all generated $e^{\pm}$. Table 1 presents a comparison of selected results. Most of the results are very consistent for both geometries.

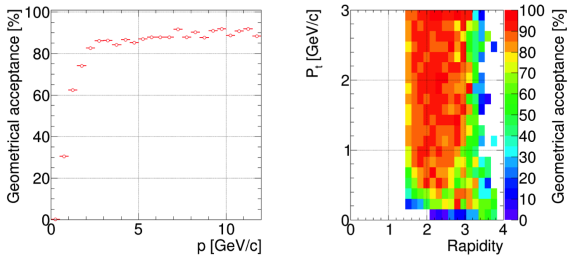

Figure 2: Geometrical acceptance of the RICH detector (v13c) in dependence on momentum (left) and transverse momentum and rapidity (right)

First results from UrQMD events for Au+Au collisions at 25A GeV beam energy are summarized in Table 1. A dramatic increase of $e^{\pm}$ from γ-conversions in the material budget between target and detector is observed. More detailed investigations show that most of these $e^{\pm}$ stem from conversions in the beam pipe and the RICH entrance.

Table 1: Comparison of v13c and v08a geometries

Geometry	v08a	v13c
Single electron events		
Geometrical acceptance [%]	85	80
Number of hits/ring	22	22
Radius resolution [cm]	0.225	0.211
A axis resolution [cm]	0.287	0.271
B axis resolution [cm]	0.211	0.208
dR_{RMS} [cm]	0.29	0.287
B/A [cm]	0.92	0.9
UrQMD events (25 AGeV, central)		
Number of hits/event	900	1700
Number of projections/event	450	360
Number of rings/event (>=1hit)	65	134
Number of rings/event (>=7hits)	45	93
Number of $e^{\pm}_{target}$ from γ/event	7.9	6.2
Number of $e^{\pm}_{nottarget}$ from γ/event	28.6	94
Number of $\pi^{\pm}$/event	24	27

Before the RICH detector will be optimized with respect to the magnetic stray field and geometrical acceptance, an optimization of the material budget is necessary in order to significantly reduce the number of secondary electrons.

CBM TRD radiator simulation in CbmRoot

C. Bergmann[1], *N. Heine*[1], *W. Verhoeven*[1], *D. Emschermann*[1], *A. Andronic*[1,2], *and J. P. Wessels*[1]
[1]Institut für Kernphysik, Münster, Germany; [2]GSI, Darmstadt, Germany

The transition radiation photon yield of a periodic radiator with N_f layers of thickness l_1 and spacing l_2 can be effectively described by

$$\frac{dN}{d\omega} = \frac{4\alpha}{\omega(\kappa+1)} \frac{(1-\exp(-N\sigma))}{(1-\exp(-\sigma))} \sum_n \Theta_n \left(\frac{1}{\varrho_1+\Theta_n} - \frac{1}{\varrho_2+\Theta_n} \right)^2 [1-\cos(\varrho_1+\Theta_n)] \quad (1)$$

according to [1] with σ being the total photon absorption cross section σ ($\sigma = \mu_1 \cdot l_1 + \mu_2 \cdot l_2$) for one foil and gas layer. This equation includes coherent and incoherent effects as well as the self-absorption of gap and foil material. Therefore it was used to calculate the total transition radiation (TR) yield per keV in `CBMROOT`. The variables are defined as

$$\varrho_i = \frac{\omega l_1}{2c} \left(\gamma^{-2} + \left(\frac{\omega_{P,i}}{\omega} \right)^2 \right), \quad (2)$$

and

$$\kappa = \frac{l_2}{l_1} \quad (3)$$

$$\Theta_n = \frac{2\pi n - (\varrho_1 + \kappa\varrho_2)}{1+\kappa} > 0. \quad (4)$$

The resulting TR photon yield spectrum is folded with the detector absorption spectrum (presented in Fig. 1) to obtain the effective energy deposition spectrum in the active gas volume of the detector. Systematic deviations between

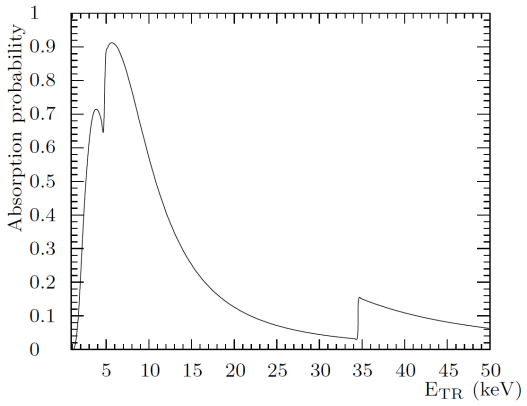

Figure 1: Approximate photon absorption probability of the 2012 MS prototypes using $XeCO_2$ (80/20)

measurements and theoretical predictions arising from the material budget between radiator and MWPC and radiator material and irregularity can be compensated by adding an attenuation factor a [0,1], with:

$$\left(\frac{dN}{d\omega}\right)_{measurement} = a \cdot \left(\frac{dN}{d\omega}\right)_{simulation}. \quad (5)$$

The parameters N_f, l_1 and l_2 have been measured for regular radiator or approximated for irregular radiators for each radiator prototype. The attenuation factors a have been evaluated by comparing in beam measurements and simulation as presented in Fig. 2. For most radiators simulations

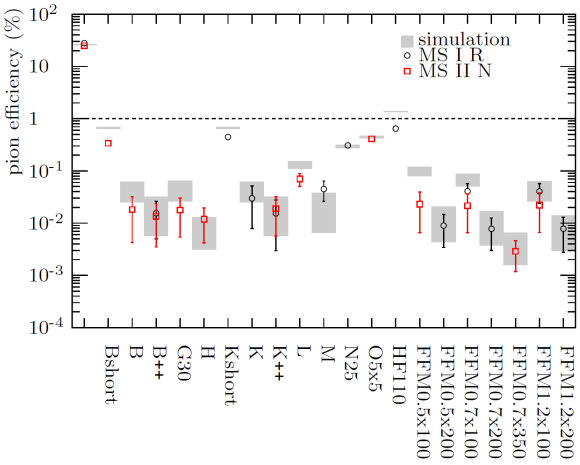

Figure 2: Comparison of different radiators showing the pion efficiency at 90 % electron efficiency with 10 detector hits. The design goal for CBM TRD consisting of 10 detecor layers is indicated by the dashed line.

and measurements are found to be in agreement within errors. Radiators B++, K++ and H have been implemented in `CBMROOT`. B++ is a classical foil Radiator made from POKALON (N_f=350, l_1=24 μm, l_2=700 μm and a=0.65), K++ is a micro-structured self-supporting foil radiator with the same parameters like B++. The best irregular radiator prototype is H made from 125×2 mm thick Polyethylene foam foils with an average bubble diameter of 900 μm, an average l_1 of 12 μm and a=0.78.

References

[1] M. N. Mazziotta, *A Monte Carlo code for full simulation of a transition radiation detector*, `arXiv:physics/9912042 [physics.comp-ph]`, 2000

Event based unpacker and digitizer for the CBM TOF in CBMROOT

P.-A. Loizeau[1], N. Herrmann[1], D. Kresan[2], F. Uhlig[2], and the CBM ToF working group
[1]Physikalisches Institut, Universität Heidelberg, Germany; [2]GSI, Darmstadt, Germany

In CBM the Time-of-Flight (TOF) method will be used to provide charged hadron identification. The measurement will be done with a wall built from Resistive Plate Chambers (RPC). The electronics and the reconstruction software for the TOF wall will follow the CBM data acquisition concept called free-streaming.

Figure 1 presents a summary of the previous status of the CBM TOF software. The software chains for real test data (top) and the one for simulated data (bottom) are fully separated. Until 2013 the unpacking, monitoring and analysis software for the TOF test setups was based on the GO4 framework [1]. A CBM dedicated library containing standard GO4 analysis sub-steps and sub-events for the CBM test hardware was developed to re-use existing software parts in the analysis of the data from various beamtimes [2]. In parallel, the tools used for the simulation of the TOF wall and the evaluation of its physics performance in the CBM setup were developed within the CBMROOT framework. These tools were mainly a direct hit producer, which converts directly the Monte-Carlo points at the TOF wall position into TOF hits with a position and time. This method, however, ignores the effect of charge sharing between channels, that in real data causes the formation of clusters (correlated hits).

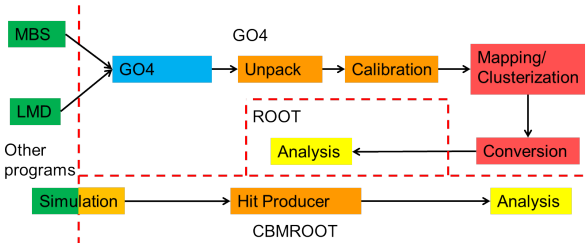

Figure 1: Status of the ToF wall analysis softwares before the integration of the unpackers in CBMROOT

In order to speed up the development of the TOF reconstruction tasks, it is necessary to have compatible unpacking and simulation chains implemented in the same framework and feeding the same reconstruction algorithm. Reconstruction tasks are e.g. the channels alignment, the clusters building or the mapping between an electronics oriented address scheme and a detector/physics oriented geometric position. The free-streaming data acquisition concept also pushes toward this software unification as the difference between the offline physics analysis software and the online event selection software needs to be minimal in order to ensure a good quality of the archived data. The final software also needs to be compatible with a time-based data organization.

The first steps toward a final time-based common software are the conversion of the existing GO4 unpacker to CBMROOT, the development of an event-based realistic digitization chain for the simulation and the development of common output objects for the unpacker and the digitization chain.

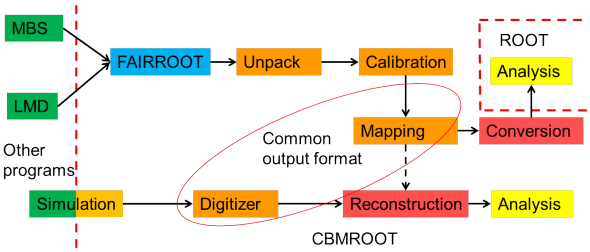

Figure 2: Currently available ToF wall analysis softwares organization using only CBMROOT and ROOT macros

These three tasks were realized. Figure 2 presents the current status of the TOF software in CBMROOT. The unpacker supports the two main TDC system used in last TOF test setups, the GET4 v1.0 [1] and the VFTX [3]. A calibration tool for the TDC data is included in the data processing chain. A conversion tool was developed in addition to keep the compatibility with the existing analysis in ROOT macros. A new TOF digitizer gives the possibility to use as input for the simulation detector parameters measured during test beamtimes, e.g. cluster size, efficiency or time resolution. It also provides a choice between various methods to obtain the signal charge and the cluster size. Both branches of the TOF software are filling objects of the CbmTofDigi class, which is the input format of a newly developed TOF clusterizer. The clusterizer delivers the same TofHit format as the direct hit producer. For testing the unpacker, its output was compared to the one of the original GO4 unpacker. No significant differences were found. The digitizer+clusterizer branch was tested in comparison to the direct hit producer. While the new implementation reproduces the results of the direct hit producer when the cluster size is minimized, it now allows for the study of a more realistic detector response.

References

[1] P.-A. Loizeau *et al.*, CBM Progress Report 2012, p. 66
[2] J. Adamczewski-Musch and S. Linev, CBM Progress Report 2011, p. 68
[3] J. Frühauf *et al.*, CBM Progress Report 2012, p. 71

The parallel Cellular Automaton track finder for the CBM experiment

V. Akishina[1,2,3] *and I. Kisel*[1,2,4]

[1]Goethe-Universität, Frankfurt am Main, Germany; [2]GSI, Darmstadt, Germany; [3]Joint Institute for Nuclear Research, Dubna, Russia; [4]Frankfurt Institute for Advanced Studies, Frankfurt, Germany

The CBM experiment at FAIR is being designed to study heavy-ion collisions at extremely high interaction rates (up to 10 MHz) and high track multiplicities (up to 1000) with data flow up to 1 TB/s. That requires the full event reconstruction and selection to be done online at the First Level Even Selection (FLES) stage. In this respect, both the speed of the reconstruction algorithms and their efficiency are crucial. The beam for the experiment will be a continuous free stream of particles without bunch structure. Due to possible overlap of events the need to analyse time slices rather than isolated events arises. In order to deal with time slices and resolve the tracks in time the measurements have to take time information into account in addition to space coordinates.

The Cellular Automaton (CA) track finder [1] being both fast and robust is used for track reconstruction in the CBM experiment. The algorithm creates short track segments in each three neighbouring stations, then combines them into track-candidates and selects the best tracks according to the maximum length and minimum χ^2 criteria. Thus, the CA track finder is intrinsically working locally with the data of a neighbourhood. This fact makes it possible to efficiently parallelise the method between cores in order to fully utilize the power of modern computer architectures.

The CA track finder algorithm efficiency proved to be stable with the growth of track multiplicity up to extreme case of 13,000 reconstructed tracks in the time slice. The track reconstruction time behaves as a second order polynomial with the increase of the track multiplicity.

Table 1: Fraction of the total execution time for the different algorithm steps on a single core

Algorithm step	Fraction of total time
Initialisation	2 %
Triplets construction	90.4 %
Tracks construction	4.1%
Final stage	3.4%

Each step of the algorithm was parallelised inside the event with the use of OpenMP and Pthreads interfaces. Contributions of the algorithm steps in total execution time while being run on a single core are given in Table 1. Since central events seem to be too small to be reconstructed in parallel on modern many-core computer architectures, the parallel algorithm was optimised for the case of 100 minimum bias Au+Au UrQMD events at 25A GeV packed into one group with no time measurement taken into account. Hits for the study were produced at the minimum bias event level.

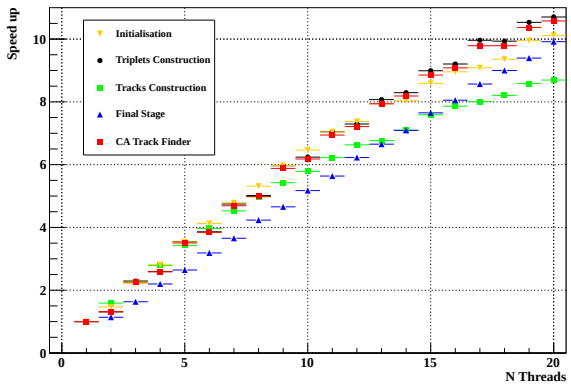

Figure 1: Speed up factor due to parallelisation for different steps and the full algorithm on Intel Xeon E7-4860 CPU with 10 physical cores and hyperthreading for the case of 100 minimum bias events grouped together

The parallel version of the algorithm was tested on a server with 4 Intel Xeon E7-4860 processors. In order to optimise the memory access and to avoid the relatively slow CPU communication, a group of events was sent to a CPU, not to a full node. Each CPU has 10 physical cores with hyper-threading, which corresponds to 20 logical cores. The resulting speed-up factors for different steps and the full algorithm within one CPU are presented in Fig. 1. The algorithm shows linear scalability. Because of hyper-threading one can expect a speed up factor of about 13 on such a CPU in the ideal case. The achieved speed-up factor is 10.6 for the full CA track finder reconstruction algorithm on 10 physical cores CPU with hyper-threading.

References

[1] I. Kisel, Nucl. Instrum. Methods **A 566** (2006) 85

[2] I. Kisel, I. Kulakov and M. Zyzak, *Standalone First Level Event Selection Package for the CBM Experiment*, IEEE Trans. Nucl. Science **60** (2013) 3703

Performance of the track parameter reconstruction algorithm on AMD Radeon HD 7970 GHz edition GPUs

D. V. Belyakov[1], *V. V. Ivanov*[1], *P. I. Kisel*[1], *and M. V. Zyzak*[2,3]
[1]LIT JINR, Dubna, Russia; [2]Goethe-Universität, Frankfurt, Germany; [3]Univ. Kyiv, Ukraine

The physics programme of the CBM experiment includes the study of the production of rare short-lived particles. To ensure a statistically significant data set, measurements have to be performed at very high interaction rates (up to 10^7 nucleus-nucleus collisions per second) and high multiplicity of produced particles (from 100 to 1000 particles in one collision).

Because of the complexity and ambiguity of the criteria for signal event selection, the DAQ system will filter out information coming from different detectors and form sets of candidate events in real-time. This task requires the reconstruction of tracks in the STS detector as well as reconstruction of primary and secondary vertices. Taking into account these features, we need the fastest and most reliable reconstruction of trajectories in the STS.

In an earlier work [1], we implemented a fast algorithm for recognition of tracks in the STS detector applying parallel computing on the LIT JINR multicore server with two Intel Xeon E5640 CPUs. The algorithm is based on the concept of the Cellular Automaton and the Kalman filter. Despite of high multiplicity events, intensive background and inhomogeneous magnetic field, the algorithm demonstrated a high efficiency of track recognition ($96\% - 97\%$) and a low level of incorrectly found tracks ($2\% - 4\%$). A high speed of processing – 220 ms per central event and 25 ms per minimum bias event on one core – was achieved.

In another work [2] we investigated the performance of the track parameter reconstruction algorithm based on the Kalman filter using Intel Xeon X5660 CPU and Nvidia GTX 480 GPU. The algorithm showed linear scalability and high performance (34 tracks/ms on CPU and 33 tracks/ms on GPU), i. e. , in this configuration the server can handle up to 70 tracks/ms.

In addition, we performed calculations on a server with two Intel Xeon E5640 processors and two high-performance AMD Radeon HD 7970 GHz edition graphics cards. Such a card is based on the GPU "Tahiti", containing 2048 stream processors, GPU with frequency 1000 MHz, an effective frequency of video memory of 6000 MHz and a memory bandwidth of 288 GB/s. This card is capable to perform 4.3 TFLOPS on single-precision numbers.

The performance results of the track parameter reconstruction algorithm based on the Kalman filter using the high-performance AMD Radeon HD 7970 GHz edition GPUs are presented in Figs. 1 and 2. Figure 1 shows the result based on one GPU (56 tracks/ms), while Figure 2 gives the performance achieved on two GPUs (105 tracks/ms). We observe an almost linear scalability depending on the number of tracks in the processing group (see details in [2]). The new cards permit to get a reconstruction speed twice as high as obtained with the Nvidia GTX 480 GPU.

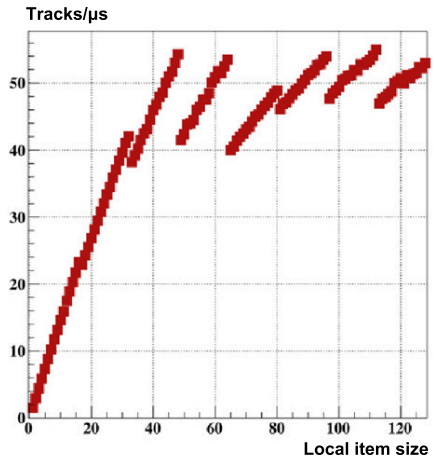

Figure 1: Performance of the Kalman fitting algorithm applying one AMD Radeon HD 7970 GHz edition graphics card

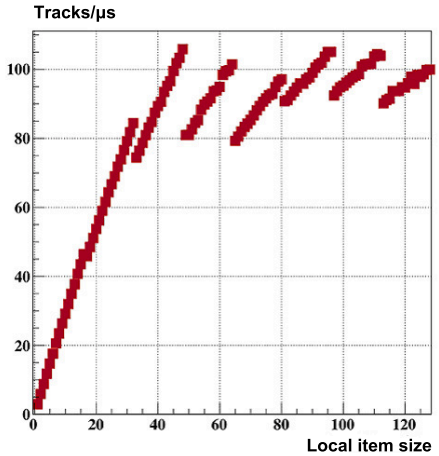

Figure 2: Performance of the Kalman fitting algorithm applying two AMD Radeon HD 7970 GHz edition graphics cards

References

[1] I. S. Kulakov *et al.*, Phys. Part. Nucl. Lett. **10** (2013) 162

[2] T. O. Ablyazimov *et al.*, Phys. Part. Nucl. Lett. **11** (2014), in press

A Monte Carlo feasibility study of the CBM event reconstruction at high interaction rates based on time information

A. Senger
GSI, Darmstadt, Germany

A Monte-Carlo simulation was performed in order to study the feasibility of event reconstruction at high interaction rates based on the timing information provided by the Silicon Tracking System (STS). The relevant parameters for event separation are the reconstructed interaction time T_0 and the variation of the track times within one event σ_T. The latter is mostly determined by the time resolution of the STS which is of the order of 5 ns.

We have studied the separation of events in time-base simulations using a cut in ΔT_0 for a reaction rate of $10^7/s$. We have to take into account two different situations: if ΔT_0 of two different interactions is smaller than the ΔT_0 cut value, there is the possibility to combine reconstructed tracks of particles from two different interactions in one event; if σ_T is larger than the ΔT_0 cut value, there is the possibility to divide the reconstructed tracks of particles from the same interaction in two different events. In Fig. 1 the relative numbers of combined and divided events are presented as function of the ΔT_0 cut value assuming $\sigma_T = 5$ ns. It can be seen that with a ΔT_0 cut value of e. g. 5 ns, the number of divided events (red squares) is about 15%, and the number of combined events (black circles) is about 6%. With increasing ΔT_0 cut value the number of divided events decreases dramatically, but the number of combined events increases up to 20% for a ΔT_0 cut value of 20 ns. It is clear that for event separation at interaction rates as high as $10^7/s$ an additional cut variable is needed.

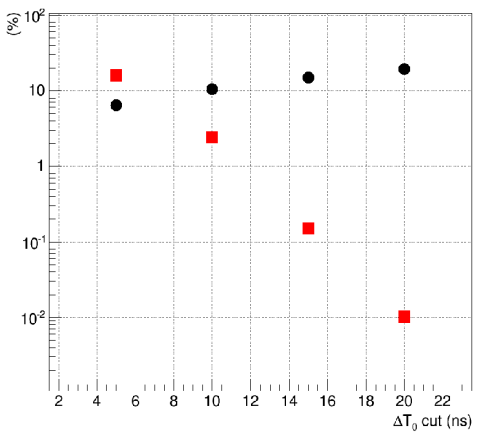

Figure 1: Fraction of combined (black circles) and divided (red squares) events as a function of the ΔT_0 cut value for $\sigma_T = 5$ ns

The separation of different events can be improved by using the information on the different positions of the primary vertices in addition to the reconstructed T_0 values. For the simulation we assume a Gaussian distribution of the beam particles at the target (i. e. of the primary vertices) with a FWHM of 1 cm. In Fig. 2 the distribution of the primary vertices in horizontal (upper plot) and vertical position (lower plot) is shown as function of time. The height and the length of the symbols correspond to a vertex resolution of 100 μm and a time variation within the event of 20 ns. It can be seen that the events are clearly separated in space and time for an interaction rate of $10^7/s$. Taking into account the position information of the primary vertex it is possible to reduce the number of combined events by up to two orders of magnitude.

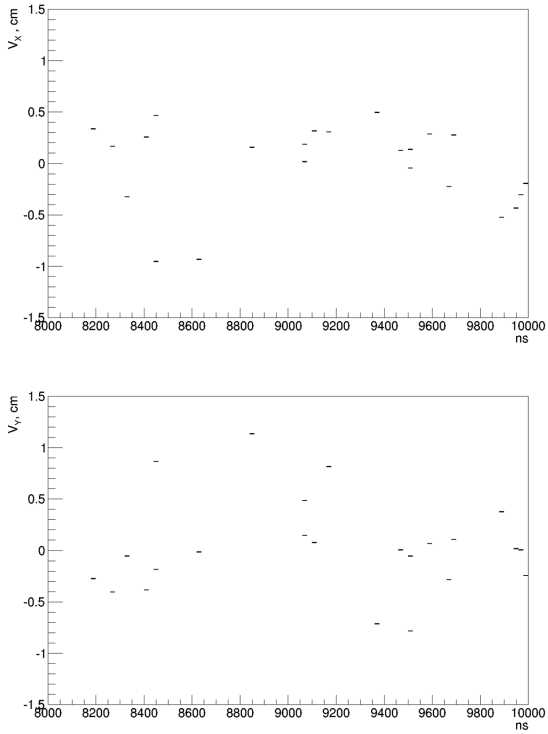

Figure 2: Primary vertex distribution in horizontal (upper plot) and vertical (lower plot) direction for a Gaussian distribution of the beam particles with FWHM = 1 cm and an interaction rate of $10^7/s$ as function of time. The symbol size corresponds to a vertex resolution of 100 μm and $\sigma_T = 20$ ns.

The CBM di-muon trigger on heterogeneous computing platforms

V. Singhal[1], *S. Chattopadhyay*[1], *and V. Friese*[2]
[1]Variable Energy Cyclotron Centre, Kolkata, India; [2]GSI, Darmstadt, Germany

The huge amount of data expected to be produced by the CBM experiment requires efficient, fast and massively parallel computing power for the online data suppression. The di-muon software trigger of CBM is based on the extrapolation of two tracklets found after the last absorber towards the target. The algorithm was described earlier [1]. We have performed a systematic study for the computation of this algorithm on heterogeneous platforms, using all currently available parallel computing paradigms like MPI (Message Passing Interface) and OpenMP (Open Multi Processing) for CPUs, OpenCL (Open Compute Language) as open standard, and CUDA (Compute Unified Device Architecture) for NVIDA GPUs. In this report, we present a comparison of the results obtained with MPI, OpenMP and OpenCL; results using CUDA have been reported in ref. [1]. The experimental setup consisted of two machines: a workstation (Dell T7500) with two Intel Xeon 2.8 Ghz 6-core processors with 2 GB/core RAM and two NVIDIA GPUs (Tesla C2075 and Quadro 4000), and a HP AMD-based server with four AMD Opteron 2.6 GHz processors with 16 cores and 4 GB/core RAM.

Fig. 1 shows the process execution time on GPU for different numbers of events processed at the same time. We find that the cross-platform standard OpenCL performs only slightly worse than the NVIDIA-native language CUDA.

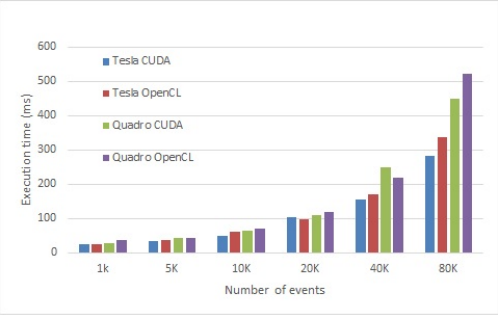

Figure 1: Time comparison between CUDA and OpenCL for NVIDIA's Tesla and Quadro GPUs

The performances of the OpenMP and MPI implementations of the algorithm on the multi-core Intel machine are compared in Fig. 2, where the execution times are shown as function of the number of parallel threads. We find for both programming paradigms an inverse linear scaling of the execution time up to 12 threads, from when on the execution time increases again; this signals that from this point on, the context switching time starts to dominate the total process time. The same test was performed on the AMD 64-core machine, with similar results. The performance of the MPI implementation is slightly better than that of OpenMP. We attribute this to the fact that the process does not use shared memory or inter-thread communication.

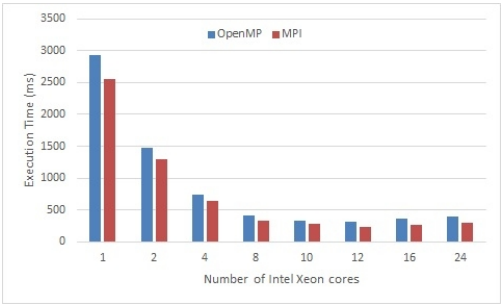

Figure 2: Time comparison between OpenMP and MPI as a function of the number of Intel CPU cores used in parallel

Figure 3 shows the comparison of the performances found with OpenCL, OpenMP and MPI on the two hardware architectures under study. On both computers, we find OpenCL to perform significantly better than the other two implementations. The reason in our opinion is the better ability of OpenCL to produce vectorized code in an automatized way. The performance of OpenMP and MPI can be possibly improved by manual vectorization.

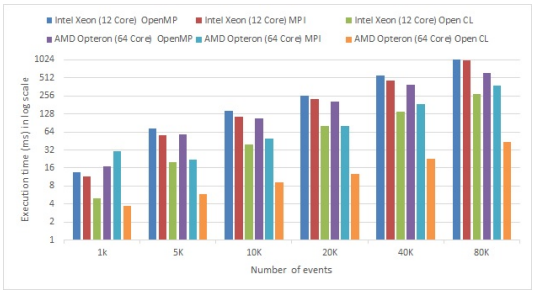

Figure 3: Time comparison between OpenMP, MPI and OpenCL on Intel and AMD CPUs

In summary, we find that OpenCL provides the most performant programming paradigm on many-core CPUs. On GPUs, it is only slightly less performant than CUDA. This performance penalty is outweighed by the big advantage to be platform-independent.

References

[1] V. Singhal *et al.*, Proc. DAE Symp. on Nucl. Phys. **57** (2012) 972

Physics Performance

Multi-strange hyperon reconstruction with the CBM experiment

I. Vassiliev[1], *I. Kisel*[1,2,3], *I. Kulakov*[1,2,3], *M. Zyzak*[1,2,3], *and the CBM Collaboration*
[1]GSI, Darmstadt, Germany; [2]FIAS, Frankfurt, Germany; [3]Goethe-Universität, Frankfurt, Germany

One of the predicted signatures of the phase transition from nuclear matter to a deconfined phase is the enhanced production of multi-strange particles. Additionally the yield of particles carrying strange quarks is expected to be sensitive to the fireball evolution. The CBM detector will provide a unique opportunity to measure yields, direct and elliptic flow, excitation functions of multi-strange hyperons with high statistics at different energies and sizes of the colliding nuclei. Multi-strange hyperons will be identified in CBM by its decay into charged hadrons, which are detected in the Silicon Tracking System (STS) and in the Time-of-Flight detector (TOF).

To study the performance of multi-strange hyperon reconstruction with the CBM experiment, several sets of $5 \cdot 10^6$ central Au+Au UrQMD events at 2, 4, 6, 10 AGeV for the SIS-100 case and at 15, 25 and 35 AGeV for the SIS-300 energy range have been simulated. High statistics allows to calculate also the $\Omega^{\pm}$ reconstruction efficiency directly, avoiding signal embedding into UrQMD events. Together with the wide range of beam energies, it allows to investigate systematic behavior of different physics observables, e.g. direct and elliptic flow, excitation function and antihyperon-to-hyperon ratios.

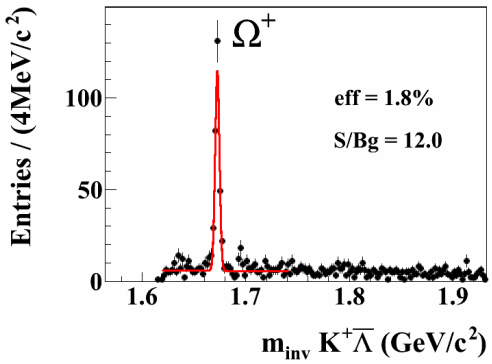

Figure 1: Reconstructed invariant mass distribution of $\bar{\Lambda}K^+$ pairs in central Au+Au collisions at 25 AGeV. The red line indicates the signal plus background fit by a polynomial plus Gaussian function.

The Ω^- decays into ΛK^- with a branching ratio of 67.8% and $c\tau$ = 2.46 cm. Decays of Λ happen most often inside the STS detector. The STS v13c geometry with 8 double-sided segmented strip detectors, cables and support frames was used for the event reconstruction. Particle identification with the realistic "umbrella" shaped TOF v13a geometry for the SIS-100 energies and v13b for the SIS-300 energies were applied. The KF Particle Finder [1] package was used to reconstruct about 50 particles and resonances including $\Omega^{\pm}$, $\Xi^{\pm}$, Λ and $\bar{\Lambda}$. Typical reconstructed invariant mass spectra of Ω^+ for SIS-300 and Ω^- for SIS-100 are shown in Fig. 1 and in Fig. 2 correspondingly. Red lines indicate fits for signal and background by a polynomial plus Gaussian function.

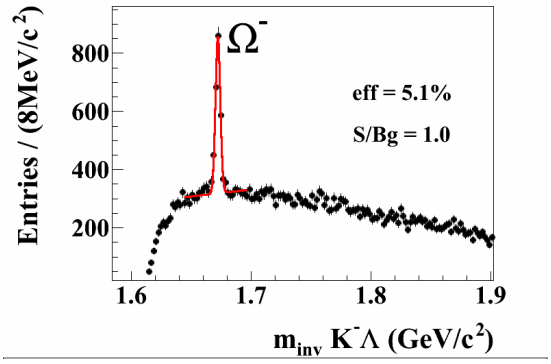

Figure 2: Reconstructed invariant mass distribution of ΛK^- pairs in central Au+Au collisions at 10 AGeV. The red line indicates the signal plus background fit by a polynomial plus Gaussian function.

The Ω^+ reconstruction efficiency results to about 1.8% for central UrQMD events. An excellent signal to background ratio of about 12 is observed due to the TOF antiproton particle identification procedure and KF Particle $\bar{\Lambda}$ reconstruction. A negative track with $\mid m^2 - m_p^2 \mid < 2\sigma$, $\mid m^2 - m_K^2 \mid > 3\sigma$ and $\mid m^2 - m_\pi^2 \mid > 3\sigma$ was used as an antiproton candidate to reconstruct $\bar{\Lambda}$. The Ω^- reconstruction efficiency is significantly higher and results to 5.1% due to less strict cuts applied for the proton identification. The reconstructed mass value 1.672 ± 0.003 GeV/c^2 is in a good agreement with the PDG's data. An invariant mass resolution of 2.3 MeV/c^2 is found. The reconstructed $\Omega^{\pm}$ candidates are accepted, if they possess good quality geometrical and topological detached vertices with $\chi^2_{geo} < 3\sigma$, $\chi^2_{topo} < 3\sigma$ and z-vertex farther than 10 σ downstream of the target plane.

References

[1] I. Kisel, I. Kulakov and M. Zyzak, *Standalone First Level Event Selection Package for the CBM Experiment*, IEEE Trans. Nucl. Sci. **60** (2013) 3703

Reaction plane reconstruction in the CBM experiment

S. Seddiki[1] *and M. Golubeva*[2]
[1]GSI, Darmstadt, Germany; [2]INR RAS, Troitsk, Russia

The determination of the reaction plane in nucleus-nucleus collisions is crucial for several measurements, including anisotropic collective flow. In CBM, the reaction plane can be measured by the forward hadronic calorimeter, referred to as the Projectile Spectator Detector (PSD). The Silicon Tracking System (STS) of the experiment, designed to cover a large fraction of the particle phase space, can also provide a complementary measurement. In this work, we investigated the capabilities of these two detectors for reconstructing the reaction plane at FAIR energies.

The simulations were carried for Au+Au collisions in the CBMROOT framework, using the event generator SHIELD, the simulation package GEANT4 and the physics list FTFP BERT. The detector model includes a 250 μm thick Au target, a STS consisting of 8 stations (located between 30 cm and 1 m from the target) embedded inside a dipole magnet and a PSD constituted transversally of 45 modules of 20 $\times$ 20 cm^2. Each module is composed longitudinally of 60 layers with combined Lead absorber and scintillator material. The central one features a cylindrical beam hole (to let beam ions pass) with a diameter of 6 cm.

The azimuthal orientation of the reaction plane has been determined using the event plane method [1]. The flow of emitted particles (used in the method) is exploited directly by measuring the momentum of charged particles in the STS, while the flow of projectile spectators is reflected in the azimuthal distribution of the energy measured in PSD modules. In this study, Monte Carlo tracks with at least 4 hits in STS stations have been used. As the elliptic flow of charged particles is relatively weak at FAIR energies, the results are given using the directed flow of emitted particles (a selection of forward rapidity particles measured by the STS is performed). The reaction plane resolution is defined as the Gaussian width ($\sigma(\Psi_1-\Psi_{MC})$) of the distribution of the measured 1$^{\rm st}$ harmonic event plane angle (Ψ_1) around the true reaction plane angle ($\Psi_{\rm MC}$).

At SIS100 energies, the PSD reaction plane resolution is optimal ($\sigma(\Psi_1 - \Psi_{MC}) \leq 40^\circ$ for collision impact parameters below 11 fm) when the detector is located at 8 m from the target (see Fig. 1), accordingly at 15 m at SIS-300 due to higher Lorentz boosts of spectators.

The integrated magnetic dipole field is of about 1 Tm in the target region at $E_{\rm beam} \geq 10A$ GeV, while it is scaled down with beam momentum at lower energies to reduce the induced bias in the PSD event plane calculation. However, a minimal field is required (of about 0.6 Tm) to keep the tracking performance on an acceptable level. A significant degradation of the PSD resolution was only seen for $E_{\rm beam} < 4A$ GeV e.g. at $E_{\rm beam}$ = 2A GeV, $\sigma(\Psi_1 - \Psi_{MC})$ increases from 39° to 51° while enhancing the field from 0.26 Tm to 0.63 Tm.

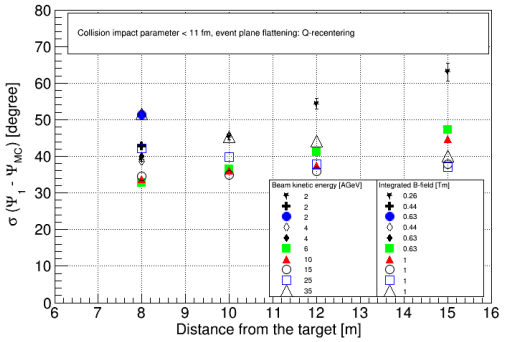

Figure 1: PSD reaction plane resolution (1$^{\rm st}$ harmonic event plane) at several distances from the target in Au+Au collisions (impact parameters below 11 fm) at FAIR energies. The Gaussian fits were performed in the range [-80, 80] degrees. The effect of the magnetic dipole field is also shown for $E_{\rm beam} \leq 4$ AGeV and a PSD distance of 8 m.

The resolutions obtained with the PSD and the STS can be compared in Fig. 2. At FAIR energies, both detectors provide good and complementary performance: $\sigma(\Psi_1 - \Psi_{MC})$ between 30° and 40°.

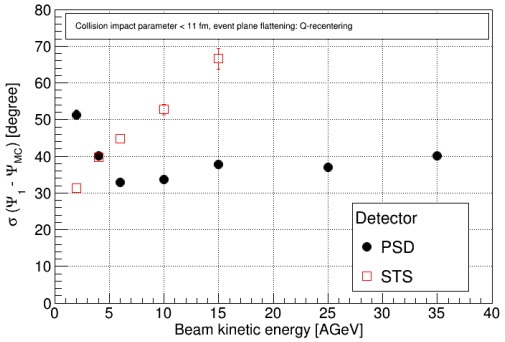

Figure 2: Reaction plane resolution (1$^{\rm st}$ harmonic event plane) as a function of beam energy. The PSD is located at 8 (15) m from the target at SIS-100 (SIS-300) energies. The integrated magnetic dipole field is of 0.63 Tm at $E_{\rm beam}$ = 2A, 4A and 6A GeV and 1 Tm at higher energies.

References

[1] A. M. Poskanzer *et al.*, Phys. Rev. **C 58** (1998) 1671

TOF PID at SIS-100

S. M. Kiselev
ITEP, Moscow, Russia

10^5 Au+Au UrQMD minimum bias and central events at $4A$ GeV and $10A$ GeV, simulated and reconstructed with `cbmroot` have been used for analysis. The set-up consists of STS, RICH and TOF at 6 m from the target (geometry versions stsv13c, richv08a and tofv13a). The TOF resolution σ_{TOF}=80 ps was taken in the TOF hit producer. For global track matching with TOF hits the "nearest hit" mode was selected. For TOF PID the $\sigma_\pi(p)$, $\sigma_K(p)$ and $\sigma_p(p)$ functions of momentum p evaluated by I.Vassiliev from the global track distribution on the plane (p, m^2) have been used. The PID region for (anti-)protons is defined as $m^2 > m_p^2 - 2\sigma_p(p)$. The PID region for kaons is restricted by the lines: $m_K^2 - 2\sigma_K(p)$, $m_K^2 + 2\sigma_K(p)$, $m_p^2 - 2\sigma_p(p)$ and $m_\pi^2 + 2\sigma_\pi(p)$. The rest region of the plane (p, m^2) is the PID region for pions. Figure 1 shows the 2σ boundaries used for the PID regions.

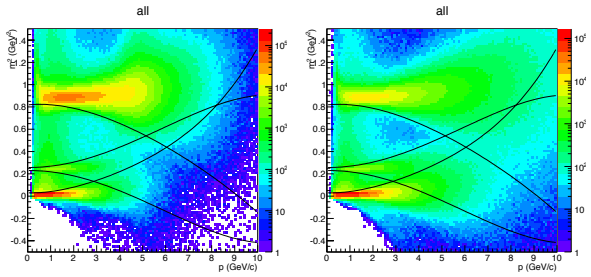

Figure 1: Global track distribution for minimum bias Au+Au events at $4A$ GeV (left) and $10A$ GeV (right) with the 2σ boundaries to define the PID regions

PID efficiency is defined as the ratio of the correctly defined tracks to all tracks, PID contamination is the ratio of the wrongly defined tracks to all identified tracks. Tables 1- 4 summarize the results of the analysis: the number of primaries, global track efficiency, defined as the ratio of global tracks to the primaries, the part of global tracks without TOF hit, PID efficiency, PID contamination and total efficiency defined as a product of global and PID efficiencies. Because of their very low multiplicity at $4A$ GeV, anti-proton are misseing in the tables. Plots for PID efficiencies and contaminations in the plane (y, p_{t}) and more analysis details can be found in [1].

Table 1: Au+Au@4 AGeV, 10^5 minimum bias events

part.	# of prim.	global eff.	wo TOF	PID eff.	PID cont.	total eff.
p	162	0.19	0.06	0.95	0.005	0.18
K^+	1.4	0.38	0.22	0.75	0.29	0.29
K^-	0.09	0.38	0.25	0.74	0.54	0.28
π^+	15	0.36	0.18	0.97	0.21	0.35
π^-	20	0.36	0.18	0.99	0.001	0.35

Table 2: Au+Au@4 AGeV, 10^5 central events

part.	# of prim.	global eff.	wo TOF	PID eff.	PID cont.	total eff.
p	172	0.61	0.07	0.94	0.007	0.57
K^+	8.0	0.40	0.26	0.72	0.23	0.29
K^-	0.6	0.38	0.24	0.73	0.49	0.28
π^+	68	0.37	0.19	0.97	0.21	0.36
π^-	68	0.36	0.19	0.98	0.002	0.36

Table 3: Au+Au@10 AGeV, 10^5 minimum bias events

part.	# of prim.	global eff.	wo TOF	PID eff.	PID cont.	total eff.
p	162	0.16	0.06	0.94	0.02	0.15
$\overline{p}$	3e-3	0.77	-	0.96	0.99	0.74
K^+	4.2	0.50	0.19	0.67	0.16	0.33
K^-	0.8	0.51	0.18	0.69	0.36	0.35
π^+	36	0.47	0.15	0.97	0.10	0.46
π^-	43	0.48	0.15	0.98	0.006	0.47

Table 4: Au+Au@10 AGeV, 10^5 central events

part.	# of prim.	global eff.	wo TOF	PID eff.	PID cont.	total eff.
p	167	0.66	0.06	0.93	0.02	0.61
$\overline{p}$	1e-2	0.65	0.08	0.94	0.99	0.61
K^+	22	0.53	0.23	0.64	0.17	0.34
K^-	4	0.52	0.21	0.65	0.36	0.34
π^+	165	0.50	0.16	0.97	0.11	0.48
π^-	191	0.50	0.16	0.98	0.008	0.48

References

[1] S. M. Kiselev, *TOF PID at SIS100*, 22nd CBM collaboration meeting, September 2013, Dubna

Reference time estimation with BFTC at SIS-100

S. M. Kiselev
ITEP, Moscow, Russia

10^4 Au+Au SHIELD minimum bias events at $4A$ GeV and $10A$ GeV have been used. The set-up consists of STS, RICH and TOF at 6 m from the target. For simulation and reconstruction the geometry versions v13c, v08a and v13a have been used for STS, RICH and TOF, respectively. The magnetic field was scaled with the factor 0.4 and 1.0 for the beam energy $4A$ GeV and $10A$ GeV, respectively. A TOF resolution of $\sigma_{\rm TOF} = 80$ ps has been used in the TOF hit producer. The central part of the TOF of the size $1.2 \times 1.2\,{\rm m}^2$ with a beam hole $0.2 \times 0.2\,{\rm m}^2$, named Beam Fragment T_0 Counter (BFTC), has been used for $t_{\rm event}$ estimation.

For every TOF hit the value t_0 is defined by $t_0 = L_{\rm TOF}/v_{\rm beam} - t_{\rm TOF}$, where $L_{\rm TOF}$ is a distance between the interaction point and the TOF hit, $v_{\rm beam}$ is the beam velocity and $t_{\rm TOF}$ is the TOF hit time. Figure 1 demonstrates the distribution of the TOF hits on t_0. The maximum of the distribution is close to zero, but there is a long tail in the range with negative t_0.

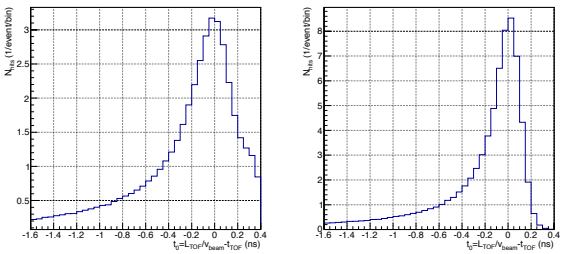

Figure 1: Distribution of the TOF hits on t_0 for $4A$ GeV (left) and $10A$ GeV (right)

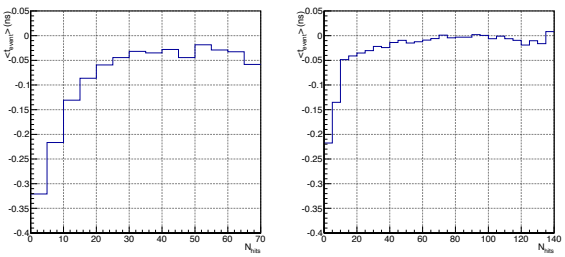

Figure 2: $\langle t_{event} \rangle$ as a function of the number of hits for $4A$ GeV (left) and $10A$ GeV (right)

For a given event, $t_{\rm event}$ is defined as average of t_0 in the range $t_0^{\rm max} \pm 2\sigma_{\rm TOF}$, where $t_0^{\rm max}$ is the maximum value of the t_0 for the event distribution of the TOF hits on t_0. The mean value, $\langle t_{\rm event} \rangle$, and RMS as a function of the number of hits in the range, $N_{\rm hits}$, are shown in Figs. 2 and 3, respectively.

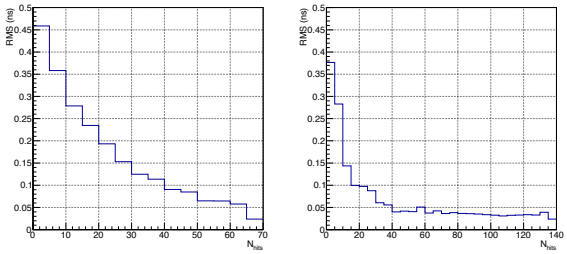

Figure 3: RMS as a function of the number of hits for $4A$ GeV (left) and $10A$ GeV (right)

Events with larger $N_{\rm hits}$ have closer to zero $\langle t_{\rm event} \rangle$ values and smaller RMS. Distributions of events in the plane $N_{\rm hits}$ and impact parameter b are presented in Fig. 4. While for the beam energy $10A$ GeV, $N_{\rm hits}$ increases with centrality, for $4A$ GeV it decreases with centrality in the range $0 < b < 8$ fm. In central collisions particles do not reach the BFTC region because of the magnetic field. For $10A$ GeV $t_{\rm event}$ can be estimated with an accuracy of $\approx$50 ps for events with $N_{\rm hits} > 40$, corresponding to impact parameters $b < 8$ fm. For $4A$ GeV the accuracy is twice larger ($\approx$100 ps), for events with $N_{\rm hits} > 40$ and $4\,{\rm fm} < b < 10\,{\rm fm}$.

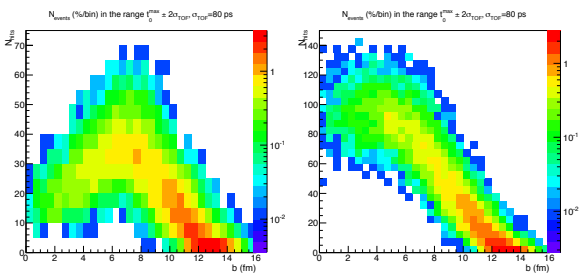

Figure 4: Distribution of events in the plane $N_{\rm hits}$ vs. impact parameter b for $4A$ GeV (left) and $10A$ GeV (right)

For peripheral events ($b > 10$ fm), most part of fast particles with $v = v_{\rm beam}$ are in the beam hole, $\langle t_{\rm event} \rangle$ deviates from zero significantly, $|\langle t_{\rm event} \rangle| > 100$ ps, RMS increases. More analysis details can be found in [1].

References

[1] S.M. Kiselev, "t_{event} *estimation with BFTC only at SIS100*", CBM-TOF weekly meeting 16.10.2013

$D^0 \to K^-\pi^+$ decay vertex reconstruction with a 4 MAPS MVD detector

G. Kozlov[1] *and I. Vassiliev*[2]
[1]LIT JINR, Dubna, Russia; [2]GSI, Darmstadt, Germany

One of the major experimental challenges of the CBM experiment is to trigger on the displaced vertex of the D-meson or Λ_c decay via hadronic modes in the environment of a heavy ion collision. This task requires a fast and efficient cluster finding and track reconstruction algorithm as well as a high resolution secondary vertex determination. Particular difficulties to identify the displaced vertex of the rare open charm decays are caused by weak K^0_S and hyperon decays which produce displaced vertices downstream the target. The very low multiplicity of the open charm production including small branching ratios and the multiple scattering inside the beam pipe and detectors challenge the identification significantly.

In this work we study the impact of δ-electrons produced by Au-ions with beam intensities up to 10^9 ions/s and a clustering algorithm on the quality of $D^0 \to K^-\pi^+$ vertex reconstruction. The geometry `v10a` of the Micro Vertex Detector (MVD) consisted of four Monolithic Active Pixel Sensors (MAPS). To study the feasibility of D^0 decays reconstruction a set of 10^4 central Au+Au UrQMD events at 25A GeV was simulated in the CBM experiment. The D^0 decay to $K^-\pi^+$ was forced and added to each event in order to simulate a signal in the environment of background hits. A realistic STS geometry with 8 double-sided (thickness 400 μm) segmented silicon strip detectors was used. Assuming 30 μs read-out time of the MAPS detectors, δ-electrons produced by Au-ions of the incident beam (up to 300 at 10^9 ions/s) were added to each central event in order to simulate additional background tracks in the MAPS detectors. The primary vertex was reconstructed with high accuracy of 5 μm in z direction, about 1 μm in x and y.

The shape of the D^0 invariant mass distributions remains almost unchanged up to the highest beam intensities. Moreover, it is almost not sensitive to the MAPS clustering algorithm. Taking a significant time for charge clustering into account, the clustering algorithm without charges has been chosen. On the other hand the vertex-z resolution value is more sensitive to the quality of the D^0 daughters track reconstruction. In Fig. 1 the vertex-z resolution with σ = (45.7 $\pm$ 1.2) μm is shown obtained for D^0 decay embedded to the UrQMD events without δ-electrons.

Using a 4 MAPS MVD detector allows to reconstruct δ-electron tracks containing at least 3 hits. It was observed that the event reconstruction time increases with increasing beam intensities. Pure UrQMD events are reconstructed within 80 ms/event/core which increases to 762 ms/event/core including δ-electrons at 5 $\times$ 10^8 Au-ions/s beam intensity. Up to the highest beam intensities the observed effect on the D^0 decay reconstruction efficiency is rather small; a reduction (from 20.5 % to 20.2 %) was observed at marginal increasing vertex-z resolution of σ = (46.9 $\pm$ 1.1) μm (see Fig. 2).

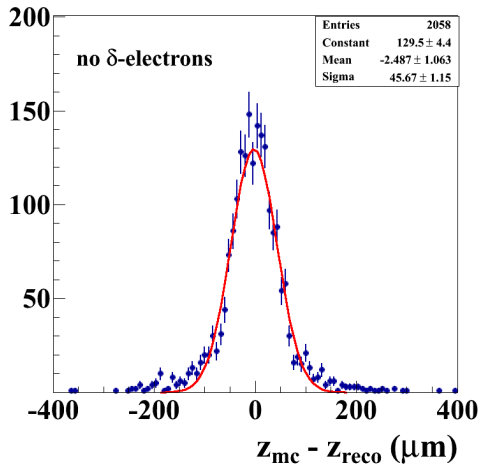

Figure 1: Vertex-z resolution for the $D^0 \to K^-\pi^+$ embedded to the UrQMD events. No δ electrons added.

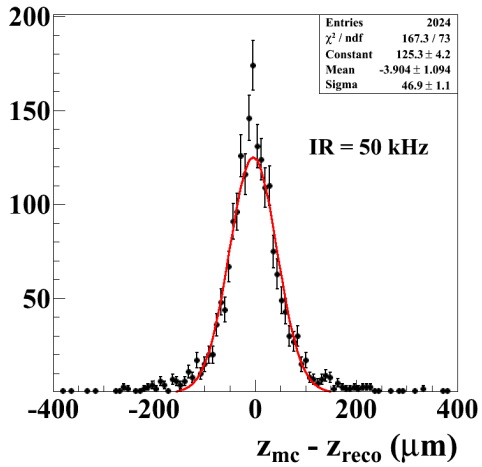

Figure 2: Vertex-z resolution for the $D^0 \to K^-\pi^+$ embedded to the UrQMD events, with δ electron tracks produced by 150 Au ions in the 1 % Au target added.

Employing the CBM MVD for background rejection in di-lepton analyses

E. Krebs[1], *T. Galatyuk*[2], *J. Markert*[1], *and J. Stroth* [1,3]

[1]Goethe-Universität, Frankfurt, Germany; [2]Technische Universität Darmstadt, Germany; [3]GSI Darmstadt, Germany

Low mass electron (muon) pairs are considered to be excellent probes of the processes taking place in the interior of extreme states of matter formed in the collision zone of heavy-ions. However, the reconstructed distribution of electron pairs contains in addition contributions from mesons decaying after freeze-out and from combinatorial pairs. Single electron or positron tracks from incompletely detected γ-conversions and Dalitz decays of π^0-mesons are the most abundant source contributing to the significant combinatorial background. The excellent position resolution of the Micro-Vertex Detector (MVD) of the CBM experiment and its proximity to the target offers a chance to reject efficiently the close pairs. This holds in particular for the abundant case, in which the magnetic field of CBM bends the low momentum partner out of the CBM acceptance while the high momentum partner contributes to the combinatorial background of the invariant mass spectrum. We tried to improve the reconstruction of the low momentum partner by including points from the MVD into the track reconstruction and to reject the pair based on the reconstructed opening angle.

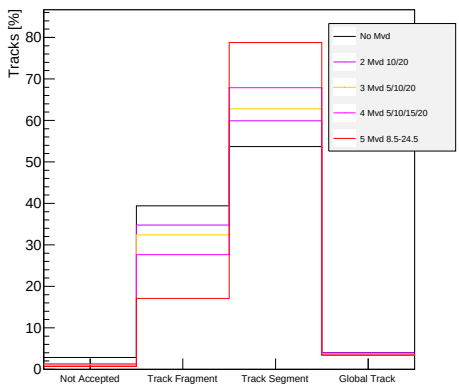

Figure 1: Track topology of dielectrons from π^0-Dalitz decays assuming different configurations of the MVD, i. e. no MVD or a MVD featuring different amount of sensor planes (see text)

Emission from a thermal source was assumed to simulate electron pairs from meson decays for Au+Au reactions at SIS-100 and SIS-300 energies. The simulation parameters were chosen such that the meson spectra are consistent with p_T and rapidity distributions measured by NA49 [1]. The pairs simulated with the Pluto event generator [2] are embedded into hadronic final states calculated with UrQMD. Two versions of the hadronic cocktail were used: one cocktail simulates vector meson decay in vacuum, the second one assumes an in-medium modification of the ρ_0.

Figure 1 shows the track type of the low momentum partner of an e^+/e^--pair from a π^0-Dalitz decay, where the high momentum partner was reconstructed and identified in the RICH. We distinguish track fragments (only individual hits are seen), track segments (also charge and momentum were reconstructed) and global tracks (also particle ID was included). The number of reconstructed track segments was found to increases substantially with the amount of MVD stations. This comes with draw backs in terms of increasing computing time. In Figure 2, the opening angle between an identified electron and its nearest track segment is correlated to the product of the momenta of these two tracks. A wedge cut can be applied to reduce the background [3, 4]. The additional number of reconstructed low-momentum electrons increases the number of background pairs, which is rejected by this cut. This suggests that the MVD might help to reduce the related background and that this capability is getting more pronounced with an increasing number of MVD-stations.

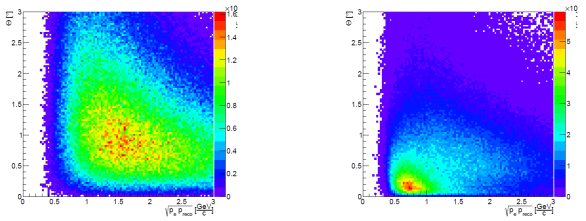

(a) ρ^0 (b) π^0-Dalitz

Figure 2: Opening angle vs. momentum of an identified electron and its nearest reconstructed track for pairs from (a) ρ^0 decays and (b) π^0-Dalitz decays

Further studies are needed to conclude on the optimal number and positions of MVD stations and the optimal magnetic field configuration. The impact of the numerous δ-electrons emitted from the target remains to be taken into account. Finally, the rejection strategy for γ-conversions occurring in the additional MVD stations has to be optimized.

References

[1] C. Alt *et al.* (NA49 Collaboration), Phys. Rev. C **78** (2008) 044907

[2] I. Froehlich *et al.*, arXiv:0708.2382

[3] T. Galatyuk, Ph. D. thesis, Goethe-Universität, Frankfurt am Main 2009

[4] E. Lebedeva and C. Höhne, CBM Prog. Report 2012, p. 106

Study of the influence of different pion suppression factors on low-mass vector meson reconstruction in the CBM experiment

E. Lebedeva and C. Höhne
Justus Liebig-Universität, Gießen, Germany

A considerable contribution to the combinatorial background to the invariant mass spectra of di-electrons can come from pions, which are misidentified as electrons. A study of the influence of different pion suppression factors on the low mass vector meson reconstruction for central Au-Au collisions at 8A GeV and 25A GeV beam energies is presented in this report.

Details on the simulation setups and current status of low mass vector meson reconstruction, also the background rejection strategy can be found in [1]: for the study presented here the detector setup includes STS, RICH, TRD and TOF detectors, however for 8A GeV beam energy the TRD detector was excluded from simulations.

In this report the pion suppression factor is defined as the number of pions which were reconstructed in STS and have track projection in RICH divided by the number of pions identified as electrons.

For 25A GeV beam energy around 395 pions are reconstructed per event, 60 of them are reconstructed only in the STS detector. For 8A GeV beam energy these numbers are less, and equal to 180 and 45, respectively.

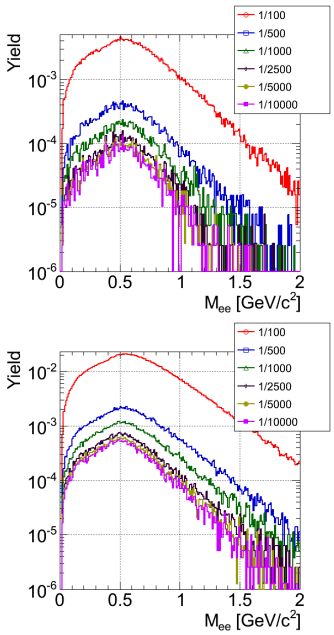

Figure 1: Combinatorial background assuming different pion suppression factors after applying all cuts for central Au+Au collisions at 8A GeV (100k events, top panel) and 25A GeV (200k events, bottom panel) beam energy

For our study all $\pi^{\pm}$ which were reconstructed in STS and have track projection in RICH were added to the electron candidate sample. Then the electron identification was performed using Monte-Carlo information and assuming a certain pion suppression factor: 100, 500, 1000, 2500, 5000, 10000 and ideal case.

The combinatorial background after applying all background rejection cuts for different pion suppression factors for 8A GeV (above) and 25A GeV (below) beam energy is shown in Figure 1. Table 1 represents the signal-to-background ratios of ω and ϕ mesons, the total contribution of physical background ($e^{\pm}$ pairs combining γ-conversion electrons or electrons from π^0-Dalitz decays) in percent to the number of pairs in the combinatorial background and the contribution of misidentified $\pi^{\pm}$ in percent to the electron sample after applying all cuts.

Table 1: Signal-to-background ratios, the contribution of physical background (PB) in percent to the total number of pairs in combinatorial background and the contribution of misidentified $\pi^{\pm}$ in percent to the electron sample after applying all cuts

π supp.	100	500	1000	2500	5000	10^4	ideal
8A GeV							
ω: S/B	0.012	0.14	0.27	0.47	0.67	0.83	0.89
ϕ: S/B	0.001	0.015	0.03	0.05	0.07	0.12	0.14
PB [%]	1.8	18.4	34.7	55.6	69.8	79.5	86.9
$\pi^{\pm}$ [%]	83.5	53.4	36.4	19.3	10.6	5.7	0.0
25A GeV							
ω: S/B	0.005	0.05	0.10	0.19	0.24	0.26	0.30
ϕ: S/B	0.002	0.02	0.04	0.07	0.10	0.12	0.14
PB [%]	1.8	18.7	35.9	57.1	69.1	76.9	86.0
$\pi^{\pm}$ [%]	83.9	52.7	36.0	18.5	10.4	5.2	0.0

As one can see starting from a pion suppression factor of 2500 the combinatorial background is rather similar in comparison to 5000 and 10000. At this factor the contribution of misidentified pions to the combinatorial background is not significant and the physical background is dominating. We conclude that a factor 5000 or higher in pion suppression is required to reasonably access the low mass vector mesons for 8 AGeV and 25 AGeV beam energy.

References

[1] E. Lebedeva and C. Höhne, CBM Progress Report 2012, p. 106

Di-muon measurements with CBM at SIS-100

A. Senger
GSI, Darmstadt, Germany

The CBM muon detection system is designed to measure muon pairs from the decay of vector mesons ($\rho, \omega, \phi, J/\psi$) produced in heavy-ion collisions. At FAIR energies the muon momenta can be rather low, therefore, we developed a muon detection concept with a variable definition of absorber thickness according to the muon momentum. The full design of the muon detector system consists of 6 hadron absorber layers (carbon block of thickness 60 cm with lead shielding around the beam pipe and iron plates of thickness 20, 20, 30, 35, 100 cm). The 18 gaseous tracking chambers are located in triplets behind each hadron absorber. The start version of the muon system consists of 4 hadron absorbers and 4 tracking stations. It will be used for measurements of low mass vector mesons at SIS-100 energies. In the following we present results of simulations for central Au+Au collisions at a beam energy of 8A GeV. It turned out that additional information from the time-of-flight system helps to further suppress protons and kaons. This is illustrated in Fig. 1 which depicts the mass squared of the particles seen by the muon detector as reconstructed from their time-of-flight as function of momentum measured in the Silicon Tracking System. Muons from ω meson decays and background particles are shown in the left and in the right panel, respectively.

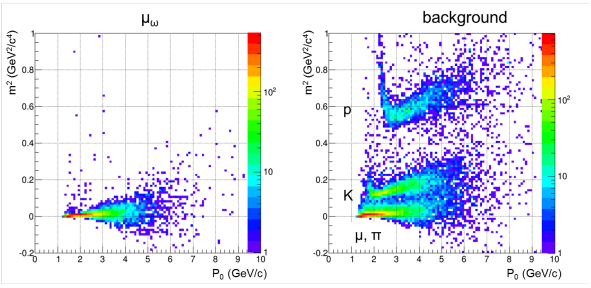

Figure 1: Mass squared of particles in the muon detector as reconstructed by their time-of-flight as function of momentum measured in the Silicon Tracking System. Left panel: muons from ω decays. Right panel: background particles.

The final invariant mass distributions of the remaining background and of low-mass vector mesons are shown in the left panel of Fig. 2, whereas the resulting signal-to-background ratio is shown in the right panel. The reconstruction efficiencies for mesons are 0.75 % for ρ, 0.78 % for ω, and 1.1 % for ϕ.

The measurement of J/ψ mesons at 10A GeV will be an exciting experiment at SIS-100 because it will provide information on the process of charm production at energies close to the threshold, in this case even below threshold. According to the HSD transport code [1], in central Au+Au collisions at 10A GeV the di-lepton yield per event is 1.04×10^{-8} for J/ψ mesons. We performed J/ψ simulations of central Au+Au collisions at 10A GeV using a full muon system. The invariant mass distribution of background and signal is shown in Fig. 3. The signal-to-background ratio is 0.13, and the J/ψ reconstruction efficiency is 0.2 %.

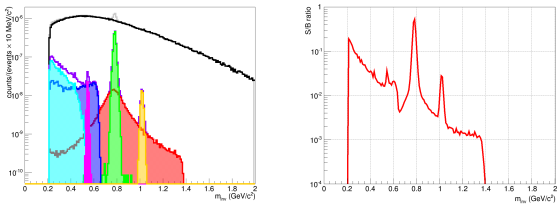

Figure 2: Left panel: Invariant mass spectrum of low mass vector mesons for 8A GeV central Au+Au collisions. Black line - combinatorial background, red - ρ, green - ω, yellow - ϕ, magenta - η, blue - ω Dalitz, light blue - η Dalitz. Right panel: Signal-to-background ratio.

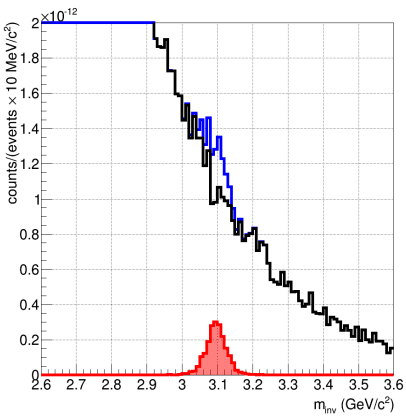

Figure 3: Reconstructed invariant mass distribution of muon pairs for central Au+Au collisions at 10A GeV. Red histogram: J/ψ meson, black histigram: combinatorial background, blue histogram: background + J/ψ meson.

References

[1] O. Linnyk *et al.*, Nucl. Phys. **A 786** (2007) 18

Identification of dimuons from low-mass vector mesons with CBM at SIS-300

S. Ahmad[1], *S. Chattopadhyay*[2], *and M. Farooq*[1]
[1]University of Kashmir, Srinagar, India; [2]Variable Energy Cyclotron Center, Kolkata, India

The Muon Chamber (MUCH) system of the CBM experiment is based on segmented hadron absorbers with detector chambers placed in between absorbers to facilitate momentum-dependent track identification, in particular for soft muons from the decay of low-mass vector mesons. The MUCH system at SIS-300 comprises six absorbers, the first one of 60 cm of carbon, the others of iron (20 cm + 20 cm + 30 cm + 35 cm + 100 cm), with a total thickness of $13.5\lambda_{\mathrm{I}}$. Between the absorber segments, six tracking stations with three detector chambers each are located.

The absorber properties like material, thickness, and position were optimized in simulations of heavy-ion collision events generated by the UrQMD event generator, and transported through the setup with the GEANT3 code. The same tools were used to study the performance of the detector in the dimuon low invariant mass region. The multiplicities of the ω, η, ρ, and ϕ mesons are taken from the HSD event generator, and their branching ratios from the PDG. Their phase-space distributions were calculated with the PLUTO event generator for 25A GeV Au+Au collisions. The combinatorial background was calculated from UrQMD events using the mixed-event technique to increase the statistics. The signal muon pairs were embedded into UrQMD events and then reconstructed. In order to reduce the background, conditions on the quality of the number of hits in STS and MUCH, on the quality of the primary vertex, and on the quality of the tracks in the MUCH were imposed in the analysis (STS hits $\geq$ 6, MUCH hits $\geq$ 14, $\chi^2_{\mathrm{vertex}} \leq 2.0$, $\chi^2_{much} \leq 1.5$). In Fig. 1, the invariant mass distribution of the reconstructed muon pairs from low-mass vector mesons is shown together with the combinatorial background.

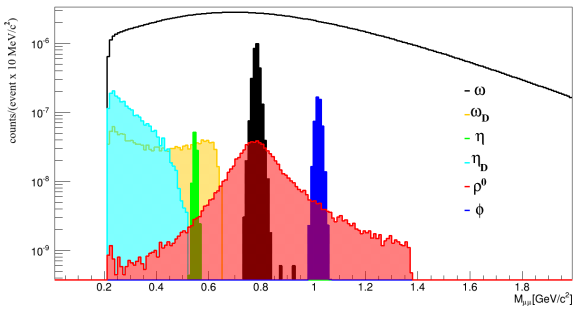

Figure 1: Invariant mass distributions of reconstructed muon pairs from decaying low-mass vector mesons together with the combinatorial background simulated for central Au+Au collisions at 25A GeV

Figure 2 depicts the signal-to-background ratio (S/B) as extracted from Fig. 1. It was found that S/B can be improved by a time-of-flight (TOF) measurement using the standard CBM TOF-RPC wall downstream the MUCH. The TOF measurement helps in the reduction of the background with minimal signal losses. The efficiency for the identification of ω, ρ, and ϕ mesons with the STS+MUCH detectors including the overall geometrical acceptance is of the order of 1 %.

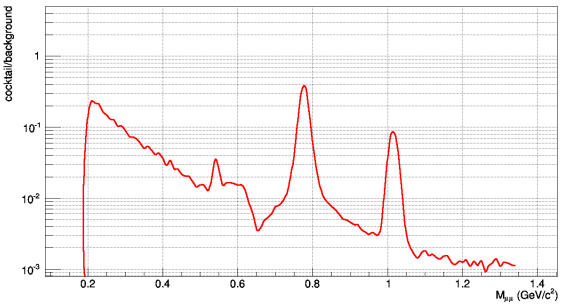

Figure 2: Signal to background ratio of the low mass dimuon invariant mass spectra for central Au+Au collisions at 25A GeV

Figure 3 shows the phase-space coverage of ω mesons detected in MUCH superimposed over the input from PLUTO (4π). It can be seen that detector only covers the region from mid-rapidity towards forward rapidity because of the absorption of soft muons in the hadron absorbers of the detector.

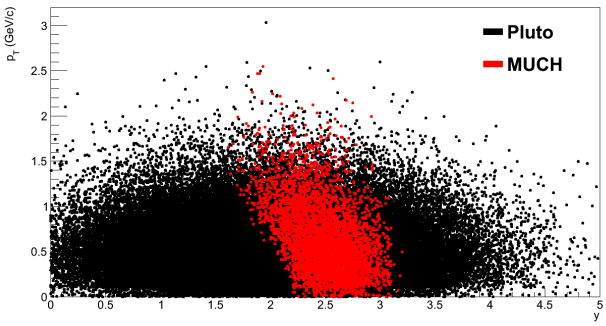

Figure 3: Acceptance of ω mesons of the MUCH (red) in comparison to the input from PLUTO (black) for central Au+Au collisions at 25A GeV

Efficiency of the CBM Muon Chamber system for low-mass vector mesons

S. Ahmad[1], *S. Chattopadhyay*[2], *and M. Farooq*[1]
[1]University of Kashmir, Srinagar, India; [2]Variable Energy Cyclotron Center, Kolkata, India

The Muon Chamber (MUCH) system of the CBM Experiment at SIS300 will comprise 6 hadronic absorbers and 6 tracking stations with three detector chambers per station located in the gaps between the absorber segments. The MUCH will be placed at a distance of 120 cm downstream the target just behind the Silicon Tracking System (STS). The STS consists of 8 low-mass layers of silicon microstrip sensors located at distances between 30 cm and 100 cm downstream of the target inside the magnetic dipole. Primary track finding and reconstruction in the STS is performed by a cellular automaton method. The reconstructed tracks then are propagated through the MUCH detector using a Kalman filter.

In this work, we study the efficiency of the MUCH for dimuons from low-mass vector meson decays. We will correct for the efficiency of the STS in order to extract the pure MUCH performance. We simulate heavy ion collision events as given by the UrQMD event generator, and propagate the particles through the detectors using the GEANT3 transport code. For the low-mass vector meson cocktail we use as input multiplicities taken from HSD, branching ratios from the Particle Data Group(PDG) database, and spectral shapes as generated by PLUTO for 25A GeV central Au+Au collisions.

Table 1: Reconstructed signal particle efficiencies of STS+MUCH, STS and MUCH (= (STS+MUCH)/STS) for central Au+Au collisions at 25A GeV

Particle	ϵ(STS+MUCH)%	ϵ(STS)%	ϵ(MUCH)%
ω	0.83	17.1	4.9
ω_{Dalitz}	0.29	16.5	1.8
η	0.46	17.3	2.7
η_{Dalitz}	0.22	16.4	1.3
ρ	0.81	16.9	4.8
ϕ	1.47	17.0	8.7

Invariant mass spectra have been calculated from the reconstructed signal muons after embedding them event by event into the UrQMD events. To separate the detector efficiencies, the tracks have been reconstructed for the STS, and for the combination of STS+MUCH. The results for the different cocktail sources are shown in Table 1. The detection efficiency of the STS includes the overall geometrical acceptance. The efficiencies have been determined using optimized conditions for the number of hits in STS and MUCH, for the quality of the primary vertex, and for the track quality in the MUCH (STS hits $\geq$ 6, MUCH hits $\geq$ 14, χ^2 vertex $\leq$ 2.0, χ^2 MUCH $\leq$ 1.5).

The efficiency for low-mass vector mesons in the STS is only of the order of 17 % for low mass vector mesons in the conditions discussed above are applied. These conditions are required to enhance the signal-to-background ratio for dimuons. If we correct for the STS efficiency, the efficiency for dimuon decays of ω, ρ, and ϕ is of the order of 5 % in 25A GeV central Au+Au collisions. The signal-to-background ratio has been found to be very good in comparison to existing or planned muons detection systems in high energy heavy-ion collision experiments (see the contribution of S. Ahmad in this report). In Fig. 1 the phase-space coverage is shown for ω mesons (upper panel) and ρ mesons (lower panel) detected in the STS (blue) and in STS+MUCH (red) superimposed over the input from PLUTO (4π). Because of the absorption of soft muons in the hadron absorbers the MUCH only covers the region from mid-rapidity towards forward rapidity.

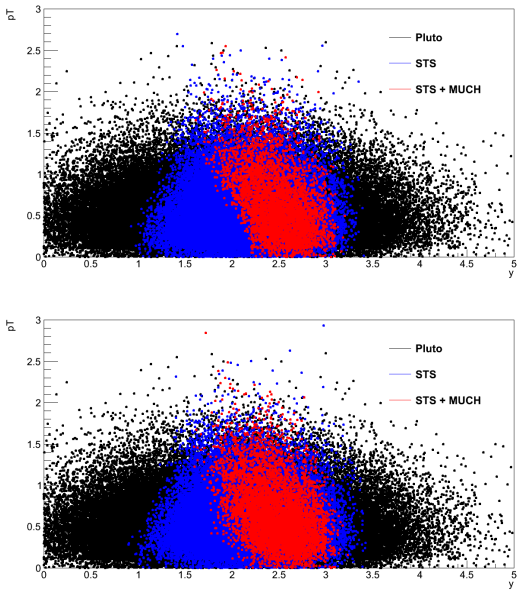

Figure 1: Acceptance for ω mesons (upper panel) and ρ^0 mesons (lower panel) of the STS (blue) and STS+MUCH (red) in comparison to the input from PLUTO (black) for 25A GeV central Au+Au collisions

Sensitivity of the CBM-MUCH to mass modifications of ρ mesons

S. Sarkar[1]*, A. Mukhopadhyay*[1]*, and S. Chattopadhyay*[2]
[1]Department of Physics, University of North Bengal, Siliguri, India; [2]Variable Energy Cyclotron Centre, Kolkata, India

With the MUCH detector system we aim to study the in-medium modification of low-mass vector mesons. NA60 [1] has not reported any shift of the ρ^0 pole mass while the widths of the invariant mass spectra have been found to get broadened. In our present analysis the sensitivity has been studied on the modification of the width of the ρ^0 invariant mass distribution measured with the MUCH detector.

The present work is performed within the CBM simulation framework with full event reconstruction. We have used (a) the PLUTO generator [2] for phase space decay of the vector mesons taking multiplicities from HSD [3], (b) the UrQMD generator [4] for the background particles and (c) the GEANT3 [5] for transport of the generated particles through the experimental setup. The CBM detector setup for di-muon identification consists of the Silicon Tracking System (STS) followed by a muon detection system (MUCH). In this simulation the MUCH *standard* setup consisting of 6 absorbers and 16 layers has been used.

The inputs used for this analysis are as follows: (i) 5K PLUTO generated ρ^0 mesons with thermal distribution in transverse momentum and Gaussian distribution in rapidity have been used as signal, and (ii) 5K UrQMD Au+Au events at 35A GeV compose the hadronic background. Cuts optimized on the low mass region have been applied for muon detection.

The invariant mass spectrum of the reconstructed ρ^0 mesons in presence of hadronic background for one set of our simulated data is shown in Fig. 1. An appropriate normalization (scale) factor has been used into the distributions arising out of the multiplicity distributions and branching ratios. The correspondence has been made between the RMS widths of the reconstructed ρ^0 invariant mass spectra with the input widths which were varied from 0.059 GeV/c^2 to 0.096 GeV/c^2 keeping the centroid of the distribution unchanged. We have calculated the ratio of the widths of the output distribution (Γ_{out}) to that of the input distribution (Γ_{in}) which is depicted in Fig. 2. The error bars contain solely statistical errors. It should be noted that, in this simulation, the background subtraction is assumed to be ideal as no effort has been made to perform the analysis obtained after background subtraction of embedded events. Given this limitation, the preliminary results show that the nearly constant ratio has been found to be above unity. The constancy of the values suggests that the MUCH detector system is sensitive to the variation of width of the ρ^0 invariant mass distribution. A detailed analysis with background subtraction procedure in place is in progress.

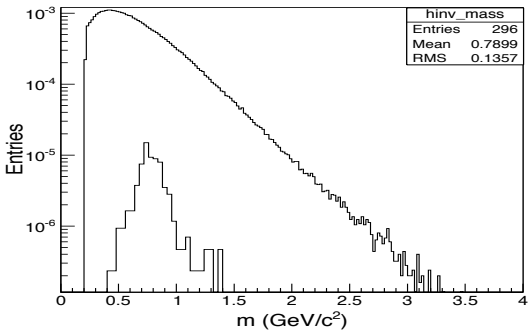

Figure 1: Invariant mass spectrum of the reconstructed ρ^0 mesons in presence of hadronic background generated by UrQMD

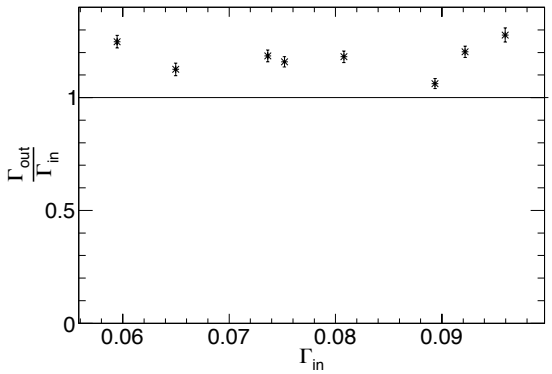

Figure 2: Ratio of output and input width of ρ^0 mesons plotted against input width

References

[1] R. Arnaldi *et al.*, Phys. Rev. Lett. **96** (2006) 162302

[2] `http://www-hades.gsi.de/computing/pluto`

[3] W. Cassing, E. L. Bratkovskaya and S. Juchem, Nucl. Phys. **A 674** (2000) 249

[4] S. A. Bass *et al.*, Prog. Nucl. Part. Phys. **41** (1998) 255

[5] R. Brun *et al.*, GEANT User Guide, CERN/DD/EE84-1 (1986)

J/ψ detection via the di-muon channel in the CBM experiment at FAIR

P. P. Bhaduri and S. Chattopadhyay
Variable Energy Cyclotron Centre, Kolkata, India

The goal of the Compressed Baryonic Matter (CBM) experiment [1] at the FAIR accelerator centre at GSI Darmstadt is the investigation of strongly interacting matter at high net-baryon densities produced in relativistic heavy-ion collisions. The proposed key observables include the measurement of J/ψ mesons, which are believed to carry information about the color confining status of the medium produced in the early stage of the collisions. J/ψ mesons will be measured via their decay into the di-lepton channels, and a muon detector system is being developed for reconstruction of the full di-muon mass spectra [2]. In this article we report our latest results, based on realistic simulations, on the performance of J/ψ detection via the di-muon channel in central Au+Au collisions at 25A GeV, relevant for the SIS-300 program of FAIR.

The presently optimized SIS-300 layout of the muon detection system is employed for this study. It comprises of six absorbers, the first one of carbon and the others of iron, and six tracking stations located between the absorber segments. Each tracking station consists of three layers of high-resolution, argon-based gaseous chambers. The total number of layers is 18 (3 behind each absorber). The total absorber length in the current design amounts to 265 cm divided into 60 cm carbon and 20 cm + 20 cm + 30 cm + 35 cm + 100 cm of iron, with a total material budget of 13.5 λ_I. An additional lead shielding is used around the beam pipe to reduce the background of secondary electrons produced in the beam pipe. The acceptance of the detector covers the laboratory polar angle range $\approx 5^\circ - 27^\circ$. The lateral size of the absorbers is sufficient to completely shield the detector chambers from particles emitted from the target. Each detector plane is subdivided into a number of trapezoidal sector-shaped modules. The number of sectors in a particular detector plane depends on the radii of the stations. Each module is arranged on a support structure with a thickness of about 2 cm. The detector modules are attached at the front and the back sides of the support structure and are filled with argon gas as active medium with a depth of 3 mm. The distance between the chamber centres is fixed to 10 cm to provide enough space for accommodating the detector profile which includes, among others, electronics boards, mechanics, and cooling arrangement. The spacing between layer and absorber is fixed to 5 cm.

In our study, the event generators PLUTO [3] and UrQMD-3.3 [4] were used for generating signal and background particles, respectively. PLUTO generates the J/ψ mesons following a thermal fireball model with a thermal $m_{\rm t}$ distribution ($T = 170$ MeV) and Gaussian rapidity distribution ($\sigma_y = 0.24$). The standard procedure, provided by the CBMROOT framework, is used for full event simulation and track reconstruction. More details of the different steps of simulation and reconstruction can be found in [2].

For the analysis, a set of track quality cuts is applied to the global tracks to identify the muon candidates. The best results, as far as J/ψ reconstruction efficiency and signal-to-background (S/B) are concerned, are obtained if tracks are selected having i) more than 6 STS hits, ii) more than 17 muon hits, iii) track STS $\chi^2 \leq 1.5$, iv) track much $\chi^2 \leq 1.5$, and v) vertex $\chi^2 \leq 2$. The invariant mass spectrum for the J/ψ mesons added to the combinatorial background is shown in Fig. 1. The J/ψ mass peak is clearly visible over the background. The pair reconstruction efficiency (including the geometrical acceptance of the detector) and the S/B ratio are found to be 7.5 % and 1.57, respectively. The di-muon mass resolution is obtained as $\sigma_m = 28$ MeV, which can be attributed to the low material budget of STS, which determines the track momentum. Use of the time-of-flight (TOF) information reduces the pair reconstruction efficiency further to 4.5 % but improves the S/B value to 1.99.

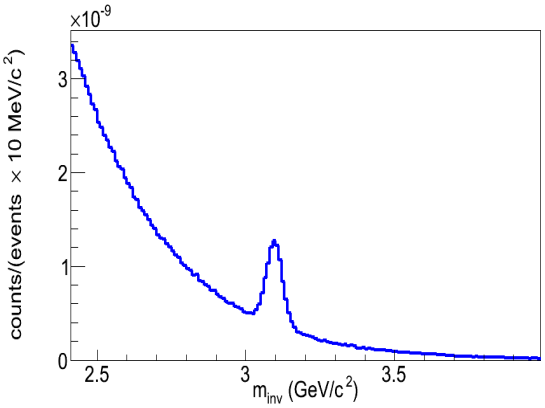

Figure 1: J/ψ invariant mass spectrum reconstructed in muon channel in 25A GeV central Au+Au collisions

References

[1] P. Senger, Nucl. Phys. **A 862-863** (2011) 139

[2] The CBM Collaboration, *Technical Design Report for the CBM Muon Detection System*, in press

[3] `http://www-hades.gsi.de/computing/pluto`

[4] S. A. Bass *et al.*, Prog. Part. Nucl. Phys. **41** (1998) 255

Hit finding efficiency and J/ψ reconstruction efficiency of the MUCH detector

K. Dey[1]*, S. Chattopadhyay*[2]*, and B. Bhattacharjee*[1]

[1]Department of Physics, Gauhati University, Guwahati, India; [2]Variable Energy Cyclotron Centre, Kolkata, India

The proposed muon chamber (MUCH) of the FAIR-CBM experiment aims to detect di-muons from the decay of both low-mass vector mesons and J/ψ [1]. The use of a thick absorber layer as in most of the existing muon detectors is not a good choice. As an alternative, a multilayer absorber system has been proposed. In this configuration, triplet-detector chambers are situated between the absorber layers placed over a considerable distance downstream of the STS detector. The sector-shaped gaseous chambers will be used as sensitive detectors for MUCH.

The large-acceptance detectors of MUCH will give access to almost the entire forward phase space depending on the particle type. The angular acceptance of the detector spans from 5° to 25°, which corresponds to the pseudo-rapidity range 3.18 – 1.5. It is expected that the particle density varies largely over the detector acceptance. Such a variation of particle density might result in a variation of the hit and track finding efficiencies of the detector in different pseudo-rapidity regions. Hence a study on pseudo-rapidity dependent hit efficiency of the detector is of considerable significance. Hit efficiency is defined as the ratio of the number of reconstructed hits to the number of MC point, the latter representing a charged track crossing a sensitive detector element.

The simulation was performed for Au+Au collisions at $E_{\rm lab} = 10A$ GeV with the CBMROOT framework (DEC13) for the SIS-100 (3 absorber) configuration. Background particles and signal muons (from J/ψ decay) were generated using the UrQMD [2] and PLUTO [3] event generators, respectively. To account for a realistic detector geometry, the readout modules are segmented in pads for obtaining the final detector response. In case of a sector geometry, projective pads of radially increasing size are implemented, the dimensions of the pads being determined by the angular separation in the transverse plane. Fired pads having a charge deposition greater than the threshold value are called digits, which are grouped into clusters using a suitable clustering algorithm. Based on particle multiplicity and associated cluster overlap, the clusters are broken into sub-clusters, which are treated as hits (advanced hit finder), or each cluster is treated as one hit (simple hit finder). The hits thus generated are used for the tracking.

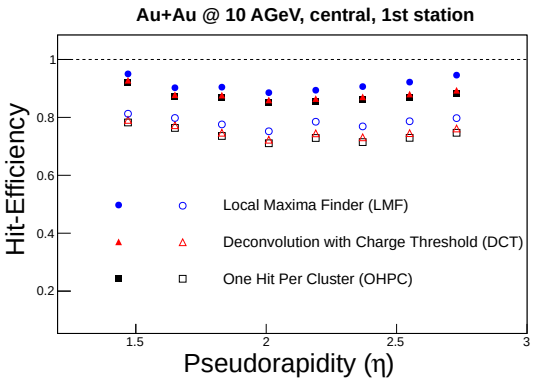

Figure 1: Hit efficiency as function of pseudo-rapidity in the $1^{\rm st}$ station for different cluster deconvolution algorithms. The solid symbols correspond to a pad angle of 0.5°, the open symbols to a pad angle of 1°.

Fig. 1 shows the hit efficiency for different segmentation schemes as well as for different cluster deconvolution algorithms as a function of pseudo-rapidity. The hit efficiency decreases towards mid-rapidity where the particle density is maximum. Furthermore, the hit efficiency is found to be larger for a pad angle of 0.5° because of the decrease of multi-hit probability. For both segmentation schemes, i. e. 0.5° and 1°, the algorithm 'local maxima finder' (LMF) seems to perform better as far as hit efficiency is concerned.

In addition to the results above, the J/ψ reconstruction efficiency was calculated for different segmentation schemes as well as for different cluster deconvolution algorithms. Table 1 shows it to be almost independent of the segmentation scheme considered. Thus, as far as cost is concerned, the pad angle of 1° seems preferrable. For both segmentation schemes, the LFM algorithm gives the maximum signal efficiency. We conclude that 1° pad angle and the LMF algorithm seem to be the optimum choice.

Table 1: J/ψ reconstruction efficiency for different cluster deconvolution algorithms and segmentation schemes

Pad angle	Algorithm	efficiency (embedded)
0.5^0	OHPC	14.0 %
	DCT	14.2 %
	LMF	14.3 %
1^0	OHPC	14.2 %
	DCT	14.2 %
	LMF	14.3 %

References

[1] P. Senger, J. Phys. **G 28** (2002) 1869

[2] S. A. Bass *et al.*, Prog. Part. Nucl. Phys. **41** (1998) 255

[3] `http://www-hades.gsi.de/computing/pluto`

Direct photons at SIS-300

S. M. Kiselev
ITEP, Moscow, Russia

The generator of direct photons described in [1] has been used. It was realized in the AliRoot framework [2] and was adapted by M.Prokudin for the CbmRoot package. The feasibility of the reconstruction of direct photons was studied for the sample of 10^5 head-on (b=0 fm) Au+Au UrQMD events at 25A GeV. Direct photons given in the rapidity range $|y - y_{\rm c.m.}| < 0.5$ by the generator with the main parameters τ_0 = 0.3 fm and T_0 = 250 MeV have been added to the particles of the UrQMD events. Since the decay channels $\omega \to \pi\gamma$ and $\rho \to \pi\pi\gamma$ are included in the UrQMD events they have been switched off in the direct photon generator.

Simulation and reconstruction have been made with the cbmroot release NOV12. The set-up consists of the MVD, STS and an ECAL wall with a size of $X \times Y = 5.76 \times 8.64\,\mathrm{m}^2$ and a beam gap of $|Y| < 0.48$ m, positioned 12 m downstream from the target. Reconstructed photons with $p > 0.5$ GeV/c, $\chi^2_{\rm cluster} < 3$ and $|y - y_{c.m.}| < 0.4$ (corresponding polar angle $100 < \theta_{lab} < 230$; polar radius on ECAL plane 2.2 m $< \rho <$ 5.4 m) have been selected for the analysis. Figure 1 demonstrates the spectra of reconstructed photons.

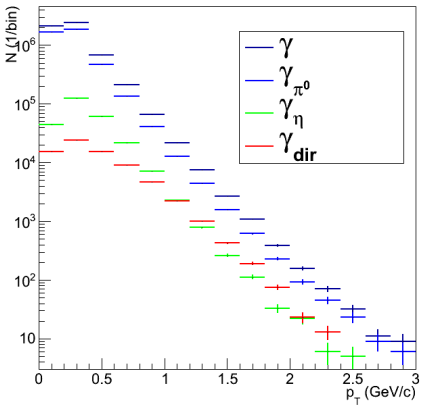

Figure 1: Spectra of reconstructed photons from main sources: π^0, η and direct photons

The photon ratios are shown in Fig. 2. In the range of $p_{\rm t} > 1$ GeV/c direct photons are the main source of photons except π^0. At $p_{\rm t}$ = 2 GeV/c the fraction of direct photons stem from π^0 reaches 20 % of the total yield.

The fraction of photons from π^0 decays can be evaluated by extracting the π^0 signal. Signal to background ratios S/B and significances in a $\pm 2\sigma$ region at different $p_{\rm t}$ bins

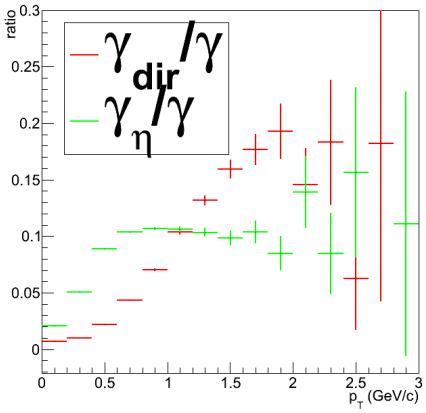

Figure 2: Photon ratios

are presented in Table 1. With the given statistics the signal from $\eta \to \gamma\gamma$ is not visible but we can estimate it using MC information on the true signal (see Table 1). With given sources of direct photons we obtain $\gamma_{\rm dir}/\gamma \approx 15\,\%$ at $p_{\rm t} > 1.5$ GeV/c in head-on Au+Au collisions at 25A GeV using the ECAL. In order to achieve a reasonable significance level of about 10, event statistics of 10^8 is required which is feasible in high intensity heavy-ion collisions planned with CBM at FAIR. More analysis details can be found in [3].

Table 1: Signal to background ratios (S/B) and significances in a $\pm 2\sigma$ region at different $p_{\rm t}$ bins.

$p_{\rm t}$ (GeV/c)	0.4-0.8	0.8-1.2	1.2-1.6	1.6-2.0	2.0-3.0
S/B ($\pi^0 \to \gamma\gamma$)	0.01	0.05	0.11	0.19	0.41
Signif.	46	39	23	13	9
S/B ($\eta \to \gamma\gamma$)	0.0005	0.0008	0.0017	0.0023	0.0041
Signif.	1.8	1.4	0.9	0.44	0.36

References

[1] S. M. Kiselev, *Fast Generators of Direct Photons*, Proceedings of the XIX International Baldin Seminar on High Energy Physics Problems, p.74, Dubna, 2008, arXiv: 0811.2634 [nucl-th]

[2] http://svnweb.cern.ch/world/wsvn/AliRoot/trunk/EVGEN/AliGenThermalPhotons.h

[3] S. M. Kiselev, *Direct Photons at SIS300*, 22nd CBM collaboration meeting, September 2013, Dubna

Reconstruction of ω mesons with the ECAL at SIS-100

S. M. Kiselev
ITEP, Moscow, Russia

The feasibility of ω reconstruction by its decay modes $\omega \rightarrow \pi^0\gamma$ (BR=8.3 %) and $\omega \rightarrow \pi^0\pi^+\pi^-$ (BR=89.2 %) was studied on samples of 10^7 p+C and 10^6 p+Cu minimum bias events at 10 GeV, 10^6 minimum bias and 10^7 head-on p+C events at 30 GeV (geometry and release as provided in [1]). Reconstructed photons with $p > 0.5$ GeV/c and $\chi^2_{\rm cluster} < 1000$ have been taken for the analysis.

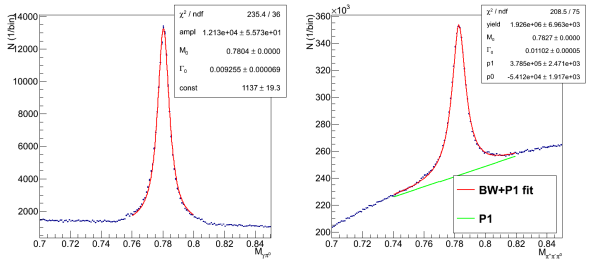

Figure 1: Invariant mass spectra of $\gamma\pi^0$ pairs (left) and $\pi^+\pi^-\pi^0$ triples (right) of primaries for p+C (b=0) at 30 GeV, fitted by a Breit-Wigner function (red line)

In the invariant mass spectrum of MC primaries there is a peak at m_ω. Figure 1 demonstrates examples for p+C (b=0) at 30 GeV. The $\gamma\pi^0$ pairs and $\pi^+\pi^-\pi^0$ triples within the invariant mass interval $0.77\,\mathrm{GeV} < \mathrm{M} < 0.79\,\mathrm{GeV}$ are taken as "primary" ω. Invariant mass distributions for pairs of reconstructed photons demonstrate a peak from π^0 with $\sigma_{\pi^0} \approx 5.3$ MeV. For π^0 candidates the $\gamma\gamma$ pairs with $m_{\pi^0} - 2\sigma_{\pi^0} < M_{\gamma\gamma} < m_{\pi^0} + 2\sigma_{\pi^0}$ were selected. No particle identification was applied for the selection of π^+ and π^- candidates, but a cut on the impact parameter in the target plane ($< 4\sigma$) was used to suppress secondary charged tracks. Figure 2 demonstrates examples of invariant mass spectra for the $\gamma\pi^0$ and $\pi^+\pi^-\pi^0$ channels with the signal width $\sigma \approx 22$ MeV and 13 MeV, respectively. Tables 1 and 2 summarize characteristics of the analysis: signal yield, acceptance, reconstruction and cut efficiencies, signal-to-background ratios $S/B_{\pm 2\sigma}$ and significances.

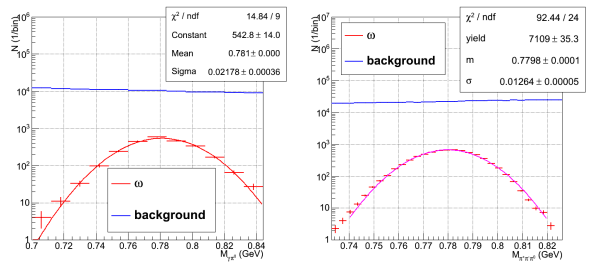

Figure 2: Invariant mass spectra of $\gamma\pi^0$ pairs (left) and $\pi^+\pi^-\pi^0$ triples (right) for p+C (b=0) at 30 GeV

Table 1: $\omega \rightarrow \pi^0\gamma$

System	yield x100	acc. eff.	rec. eff.	cut eff.	S/B /sign.
p+C 10GeV	0.16	0.024	0.78	0.65	0.04/2.6
p+Cu 10GeV	0.5	0.018	0.75	0.74	0.08/1.2
p+C 30GeV	0.5	0.067	0.83	0.37	0.04/1.9
p+C 30GeV b=0	1.4	0.060	0.81	0.36	0.03/8.5

Table 2: $\omega \rightarrow \pi^0\pi^+\pi^-$

System	yield x10	acc. eff.	rec. eff.	cut eff.	S/B /sign.
p+C 10GeV	0.2	0.038	0.61	0.40	0.10/8.5
p+Cu 10GeV	0.6	0.018	0.61	0.39	0.08/1.2
p+C 30GeV	0.7	0.098	0.68	0.49	0.04/3.8
p+C 30GeV b=0	1.4	0.084	0.68	0.50	0.03/11

In order to achieve a reasonable significance level of about 10, event statistics of 10^8 is required. In Table 3 the $p_{\rm t}$ dependence of the S/B ratio is presented for high statistic samples (10^7).

Table 3: (S/B) / significance for $\omega \rightarrow \pi^0\pi^+\pi^-$ divided into four $p_{\rm t}$ bins

p_t (GeV/c)	0.4 - 0.8	0.8 - 1.2	1.2 - 1.6	1.6 - 2.0
p+C 10 GeV	0.11 / 5.6	0.09 / 2.0	-	-
p+C 30 GeV b=0	0.02 / 7.1	0.03 / 8.3	0.06 / 7.0	0.10 / 5.3

References

[1] S. M. Kiselev, *Reconstruction of π^0 and η with ECAL*, this report

Reconstruction of π^0 and η with the ECAL

S. M. Kiselev
ITEP, Moscow, Russia

UrQMD events simulated and reconstructed with the FEB12 trunk version of `cbmroot` have been used: 10^7 p+C and 10^6 p+Cu minimum bias events at 10 GeV, 10^6 minimum bias and 10^7 head-on p+C events at 30 GeV, 10^5 Cu+Cu and 5×10^4 minimum bias Au+Au events at $10A$ GeV as well as 10^5 minimum bias Au+Au events at $25A$ GeV. The set-up consists of the MVD, STS, TOF and the ECAL wall with a size of $X \times Y = 5.76 \times 8.64\,\mathrm{m}^2$ and a beam gap of $|Y| < 0.48\,\mathrm{m}$, positioned 12 m downstream from the target. Reconstructed photons with $p > 0.5\,\mathrm{GeV/c}$ and $\chi^2_{\mathrm{cluster}} < 25$ have been selected for the analysis.

A signal in the π^0 range of the invariant mass spectrum is seen for all collision systems. It was fitted by the sum of a Gaussian and a 2^{nd} order polynomial resulting to a signal width of $\sigma_\pi \approx 6 - 7\,\mathrm{MeV}$. The signal-to-background ratios S/B and significances for different p_t bins are presented in Table 1.

Table 1: Signal-to-background ratios ($S/B_{\pm 2\sigma}$) and significances (in brackets) for π^0

p_t (GeV/c)	0.4 - 0.8	0.8 - 1.2	1.2 - 1.6
p+C 10GeV	13.2 (273)	63.4 (106)	-
p+Cu 10GeV	11.1 (117)	35.3 (43)	-
p+C 30GeV	4.9 (161)	15.1 (79)	35.7 (36)
p+C 30GeV (b=0)	4.5 (810)	14.4 (405)	33.8 (187)
Cu+Cu 10AGeV	0.21 (65)	0.61 (36)	1.54 (16)
Au+Au 10AGeV	0.05 (40)	0.12 (22)	0.34 (9)
Au+Au 25AGeV	0.04 (74)	0.11 (56)	0.26 (33)

Table 2: Signal-to-background ratios ($S/B_{\pm 2\sigma}$) and significances (in brackets) for η, divided in three p_t bins

p_t (GeV/c)	0.4 - 0.8	0.8 - 1.2	1.2 - 1.6
p+C 10GeV	0.43 (25)	1.06 (11)	-
p+Cu 10GeV	0.47 (13)	-	-
p+C 30GeV	0.16 (14)	0.33 (8)	-
p+C 30GeV (b=0)	0.15 (65)	0.33 (50)	0.74 (32)
Cu+Cu 10AGeV	0.007 (3)	0.01 (1)	-
Au+Au 10AGeV	0.002 (2)	0.002 (1)	-
Au+Au 25AGeV	0.001 (3)	0.002 (2)	0.004 (1)

A signal in the η range is seen only for the systems with proton beam. For the systems with ion beams signal parameters have been estimated from the "true signal". The signal has $\sigma_\eta \approx 20 - 25\,\mathrm{MeV}$. The signal-to-background ratios S/B and significances for different p_t bins are presented in Table 2.

To achieve a reasonable significance level of about 10, the event statistics should be two order of magnitude larger for ion beams. Tables 3 and 4 summarize other characteristics of the π^0 and η analyses: event statistics, signal yield, acceptance and reconstruction efficiencies.

Plots for acceptance and reconstruction efficiencies and the invariant mass distributions for all systems can be found in Ref. [1].

Table 3: $\pi^0 \to \gamma\gamma$. Event statistics, signal yield, acceptance and reconstruction efficiencies

Collision system	events	yield/ev.	accept.	recon.eff
p+C 10GeV	10^7	0.48	0.044	0.94
p+Cu 10GeV	10^6	1.58	0.025	0.93
p+C 30GeV	10^6	0.84	0.084	0.95
p+C 30GeV (b=0)	10^7	2.5	0.074	0.95
Cu+Cu 10AGeV	10^5	12.5	0.055	0.83
Au+Au 10AGeV	$5 \cdot 10^4$	41.7	0.054	0.76
Au+Au 25AGeV	10^5	76.4	0.083	0.54

Table 4: $\eta \to \gamma\gamma$. Event statistics, signal yield, acceptance and reconstruction efficiencies

Collision system	events	yield/ev.	accept.	recon.eff
p+C 10GeV	10^7	0.02	0.061	0.98
p+Cu 10GeV	10^6	0.06	0.032	0.98
p+C 30GeV	10^6	0.03	0.112	0.98
p+C 30GeV (b=0)	10^7	0.1	0.100	0.98
Cu+Cu 10AGeV	10^5	0.47	0.082	0.93
Au+Au 10AGeV	$5 \cdot 10^4$	1.5	0.081	0.83
Au+Au 25AGeV	10^5	3.0	0.125	0.70

References

[1] S. M. Kiselev, *Reconstruction of π^0 and η with ECAL*, 21st CBM collaboration meeting, April 2013, Darmstadt

CBM Physics

Net baryon density at FAIR energies in a thermal model approach

A. Prakash, P. K. Srivastava, B. K. Singh, and C. P. Singh
Department of Physics, Banaras Hindu University, Varanasi, India

The Compressed Baryonic Matter (CBM) experiment planned at the Facility for Antiproton and Ion Research (FAIR) will constitute a major scientific effort for exploring the properties of strongly interacting matter in the high baryon density regime. One of its important goals is to precisely determine the equation of state (EOS) of strongly interacting matter at extreme baryon density. We have employed a thermal model EOS incorporating excluded volume description for the hot and dense hadron gas (HG) for our study. We have calculated the variation of net baryon density with respect to the center of mass energy $\sqrt{s_{NN}}$ in our model and compared it with the corresponding result obtained in [1].

Recently we have proposed a thermodynamically consistent excluded volume model for the hot and dense hadron gas (HG). In this model, the grand canonical partition function for the HG with full quantum statistics and after suitably incorporating an excluded volume correction is considered. The number density after excluded volume correction can be written as [2]:

$$n_i^{ex} = \frac{\lambda_i}{V}\left(\frac{\partial ln Z_i^{ex}}{\partial \lambda_i}\right)_{T,V}, \qquad (1)$$

where λ_i is the fugacity of the ith baryon species and Z_i^{ex} is the grand canonical partition function for finite-size baryons. In our model we consider the hard-core repulsion arising between two baryons only, meaning that mesons can interpenetrate each other but baryons cannot owing to their hard-core size. In this calculation, we have taken an equal volume $V^0 = \frac{4\pi r^3}{3}$ for each type of baryon with a hard-core radius $r = 0.8$ fm. We have taken all baryons and mesons and their resonances with masses up to $2\,\mathrm{GeV/c^2}$ in our calculation for the HG pressure. We have also imposed the condition of strangeness conservation by putting $\sum_i S_i(n_i^s - \bar{n}_i^s) = 0$, where S_i is the strangeness quantum number of the ith hadron, and $n_i^s(\bar{n}_i^s)$ is the strange (antistrange) hadron density, respectively. Using this constraint equation, we get the value of the strange chemical potential in terms of μ_B.

The extracted freeze-out temperature in statistical hadron gas models generally increases monotonically with the collision energy. However, the corresponding net baryon density exhibits a more complicated behaviour [3]. Figure 1 demonstrates the variation of ρ_B with $\sqrt{s_{NN}}$. To calculate ρ_B, we first use our parametrization to get the values of μ_B and T for given $\sqrt{s_{NN}}$. At this T and μ_B, we have calculated the value of net baryon density ρ_B. In the present excluded volume model, the net baryon density increases with $\sqrt{s_{NN}}$ (see Fig. 1), reaches a maximum value near $\sqrt{s_{NN}} = 8 - 9$ GeV and then starts decreasing. The maximum freeze-out net baryon density is approximately half of the normal nuclear density $\rho_0 = 0.15\,\mathrm{fm}^{-3}$. We have compared our model results with the net baryon density obtained in [1] using the excluded volume model based on [4]. There, the baryon density at various $\sqrt{s_{NN}}$ is calculated using 0.5 fm as hard core radius (r_b) for each baryon, and all mesons are treated as pointlike particles, i. e. $r_m = 0$. On the other hand, we have taken a value of 0.8 fm as hard-core radius for each baryon. The values of maximum freeze-out density achieved in heavy ion collisions are almost the same in both models. However, the maximum is shifted towards lower energies in the results reported in [1]. The maximum value of ρ_B obtained in our model as well as in the excluded volume model of [1] is also lower than the value obtained in [3] where a HRG model is used without any excluded volume correction. Obviously the excluded volume effect shifts the net baryon density achieved at freeze-out towards the lower value.

In summary, we have calculated the net baryon density at freeze-out in the FAIR energy range, which comes out to be the maximum achievable density in heavy ion collisions.

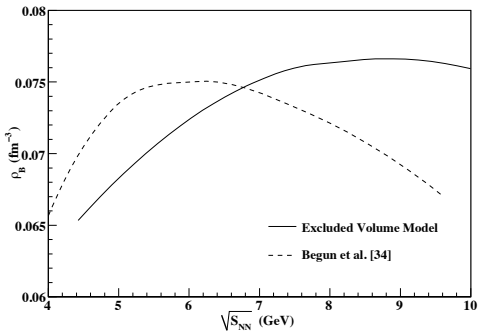

Figure 1: Variation of net baryon density at freeze-out with respect to the center of mass energy ($\sqrt{s_{NN}}$)

References

[1] V. V. Begun, M. Gazdzicki and M. I. Gorenstein, Phys. Rev. **C 88** (2013) 024092 (2013)

[2] S. K. Tiwari, P. K. Srivastava and C. P. Singh, Phys. Rev. **C 85** (2012) 014908; P. K. Srivastava and C. P. Singh, Phys. Rev. **D 85** (2012) 114016; P. K. Srivastava and C. P. Singh, Int. J. Mod. Phys. **A 28** (2013) 1350051; S. K. Tiwari and C. P. Singh, Advances in HEP **2013** (2013) 805413; A. Prakash, P. K. Srivastava and B. K. Singh, Advances in HEP **2014** (2014) 983861

[3] J. Randrup and J. Cleymans, Phys. Rev. **C 74** (2006) 047901

[4] D. H. Rischke *et al.*, Z. Phys. **C 51** (1991) 485

Production of hyperons at FAIR energies

H. Jahan[1], *S. Chattopadhyay*[2], *P. Senger*[3], *N. Ahmad*[1], *and M. Irfan*[1]
[1]AMU, Aligarh, India; [2]VECC, Kolkata, India; [3]GSI, Darmstadt, Germany

One of the main aims of studying relativistic heavy-ion collisions is to investigate the characteristics of nuclear matter under extreme conditions of temperature and energy density. Under high temperature and/or baryon density, nuclear matter is expected to undergo a transition to a state of free quarks and gluons, known as quark-gluon plasma (QGP)[1]. The determination of yields of strange particles is one of the key parameters to study the properties of the matter created in high energy heavy-ion collisions. The relative enhancement of strange and multi-strange baryons as well as their ratios in central heavy ion collisions in comparison to those for proton induced interactions have also been suggested as a possible signature for the formation of QGP [2]. In the present work, A Multi-Phase Transport (AMPT) model [3] is employed to study production of strange particles in cental Au+Au collisions at FAIR energies (i.e. $E_{\rm lab}$ = 5A to 40A GeV). In order to see whether the hyperon production is sensitive to the degrees of freedom in the collision volume, both the string melting (partonic matter) and the default mode (hadronic matter) of the AMPT model were used for calculating the particle yields.

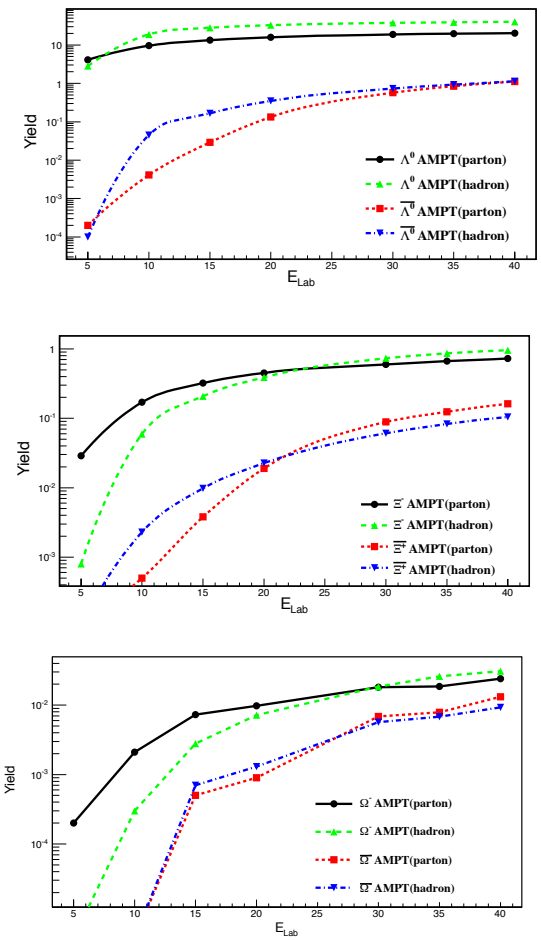

Figure 1: Yield of hyperons in central Au+Au collisions as function of beam energy calculated with the AMPT code with string melting (partonic) and without (hadronic). Upper panel: Λ^0 and $\overline{\Lambda}^0$ hyperons. Center panel: Ξ^- and $\overline{\Xi}^+$ hyperons. Lower panel: Ω^- and $\overline{\Omega}^+$ hyperons.

The results of the calculations are shown as excitation functions of Λ^0 and $\overline{\Lambda}^0$ hyperons, Ξ^- and $\overline{\Xi}^+$ hyperons, and Ω^- and $\overline{\Omega}^+$ hyperons in the upper, center, and lower panel of Fig. 1, respectively. The yields have been calculated in the FAIR energy range for both modes of AMPT, i. e., string melting (partonic) and default (hadronic). In the case of $\overline{\Lambda}^0$ hyperons, the yield for hadronic production is one order of magnitude higher than the yield for partonic production at top SIS-100 energy (11A GeV), an effect which is clearly measurable. A similar effect, although smaller in magnitude, is found for $\overline{\Xi}^+$ hyperons. In contrast, the yields of Ξ^- and Ω^- hyperons for partonic production are well above the yield for hadronic production in the SIS-100 beam energy range. The yield of $\overline{\Omega}^+$ hyperons seems not to be sensitive to the production mechanism. However, this result should be checked by a calculation with much better statistics. In conclusion, according to the AMPD code the yields of hyperons and anti-hyperons produced in central Au+Au collisions at FAIR energies exhibit a measurable sensitivity to the degrees of freedom in the fireball.

References

[1] S. A. Bass *et al.*, J. Phys. **G 25** (1999) R1

[2] J. Rafelski and B. Müller, Phys. Rev. Lett. **48** (1982) 1066; J. Rafelski, Phys. Rep. **88**, (1982) 331; P. Koch, B. Müller and J. Rafelski, Phys. Rep. **142** (1986) 167

[3] B. Zhang *et al.*, Phys. Rev. **C 61** (2000) 067901; Z. W. Lin *et al.*, Phys. Rev. **C 64** (2001) 011902

Estimation of the J/ψ multiplicity at FAIR energies

P. P. Bhaduri and S. Chattopadhyay
Variable Energy Cyclotron Centre, Kolkata, India

One of the major goals of the CBM experiment at FAIR is the measurement of J/ψ production via the decay into di-muons. This measurement is particularly challenging for heavy-ion reactions, where no data exist below 158A GeV. In the FAIR energy regime, J/ψ mesons will be produced close to their kinematic production threshold which results in extremely low production cross sections. A realistic simulation to study the feasibility of J/ψ detection in di-muon channel thus requires a precise estimate of the charmonium multiplicity in nuclear collisions at FAIR, in order to estimate the data sample to be collected at FAIR as well as the signal-to-background (S/B) ratio, the figure-of-merit for experimental studies. In this report, we attempt to make an estimate of the rate of J/ψ production in Au+Au collisions at the typical FAIR energy of 25A GeV.

To start with, let us first survey the different parameterizations available in the literature for inclusive J/ψ production in elementary NN collisions. One of the oldest parameterizations, available from the E672 collaboration and valid for collision energies $\sqrt(s) \leq 31$ GeV, is called Schuler parametrization [1]. It gives the total cross section in the forward hemisphere ($x_F \geq 0$) without including the branching ratio to lepton pairs. A slightly different parametrization is available from the E771 collaboration [2] which studied J/ψ production in p+Si interactions with a 800 GeV/c proton beam. Data were collected in the di-muon channel with an open-geometry, large-acceptance spectrometer in fixed-target mode. The inclusive cross section per nucleon is obtained with an atomic weight dependence A^α with $\alpha = 0.92 \pm 0.008$. A more recent phenomenological calculation based on scaling analysis of near threshold quarkonium production off cold nuclear matter is also available [3]. The mean values of σ_{nn} in the di-muon channel as obtained from different parameterizations for a beam kinetic energy 25A GeV is seen to vary from 0.063 nb to 0.066 nb. For a conservative estimate let us choose $\sigma_{nn} = 0.063$ nb.

Since at FAIR energies, J/ψ production will be dominated by initial hard scatterings, in absence of all possible medium effects the J/ψ multiplicity in Au+Au collisions at 25A GeV at an impact parameter b can be written as $N_{J/\psi}^{\rm Au+Au}({\rm b}) = T_{\rm AuAu}({\rm b}) \times \sigma_{J/\psi}^{\rm pp}$, where $T_{\rm AuAu}$ is the nuclear overlap function calculable using the Glauber model. At large impact parameters, not every encounter of two nuclei leads to an inelastic collision. To compute the multiplicity, one hence needs to consider the probability of an inelastic collision, given by $p_{\rm inel}^{\rm Au+Au}({\rm b}) \approx 1 - e^{-N_{\rm coll}({\rm b})}$. $N_{\rm coll}(b)$ is the number of binary collisions. The thus obtained impact parameter dependence of the J/ψ multiplicity in Au+Au collisions at 25A GeV is shown in Fig. 1. Note that our multiplicity values are slightly larger than those previously obtained with the HSD model.

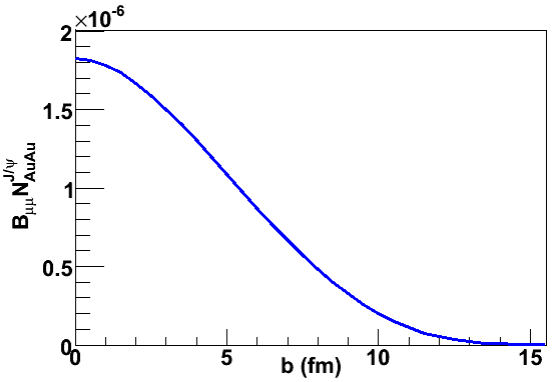

Figure 1: J/ψ multiplicity in the di-muon channel as function of the collision impact parameter in Au+Au collisions at 25A GeV

In minimum bias Au+Au collisions, the average J/ψ multiplicity is given by $\langle N_{J/\psi}\rangle^{\rm Au+Au} = \sigma_{\rm pp}^{J/\psi}\langle T_{\rm AuAu}\rangle$, where $\langle T_{\rm AuAu}\rangle = 62.94$ fm^{-2}. Substituting for $\sigma_{\rm pp}^{J/\psi}$, the J/ψ multiplicity in minimum bias Au+Au collisions at 25A GeV is obtained to be 3.9×10^{-7}. For Au beams with an intensity of 10^9 ions/s and a 250 μm thick Au target, which corresponds to about 1% interaction length (λ_I) of Au, the event rate is 10 MHz. Hence the J/ψ production rate in the di-muon channel at this energy, in absence of any medium effect (primary or secondary), is around 3.9 per second.

To calculate the number of detected J/ψ, the detector acceptance as well as the J/ψ detection efficiency need to be taken into account. In the case of the CBM experiment, simulations with a realistic muon detector system show that in minimum bias Au+Au collisions at 25A GeV the product of geometrical acceptance and pair reconstruction efficiency is ≈11 %. Te corresponding J/ψ collection rate will be ≈ 0.39 J/ψ per second.

References

[1] R. Vogt, Phys. Rep. **310** (1999) 197

[2] T. Alexopoulos *et al.* (E771 Collaboration), Phys. Lett. B **374** (1996) 271

[3] P. P. Bhaduri and S. Gupta, Phys. Rev. **C 88** (2013) 045205 (2013)

An estimation of the thermal di-muon contribution at FAIR energies

S. Samanta[1], *P. P. Bhaduri*[2], *S. Chattopadhyay*[2], *S. Das*[1], *and S. K. Ghosh*[1]
[1]Bose Institute, Kolkata, India; [2]Variable Energy Cyclotron Centre, Kolkata, India

Leptons are electromagnetically interacting particles. Their mean free path exceeds the size of the system formed after the heavy ion collisions, and hence the leptons leave the system undisturbed after their production, carrying the information about the initial state of the system. In heavy-ion collisions, the di-lepton sources are (1) the Drell-Yan process during the initial $q\bar{q}$ collisions, (2) decays of heavy quarkonia, and (3) thermal radiation resulting from interactions between secondary partons or even in a locally thermalized Quark-Gluon Plasma (QGP). The di-lepton yield from thermal radiation is expected to serve as a probe of the QGP. Here we report on a study of the thermal contribution to the di-lepton continuum relevant for the muon physics simulation for the CBM experiment at FAIR.

We assume that in heavy-ion collisions, the large initial temperature T_i leads to the formation of a thermally equilibrated quark-gluon plasma (QGP). The system then evolves in space and time and cools from the initial temperature T_i to the critical temperature T_c at time τ_c via a first order phase transition. In the QGP phase, lepton pairs are produced dominantly from quark-antiquark annihilation processes. In these processes, a quark interacts with an antiquark to form a virtual photon which subsequently decays into a lepton pair.

In case of massless quarks and antiquarks, the number of leptons pairs produced per unit of squared invariant mass M^2 and per unit of four-volume is given by [1]

$$\frac{dN_{l^+l^-}}{dM^2d^4x} = N_cN_s^2\sum_{f=1}^{N_f}(\frac{e_f}{e})^2\frac{\sigma(M)}{2(2\pi)^4}M^2 \times f_1(\epsilon)F_2(\frac{M^2}{4\epsilon})(\frac{2\pi}{w(\epsilon)})^{1/2}, \quad (1)$$

where N_c and N_s are color and spin degeneracy factors, respectively, N_f is the number of flavours, e_f is the electric charge of a quark with flavour f, $\sigma(M) = \frac{4\pi}{3}\frac{\alpha^2}{M^2}\sqrt{(1-\frac{4m_l^2}{M^2})}(1+\frac{2m_l^2}{M^2})$, α is the fine structure constant, m_l is the mass of the leptons (in our present analysis the muon mass), $F_2(E) = -\int_\infty^E f_2(E')dE'$, f_1 (f_2) is the quark (antiquark) distribution function, $\epsilon(M)$ is the root of the equation $\frac{d}{dE}[lnf_1(E) + lnF_2(\frac{M^2}{4E})]_{E=\epsilon} = 0$, and $w(\epsilon) = -[\frac{d^2}{dE^2}(lnf_1(E) + lnF_2(\frac{M^2}{4E}))]_{E=\epsilon}$.

For simplicity we assume one-dimensional Bjorken expansion [2] for which $d^4x = \pi R_A^2\tau d\tau dy$, where R_A is the radius of the colliding nuclei, y the fluid rapidity and τ the proper time. The initial time of the thermalized fireball can be estimated as $\tau_i = \frac{2R_A}{\gamma\beta}$. For Au+Au collisions at $\sqrt{s} = 8$ GeV, $\tau_i \sim 3$ fm. τ_f is taken approximately as 15 fm.

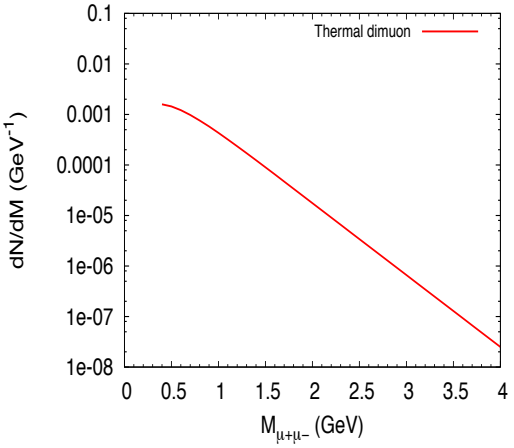

Figure 1: Invariant mass distribution of thermal di-muons

Figure 1 shows the resulting invariant mass distribution of di-muons created from the thermal QGP source. As a part of the future plan for the performance studies of the CBM Muon Detector System, we have implemented a generator of thermal muon pairs into the CBM software framework CBMROOT, such that the background from thermal di-muons can be included in simulations, which is not the case if UrQMD alone is used to generate the background.

In summary, we have estimated the production of di-muons from a thermal QGP source which could be used as the input for physics performance studies of the CBM-MUCH. It will be challenging to disentangle the thermal continuum from the combinatorial background. The present study is just a preliminary case study to understand the feasibility of such an approach. We need to build up large statistics to establish the feasibility of this method beyond the statistical limit.

References

[1] C. Y. Wong, Phys. Rev. **C48** (1993) 902

[2] J. D. Bjorken, Phys. Rev. **D 27** (1983) 140

Study of the multiplicity distribution moments

C. Ristea, O. Ristea, and A. Jipa
Atomic and Nuclear Physics Chair, Faculty of Physics, University of Bucharest, Romania

Higher moments (skewness and kurtosis) of multiplicity distributions are proposed to provide one of the most sensitive probes in the search for the Critical Point, because they are conjectured to reflect the large fluctuations associated with the hadron-quark phase transition. In the last years the multiplicity moments have been intensively studied, both experimentally [1] and theoretically [2].

The skewness and kurtosis of the event-by-event multiplicity distributions are defined as:

$$S = \frac{\langle (N - \langle N \rangle)^3 \rangle}{\sigma^3}, \quad K = \frac{\langle (N - \langle N \rangle)^4 \rangle}{\sigma^4} - 3\,, \quad (1)$$

where N is the particle number (multiplicity) in one event and $\langle N \rangle$ is the averaged particle multiplicity over the whole event ensemble. We analyzed the net-kaon multiplicities $N_{K^+-K^-} = N_{K^+} - N_{K^-}$, and total proton multiplicities $N_{p+\bar{p}} = N_p + N_{\bar{p}}$ from Au+Au collisions using the UrQMD code [3] at FAIR energies: $p_{\rm lab}$ = 2 AGeV/c, 11 AGeV/c, 25 AGeV/c, and, for reference, at RHIC energies $\sqrt{s_{NN}}$ = 62.4 and 200 GeV. The aim of the present study is to have a baseline for the case of the absence of the critical point, since the UrQMD code does not include the physics of the critical point.

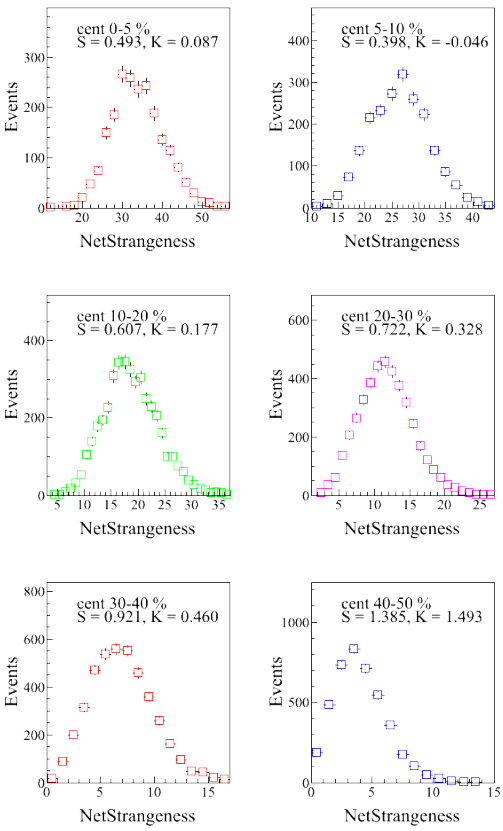

Figure 1: Centrality dependence of the net-kaon multiplicity distributions from the UrQMD code in Au+Au collisions at p_{lab} = 25 AGeV/c

Going from peripheral to central collisions in Fig. 1, the net-kaon distributions become broader and more symmetric for central collisions. For peripheral collisions the mean is shifted towards zero. These event-by-event distributions for each centrality were used to compute higher order moments. The moments are decreasing from peripheral to central events.

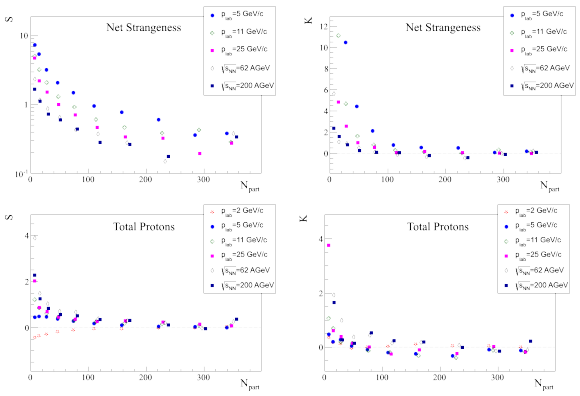

Figure 2: $3^{\rm rd}$ and $4^{\rm th}$ order multiplicity distribution moments for net-kaons (upper row) and net-protons (lower row) as a function of $N_{\rm part}$

Figure 2 shows that the energy dependence of the moments is stronger in peripheral collisions, both for net-kaons and total protons. For the same collision centrality, the skewness and kurtosis values for net-kaons decrease with increasing energy. In the case of total protons, for the same collision centrality, the skewness and kurtosis values increase with beam energy. The presented results are relevant for the absence of the critical point (as extracted from UrQMD code) and it would be interesting to compare them to future experimental data at SIS-100.

References

[1] M. Aggarwal *et al.* (STAR Collaboration), Phys. Rev. Lett. **105** (2010) 022302

[2] F. Karsch and K. Redlich, Phys. Lett. **B 695** (2011) 136

[3] S. A. Bass *et al.*, Prog. Part. Nucl. Phys. **41** (1998) 225; M. Bleicher *et al.*, J. Phys. **G 25** (1999) 1859

CBM Publications 2013

- A. Abuhoza *et al.*:
Setup optimization toward accurate ageing studies of gas filled detectors
Nucl. Instrum. Methods **A 718** (2013) 400
doi:10.1016/j.nima.2012.08.045

- S. Biswas *et al.*:
Study of the characteristics of GEM detectors for the future FAIR experiment CBM
Nucl. Instrum. Methods **A 718** (2013) 403
doi:10.1016/j.nima.2012.08.044

- S. Chatterji *et al.*:
Exploring various isolation techniques to develop low noise, radiation hard double-sided silicon strip detectors for the CBM Silicon Tracking System
IEEE Trans. Nucl. Sci. **60** (2013) 2254
doi:10.1109/TNS.2013.2262575

- M. Deveaux *et al.*:
A first generation prototype for the CBM micro vertex detector
Nucl. Instrum. Methods **A 718** (2013) 305
doi:10.1016/j.nima.2012.10.013

- D. Doering *et al.*:
Pitch dependence of the tolerance of CMOS monolithic active pixel sensors to non-ionizing radiation
Nucl. Instrum. Methods **A 730** (2013) 111
doi:10.1016/j.nima.2013.04.038

- C. Dritsa (for the CBM collaboration):
The Ring Imaging Cherenkov detector for the CBM-Experiment
J. Phys.: Conf. Ser. **426** (2013) 012025
doi:10.1088/1742-6596/426/1/012025

- A. Dubey *et al.*:
GEM detector development for CBM experiment at FAIR
Nucl. Instrum. Methods **A 718** (2013) 418
doi:10.1016/j.nima.2012.10.043

- J. Heuser *et al.*:
The Compressed Baryonic Matter Experiment at FAIR
Nucl. Phys. **A 904-905** (2013) 941c
doi:10.1016/j.nuclphysa.2013.02.170

- C. Höhne:
Physics of compressed baryonic matter
J. Phys.: Conf. Ser. **420** (2013) 012016
doi:10.1088/1742-6596/420/1/012016

- M. Koziel *et al.*:
The prototype of the Micro Vertex Detector of the CBM Experiment
Nucl. Instrum. Methods **A 732** (2013) 515
doi:10.1016/j.nima.2013.07.041

- F. Lemke and U. Brüning:
A Hierarchical Synchronized Data Acquisition Network for CBM
IEEE Trans. Nucl. Sci. **60** (2013) 3654
doi:10.1109/TNS.2013.2272939

- M. Petriş *et al.*:
Two-dimensional position sensitive transition radiation detector
Nucl. Instrum. Methods **A 714** (2013) 17
doi:10.1016/j.nima.2013.02.039

- M. Petriş *et al.*:
TRD detector development for the CBM experiment
Nucl. Instrum. Methods **A 732** (2013) 375
doi:10.1016/j.nima.2013.07.087

- I. Sorokin *et al.*:
The Silicon Tracking System of the CBM experiment at FAIR: Overview and development progress
Nucl. Instrum. Methods **A 718** (2013) 366
doi:10.1016/j.nima.2012.10.118

- C. Z. Xiang *et al.*:
The online data pre-processing for CBM-TOF
JINST **8** (2013) P02002
doi:10.1088/1748-0221/8/02/P02002

CBM presentations 2013

http://cbm-wiki.gsi.de/cgi-bin/view/Public/PublicPresentations2013

Doctoral, diploma, master and bachelor theses 2013

http://cbm-wiki.gsi.de/cgi-bin/view/Public/Thesis2013

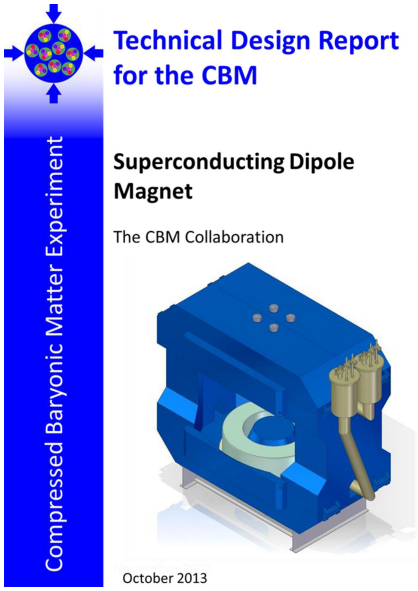

Approved by FAIR-ECE, January 2014

Approved by FAIR-ECE, August 2013

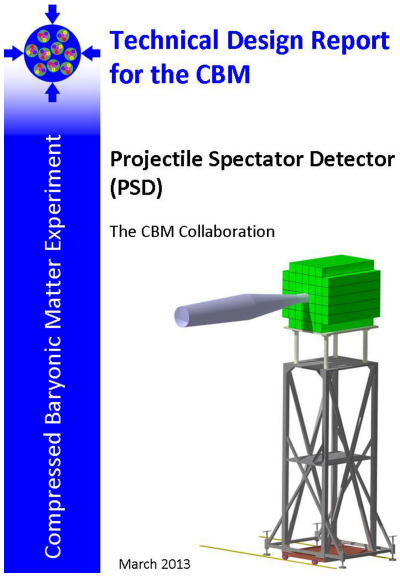

Submitted to FAIR-ECE, April 2013

Approved by FAIR-ECE, January 2014

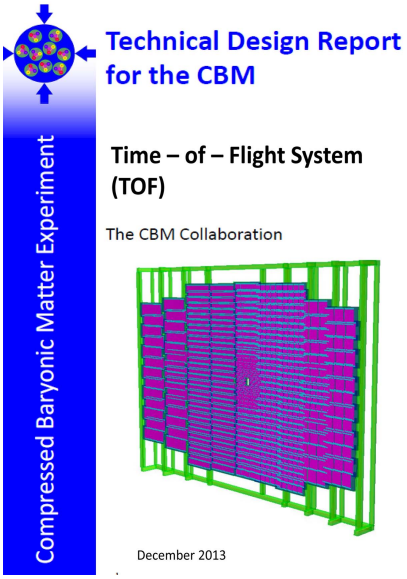

Submitted to FAIR-ECE, December 2013

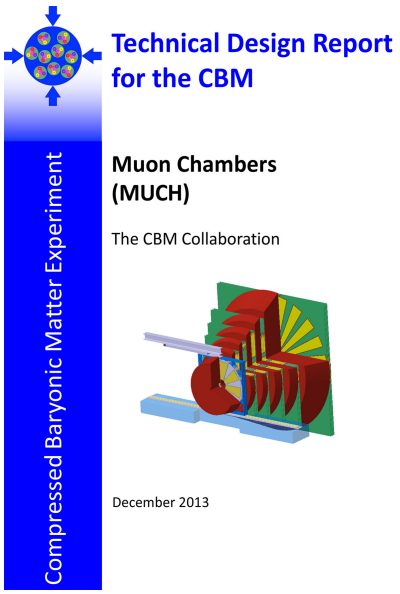

Submitted to FAIR-ECE, December 2013

Workshops and Meetings 2013

21st CBM Collaboration Meeting

8 – 12 April 2013, GSI, Darmstadt, Germany

https://indico.gsi.de/conferenceDisplay.py?confId=1912

Workshop on Module and Ladder Assembly for the CBM-STS

6 – 7 June 2013, JINR, Dubna, Russia

Scientists, engineers and industrial partners involved in the silicon tracking detector projects of the CBM experiment at FAIR and the BM@N experiment at Nuclotron met from 6-7 June 2013 at JINR, Dubna, Russia, during a workshop on module and ladder assembly. The meeting was organized as a parallel session of the international conference "Prospects for experimental research on the Nuclotron Beams" at the Laboratory of High Energy Physics. Detailed aspects of the assembly procedures were discussed and tasks and timelines for the workgroups defined. The presentations given at the workshop and the conclusions drawn are summarized on the workshop's web page.

https://indico.gsi.de/conferenceDisplay.py?confId=2220

CBM-China Meeting

21 – 24 August 2013, Tsinghua University, Beijing, China

A CBM China meeting took place at Tsinghua University in Beijing from August 21 to 24, 2013 to discuss the Chinese contributions to the TOF-RPC wall and to define the work packages. As a result of the meeting, the CBM preconstruction MoU has been signed by the Tsinghua University Beijing, the Central China Normal University (CCNU) in Wuhan, and the University of Science and Technology of China (USTC) Hefei.

Workshop on STS-XYTER front-end electronics

12 – 13 September 2013, GSI, Darmstadt, Germany

Participants from the CBM teams at GSI, Darmstadt, and AGH, Crakow, met in September 2013 to work on the front-end chip STS-XYTER under development for the Silicon Tracking System. The first prototypes of this chip were produced in late 2012. The next iteration of the chip, including back-end compatibility with the planned data acquisition system, and the path towards mass production and integration into the STS were the subjects of the work meeting. Details of the work meeting are collected at

https://indico.gsi.de/conferenceDisplay.py?confId=2416

22nd CBM Collaboration Meeting

23 – 27 September 2013, JINR, Dubna, Russia

https://indico.gsi.de/conferenceDisplay.py?confId=2054

IV All-Russian Methodology Workshop on Computer Aided Design of Integrated Circuits for Physical Instrumentation

29 – 31 October 2013, MEPHI, Moscow, Russia

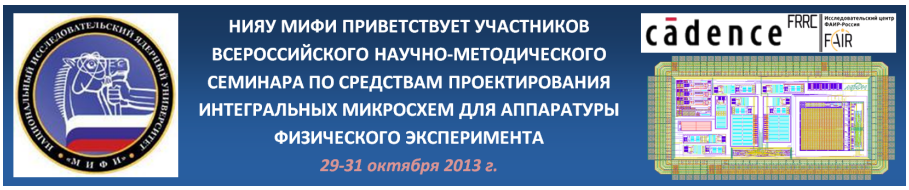

The 4th issue in this workshop series was held from 29 to 31 October 2013 in NRNU MEPHI. The Workshop was jointly organized by NRNU MEPHI, Cadence Design Systems (www.cadence.com) and FAIR-Russia Research centre (frrc.itep.ru). The aim of the Workshop was to introduce the Cadence methodology of computer-aided design (CAD) of mixed-signal integrated circuits and to conduct practical masterclasses to popularize microelectronic CAD for institutions of the Russian Federation, who participates in large projects, such as ones at FAIR and NIKA accelerator facilities.

http://cad.mephi.ru/eng/index.php

Workshop on FAIR Computing: Accelerated Computing via GPU

11 – 15 November 2013, Bose Institute, Kolkata, India

"FAIR Computing: Accelerated Computing via GPU", the 2nd workshop in the IFCC (Indo-Fair Coordination Centre) workshop series, was held at the Salt Lake Campus of Bose Institute during 11–15 November 2013, organized by Vikas Singhal (VECC). The workshop was focused on programming on heterogeneous computing platforms with many/multi core architectures and secondary processors like GPU, co-processors or "accelerators". Lectures and tutorials dealt with frameworks which are required for harnessing these types of processors, in particular for FAIR Computing. Experts both from industry (Intel, NVIDIA, AMD) and from research institutions (GSI, BARC) delivered lectures on the subject and acquainted everyone with the latest technology in the field of heterogeneous computing by providing hands-on on the particular hardware. The workshop was arranged in a 5-days extensive program. V. Friese, CBM computing coordinator, introduced into the requirements and challenges of FAIR Computing. During the workshop, the following topics were covered: Parallel computing on CPU by Intel and BARC experts, GPU computing in detail with CUDA and OpenACC, including hands-on on the NVIDIA TESLA GPU by the NVIDIA delegate, and OpenCL programming for heterogeneous platforms by the AMD delegate. In the closing ceremony, Dr. D. K. Srivastava, Director VECC, presented a memento to the delegates and certificates to all participants. The workshop was very much interactive as all the participants connected wireless to a dedicated 16-node cluster and two NVIDIA and AMD GPU servers, and did hands-on on their laptops. The about 25 participants to the workshop came from institutes across India like Kashmir University, Jammu University, IIT Indore, AMU, Guahati University, NIBM Kalyani, VECC, BI, and others. The workshop proved that collaboration between Industry and academics can be set up, in which both together start research and explore new possibility in the area of heterogeneous computing.

http://bic.boseinst.ernet.in/ifcc/

Successful in-beam tests of CBM/HADES prototype detectors

9 – 16 December 2013, COSY, Jülich Germany

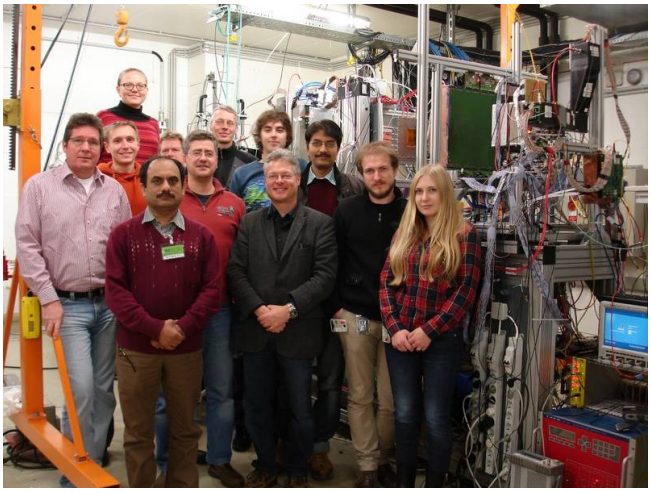

Three groups of the CBM and HADES collaborations have successfully tested recently developed prototype detectors in the 2.8 GeV high-intensity proton beam extracted from COSY. The beam was provided at Research Center Jülich, Germany, within a week long shift block dedicated to FAIR detector tests. On the test bench were several prototype modules of the CBM Silicon Tracking System, developed by the GSI team and built in Kharkiv, Ukraine, several prototypes of GEM detectors for the CBM muon detection system developed by the CBM groups at VECC, Kolkata, India, and GSI, and diamond detectors for the T0 determination in CBM and HADES developed by GSI and the Technical University Munich. The beam definition was made with the already approved scintillating fiber hodoscopes built at Wuppertal University. The team of more than 20 scientists, students and technical staff returned with a large data volume for detailed analyses of the detectors' performance.

Workshop on FAIR Physics: Compressed Baryonic Matter at FAIR

20 – 24 January 2014, Bose Institute Mayapuri, Darjeeling, India

The FAIR Physics workshop on CBM was held at the Darjeeling campus of Bose Institute. Around 25 student participants from all over India, mostly in their doctoral research period, and around 12 lecturers participated in this workshop. Most of the topics covered here started with introductory levels, and many of the lectures were actually delivered using the board instead of the presentation mode. The participants continued to interact during the whole length of the lectures. Along with theoretical discussions on finite temperature field theory, QCD, Lattice QCD, effective models and in-medium physics, experimental techniques in the area of particle identification, correlations and fluctuations, and jet physics were discussed in detail.

The CBM Collaboration

- **Aligarh, India, Department of Physics, Aligarh Muslim University**

  N. Ahmad, M.D. Azmi, M. Irfan, H. Jahan, M.M. Khan

- **Beijing, China, Department of Engineering Physics, Tsinghua University**

  Jianping Cheng, Zhi Deng, Xinjie Huang, Jin Li, Yuanjing Li, Yulan Li, Yi Wang, Xianglei Zhu

- **Bhubaneswar, India, Institute of Physics**

  D.P. Mahapatra, N.R. Panda, P.K. Sahu

- **Bucharest, Romania, Horia Hulubei National Institute of Physics and Nuclear Engineering (IFIN-HH)**

  C. Andrei, D. Bartoş, I. Berceanu, G. Caragheorgheopol, V. Cătănescu, F. Constantin, A. Herghelegiu, M. Petriş, A. Petrovici, M. Petrovici, A. Pop, C. Schiaua, M.-G. Târzilă

- **Bucharest, Romania, Atomic and Nuclear Physics Department, University of Bucharest**

  D. Argintaru, V. Baban, C. Beşliu, M. Călin, V. Covlea, T. Eşanu, A. Jipa, I. Lazanu, C. Ristea, O. Ristea, A. Scurtu

- **Budapest, Hungary, Eötvös Loránd University (ELTE)**

  M. Csanád, Á. Fülöp, A. Kiss

- **Budapest, Hungary, Institute for Particle and Nuclear Physics, Wigner Research Centre for Physics, Hungarian Academy of Sciences**

  T. Kiss, T. Tolyhi, Gy. Wolf

- **Chandigarh, India, Department of Physics, Panjab University**

  M.M. Aggarwal, A.K. Bhati, M. Kaur

- **Darmstadt, Germany, Facility for Antiproton and Ion Research in Europe GmbH (FAIR)**

  J. Eschke[1], W.F.J. Müller[1]

- **Darmstadt, Germany, GSI Helmholtzzentrum für Schwerionenforschung GmbH (GSI)**

  A. Abuhoza[8,2], M. Al-Turany, A. Andronic, R. Averbeck, E. Badura, T. Balog[9], D. Bertini, O. Bertini, S. Chatterji, M.I. Ciobanu[10], H. Deppe, H. Flemming, U. Frankenfeld, V. Friese, J. Frühauf, J. Hehner, J.M. Heuser, R. Holzmann, M. Ivanov, R. Karabowicz, M. Kiš, V. Kleipa, K. Koch, P. Koczoń, W. König, B.W. Kolb, D. Kresan, J. Kunkel, A. Lebedev[3], J. Lehnert, S. Löchner, A.M. Marin Garcia, S. Masciocchi, D. Miskowiec, W. Niebur, J. Pietraszko, J. Sánchez Rosado, S. Schatral[4], C.J. Schmidt, K. Schweda, S. Seddiki, I. Selyuzhenkov, A. Senger, P. Senger[2], C. Simons, I. Sorokin[2,5], D. Soyk, C. Sturm, A. Toia[2], F. Uhlig, I. Vassiliev, P. Zumbruch

- **Darmstadt, Germany, Institut für Kernphysik, Technische Universität Darmstadt**

  T. Galatyuk[1], A. Rost, F. Seck

- **Dresden, Germany, Institut für Strahlenphysik, Helmholtz-Zentrum Dresden-Rossendorf (HZDR)**

  K. Heidel, B. Kämpfer[11], R. Kotte, A. Laso Garcia[11], L. Naumann, C. Wendisch, J. Wüstenfeld

- **Dubna, Russia, Laboratory of Information Technologies, Joint Institute for Nuclear Research (JINR-LIT)**

  T. Ablyazimov, P. Akishin, E. Akishina, T. Akishina, E. Alexandrov, I. Alexandrov, O. Derenovskaya, I. Filozova, Valery Ivanov, Victor Ivanov, P. Kisel, G. Kozlov, G. Ososkov, A. Raportirenko, P. Zrelov

- **Dubna, Russia, Veksler and Baldin Laboratory of High Energy Physics, Joint Institute for Nuclear Research (JINR-VBLHEP)**

  Yu. Anisimov, S. Avdeev, A. Bychkov, V. Chepurnov, S. Chernenko, K. Davkov, V. Davkov, D. Dementiev, S. Dubnichka, A. Dubnichkova, O. Fateev, V. Golovatyuk, Yu. Gusakov, A. Ierusalimov, E.-M. Ilgenfritz, V. Karnaukhov, G. Kekelidze, V. Kirakosyan, P. Kurilkin, V. Ladygin, A. Malakhov, V. Mialkovski, Yu. Murin, S. Parzhitskiy, D. Peshekhonov, V. Peshekhonov, E. Plekhanov, S. Razin, A. Shabunov, N. Shumeiko, I. Tsakov, Yu. Zanevsky, A. Zinchenko, V. Zryuev

- **Frankfurt, Germany, Frankfurt Institute for Advanced Studies, Goethe Universität Frankfurt (FIAS)**

  V. Akishina[3,1], M. Bach, J. de Cuveland, D. Eschweiler, S. Gorbunov, D. Hutter, E. Iakovleva, S. Kalcher, I. Kisel, M. Kretz, I. Kulakov[1], V. Lindenstruth[1], V. Vovchenko, M. Zyzak[1]

- **Frankfurt, Germany, Institut für Kernphysik, Goethe Universität Frankfurt**

  S. Amar-Youcef, H. Appelshäuser, A. Arend, T. Balle, C. Blume, H. Büsching, M. Deveaux, P. Dillenseger, D. Doering, I. Fröhlich, P. Ghosh[1], E. Hellbär, A. Kotynia[1], M. Koziel, E. Krebs, G. Kretschmar, P. Larionov[1], Qiyan Li[6], B. Linnik, H. Malygina[5,1], J. Markert, J. Michel, B. Milanović, C. Müntz, J. Pieper, P. Reichelt, F. Roether, M. Singla[1], S. Strohauer, J. Stroth[1], M. Tanha, T. Tischler, M. Wiebusch

- **Frankfurt, Germany, Institute for Computer Science, Goethe Universität Frankfurt**

  S. Böttger, T. Breitner, H. Engel, C. García Chávez, J. Gebelein, A. Gómez Ramírez, T. Janson, U. Kebschull, C. Lara, J. Lehrbach, S. Manz, A. Oancea

- **Gatchina, Russia, Petersburg Nuclear Physics Institute, NRC Kurchatov Institute (PNPI)**

  V. Baublis, V. Dobyrn, V. Golovtsov, Vladimir Ivanov, A. Khanzadeev, L. Kochenda, B. Komkov, P. Kravtsov, E. Kryshen, L. Kudin, N. Miftakhov, V. Nikulin, E. Rostchin, Yu. Ryabov, V. Samsonov, O. Tarassenkova, S. Volkov, E. Vznuzdaev, M. Vznuzdaev, M. Zhalov

- **Gießen, Germany, Justus-Liebig-Universität Gießen**

  J. Bendarouach, C.A. Deveaux, M. Dürr, C. Höhne, S. Lebedev[3], E. Lebedeva, T. Mahmoud

- **Guwahati, India, Department of Physics, Gauhati University**

  B. Bhattacharjee, B. Debnath, K. Dey, R. Talukdar

- **Hefei, China, Department of Modern Physics, University of Science & Technology of China (USTC)**

  Ping Cao, Hongfang Chen, Cheng Li, Ming Shao, Yongjie Sun, Zebo Tang, Yifei Zhang

- **Heidelberg, Germany, Physikalisches Institut, Universität Heidelberg**

  I. Deppner, D. Gottschalk, N. Herrmann, Tae Im Kang, P.-A. Loizeau, C. Simon, Ya Peng Zhang

- **Heidelberg, Germany, Zentrales Institut für Technische Informatik, Universität Heidelberg, Standort Mannheim**

  U. Brüning, P. Fischer, C. Kreidl, M. Krieger, F. Lemke, I. Peric, D. Wohlfeld

- **Jaipur, India, Physics Department, University of Rajasthan**

  R. Raniwala, S. Raniwala

- **Jammu, India, Department of Physics, University of Jammu**

  A. Bhasin, A. Gupta, S. Mahajan, B.V.K.S. Potukuchi, S.S. Sambyal, M.K. Sharma

- **Katowice, Poland, Institute of Physics, University of Silesia**

  A. Bubak, A. Grzeszczuk, E. Kaptur, S. Kowalski, K. Schmidt, E. Stephan, W. Zipper

- **Kharagpur, India, Indian Institute of Technology**

  P. Banerjee, T.K. Bhattacharyya, A. Haldar, S. Haldar, A.K. Singh

- **Kolkata, India, Department of Physics, Bose Institute**

  R. Adak, S. Das, S.K. Ghosh, S. Raha, R. Ray, S. Samanta

- **Kolkata, India, Department of Physics and Department of Electronic Science, University of Calcutta**

  S. Bandyopadhyay, A. Bhattacharyya, A. Chakrabarti, Sanatan Chattopadhyay, G. Gangopadhyay

- **Kolkata, India, Variable Energy Cyclotron Centre (VECC)**

  Z. Ahammed, P.P. Bhaduri, Subhasis Chattopadhyay, M. Dey, A.K. Dubey, S.A. Khan, S. Mandal, T. Nayak, S. Pal, A. Roy, J. Saini, R.N. Singaraju, V. Singhal, Y.P. Viyogi

- **Kraków, Poland, AGH University of Science and Technology (AGH)**

  M. Baszczyk, A. Drozd, J. Gajda, P. Gryboś, K. Kasiński, R. Kłeczek, P. Kmon, W. Kucewicz, P. Maj, P. Otfinowski, J. Rauza, R. Szczygieł, M. Żołądź

- **Kraków, Poland, Marian Smoluchowski Institute of Physics, Jagiellonian University**

  M. Adamczyk, T. Barczyk, J. Brzychczyk, L. Dutka, Z. Majka, R. Najman, R. Płaneta, Z. Sosin, P. Staszel, A. Wieloch

- **Kyiv, Ukraine, High Energy Physics Department, Kiev Institute for Nuclear Research (KINR)**

  M. Borysova, A. Kovalchuk, V. Kyva, V. Militsija, I. Panasenko, M. Pugach, V. Pugatch, D. Storozhyk

- **Kyiv, Ukraine, Department of Nuclear Physics, Taras Shevchenko National University of Kyiv**

  O. Bezshyyko, L. Golinka-Bezshyyko, I. Kadenko, Y. Onishchuk, V. Plujko

- **Moscow, Russia, Institute for Nuclear Research (INR)**

  O. Andreeva, D. Finogeev, M. Golubeva, F. Guber, A. Ivashkin, O. Karavichev, T. Karavicheva, E. Karpechev, A. Kurepin, A. Maevskaya, O. Petukhov, I. Pshenichnov, A. Reshetin, A. Sadovsky, N. Topil'skaya, E. Usenko

- **Moscow, Russia, Institute for Theoretical and Experimental Physics (ITEP)**

  A. Akindinov, S. Belogurov, A. Chernogorov, D. Golubkov, F. Khasanov, S. Kiselev, A. Kolosova, I. Korolko, D. Malkevich, K. Mikhailov, A. Nedosekin, E. Ovcharenko, V. Plotnikov, M. Prokudin, I. Rostovtseva, A. Semennikov, R. Sultanov, Yu. Zaitsev

- **Moscow, Russia, National Research Nuclear University MEPhI**

  E. Atkin, Yu. Bocharov, E. Malankin, O. Malyatina, D. Normanov, D. Osipov, A. Petrovskiy, V. Shumikhin, A. Simakov, M. Strikhanov

- **Moscow, Russia, National Research Centre "Kurchatov Institute"**

  D. Blau, A. Kazantsev, V. Manko, I. Yushmanov

- **Moscow, Russia, Skobeltsyn Institute of Nuclear Phyiscs, Lomonosov Moscow State University (SINP-MSU)**

  N. Baranova, D. Karmanov, M. Korolev, M. Merkin, V. Popov, A. Voronin

- **Münster, Germany, Institut für Kernphysik, Westfälische Wilhelms Universität Münster**

  R. Berendes, C. Bergmann, D. Emschermann, N. Heine, Ch. Klein-Bösing, W. Verhoeven, J.P. Wessels

- **Obninsk, Russia, National Research Nuclear University**

  N. D'Ascenzo, A. Galkin, D. Ossetski, V. Saveliev

- **Prag, Czech Republic, Czech Technical University (CTU)**

  V. Petráček, V. Pospisil, L. Škoda

- **Protvino, Russia, Institute for High Energy Physics (IHEP)**

  S. Golovnya, S. Gorokhov, A. Kiryakov, I. Lobanov, E. Lobanova, V. Rykalin, S. Sadovsky, Yu. Tsyupa, A. Vorobiev

- **Pusan, Korea, Pusan National University (PNU)**

  Kyung-Eon Choi, Jongsik Eum, Sanguk Won, Jun-Gyu Yi, In-Kwon Yoo

- **Řež, Czech Republic, Nuclear Physics Institute, Academy of Sciences of the Czech Republic**
  A. Kugler, V. Kushpil, V. Mikhaylov, O. Svoboda, P. Tlustý
- **Split, Croatia, University of Split**
  M. Anđelić, I. Carević, M. Dželalija
- **Srinagar, India, Department of Physics, University of Kashmir**
  F. Ahmad, S. Ahmad, S. Bashir, M.F. Mir, W. Raja
- **St. Petersburg, Russia, Ioffe Physico-Technical Institute, Russian Academy of Sciences**
  V. Eremin, E. Verbitskaya
- **St. Petersburg, Russia, V.G. Khlopin Radium Institute (KRI)**
  O. Batenkov, V. Jakovlev, V. Kalinin, A. Veshikov
- **St. Petersburg, Russia, St. Petersburg State Polytechnic University (SPbSPU)**
  A. Berdnikov, Y. Berdnikov
- **Strasbourg, France, Institut Pluridisciplinaire Hubert Curien (IPHC), IN2P3-CNRS and Université de Strasbourg**
  G. Claus, A. Dorokhov, W. Dulinski, M. Goffe, A. Himmi, K. Jaaskelainen, F. Rami, I. Valin, M. Winter
- **Tübingen, Germany, Physikalisches Institut, Eberhard Karls Universität Tübingen**
  B. Heß, E. Lavrik, A. Lymanets[5], H.R. Schmidt, J. Wiechula
- **Varanasi, India, Department of Physics, Banaras Hindu University**
  A. Prakash, B.K. Singh, C.P. Singh
- **Warsaw, Poland, Institute of Electronic Systems, Warsaw University of Technology**
  A. Byszuk, G. Kasprowicz, J. Pluta, K. Poźniak[7], R. Romaniuk, D. Wielanek, W. Zabołotny[7]
- **Warsaw, Poland, Institute of Experimental Physics, University of Warsaw**
  M. Kirejczyk, T. Matulewicz, K. Piasecki, J. Rożynek, B. Sikora, K. Siwek-Wilczyńska, I. Skwira-Chalot, J. Tarasiuk, A. Turowiecki, K. Wiśniewski
- **Wuhan, China, College of Physical Science and Technology, Central China Normal University (CCNU)**
  Xu Cai, Guangming Huang, Feng Liu, Dong Wang, Yaping Wang, Changzhou Xiang, Nu Xu, Zhongbao Yin, Daicui Zhou
- **Wuppertal, Germany, Fachbereich Physik, Bergische Universität Wuppertal**
  K.-H. Becker, K.-H. Kampert, J.M. Kopfer, C. Pauly, J. Pouryamout, S. Querchfeld, J. Rautenberg, S. Reinecke

Additional affiliations:
[1] GSI Helmholtzzentrum für Schwerionenforschung GmbH (GSI), Darmstadt, Germany
[2] Institut für Kernphysik, Goethe Universität Frankfurt, Frankfurt, Germany
[3] Laboratory of Information Technologies, Joint Institute for Nuclear Research (JINR-LIT), Dubna, Russia
[4] Zentrales Institut für Technische Informatik, Universität Heidelberg, Standort Mannheim, Heidelberg, Germany
[5] High Energy Physics Department, Kiev Institute for Nuclear Research (KINR), Kyiv, Ukraine
[6] College of Physical Science and Technology, Central China Normal University (CCNU), Wuhan, China
[7] Institute of Experimental Physics, University of Warsaw, Warsaw, Poland
[8] also: King Abdulaziz City for Science and Technology (KACST), Riyadh, Saudi Arabia
[9] also: Comenius University in Bratislava, Bratislava, Slovakia
[10] also: Institute of Space Science, Bucharest, Romania
[11] also: Technische Universität Dresden, Dresden, Germany

Contacts

Chairman of the Collaboration Board
Yogendra P. Viyogi
viyogi@veccal.ernet.in

Spokesman
Peter Senger
p.senger@gsi.de

Deputy Spokesman
Yuri Zaitsev
zaitsev@itep.ru

Deputy Spokesman
Subhasis Chattopadhyay
sub@veccal.ernet.in

Technical Coordinator
Walter Müller
w.f.j.mueller@gsi.de

Physics Coordinator
Volker Friese
v.friese@gsi.de

Ressource Coordinator
Jürgen Eschke
j.eschke@gsi.de

Management Board
S. Chattopadhyay, N. Herrmann, M Petrovici, F. Rami, J. Stroth, Y. Zaitsev

http://www.fair-center.eu/for-users/experiments/cbm.html

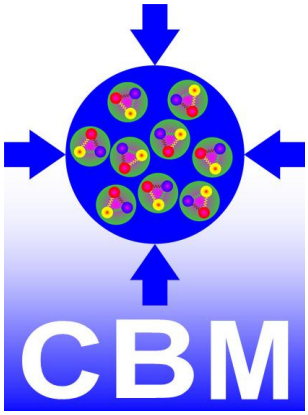
CBM


FAIR


HELMHOLTZ
GEMEINSCHAFT


GSI


Bundesministerium
für Bildung
und Forschung


HIC
for
FAIR
Helmholtz International Center

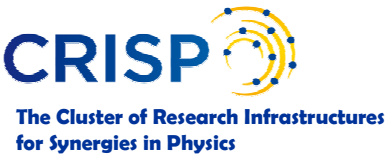
CRISP
The Cluster of Research Infrastructures
for Synergies in Physics


Study of Strongly Interacting Matter
HadronPhysics